

Biomimetic Growth and Morphology Control of Calcium Oxalates

D I S S E R T A T I O N

zur Erlangung des akademischen Grades

Doctor rerum naturalium
(Dr. rer. nat.)

vorgelegt

der Fakultät Mathematik und Naturwissenschaften
der Technischen Universität Dresden

von

M.Sc. Annu Thomas

geboren am 06.12.1979 in Calicut, Indien

Eingereicht am 30.07.2009

Die Dissertation wurde in der Zeit von Oktober / 2005 bis
Juli / 2009 im Max-Planck Institut für Chemische Physik fester Stoffe angefertigt.

Tag der Verteidigung: 16.11.2009

Gutachter:

Prof. Dr. Rüdiger Kniep

Prof. Dr. Stefan Kaskel

Acknowledgements

First and foremost, I would like to extend my deep sense of gratitude towards Prof. Dr. Rüdiger Kniep for his guidance, creative suggestions and tolerance for my research work. It is an honor to be his student and a prestigious bliss to be going forth with the valuable skills and expertise he has imparted on me during the past years.

I thank the International Max Planck Research School (IMPRS) for admitting me into the program and giving me an opportunity to carry out my Doctoral studies here at the Max-Planck Institute in Dresden.

I especially thank my supervisor Dr. Oliver Hochrein for his advices and constructive discussions even after leaving the institute.

My special thanks to Dr. Paul Simon and Dr. Wilder Carrillo-Cabrera for carrying out the TEM measurements and their guidance in my work. I acknowledge them with much appreciation for the valuable corrections they made on my thesis.

My sincere thanks to Dr. Stefan Hoffmann for the productive and fruitful scientific discussions and helping me to tackle with innumerable problems many a time.

I would also like to thank Ms. Jana Buder, Dr. Ya-Xi Huang and Ms. Elena Rosseeva for their help during many phases of my lab work.

I thank Dr. Dirk Zahn and Mr. Patrick Duchstein for carrying out the theoretical calculations for my work.

I also thank Ms. Susanne Zücker, Ms. Katrin Demian, Ms. Claudia Strohbach, Ms. Katarina Klein and Ms. Tatjana Vögel for helping me to do all the administrative works during the initial days in Dresden.

I thank all my colleagues for melting the differences during the nice gatherings in the institute. You all have truly made me feel at home!

Special thanks to Dr. Horst Borrmann, Dr. Raul Cardoso-Gil, Dr. Yurii Prots, Mr. Steffen Hückmann, Dr. Ulrich Schwarz, Dr. Gudrun Auffermann, Ms. Ulrike Schmidt, Ms. Anja Völzke, Dr. Ulrich Burkhardt, Ms. Petra Scheppan and Ms. Susann Müller, for the time to time assistance in characterization methods.

Let me also thank my parents and sisters for their permissiveness to send me so far away in pursuit of my research goals. I also remember my parents-in-law with gratitude for their love, support and prayers during my doctoral study.

Nothing would have been possible if not for my better half who shares my passion for research and has been implausibly supportive all along even though we missed the beauty of being together after our wedding and initial years of our marriage. I owe you so much, Anish, more than words can say and thanks a million for being there for me always.

Last but not the least; I would like to thank all my friends who made my stay in Germany a pleasant and comfortable one.

Thank you my God for guiding me throughout.....

CONTENTS

1 INTRODUCTION	1
1.1 Biomineralization: The art of Nature!	1
1.2 Bioactivity of calcium oxalates: A curse or a boon?	2
1.2.1 Crystal chemistry of calcium oxalates and morphological aspects	3
1.2.2 Comparison of the crystal structures: COM, COD and COT	10
1.2.3 Anhydrous calcium oxalate	12
1.2.4 Morphological aspects of biogenic calcium oxalates	13
1.2.5 Biomimetic Morphogenesis: Self-assembly or self-organization	17
1.3 Overview on calcium oxalates growth	20
1.3.1 Crystallization of calcium oxalates: The conventional precipitation	20
1.3.2 Gel-mediated growth of calcium oxalates: Bio inspired strategy	20
1.4 Objectives	24
1.4.1 Crystal structure of anhydrous calcium oxalate	24
1.4.2 Additives as growth modifiers	25
1.4.2.1 Control of morphology of calcium oxalates in the presence of PAA	25
1.4.2.2 “Organic” gel-mediated growth of calcium oxalates	26
2 EXPERIMENTAL SECTION	27
2.1 Crystallization of calcium oxalates by slow evaporation of the solvent	27
2.1.1 Growth of calcium oxalates without additives	27
2.1.2 Growth of calcium oxalates in the presence of PAA	27
2.2 Biomimetic growth of calcium oxalates: The double diffusion technique	28
2.3 Characterization techniques	29
2.3.1 Optical microscopy	29
2.3.2 Powder X-ray diffraction	29
2.3.3 Chemical analysis	30
2.3.4 FT-IR, Raman spectroscopy	30
2.3.5 Difference thermal analysis (DTA), thermogravimetry (TG)	31
2.3.6 Scanning electron microscopy (SEM)	31
2.3.7 Transmission electron microscopy (TEM)	31

3 RESULTS AND DISCUSSIONS	32
3.1 Growth of calcium oxalates without additives	32
3.1.1 The effect of pH and initial supersaturation	32
3.1.2 Characterization of calcium oxalate monohydrate (COM)	35
3.2 Anhydrous calcium oxalate	39
3.2.1 Synthesis and characterization	39
3.2.2 Crystal structure from a combination of atomistic simulations and rietveld refinements	41
3.3 Growth of calcium oxalates in the presence of PAA	46
3.3.1 The effect of pH and initial supersaturation	46
3.3.2 Morphological control of COD	67
3.3.3 Summary	94
3.4 Biomimetic approach towards Calcilogenesis: The double diffusion technique ..	96
3.4.1 Morphological aspects of calcium oxalates grown in agar gel	96
3.4.1.1 The effect of concentration of agar	96
3.4.1.2 The effect of pH	99
3.4.1.3 Agar gel of pH 8.5	99
3.4.1.4 Agar gel of pH 11.5	125
3.4.1.5 Summary and discussion of results	136
3.4.2 Growth of calcium oxalates in other organic gels	142
3.4.2.1 Agarose	142
3.4.2.2 Carrageenan	143
3.4.2.3 Gelatine	144
4 CONCLUSION AND OUTLOOK	146
5 REFERENCES	148
6 APPENDIX	166

1 Introduction

1.1 Biomineralization: The art of Nature!

According to its most broad definition, “Biomineralization” refers to the formation of inorganic minerals with fascinating morphologies, hierarchical organization and superior properties, with the aid of organic materials in nature [1-3]. The nucleation, growth, type of polymorph and orientation of the inorganic compounds is highly controlled by the biomolecules incarcerated. Some of the biominerals found in nature which are in fact highly organized organic/inorganic hybrid materials with remarkable properties are listed in table 1.1.

Table 1.1. Examples for inorganic mineral phases in biological systems.

Mineral	Formula	Organism	Function
Calcite, aragonite	CaCO_3	Coccoliths, Mollusks, Mammals	Exoskeleton Otoconia – gravity receptor
Hydroxyapatite (HAP)	$\text{Ca}_5(\text{PO}_4)_3(\text{OH})$	Vertebrates	Endoskeleton,teeth
Fluorapatite (FAP)	$\text{Ca}_5(\text{PO}_4)_3(\text{F})$	Shark, conodont	Teeth enamel
Gypsum	$\text{CaSO}_4 \cdot 2\text{H}_2\text{O}$	Jellyfish	Gravity receptor
Silica	$\text{SiO}_2 \cdot n\text{H}_2\text{O}$	Diatoms, Radiolaria	Exoskeleton
Magnetite	Fe_3O_4	Bacteria	Magnetotaxis
Ferrihydrite	$\text{Fe}_2\text{O}_3 \cdot n\text{H}_2\text{O}$	(In)Vertebrates	Fe-storage

The extraordinary properties and functions of biominerals have piqued the curiosity of researchers which paved way to the development of “Biomimetic materials chemistry”. Adapting the concepts of biomineralization such as understanding the role of organic phases in controlling the structure and phase of inorganic materials develops novel approaches to “tailor-made” inorganic materials [4,5]. However, it is usually intricate to achieve the assembly of the structural inorganic matrix over several hierarchy levels by synthetic routes as the “organic” part in a biogenic system is usually a mixture of many biopolymers in tiny quantities. Nevertheless, a model system which mimics much aspects of a biomineralization process can be considered successful even if the formation of the natural archetype is not yet completely understood. On the other hand, a model system, which mimics organic and/or inorganic matrix, is an efficient way to understand biomineralization processes and to mimic them. An excellent prototype to such an approach is the biomimetically grown fluorapatite-gelatine composite aggregates

which mimic the processes involved in bone and tooth formation by Kniep and co-workers [6-8]. This biomimetic model system is perfectly suited to unravel the complexities related to osteo- and dentino-genesis.

A systematic investigation of the morphological evolution and the interaction of organic components with inorganic phases are essential for understanding biomineralization and developing biomimetic materials processing. Synthetic polymers with precisely known functions and solution behaviours are better choices in terms of a suitable and simplified model system to understand the polymer-mineral interactions. Off late, biopolymers and various synthetic polymers have been widely used for the formation of unusual hierarchical superstructures of CaCO_3 [9], BaCO_3 [10], BaSO_4 [11], $\text{Ca}_8\text{H}_2(\text{PO}_4)_6 \cdot \text{H}_2\text{O}$ [12] and $\text{CaC}_2\text{O}_4 \cdot 2\text{H}_2\text{O}$ [13]. But it is worth to mention that calcium oxalates are less studied among the crystallization of other calcium salts. Compared with tooth, bone, and shell formation, calcium oxalate crystallization is a more specialized example of biomineralization due to their pathogenic role as kidney- or urinary- stones.

1.2 Bioactivity of calcium oxalates: A curse or a boon?

An intriguing aspect of biogenesis of calcium oxalates is that it constitutes a normal physiological process in plants and fungi, where as it is manifested in the pathophysiology of “urolithiasis” in humans and livestock. Therefore, biomineralization can be physiological or pathological and it is very necessary to delineate the extent of mineralization to understand the mechanism of “pathological biomineralization”. Pertinent examples of pathological calcifications are listed (Table 1.2).

Table 1.2. List of pathological calcifications.

Pathogenic calculi	Inorganic constituents
Uroliths/ Urinary stones	CaOx^\ddagger , CaP^*
Choleliths/ Gall stones	CaOx , CaP , CaCO_3
Rhinoliths/ Nasal cavity stones	CaOx , CaP , CaCO_3
Sialoliths/ Salivary stones	CaOx , CaP , CaCO_3
Odontoliths/ Dental pulp stones	CaP , CaCO_3
Pneumoliths/ Lung stones	$\text{CaCO}_3 + \text{MgCO}_3$
Cardiolites/ Cardiac valve concretions	CaP , CaCO_3
Brain Sand/ Pineal gland calcification	CaP , CaCO_3

‡ Ox- Oxalates, * P- Phosphates

All the pathological calcifications consist of calcium-phosphates (CaP), -carbonates (CaCO_3) and -oxalates (CaOx) amalgamated with organic macromolecules.

The reasons and mechanisms of the processes that generate uroliths, gallstones, and other concretions still remain a point of discussion. Urolithiasis which is often called the “disease of civilization” refers to the formation of stones (calculi) in kidneys, urinary tract, ureter or bladder [14,15].

Approximately 70% of all kidney stones are composed of calcium oxalates either alone or mixed with calcium phosphates [16]. Other inorganic phases such as struvite are also detected (Fig. 1.1). Calcium phosphates which forms a minor fraction is usually present as apatite (hydroxyapatite or carbonateapatite) sometimes as brushite ($\text{CaHPO}_4 \cdot 2\text{H}_2\text{O}$) and rarely as whitlockite ($\text{Ca}_3(\text{PO}_4)_2$). Hydroxyapatite ($\text{Ca}_5(\text{PO}_4)_3(\text{OH})$), is present in stones formed in sterile urine and carbonateapatite (with a varying content of carbonate ions), in stones associated with infection.

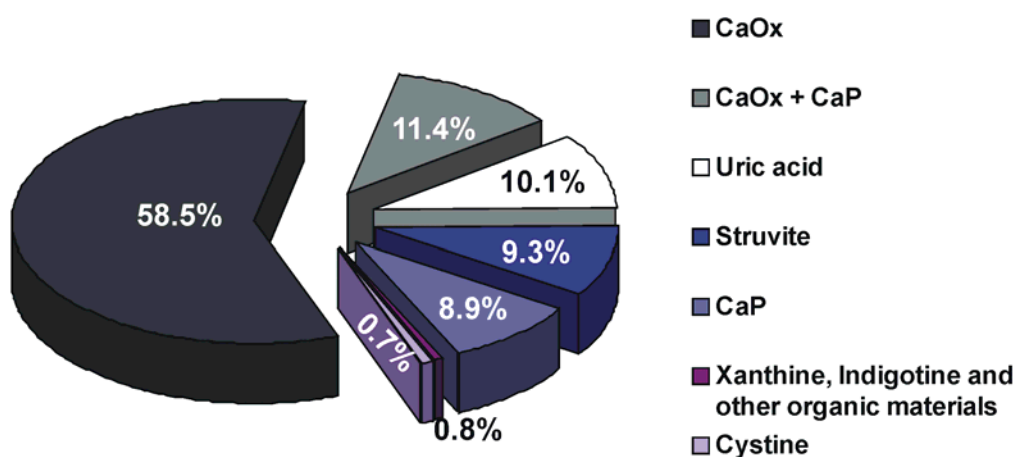


Fig. 1.1. Composition of urinary stones. Calcium oxalates (CaOx) and calcium phosphates (CaP) constitute the major fraction of urinary stones [16].

Oxalate occurs in plants as oxalic acid, or as salts of sodium, potassium, magnesium and calcium. The amount of oxalate in plants can range from a few percent of dry weight up to 80% of the total weight of the plant as with some cacti. Therefore, apart from the pathogenic activity of calcium oxalates, it is the most common insoluble mineral found in higher plants that help in the calcium regulation and protection against herbivores [17-19].

1.2.1 Crystal chemistry of calcium oxalates and morphological aspects

In nature, calcium oxalate exists in three different hydration states: the monoclinic calcium oxalate monohydrate (COM, $\text{CaC}_2\text{O}_4 \cdot \text{H}_2\text{O}$, whewellite), which is

thermodynamically the most stable phase at room temperature, the tetragonal calcium oxalate dihydrate (COD, $\text{CaC}_2\text{O}_4 \cdot (2+x)\text{H}_2\text{O}$; $x \leq 0.5$, weddellite) and the triclinic calcium oxalate trihydrate (COT, $\text{CaC}_2\text{O}_4 \cdot (3-x)\text{H}_2\text{O}$; $x < 0.5$, caoxite).

The generally accepted crystal structure analysis of COM was performed by Tazzoli and Domeneghetti [20,21] (JCPDS database entry 75-1313). Accordingly, COM relates to the prismatic class of the monoclinic system; there is one symmetry plane and the second-order axis (b) is perpendicular to the symmetry plane. The elementary cell has the symmetry space group $P2_1/c$ with the parameters $a = 6.290(1) \text{ \AA}$, $b = 14.583(1) \text{ \AA}$, $c = 10.116(1) \text{ \AA}$, $\beta = 109.46^\circ$, $Z = 8$, $V = 876.228 \text{ \AA}^3$. The unit cell and the calcium coordination polyhedron are shown in figure 1.2 (A,B).

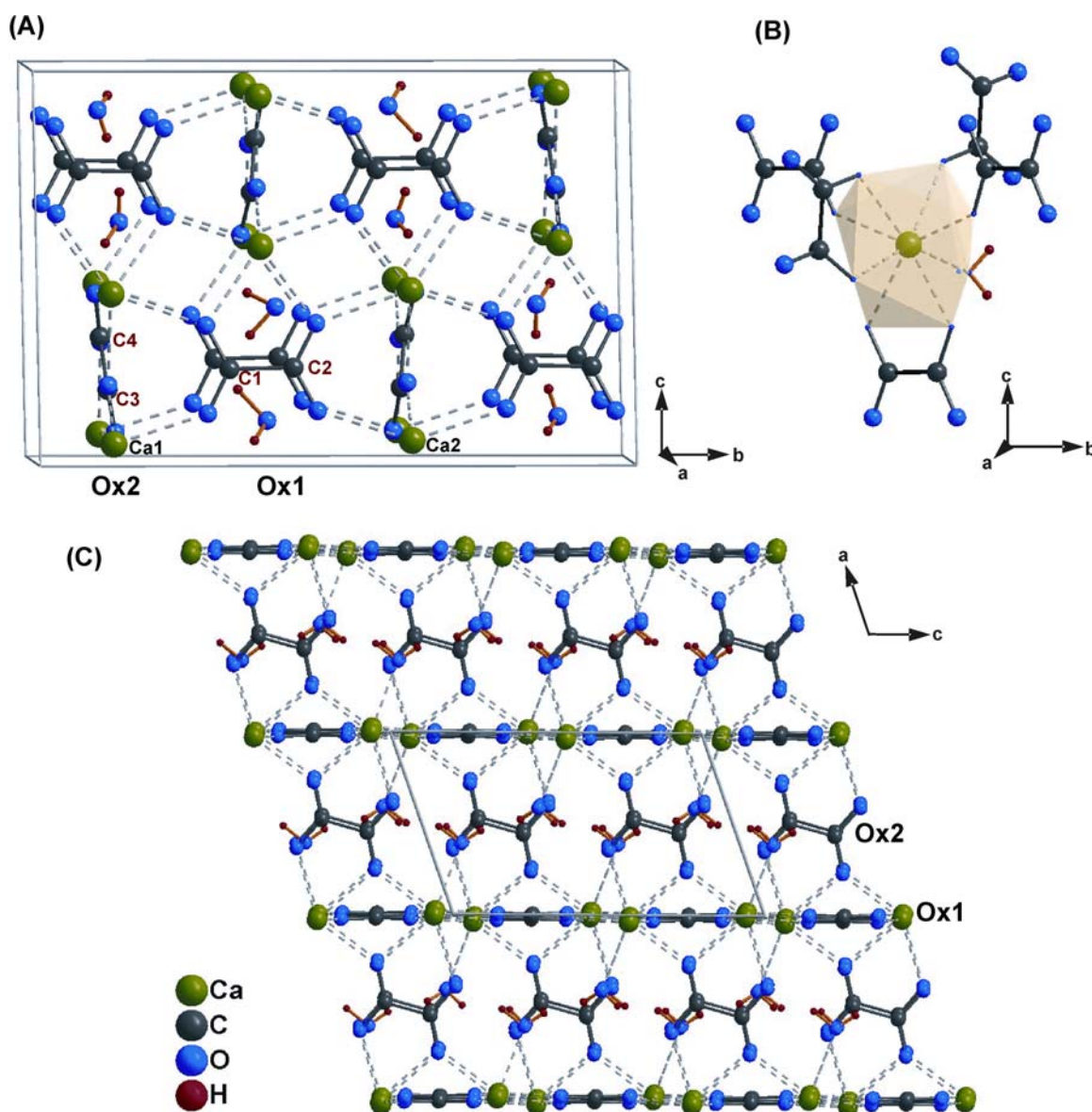


Fig. 1.2. Crystal structure of COM: (A) unit cell of COM, (B) CaO8 polyhedron, (C) stacking of Ca together with Ox groups along [100].

The coordination polyhedra of the pseudo-equivalent atoms Ca1 and Ca2 are distorted square antiprisms with each Ca ion coordinated by eight oxygen atoms. Two oxalate ions are two-fold coordinating to calcium whereas three oxalate ions act as monodentate ligands (Fig. 1.2 B). The eighth oxygen atom is from a water molecule. Each Ca polyhedron shares three edges with three adjacent Ca polyhedra. In this way, polyhedral layers are formed running parallel to (100). There are crystallographically two non-equivalent oxalate ions, Ox1 and Ox2 which are in two different structural environments: Ox1 is in a planar coordination by six calcium ions and Ox2 is surrounded by four calcium ions and two additional water molecules are connected *via* hydrogen bonds to the oxygen atoms of Ox2 (further details in section 3.2.2, Figs. 3.2.3 and 3.2.4). Ox1 units are disposed parallel to the (100) plane with the C1-C2 bonds nearly parallel to the *b*-axis (Fig. 1.2 A). Ox2 units alternate with water molecules and form ribbons lying in the (010) plane running along *c*. The Ca-Ox1 layers are connected to one another through Ox2 and the water molecules (Fig. 1.2 C). In other words, the crystal structure of COM contains layers consisting of Ca together with Ox1 (layer1) and of Ox2 (layer2), respectively, which are stacked along [100].

Rarely known is that COM presents three polymorphs. One of them is obtained only by the dehydration of the dihydrate form of calcium oxalate at 118 °C [22]. It has orthorhombic symmetry with lattice parameters, $a = 12.088(9)$ Å, $b = 10.112(7)$ Å, $c = 14.634(12)$ Å, $\alpha = \beta = \gamma = 90^\circ$ and the space groups $A2_1am$, $Ama2$ or $Amam$ are reported to be possible, whereby only $Amam$ has a centre of symmetry like the space group of the parent weddellite structure.

The other two phases transform reversibly in the temperature range 38 to 45 °C. Both have monoclinic structures and are designated as basic/high temperature (HT) structure (stability range *ca.* 45 to 152 °C) and the derivative/low temperature (LT) structure (stability range *ca.* 20 to 45 °C) according to Deganello [23-25]. The transition from the HT to the LT form takes place upon ordering below 45 °C. The HT form possesses a unit cell with *b*-parameter one half of that of the LT form (Table 1.3).

This space group setting and the accompanying unit cell choice differs from those proposed by Tazzoli and Domeneghetti ($P2_1/c$, $a = 6.290(1)$ Å, $b = 14.583(1)$ Å, $c = 10.116(1)$ Å, $\beta = 109.46^\circ$, $Z = 8$) [20]. The crystal structures of both collected at room temperature are identical. Tazzoli and Domeneghetti [20] report the space group of

whewellite as $P2_1/c$, actually the same space group (C_{2h}^5) as $P2_1/n$ but with a different choice of axes.

Table 1.3. Unit cell parameters for the HT and the LT structures of whewellite.

Whewellite	a (Å)	b (Å)	c (Å)	β (°)	Space group	Z
Basic structure (HT)	9.978(1)	7.295(1)	6.291(1)	107.04(2)	$I2/m$	4
Derivative structure (LT)	9.9763(3)	14.5884(4)	6.2913(3)	107.03(2)	$P2_1/n$	8

For both LT and HT forms [23-25], like the Tazzoli structure [20], there are two sets of crystallographically non-equivalent oxalate groups which are in a nearly perfect orthogonal orientation to one another, Ox1 and Ox2. Both the oxalate groups together with Ca layer along the $[-101]$ direction (Fig. 1.3 A,B).

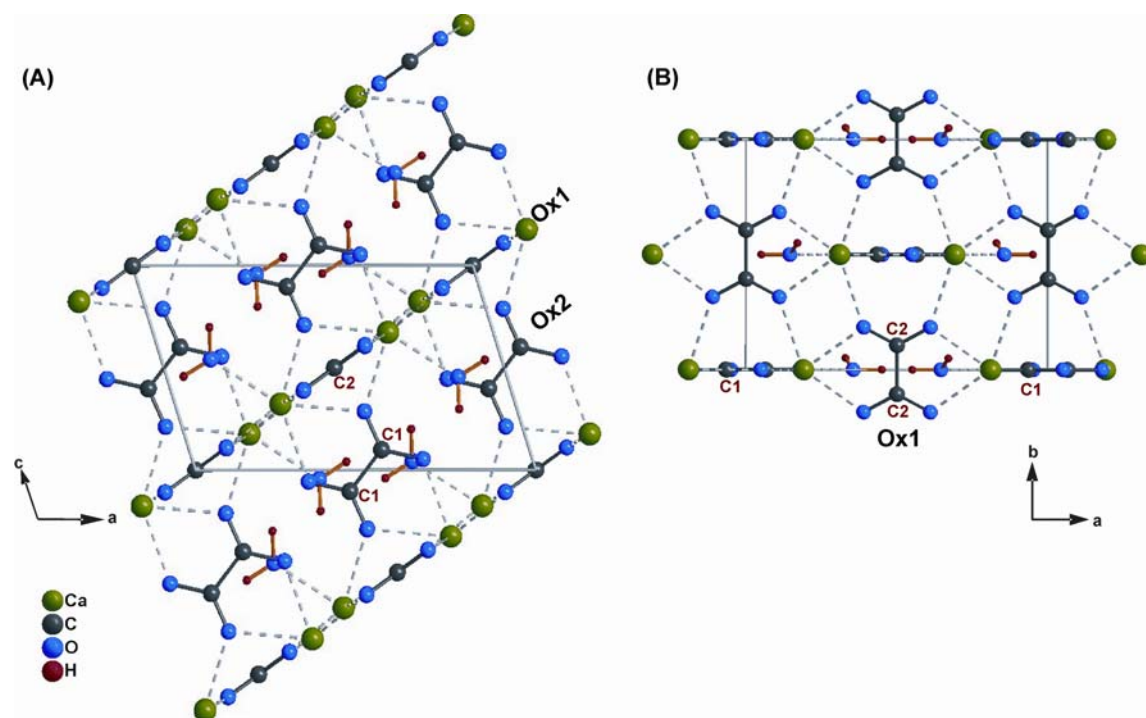


Fig. 1.3. The crystal structure of COM according to Deganello [25]. (A) The stacking of Ca together with Ox groups along $[-101]$. (B) The crystallographic projection along $[001]$.

Both the LT- and HT-forms are identical with respect to the ion coordination as well. The main difference concerns Ox1. A comparison of the oxalate groups is depicted in figure 1.4. In the LT form, Ox1 ions suffer a slight distortion of bond angles (a few tenths of a degree) and bond distances (differences lower than 0.01 Å) (Fig. 1.4).

At the same time, they get slightly off the (-101) crystal plane and are no longer coplanar. In this way, they lose the $2/m$ local symmetry and the dimensions of the b -axis are doubled. Whereas for the HT form, the space group is $I2/m$ (C_{2h}^3) and Ox2 is bisected by a mirror plane normal to the C-C bond which is located along the unique monoclinic axis. At the same time Ox1 is located on the mirror plane and the C-C bond is bisected by a two fold crystallographic axis (Fig. 1.3 B). This results in identical C-O distances and planarity of Ox1 (Fig. 1.4).

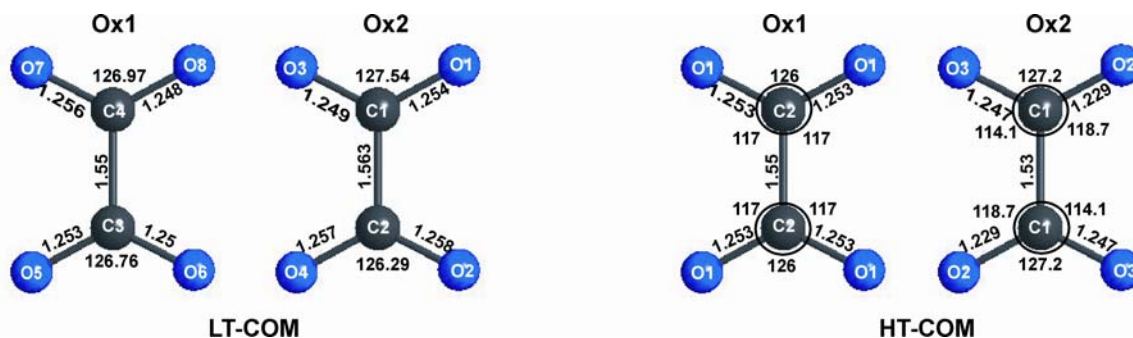


Fig. 1.4. (Left) Oxalate groups in the LT modification of COM. Distances (Å) and angles ($^{\circ}$) have average e.s.d.'s of 0.004 Å and 0.4° . (Right) Oxalate groups in the HT modification of COM. Distances (Å) and angles ($^{\circ}$) have average e.s.d.'s of 0.008 Å and 0.6° [23,25].

However, the Tazzoli setting [20] is widely accepted for convenience because it allows assignment of more prominent faces to lower index values [26]. The indices for both unit cell choices and the equivalent planes for each of the settings have been catalogued [27]. For example, the (100) plane of the Tazzoli notation is the (-101) plane of the Deganello notation (Fig. 1.5) [29-31].

It is well known that both natural and synthetic COM does not commonly occur as single crystals, but as twins and intergrowths of twins [26]. Twinned crystals are described as *contact twins* if a definite composition plane is present; *penetration twins* if two or more parts of a crystal appear to interpenetrate each other, the surface between the parts being indefinable and irregular. Single crystals of COM exhibit monoclinic prismatic habit (also called polyhedral habit) bound by (100), (010), (021) and (12-1) faces (Fig. 1.5 A) [14]. Twinned crystals of COM show two types of twinning morphologies as shown in figures 1.5 B and 1.5 C. They are often classified by crystallographers as penetration and contact twins respectively, even though they do not appear to be so [26-28]. In both the twins, the twin planes are (100). COM crystals grown from high ionic strength media are six-sided platelets bound by (100), (010) and (121) faces (mostly called in literatures as elongated hexagonal, even though the crystal

system is monoclinic). It is known that in contact with the mother liquor for adequate time, plate-like crystals gradually transform into typical COM polyhedral crystals (Fig. 1.5 A) or elongated multiple twins with acute edges at the ends [14,27, Section 3.4.1.1].

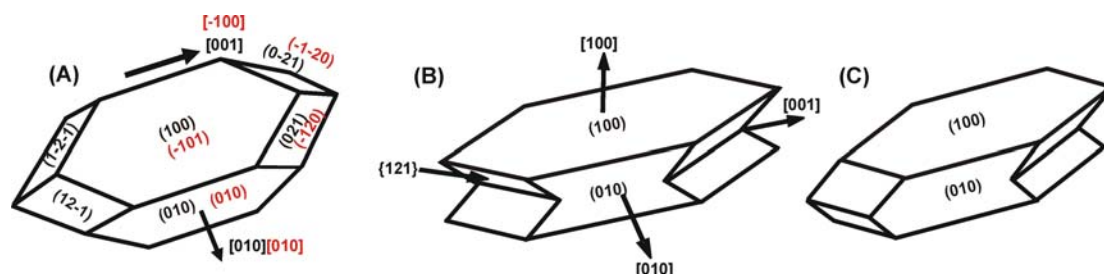


Fig. 1.5. (A) The crystal faces developed and major crystallographic directions indicated for a COM single crystal of six-sided polyhedral habit. Twinned crystals of COM which are often classified as penetration twin (B) and contact twin (C) [26-28]. Indexing with black letters corresponds to Tazzoli's notation and with red to Deganello's notation [27].

Calcium oxalate dihydrate (COD) belongs to the tetragonal crystal system with the unit cell parameters, $a = b = 12.371(3) \text{ \AA}$, $c = 7.357(2) \text{ \AA}$, $\alpha = \beta = \gamma = 90^\circ$, $Z = 8$, $V = 1125.937 \text{ \AA}^3$ and space group $I4/m$ [20,32,33]. Clearly, eight water molecules are coordinated with the four Ca ions so forming a dihydrate $\text{CaC}_2\text{O}_4 \cdot 2\text{H}_2\text{O}$ (Fig. 1.6 A,B).

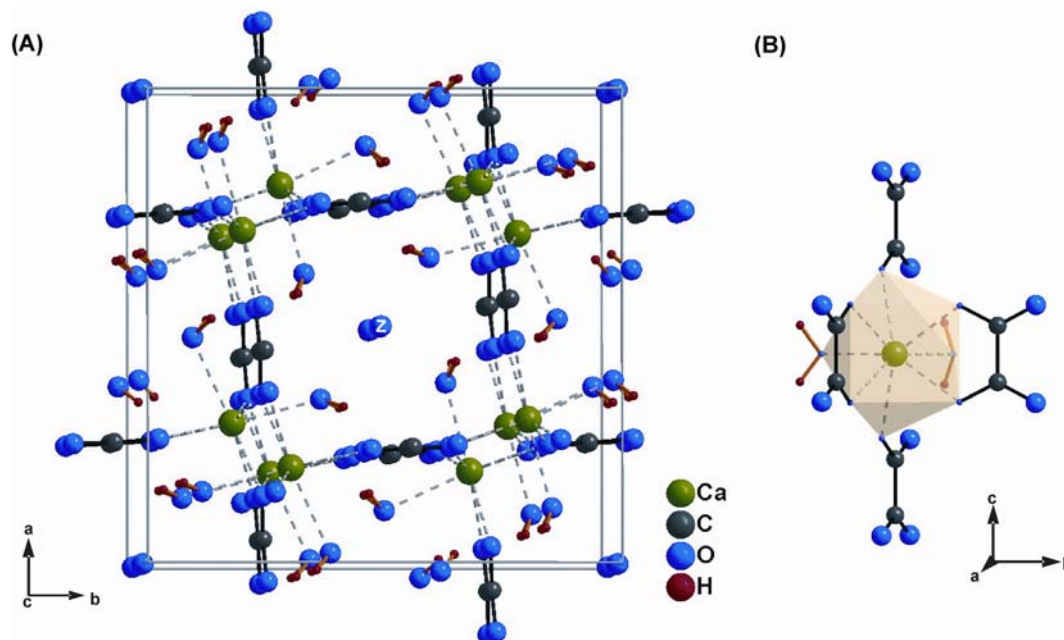


Fig. 1.6. The crystal structure of COD viewed along $[001]$ (A) and the coordination polyhedron around Ca (B).

The Ca ion is coordinated by eight oxygen atoms from two water molecules and four oxalate ions. The coordination polyhedron around Ca is a distorted square anti prism

and forms an open space/channel in the centre of the structure running along the four-fold axis, in which the zeolitic water (denoted as z in Fig. 1.6 A) molecules are placed. The maximum water content of $2.5 \text{ H}_2\text{O}$, described with split positions was confirmed by Tazzoli and Domeneghetti [20].

COD crystals grown from aqueous solutions are generally tetragonal bipyramids with dominant (101) faces and tetragonal prisms with (100) prism faces and (101) pyramidal faces (Fig. 1.7) [29-31].

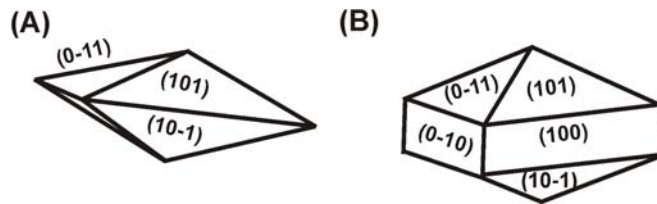


Fig. 1.7. Crystal habits of COD. Tetragonal bipyramid (A) and tetragonal prism (B).

Calcium oxalate trihydrate (COT) crystallizes in the triclinic crystal system ($P\bar{1}$, $a = 6.11(1) \text{ \AA}$, $b = 7.167(2) \text{ \AA}$, $c = 8.457(2) \text{ \AA}$, $\alpha = 76.5(2)^\circ$, $\beta = 70.35(2)^\circ$, $\gamma = 70.62(2)^\circ$, $Z = 2$, $V = 325.9(2) \text{ \AA}^3$) [21,34,35]. In COT, three of the eight Ca-coordinating oxygen atoms belong to water molecules, four are from two oxalate ions and one oxygen is from a third oxalate ion (Fig. 1.8 A,B). Generally, COT crystallizes in triclinic prismatic or in parallelogram-like platy morphology (Fig. 1.8 C) [29-31,36].

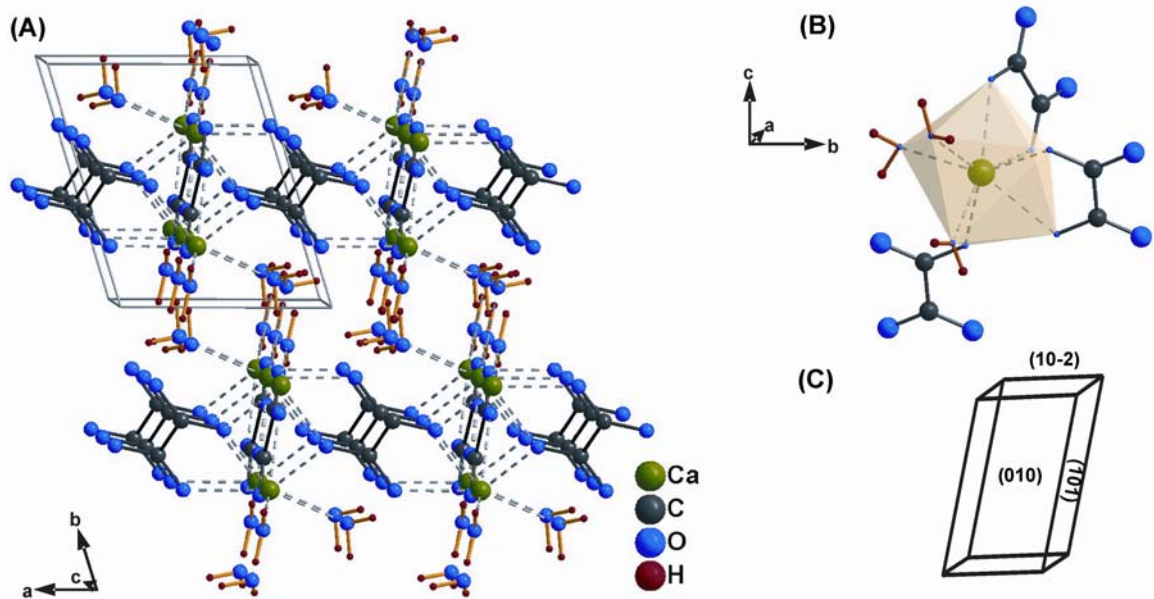


Fig. 1.8. Crystal structure of COT (A) and the Ca coordination polyhedron (B). Triclinic prismatic habit of COT grown from aqueous solution (C).

1.2.2 Comparison of the crystal structures: COM, COD and COT

A comparison of the structural features of the calcium oxalate hydrates was performed by Echigo *et al.* [21]. Accordingly, COT and COM have a sheet structure consisting of Ca^{2+} ions and oxalate ions while COD does not possess such a sheet structure. In COM, oxalate groups (Ox) alternate with the Ca^{2+} ions, and form chains lying in the (010) plane and running along a (Fig. 1.9 top). Viewing along a , adjacent chains are bound together by independent oxalate ions lying in the (100) plane to form the structure with chain-oxalate sheets (Fig. 1.9 bottom). The hydrogen bonds (through H3) between the two interlayer water molecules contribute to the construction of the sheet structure (Fig. 1.9 top).

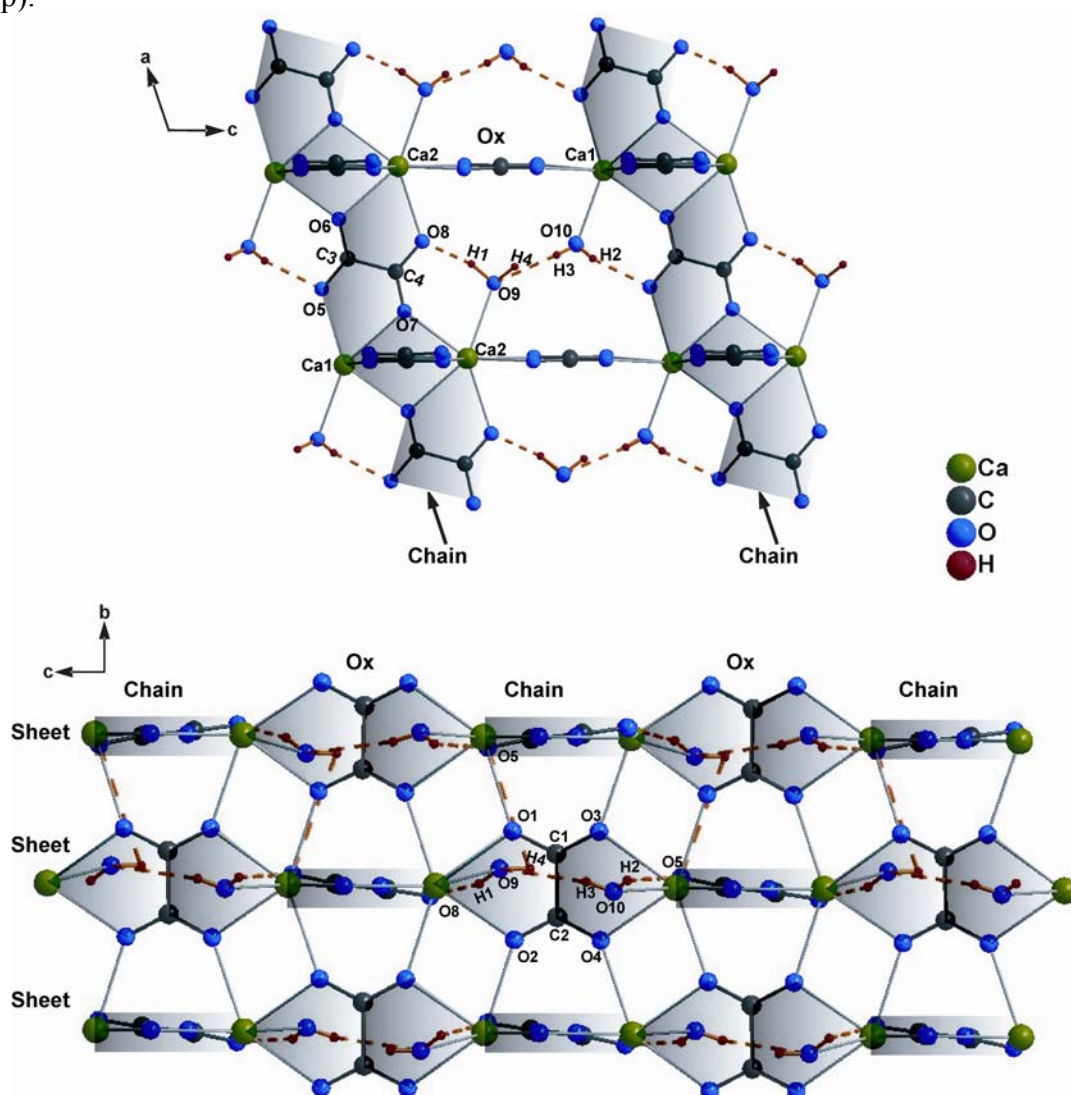


Fig. 1.9. (Top) The Tazzoli structure of COM with *zig zag* chains consisting of calcium (Ca) and oxalate (Ox) ions shaded. These chains are linked by oxalate ions (Ox) and hydrogen bonds (yellow dotted lines) of the interlayer water molecules which make the chain-oxalate sheet structure parallel to (010). (Bottom) The [100] projection of the structure of COM with the chain-oxalate sheet structure (indicated with shading) [20,21].

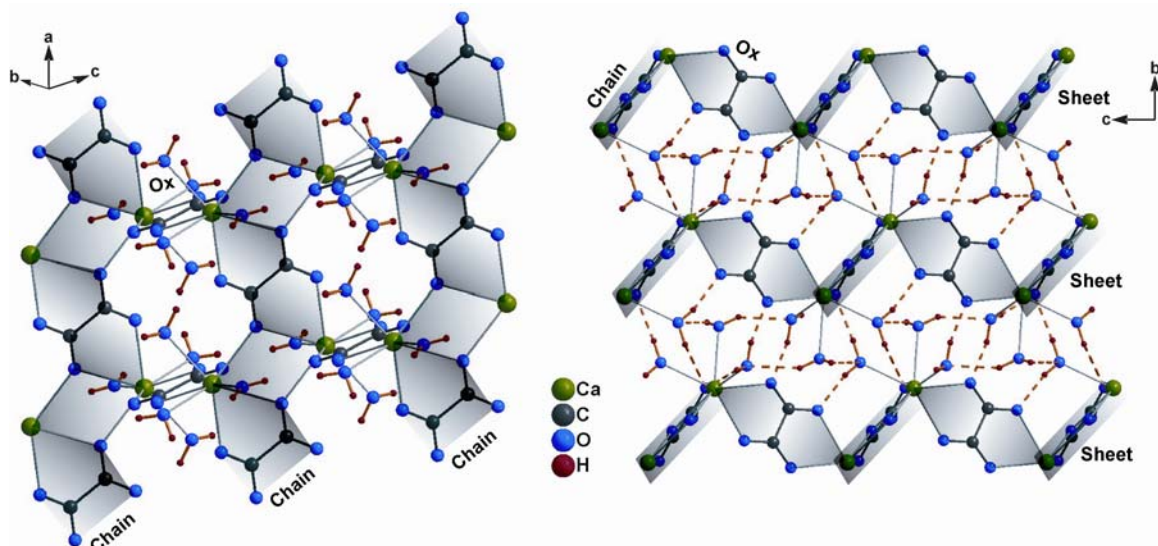


Fig. 1.10. (Left) The crystal structure of COT with *zig zag* chains consisting of calcium and oxalate (Ox) ions shaded. The chains are linked by oxalate ions to form corrugated sheet structures (Right). The sheets are corrugated by water molecules intercalated into the sheets with hydrogen bonding (yellow dotted lines).

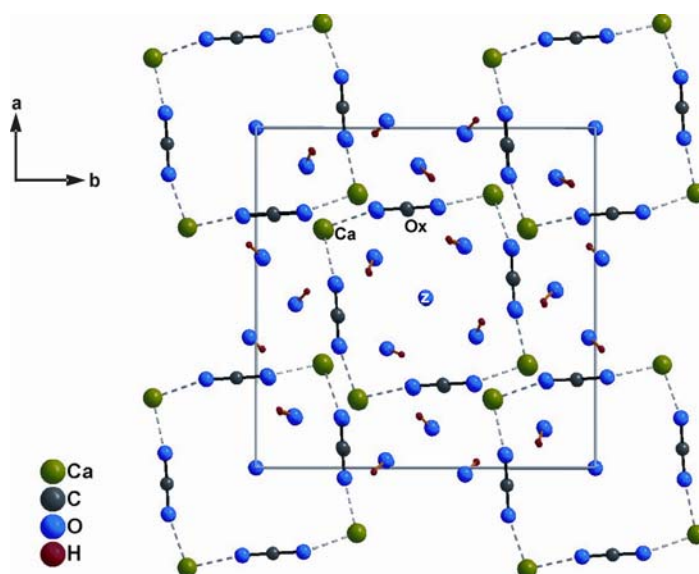


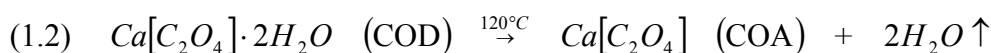
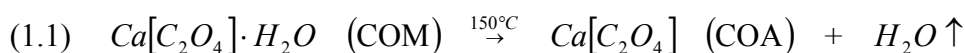
Fig. 1.11. The channel structure (running along the four-fold axis) in COD consisting of calcium ions and oxalate ions where the “zeolitic” water (z) is preserved [20,21].

In COT, similar *zig zag* chains consisting of Ca^{2+} ions and oxalate ions run along *a* (Fig. 1.10 left). These chains are bound together by independent oxalate ions (Ox) to form the chain-oxalate sheets. In addition, the water molecules in COT appear to be intercalated between the sheets to corrugate them by hydrogen bonding (Fig. 1.10 right). With increasing temperature and dehydration, *i.e.* with decreasing hydrogen bonding of the interlayered water molecules, the sheets can be flattened and the oxalate ions combining the chains would form bonds with Ca^{2+} ions included in opposite sheets, giving the COM structure as a result (Fig. 1.9 bottom).

In contrast, such a sheet structure cannot be found in COD (Fig. 1.11). Alternatively, oxalate groups and Ca^{2+} ions constitute the channel structure where zeolitic water is preserved. Therefore, the crystal structure of COD is appreciably different from those of COM and COT.

1.2.3 Anhydrous calcium oxalate

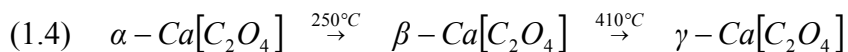
Apart from the three hydrated forms, calcium oxalate exists also in the anhydrous form (COA). Several thermal investigations of calcium oxalates are reported in literature [37,38]. The full dehydration of COM and COD takes place according to equations (1.1) and (1.2) in one step reactions by the loss of one and two water molecules, respectively.



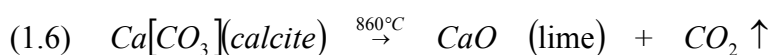
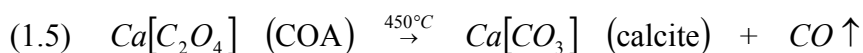
The full dehydration of COT proceeds in a two step process. As shown in equation (1.3) COT first decomposes to COM by the loss of two water molecules, followed by a second step to the form anhydrous calcium oxalate (COA) as described in equation (1.1). The dehydration of COT into anhydrous calcium oxalate through COM and not COD is due to the structural similarity of COT to COM (Section 1.2.2).



COA itself was reported to undergo temperature dependent phase transitions from an α -, to β - and γ - modification as noted in equation (1.4), but this is controversially discussed [39-44].



Further increase of the temperature leads to decomposition of COA to calcite (eq. (1.5)), which itself decomposes at higher temperature to lime (eq. (1.6)).



1.2.4 Morphological aspects of biogenic calcium oxalates

Monoclinic COM and tetragonal COD are the most common phyto-crystals and the main constituents of kidney and urinary stones. Even though the triclinic COT is rarely found in kidney stones, it is assumed to be a precursor of COD [45,46].

The occurrence of calcium oxalates in plants represents a relatively harmless biogenesis unlike the devastating occurrence in renal tubules. Vascular plants accumulate crystals of calcium oxalate in a striking range of shapes, sizes, amounts and spatial locations. Both the morphology and distribution of calcium oxalate crystals within plants exhibit 'species-specific' patterns, indicating that their development is genetically controlled.

The morphologies of calcium oxalates in plants are classified into five categories as: druses (spherical aggregates with many facets radiating from a central core, Fig. 1.12 a), raphides (needle-like crystals formed in bundles, Fig. 1.12 b), styloids (acicular crystals (needle-like) that form singly, Fig. 1.12 c), crystal sands (small tetrahedral crystals formed in clusters, Fig. 1.12 d) and prismatic crystals (regular or twinned prismatic shape, Fig. 1.12 e). These crystals are important in calcium regulation, defence against grazers, detoxification, ion balance, tissue support/plant rigidity and even light gathering and reflection [17-19,47,48].

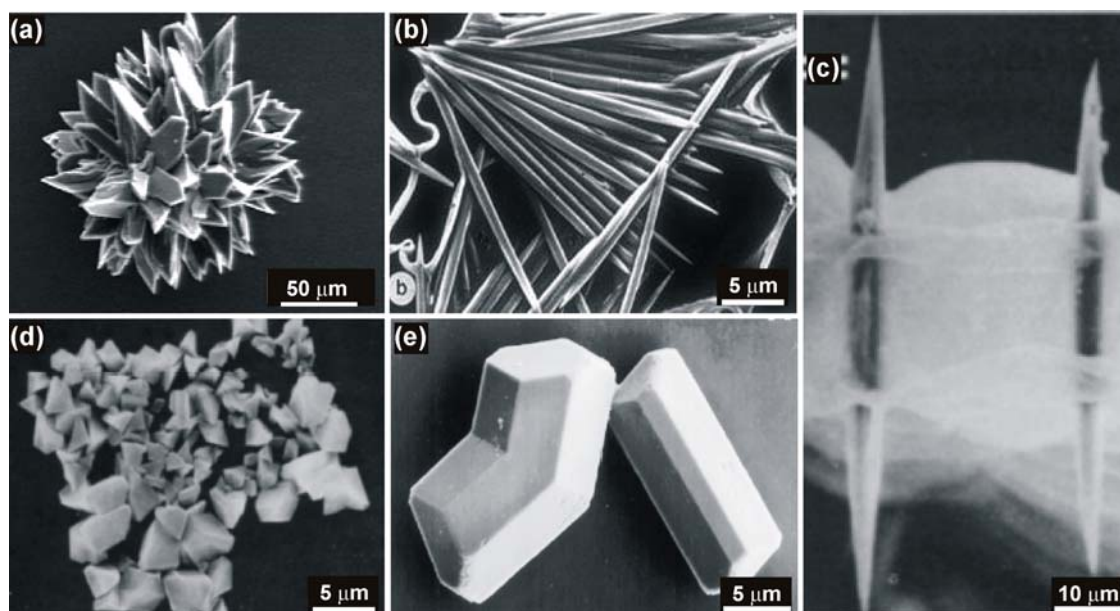


Fig. 1.12. (a) COM druse crystal isolated from the cactus *Opuntia auranthiaca* [19], (b) COM raphides from a ruptured *Pistia* idioblast [17], (c) Two styloid COM crystals from *Eichhornia* [17], (d) crystal sand (COM) from *Nicotiana glauca* [17], (e) prismatic COM crystals from the seed coat of bean [18].

Kidney stones like their salubrious counterparts always contain a macromolecular matrix distributed throughout the structure which is a complex stew of proteins, lipids, glycosaminoglycans, polysaccharides and cellular debris [49-52]. The identified macromolecules in urinary stones are listed in appendix table 6.1. The organic matrix is an inevitable and integral part of the stones, meandering throughout the entire structure and occupying far more space than would be expected from its contribution of only 2-3% to the total mass. The scheme for the formation of calculi is demonstrated in figure 1.13. COD is more likely prevalent in voided urine whereas the stones found in the kidney are mainly COM. This is due to the reduced capacity of COD to form stable aggregates and strongly attach to renal epithelial cells [49].

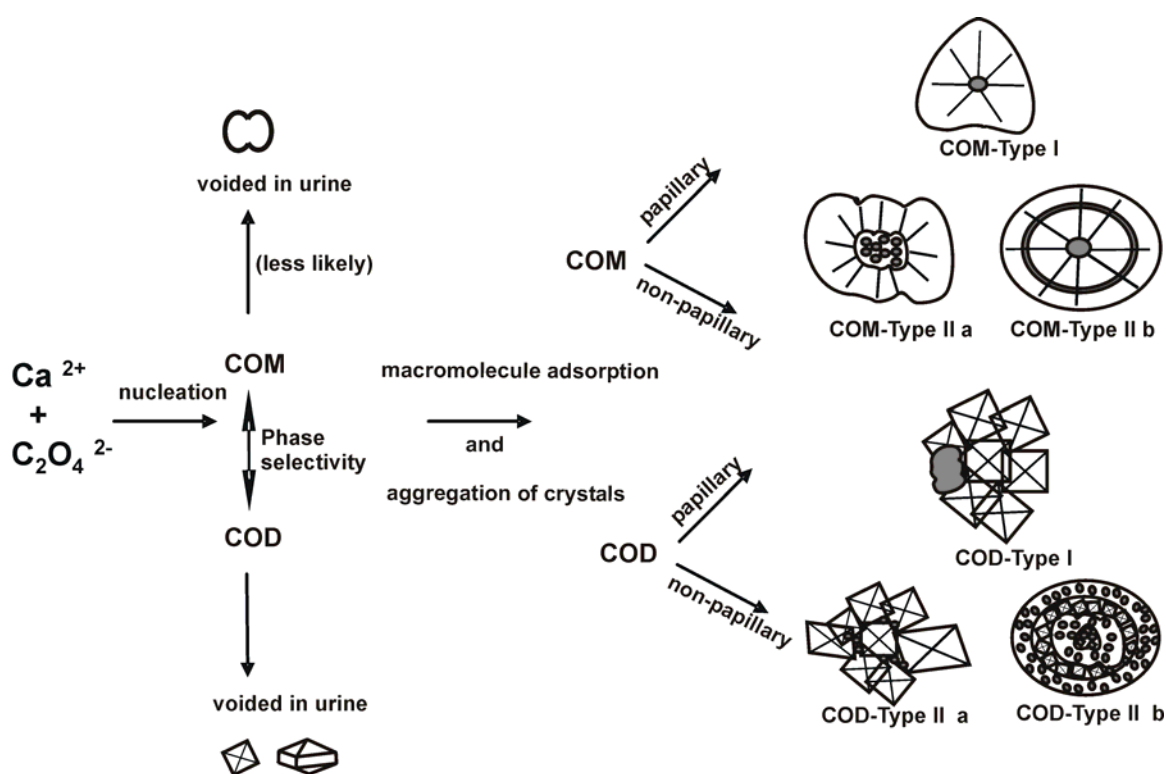


Fig. 1.13. Pathway for the formation of COM and COD calculi. The crystals which are not voided through urine are aggregated through the adsorption of macromolecules and grow into larger aggregates. The morphology of COM and COD calculi are generally classified as type I (papillary) and type II (non-papillary). The regions shaded with grey colour are either organic matter or hydroxyapatite or a minor fraction of COM. For further details refer to the text.

COM calculi are classified into two groups: (Type I) papillary calculi and (Type II) non-papillary calculi (Fig. 1.13). Type I calculi have conical appearance and appear attached to the renal papillae. It contains a core, a radially striated intermediate layer and a concentrically laminated peripheral layer. The core may consist of inter grown COM

crystals or organic matter or hydroxyapatite. The outer region of the core is covered with a layer of organic material on which the columnar juxtaposed sheet-like crystals grow perpendicular to the core surface. The concentric laminations are formed by the interruption of the columnar crystals by the accumulation of organic matter.

Type II COM calculi are typically spherical and are formed in the renal calyx. They are classified into two groups; IIa and IIb. The IIa type calculi contain no core but contain a number of cavities irregularly distributed over the stone interior which may enclose small spheres of hydroxyapatite. The IIb calculi contain a core made up of organic matter (alone or mixed with hydroxyapatite or COM) and a shell of columnar COM crystals emerging from the core. Such calculi are spherical with radial striations and concentric lamination [53-55]. The type IIb calculi is relevant to the present study.

COD calculi are also divided into type I (papillary calculi) and type II (non-papillary calculi). Type I COD calculi are large aggregates of COD crystals formed on a very small COM papillary calculus or on a hydroxyapatite papillary deposit. Type II COD calculi are further classified into IIa and IIb calculi. Type IIa calculi consist of COD crystals with variable amount of COM or hydroxyapatite irregularly distributed. Type IIb calculi also may contain variable amounts of COM and characterised by alternative layers of COD crystals and hydroxyapatite combined with organic matter. COM found in COD calculi is demonstrated to have formed by the transformation of COD into thermodynamically stable COM [14]. The causes of COD calculi include high Ca^{2+} to oxalate ratios, high ionic strength and existence of urinary pH values superior to six.

Calcium oxalate crystals are also observed in neutral and alkaline urine, where COM forms oval or dumbbell shaped [56] crystals and COD forms tetragonal crystals (Fig. 1.13). Excessive amount of dumbbell shaped monohydrate form is also observed in the case of ethylene glycol (anti-freeze) poisoning [57]. The dumbbells are formed by the stacking of plate-like COM crystallites with flat (100) faces on one above the other (Fig. 1.14 a) [53,58,59].

In general, COM stones are formed by the aggregation of micro crystals to form various morphologies ranging from dumbbells to spherulites (Fig. 1.14 a,b). The agglomeration of COM crystals is recognized as an important step in renal stone development [58]. The organic matter embedded within the stones promotes aggregation and crystal attachment to cells by acting as an adhesive [49]. It has been reported that a combination of primary agglomeration of crystals forming stones and the nucleation of

new crystals on a (glyco-) muco-protein layer partially covering their surface constitutes the possible mechanism of stone development [54,55].

The surface of spherical COM calculi (Fig. 1.14 c) often exhibit stacks of microscopic plate-like COM crystals under higher magnification [53,56-60] (Fig. 1.14 d,e). This indicates that the peripheral layer of such stones is composed of stacking of smaller crystals with flat (100) faces. Such plate-like arrangement of the crystals also account for the radial striation of the spherulitic stones. The macromolecules are situated between the COM crystal plates in a sandwich arrangement (Fig. 1.14 f-bottom) in contrast to that grown from aqueous solutions (Fig. 1.14 f-top) [53].

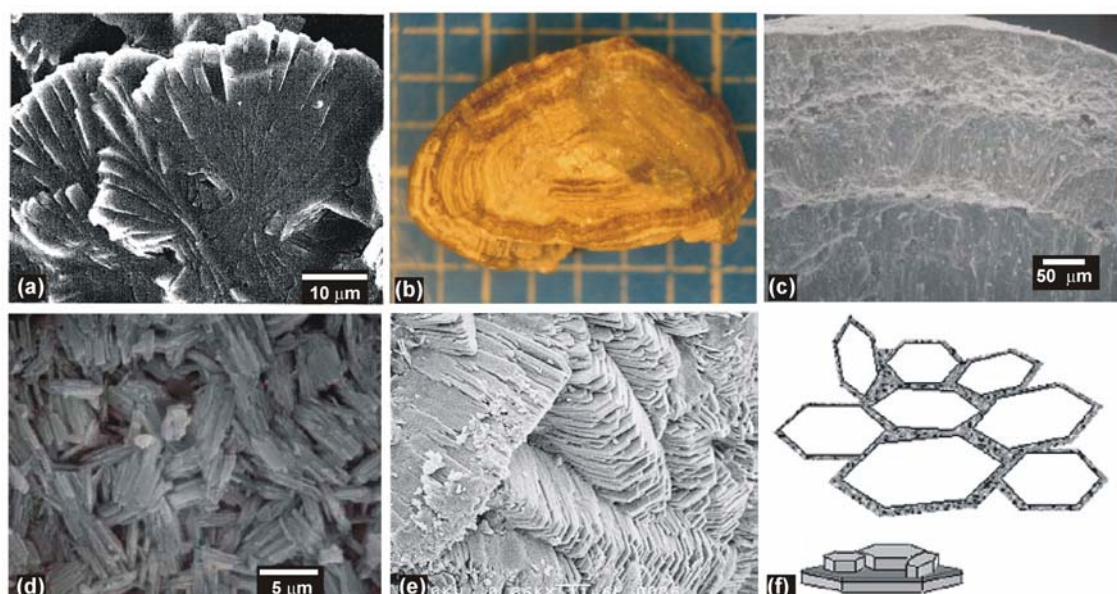


Fig. 1.14. (a) COM stone with dumbbell /fan-like morphology [56]. (b) Cross-section of a COM spherulitic stone representing concentric laminations [49], (c) fractured surface of COM stone showing radial striation and concentric lamination. Concentric lamination arises due to outward growth of the stone. Radial striation is due to the arrangement of plate-like COM crystals [52]. (d,e) The surface of a COM stone exhibiting the edges of the plate-like crystals. These crystals are stacked by contacts between their (100) faces [52,49]. (f) Mode of aggregation of COM in aqueous solutions (top) and in renal calculi (bottom) [53]. In renal calculi, the aggregation occurs by stacking on the (100) crystal faces.

The dumbbell and spherulitic morphologies of biogenic calcium oxalates suggest that the crystallization phenomenon of spherulites which is discussed as a consequence of rapid crystallization in a highly viscous medium is relevant to this system. Moreover, it has been opined that the formation of stones in gel-like media of macromolecules by the flow of supersaturated urine, is one of the probable causes for the spherulitic growth [45,55]. The spherulitic structure represents a fundamental form of crystallization in viscous media. It is common in nature and frequently associated with biomineralization.

True spherulites are polycrystalline aggregates consisting of radially arranged micro crystallites forming an approximate sphere [61,62].

1.2.5 Biomimetic Morphogenesis: Self-assembly or self-organization

Generally, the morphologies of inorganic crystals are categorised as self-assembly or self-organization depending on the degree of the driving force for the crystallization (Fig. 1.15).

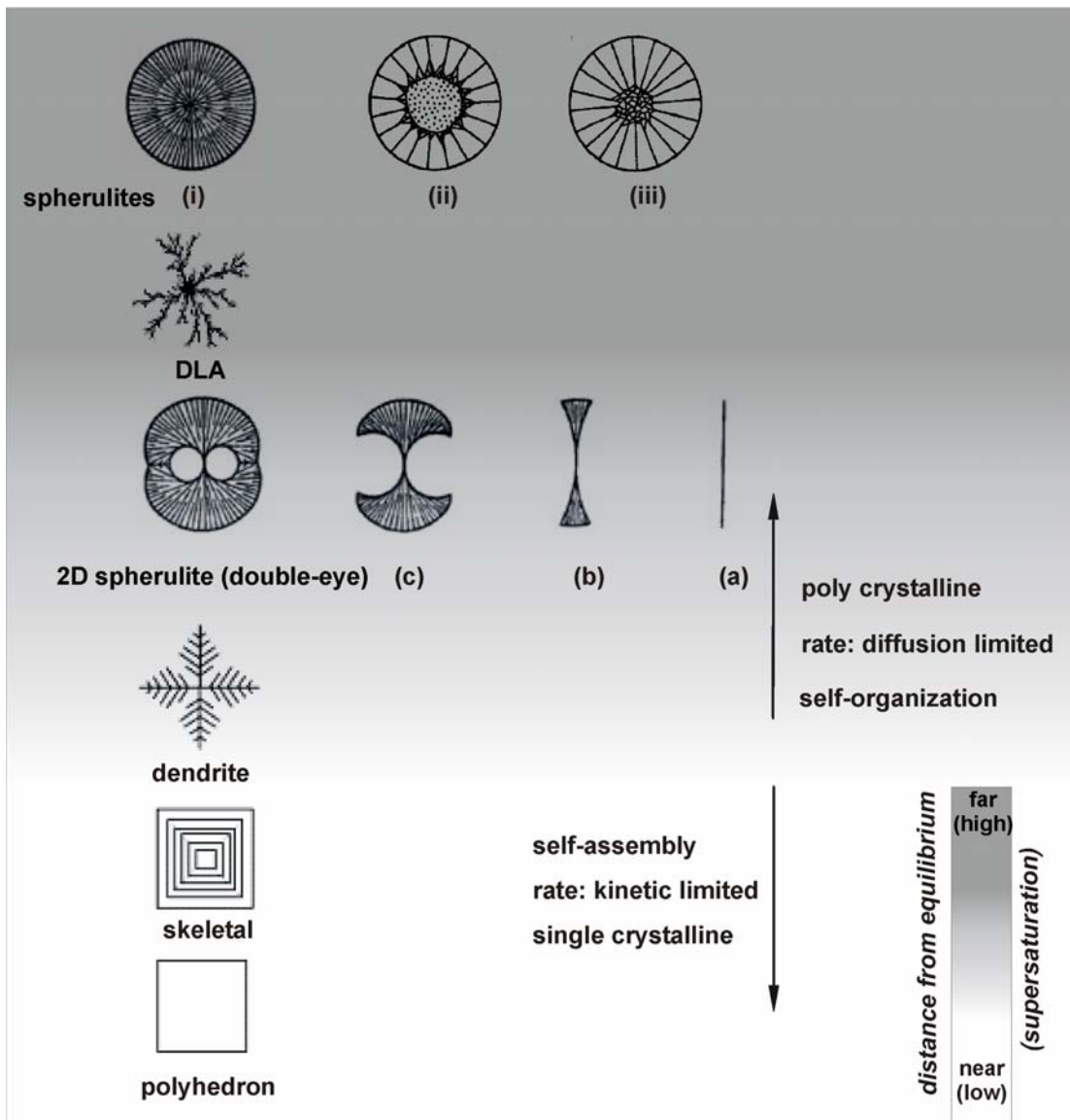


Fig. 1.15. Self-assembly and self-organization on morphological variation of crystals [64]. The sequence from (a) to 2D spherulite represents the ontogeny of spherulites formed by split growth mechanism as proposed by Grigorev [67] and Maleev [69]. At higher supersaturation complete spherulites are formed: (i) by dense branching (ii) on a spherical particle of a foreign material or (iii) on a polycrystalline aggregate of the same species [61].

At very low supersaturation levels or when the crystal growth occurs near the equilibrium state, polyhedral crystals bound by flat faces are formed by spiral growth mechanism. As the supersaturation increases, crystals grow by two-dimensional nucleation mechanism and develop hopper (skeletal) morphologies. With further increase in supersaturation, the growth rate is governed by mass diffusion and dendrite forms are produced by the competition between the promotion and suppression of the crystal growth (the interface will be rough and adhesive-type growth mechanism prevails). When the driving force greatly increases, spherulites and diffusion-limited aggregates (DLA) are formed with disappearance of the original crystallographic symmetry. The crystallization process of polyhedral and skeletal forms are categorised under self-assembly as the macroscopic shape of the crystal reflects the arrangement and the symmetry of the microscopic atomic lattice. When the crystallization processes of morphologies occur by ordering at far-from equilibrium and depends on the diffusion rate of the components, it should be categorised as self-organization.

Likewise, the morphogenesis and pattern formation in biomineralization can also be discussed in terms of self-assembly and self-organization. In biomimetic systems, the mass transport during mineralization process is controlled by the organic matrix and the molecular recognition between the inorganic crystals and the organic substrates modulates the formation of inorganic crystals with biomimetic hierarchical architectures.

As the present work deals with the crystallization of spherulites, the case of spherulites need to be emphasized. Spherulites are a form of polycrystalline aggregates occurring under a high driving force condition. In such situations, spontaneously nucleated crystals grow with various orientations and the crystals are selected simply by their geometric relation with the substrate surface (geometric selection predicted by Kolmogorov's theory, see ref 61 for details). As a result, various textures of polycrystalline aggregates appear that are controlled by the form of the substrate surface. Spherulites are formed if geometric selection takes place on a spherical substrate particle. Substrate particles may be a different material from those forming the spherulites (Fig. 1.15 ii) or a spherical particle of the polycrystalline aggregate of the same species (Fig. 1.15 iii). Crystals whose *habitus* is characteristically thin platy exclusively take the spherulitic form under high driving force conditions (Fig. 1.15 i).

Sometimes, instead of formation of a perfect (completely developed) spherulite, various incomplete spherulites such as sheaf-like (Fig. 1.15 b,c) and two-dimensional spherulites with two-eye forms appear (Fig. 1.15. 2D spherulite). Such crystals grow

initially as threadlike fibres, subsequently forming new grains at the growth front (Fig.1.15 a) [65]. This branching of the crystallization pattern ultimately leads to a crystal “sheaf” that increasingly splays out during growth (Fig.1.15 b,c). At still longer times, these sheaves develop two “eyes” (uncrystallized regions) on each side of the primary nucleation site and settles down into a two-dimensional spherical growth pattern, with eye structures apparent in its core region (Fig.1.15 2D spherulite).

Since long time, the origin of spherulitic morphology was predominantly described and discussed on the base of “classical crystal splitting” growth mechanism, which is generally associated with fast crystal growth and caused by existence of internal crystal strain and high supersaturation of the medium [66-69]. According to Grigor’ev, split crystals partially separate during growth into sub individuals as a result of the accumulation of structural defects (*mechanical splitting*), or when different ions are incorporated as impurities from the parent solution (*chemical splitting*) [67].

However, the mechanism of formation of spherulitic biominerals remains subtle. Very few examples are reported which analyses the exact growth mechanism of such biominerals. One such well investigated biomimetic system is the hexagonal prismatic seed crystal of fluoroapatite, formed in a gelatine gel, which further grows to spherical particles *via* dumbbell intermediates which gives the first experimental evidence for a direct correlation between intrinsic electric fields and the self-organized growth of fluorapatite–gelatine [70-72]. Very recently, some evidence has been reported that in organic-inorganic nanocomposite structures with complex morphology, such crystallization events are not categorized as classical single crystals and polycrystals, but as non-classical crystallization involving particle-mediated pathways, which describes the formation of such types of aggregates by special mechanism such as oriented attachment of subunits [73-76], mesoscale transformation of nanoparticles from amorphous precursor [75] and formation of mesocrystal by “brick-by-brick” self-assembly mechanism [77-79].

The formation of spherulites with the aid of organic macromolecules is commonly associated with calculi. Therefore, as a first step to unravel the complex pathology of uro/nephro lithiasis, it is obligatory to investigate the structure and morphology of calcium oxalates crystallized in the presence of organic additives. Therefore, the present work focuses mainly on the influence of additives on controlling the morphology of calcium oxalates crystallized from aqueous solutions and from organic gel matrices, respectively.

1.3 Overview on calcium oxalates growth

1.3.1 Crystallization of calcium oxalates: The conventional precipitation

Precipitation from aqueous solution is one of the oldest chemical operations to have been exploited vastly. But the problem associated with calcium oxalate crystallization from solutions is that, a multitude of microscopic crystals are formed during rapid mixing of calcium and oxalate solutions caused by the poor solubility of calcium oxalates. In water at 25 °C the solubility product, K_{sp} of COM is 2×10^{-9} [80], COD is 4.89×10^{-9} [81] and COT is $7.19 \times 10^{-9} \text{ mol}^2/\text{l}^2$ [82]. These crystals are usually too small and also easily damaged by electron beam making it inadequate to study the specimen in detail.

Only a very few of the previous studies are dealt with the “real” biomineralization or the morphogenesis of calcium oxalates. Among them the effects of polyelectrolytes on the crystallization of calcium oxalate have been the subject of research since 1960s in an attempt to find the methodology for the inhibition of stone formation by acid-rich urinary proteins that suppress the crystallization of calcium oxalate even under supersaturated conditions [83]. These experiments have proved that the precipitation of calcium oxalate is affected by polyelectrolytes. The amount of COD is reported to increase with the increase in concentration of the polymer used in accordance with the human body’s self defence mechanism.

Recently it was shown how to control hydration states (COM or COD) as well as morphologies by simple crystallization from slightly oversaturated aqueous solutions in the presence of acid-rich polymer additives like, poly-L-aspartate, poly-L-glutamate and polyacrylate (PAA) [84]. These polymers have been observed to change the shape of COD from tetragonal bipyramids to dumbbells, and even spheres based on the preferential interaction of the polymer with the (100) faces of COD on increasing the concentration of the polymer (Section 3.3). The activity of these biopolymers with calcium oxalates seems to be rather complex. Arguments have been put forward that their effectiveness is due to particular molecular weights, to hydrophobic and hydrophilic regions and to a close match between spacing of acid groups and the spacing of cations on the crystal surfaces [85].

1.3.2 Gel-mediated growth of calcium oxalates: Bio inspired strategy

In order to understand the pathological biomineralization of uroliths, it is necessary grow calcium oxalates comparable in morphology to uroliths under similar growth conditions.

The formation of calcium oxalate calculi within a gel-like state of proteins, polysaccharides, lipids and other biomacromolecules under a flow of supersaturated urine supports the fact that an “organic” gel model can simulate the process of urinary stone formation under *in vitro* conditions.

The “double diffusion technique” using a gel matrix is normally used for the growth of crystals of compounds of low solubility [86]. Ideally, the gel takes over control of the diffusion of ions only and does not actively take part in the process of crystallization [87,88]. Apart from the extensive experimentations conducted in the past, attempts to grow calcium oxalates in gel systems, similar to natural conditions, have so far met with little success. Bisailon and Tawashi (1975) [89] and Frey-Wyssling (1981) [90] attempted to grow COM crystals in calfskin gelatine and agar gels respectively, but the size of the crystals formed was limited by the various amounts of organics present in these gels. Therefore, the proceeding studies opined the feasibility of COM growth in synthetic gels like sodium metasilicate gel or bentonite clay [91-93]. Very recently COM crystals grown by the counter diffusion method in various gels like gelatine, agar-agar, agarose and sodium silicate was reported by Petrova *et al.* [94]. In all the above cases various twins, rosettes and clusters of COM were formed and there was no traces of COD or COT.

Nonetheless, the paradoxical effects including promotion of crystal nucleation, growth and aggregation of calcium oxalates in an ever-lengthening list of macromolecules has been too tempting to ignore that the present work is a re-do of the biomimetic growth of calcium oxalates in organic gels, *viz.* agar, carrageenan and gelatine.

Agar: Agar ($C_{12} H_{18} O_9$)_x, is a biopolymer which is generally considered to be a mixture of agarose and agarpectin. It is commercially obtained from species of *Gelidium* and *Gracilariae* which belong to the family of red seaweeds (*Rhodophyceae*). Agarose is a linear polymer, consisting of (1-3)- β -D-galactopyranose-(1-4)-3,6-anhydro- α -L-galactopyranose units (Fig.1.16 a) [95].

Agarpectin is a heterogeneous mixture of smaller molecules that occur in fewer amounts and forms only a poor gel. Their structures are similar but slightly branched and sulphated, and they may have methyl and pyruvic acid ketal substituents. Agar has the ability to form gels upon cooling from a hot solution to 30–40 °C and to melt to sols

upon heating to 90–95 °C. The mechanism of gelation of agar is shown in figure 1.16 (b). At temperatures above the melting point of the gel, thermal agitation overcomes the tendency to form helices and the polymer exists in solution as a random coil. On cooling, a three-dimensional network builds up in which double helices form the junction points of the polymer chains (Gel I). Further cooling leads to aggregation of these junction points (Gel II).

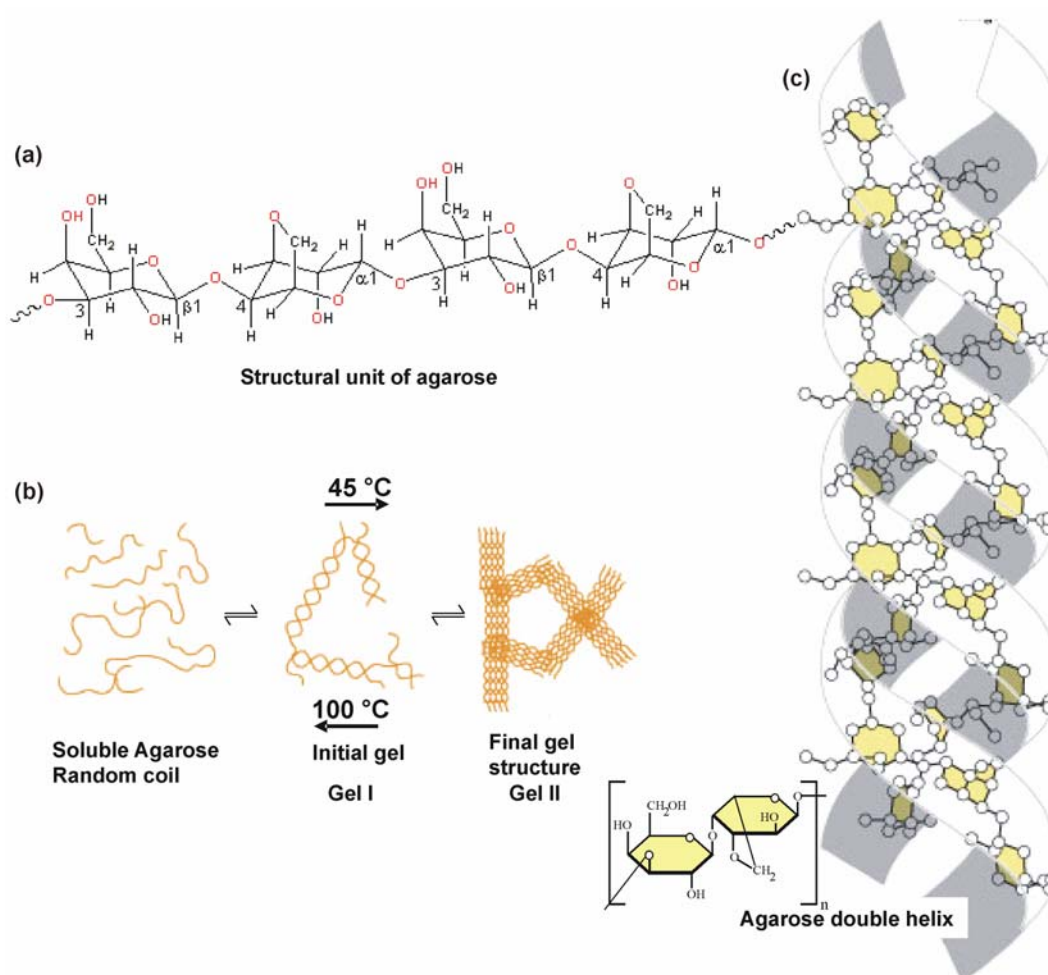


Fig. 1.16. (a) Structural unit of agarose, (b) gelation of agar, (c) agarose double helix in agar gel.

The quality of agar is improved by alkaline treatment that converts any L-galactose-6-sulphate to 3,6-anhydro-L-galactose (more details in section 3.4.1). The gel network of agarose contains double helices with a pitch of 2.85 nm (Fig. 1.16 c). These double helices are stabilized by the presence of water molecules bound inside the double helical cavity [96-98]. Exterior hydroxyl groups allow aggregation of up to 10,000 of these helices to form superfibers.

Carrageenan: Carrageenan is a collective term for polysaccharides prepared by alkaline extraction (and modification) from red seaweed (*Rhodophyceae*), mostly of genus *Chondrus*, *Eucheuma*, *Gigartina* and *Iridaea*. Carrageenans are linear polymers of about 25,000 galactose derivatives with regular but imprecise structures, dependent on the source and extraction conditions. It consists of alternating 3-linked- β -D-galactopyranose and 4-linked- α -D-galactopyranose units (Fig. 1.17).

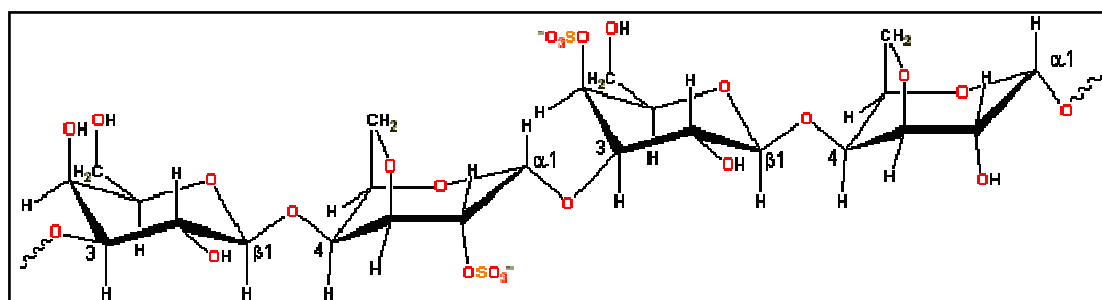
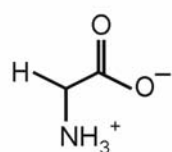
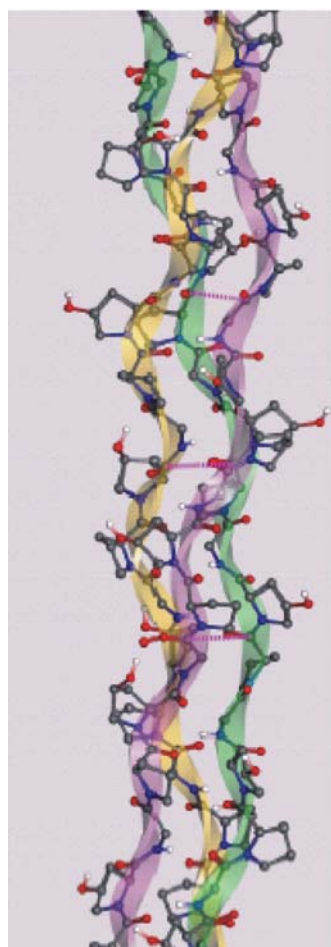


Fig. 1.17. Structural unit of Carrageenan.

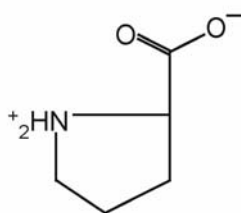
There are mainly three types of carrageenans, κ -carrageenan (kappa-carrageenan), ι -carrageenan (iota-carrageenan) and λ -carrageenan (lambda-carrageenan). The structural unit of κ -carrageenan is (1-3)- β -D-galactopyranose-4-sulphate-(1-4)-3,6-anhydro- α -D-galactopyranose-(1-3). κ - and ι -carrageenans form thermoreversible gels on cooling in the presence of appropriate counterions. κ -carrageenan forms a firm clear gel with poor freeze-thaw stability; the coil-double helix transition being followed by a cation induced aggregation of the helices [99,100]. Carrageenan is most stable at pH 9 and the rate of hydrolysis increases rapidly with lowering the pH or increasing the temperature. Carrageenan forms a softer gel than agar. κ -carrageenan forms parallel double helices with a pitch of 2.5 nm. The major difference from agar is the presence of D-3,6-anhydro- α -galactopyranose rather than L-3,6-anhydro- α -galactopyranose units and the lack of sulphate groups.

Gelatine: Gelatine is prepared by the denaturation of collagen, isolated from animal skin and bones. The characteristic of a collagen molecule is its rigid triple helical structure with three polypeptide chains helically wound around each other. A section of the triple helical structure is shown in figure 1.18. Each helical chain is made of about 1000 amino acids. These amino acids include glycine, proline and 4-hydroxyproline residues [101,102]. Solutions undergo coil-helix transitions followed by aggregation of

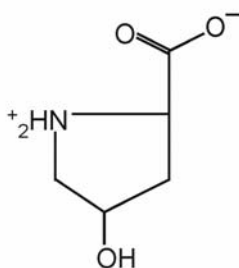
the helices to form collagen-like right-handed triple-helical proline/ hydroxy proline rich junction zones.



Glycine



Proline



Hydroxyproline

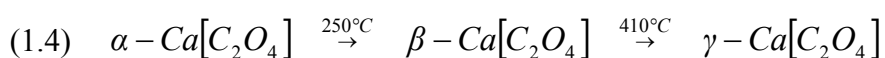
Fig. 1.18. Part of the structure of a gelatine triple helix with three polypeptide strands of-(Pro-Hyp-Gly)_n [103]. Carbon, nitrogen, oxygen and hydrogen atoms are in grey, blue, red and white in colour.

1.4 Objectives

1.4.1 Crystal structure of anhydrous calcium oxalate

Apart from the biomimetic growth and morphology control of calcium oxalate hydrates, the crystal structure of anhydrous calcium oxalate, which remained unknown for decades, is revealed in the present work (Section 3.2).

The anhydrous calcium oxalate, COA, is reported to undergo temperature dependent phase transitions to form α -, β - and γ - modifications, (as noted in equation (1.4)) but this was controversially discussed [39-44].



The crystal structure of the so called β -modification of COA is resolved by a combination of atomistic computer simulations and Rietveld refinements on the basis of the X-ray powder pattern [104].

1.4.2 Additives as growth modifiers

1.4.2.1 Control of morphology of calcium oxalates in the presence of PAA

The second target of the present study was the structural and habitual modifications of calcium oxalates formed in the presence of the sodium salt of polyacrylate (PAA) (Fig. 1.19). As already stated, it has been demonstrated that PAA not only inhibits the growth of COM, but also controls the morphology of COD [84,105,106]. PAA has been found to change the shape of COD from tetragonal bipyramids to tetragonal prisms to dumbbells, and even to spheres on increasing the concentration of the polymer. A similar trend was observed for COD grown in the presence of double-hydrophilic block polymer and carboxylate modified Inulin biopolymers [85,107]. It was speculated that the change in morphology from tetragonal bipyramids to tetragonal prisms was caused by the preferential adsorption of PAA on the (100) faces of COD and preferred crystal growth along the [001] direction.

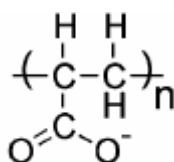


Fig. 1.19. Molecular configuration of PAA.

The unusual COD dumbbells formed in the presence of PAA bears shape similar to the fluorapatite-gelatine aggregates reported by Kniep *et al.*, however very little was known about the COD-PAA system. It is easier to interpret the results when a better defined component such as PAA is used as the organic part. Therefore, the influence of PAA on controlling the morphologies of calcium oxalates by simple crystallization from slightly oversaturated aqueous solutions was investigated “systematically” with the aim to clarify the role of PAA and understand the inner architecture as well as the morphogenesis of the so-formed unusual COD dumbbells (Section 3.3). The experiments were performed by varying the pH of the stock solutions and the molar ratio of calcium

oxalate to PAA. Apart from the experimental investigations, the interaction of PAA on the (100) faces and the (101) faces of COD is compared with the aid of atomistic computer simulations.

1.4.2.2 “Organic” gel-mediated growth of calcium oxalates

In addition to the precipitation reactions, the growth of calcium oxalates in organic gels, agar, agarose, carrageenan and gelatine were investigated in order to generate biomimetic calcium oxalates (Section 3.4).

Biogenic calcium oxalates are formed in the presence of polysaccharides such as chondroitin sulphate A, chondroitin sulphate C, heparan sulphate, keratan sulphate, *etc.* and proteins such as osteopontin, Tamm-Horsfall protein and many other acid rich urinary proteins [Appendix Table 6.2, 50-52]. Proteins and polyelectrolytes have commanded a lion’s share of research into the role of macromolecules in stone genesis, while polysaccharides are almost ignored [108-112]. As already stated, the growth of calcium oxalates in organic gels by double diffusion technique have so far met with little success in generating calcium oxalates with similar in morphology with the biogenic forms. Moreover, relatively little is currently known about the true nature of the association between stone macromolecules and their mineral components, or their functional role, if any, in urolithiasis. This is due to the lack of a model system. Agar and carrageenan were used therefore, with an intention to mimic the urinary polysaccharides; and gelatine was used to mimic the proteins present in the kidney.

Experiments using agar gel were done extensively to discover the true role of polysaccharides on calcium oxalate “calculogenesis”. The influence of initial calcium oxalate concentration, pH and concentration of the gel on the formation of hydration states of calcium oxalates have been investigated along with the stated general methods. Commonly, the study of calcium oxalate crystallization is performed in pH ranges from 6 to 7 [83,113,114]. This work concerns mainly with the use of pH values superior to 6. Such knowledge of the influence of pH on varying the phase and morphology of calcium oxalates is significant in view of the potential applications in the inhibitory processes.

2 Experimental section

2.1 Crystallization of calcium oxalates by slow evaporation of the solvent

2.1.1 Growth of calcium oxalates without additives

For the crystallization of calcium oxalate monohydrate (COM), 0.5 mM of $\text{CaCl}_2 \cdot 2\text{H}_2\text{O}$ (Merck) in 500 ml of water were added to 500 ml of distilled water at 75 °C followed by the drop wise addition of 500 ml of 15 mM $\text{Na}_2\text{C}_2\text{O}_4$ (Merck). The final concentration of calcium oxalate was approximately 5 mM. The system was then stirred slowly for one hour at 75 °C and finally cooled to 25 °C under continuous stirring. The crystals obtained were separated from the mother liquor by centrifugation and thoroughly washed with distilled water and dried at 40 °C.

2.1.2 Growth of calcium oxalates in the presence of PAA

In the experiments to study the effect of the sodium salt of polyacrylic acid (PAA) on the crystallization of calcium oxalates, 0.1 M solutions of both $\text{CaCl}_2 \cdot 2\text{H}_2\text{O}$ (Merck) and $\text{Na}_2\text{C}_2\text{O}_4$ (Merck) in distilled water were first prepared as stock solutions. In a typical synthesis, an aqueous solution of $\text{Na}_2\text{C}_2\text{O}_4$ (0.8 mM) was added to an aqueous solution of PAA (Fluka, Average $M_w = 5100$ g/mol) followed by moderate stirring with a magnetic stirrer for a minute. The concentration of PAA was varied from 0 to 300 $\mu\text{g/mL}$. Addition of an aqueous solution of $\text{CaCl}_2 \cdot 2\text{H}_2\text{O}$ to the PAA- $\text{Na}_2\text{C}_2\text{O}_4$ solution resulted in a final concentration of 0.8 mM calcium oxalate. The mixture was stirred for another minute and left open in a humidity controlled chamber (BINDER) for 3 days at 26 °C, 70% humidity, 30% fan speed, to ensure the slow evaporation of water and thereby to overcome the difficulty of obtaining bigger crystals. No efforts were made to adjust the pH except for experiments in which specific variations of pH were needed. After 3 days the grown aggregates were washed 3 times with water, centrifuged and dried at 40 °C. The effects of PAA on the crystallographic and morphological properties of calcium oxalates have also been investigated over a range of physiological supersaturation values. For the experiments with specific variation of pH, the stock solutions were made acidic or alkaline by the use of 2 N HCl and 2 N NaOH respectively. For specific pH values like 3.6 and 5.6, acetate buffer (by mixing 185 mL of 0.1 N acetic acid and 181 mL of 0.1 N sodium acetate and 19 mL of 0.1 N acetic acid and 15 mL of 0.1 N sodium

acetate to achieve pH of 3.6 and 5.6 respectively) was used since it is difficult to achieve these pH values without any buffer.

2.2 Biomimetic growth of calcium oxalates: The double diffusion technique

The biomineralization of calcium oxalate was mimicked using a double-diffusion set-up (Fig. 2.1) according to procedures reported previously for fluorapatite-gelatine nanocomposites [7].

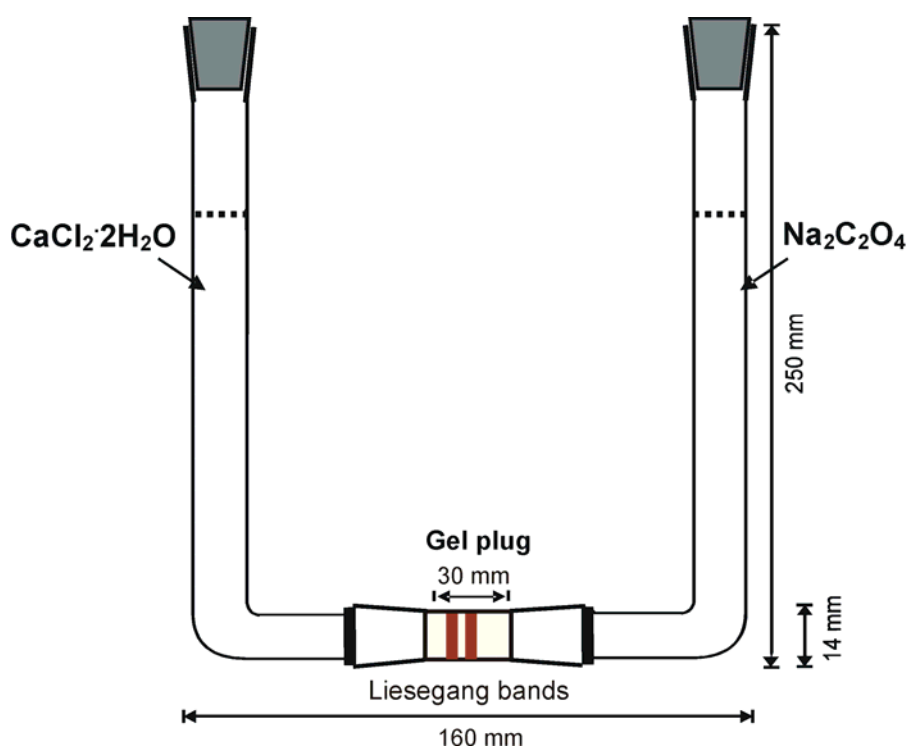


Fig. 2.1. Sketch of the double diffusion set-up.

The set-up consists of two L-shaped tubes filled with aqueous solutions of $\text{CaCl}_2 \cdot 2\text{H}_2\text{O}$ (0.05 M, 25 mL) and $\text{Na}_2\text{C}_2\text{O}_4$ (0.05 M, 25 mL), respectively. These reservoirs of stock solutions are separated by a horizontal tube (16.5 mm in diameter, 75 mm in length) which is filled with a gel of pre-adjusted pH. Four organic gels were used in the present study, agar, agarose, carrageenan and gelatine. The gel plug was approximately 30 mm in length and 5 cm³ in volume. The temperature was held constant during the experiments using a water bath. Within a few days, the calcium oxalate aggregates were formed inside the gel matrix in periodically arranged bands called Liesegang bands. The Liesegang band, located close to the calcium source is named C and the one close to the

oxalate source is named O. The M band (middle band) is located between C and O bands. In order to isolate the aggregates from the gel, the gel plug was pressed out of the tube and cut into slices consisting of the respective Liesegang bands. The pH of the separated bands was measured with a Mettler Toledo surface electrode. The isolated Liesegang segments were treated with water and the products were washed five times in hot distilled water, centrifuged and finally dried at 40 °C.

2.3 Characterization techniques

2.3.1 Optical microscopy

Light microscopy images were taken by using an “Axioplan 2 imaging” microscope from the company Carl-Zeiss equipped with different interchangeable objectives with magnifications of 5-, 10-, 20-, 50- and 100-times and an eyepiece with 10-times magnifying power. Pictures were recorded using the software programme AnalySIS labFlow [Soft Imaging System GmbH, Version 5, Munster].

2.3.2 Powder X-ray diffraction

The phase composition of the samples was determined by X-ray diffraction analyses. The samples were ground well, suspended in ethanol and mounted on a Kapton film adhering on aluminium rings. The air and moisture sensitive samples (anhydrous calcium oxalate) for powder X-ray diffraction measurements were prepared inside an argon glove box. The air sensitive samples were filled in Lindemann glass capillary tubes with a diameter of 0.5 mm up to a length of 2-3 cm. Another capillary tube of lower diameter was inserted inside the first one to fix the powder and the ends of both the tubes were sealed with two component epoxy glue. Samples for High temperature powder X-ray diffraction (HT XRD) were filled in quartz capillaries of 0.5 mm diameter.

X-ray powder data were collected in transmission mode using a Huber G670 Image Plate Camera, Cu $K\alpha_1$ - radiation ($\lambda = 1.540598 \text{ \AA}$) and a germanium (111) monochromator. Data collections were made in the range of $3^\circ \leq 2\theta \leq 100^\circ$ with a step size of $0.005^\circ 2\theta$ (exposure time 90 min). HT XRD was carried out on a STOE-diffractometer (STOE STADI P, Debye-Scherrer, linear PSD, Cu $K\alpha_1$ - radiation, Ge monochromator, High Temperature Attachment 0.65.3). Data manipulation of the X-ray powder diffraction data was made by using the commercially available STOE WinXPOW software package [Version 1.2, Programm zur Messung und Auswertung

von Röntgenpulverdiffraktogrammen, STOE & Cie GmbH., Darmstadt]. Lattice parameters were calculated by least squares refinements using LaB₆ (cubic, $a = 4.15692$ Å) as internal standard and the program package WinCSD [115].

2.3.3 Chemical analysis

The composition of the compounds under investigation was checked by elemental analyses. Calcium was determined using Inductive Coupled Plasma–Optical Emission Spectroscopy (ICP-OES); (Simultaneous ICP-OES spectrometer, Varian “Vista RL” with CCD detector and radial argon plasma, wavelength coverage 167-785 nm). A CHNS-analyzer 932 (Leco, USA) was used for C, H and N analysis. The determination of nitrogen and oxygen is accomplished by the carrier gas- hot extraction method. For the determination of nitrogen and oxygen, the samples (approximately 15 mg inside tin capsules) were usually pyrolysed in O₂ atmosphere. The oxygen content is detected by measuring CO and CO₂ with the help of Non- Dispersive Infrared Spectroscopy (ND-IR) and the nitrogen content by thermal conductivity detection. For the determination of the carbon content, the samples were mixed with metallic-ash catalysts (oxygen donors) and were heated in O₂ atmosphere in a high frequency furnace ($T_{\max} = 2473\text{K}$). The determination of the carbon content was made by detecting CO₂ by means of the infrared detectors (ND-IR).

2.3.4 FT-IR, Raman spectroscopy

For the measurement of infrared spectra, the samples were prepared by mixing homogeneously typically 1 mg of the material under investigation in approximately 150 mg dried potassium bromide (Merck, *Uvasol* for Infra-Red Spectroscopy), and pressing under 10 tons of pressure for 15 minutes to make a pellet of 8.0 mm diameter. Fourier transform infrared (FT-IR) spectra in the region of 4000 - 400 cm⁻¹ were recorded at room temperature using a Bruker spectrometer (IFS 66v/S; Global (MIR), KBr, DTGS-Detector; Program Opus/IR 3.0.3). In order to separate the overlapping bands the spectral ranges were fitted with Pseudo-Voigt 1 distributions for the bands. The software package Origin 7.0 (Origin Lab Corporation, MA, USA) was used for the calculations. Raman spectra in the region 1500 - 300 cm⁻¹ were collected at room temperature using LabRam System 010 (Horiba Jobin Yvon, France) in the back scattering mode. The 633.817 nm line of a He-Ne laser with 1 mW light power was used for excitation of the samples

under a microscope (20-times magnification). For the measurements, the ground powder was spread on a glass plate. The spectrometer was calibrated using Si as a reference.

2.3.5 Difference thermal analysis (DTA), thermogravimetry (TG)

The decomposition processes of the aggregates were investigated by means of a Netzsch Thermal Analyser STA 409, coupled with a capillary mass spectrometer QMS 403C-Aeolos. The sample weights were 30 mg and heating was performed in an alumina crucible with a rate of 5 K/min up to 1200 °C in air. Data analysis was performed with the software program from NETZSCH (NETZSCH Proteus-Thermal Analysis-Version 4.8.3. beta).

2.3.6 Scanning electron microscopy (SEM)

The samples were mounted onto conductive carbon tapes adhered on aluminium or brass holders and were sputter coated with gold for a minute with Cressington108 Auto Sputter coater. The morphology of the aggregates obtained was investigated by means of an ESEM FEI Quanta 200 FEGi system operated in a low vacuum (70 Pa) mode and at an acceleration voltage of 15 kV (FEI Company, Eindhoven, NL). High resolution images were obtained using a solid-state back scattered electron (SSD-BSE) detector.

2.3.7 Transmission electron microscopy (TEM)

For TEM investigations focused ion beam (FIB) thin cuts of the aggregates were prepared by means of a FEI Quanta 200 3D dual beam device (FEI Company, Eindhoven, NL). For this purpose the samples were deposited onto a thin silicon wafer bar and thin sections were obtained using the FIB technique in a dual SEM/SIM (Scanning Ion Microscope). Extreme care had to be taken to protect the samples against electron beam destruction. For this, the sample was protected using platinum support. This is done by ion beam (Ga^+) assisted chemical vapour (Trimethyl [(1,2,3,4,5-ETA)-1 Methyl 2,4-Cyclopentadien-1-YL] Platinum) deposition. TEM experiments were carried out by using a FEI Tecnai 10 electron microscope (FEI Company, Eindhoven, NL) with LaB_6 -source at 100 kV acceleration voltage. Images were recorded by means of a Tietz slow scan CCD F224HD TVIPS camera (2k x 2k pixels, pixel size 24 μm , digitization 16 bit) with an active area of 49 mm x 49 mm. (Tietz Video and Image Processing Systems GmbH, Gauting, Germany).

3 Results and discussions

3.1 Growth of calcium oxalates without additives

3.1.1 The effect of pH and initial supersaturation

Under stoichiometric conditions, the reactant concentration was varied from 0.6 to 1.4 mM to study the influence of initial supersaturation and pH on the hydration state of calcium oxalate formed in the absence of any additives. Equation 3.1.1 defines the saturation level S , the ratio of the ion activity product to the ion solubility product.

$$(3.1.1) S = \{\gamma_{Ca} [Ca] \gamma_{C_2O_4} [C_2O_4]\} / K_{sp}$$

γ is the activity coefficient and K_{sp} is the solubility product of calcium oxalate at the temperature evaluated. The activity coefficient is calculated from the Davies extension of the Debye-Hueckel equation (Equation 3.1.2),

$$(3.1.2) -\log \gamma_z = A z^2 [I^{0.5} / (1+I^{0.5}) - 0.3 I]$$

(A: Debye-Hueckel constant = 0.5115, I: ionic strength = $\sum z^2 c$, z: valency, c: molarity for all the ions in solution).

The analytical value for calcium is used as the calcium concentration. The oxalate ion concentration is estimated from the analytical value for total oxalic acid which is done using the alpha distribution method. The alpha distribution method calculates the ion fractions for a diprotic acid such as oxalic acid as follows.

$$(3.1.3) [Oxalic_{total}] = [H_2C_2O_4] + [HC_2O_4^-] + [C_2O_4^{2-}]$$

$$(3.1.4) \alpha_0 = [H_2C_2O_4] / [Oxalic_{total}]$$

$$(3.1.5) \alpha_1 = [HC_2O_4^-] / [Oxalic_{total}]$$

$$(3.1.6) \alpha_2 = [C_2O_4^{2-}] / [Oxalic_{total}]$$

$$(3.1.7) \alpha_0 = [H]^2 / ([H]^2 + K_1 [H] + K_1 K_2)$$

$$(3.1.8) \alpha_1 = K_1 [H] / ([H]^2 + K_1 [H] + K_1 K_2)$$

$$(3.1.9) \alpha_2 = K_1 K_2 / ([H]^2 + K_1 [H] + K_1 K_2)$$

$$(3.1.10) [C_2O_4^{2-}] = \alpha_2 [Oxalic_{total}]$$

Figure 3.1.1 (a) shows a full distribution of oxalic acid species (protonated and non-protonated) at 25 °C, as calculated using the alpha distribution method. The values used for K_1 , K_2 and K_{sp} are 5.62×10^{-2} , 5.37×10^{-5} and 2×10^{-9} respectively [116-118].

The base ten logarithm of the saturation level is used for interpretation. Accordingly, the general variation of supersaturation of COM (corresponding to an initial concentration of 1mM calcium and oxalate solutions) with respect to pH values is as shown in figure 3.1.1 (b). The CaOx supersaturation increases up to pH 6 and remains constant afterwards.

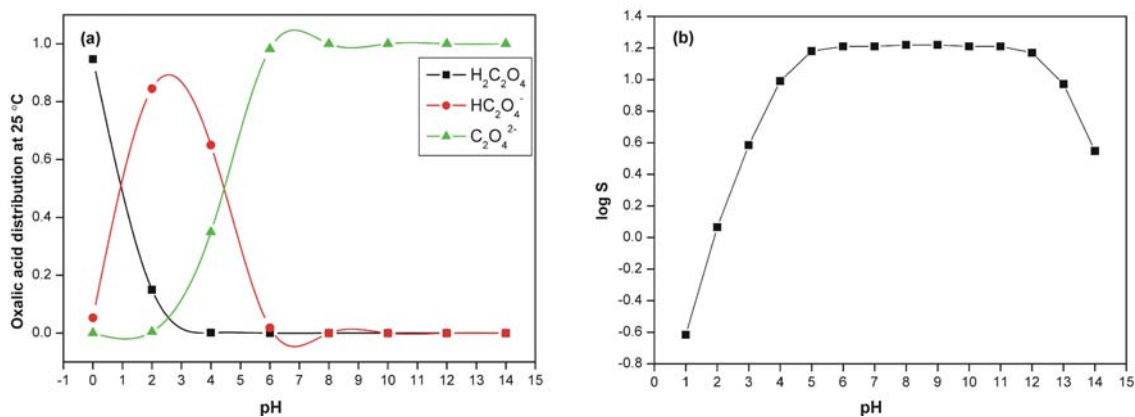


Fig. 3.1.1. (a) Distribution of oxalic acid species at 25 °C at different pH values and the variation of COM supersaturation at different pH (b). The COM supersaturation is more or less unaffected at pH > 6.

The morphology and hydration state of calcium oxalates was found to vary with change in initial CaOx concentrations and pH values. The observed results are shown in the form of a map (Fig. 3.1.2). We confined our investigations mainly to pH 3, 7 and 9. At pH 3, COM was formed at all supersaturation levels. At pH 7, COD crystals dominated up to 0.9 mM CaOx and COM for 1 to 1.4 mM CaOx concentrations. Although the solution CaOx supersaturation remains the same after pH 7, we observed a dominance of COT crystals at pH greater than 8. At pH 9, COT was formed at low supersaturation and a mixture of COM and COT at higher supersaturation. This method turned out to be a simple procedure for the production of COT. Under non stoichiometric conditions (unequal calcium and oxalate solution concentrations), an excess calcium concentration favoured the production of COD and excess oxalate, COM [119].

COM crystals formed were mostly twinned crystals (Fig. 3.1.3 a) and very few single crystals with six-sided platy morphology (Fig. 3.1.3 b). COD crystals were tetragonal bipyramids (Fig. 3.1.3 c,d, XRD pattern in appendix Fig. 6.2) whereas COT had a platy parallelogram-like morphology (Fig. 3.1.3 e,f, XRD pattern in appendix Fig. 6.2).

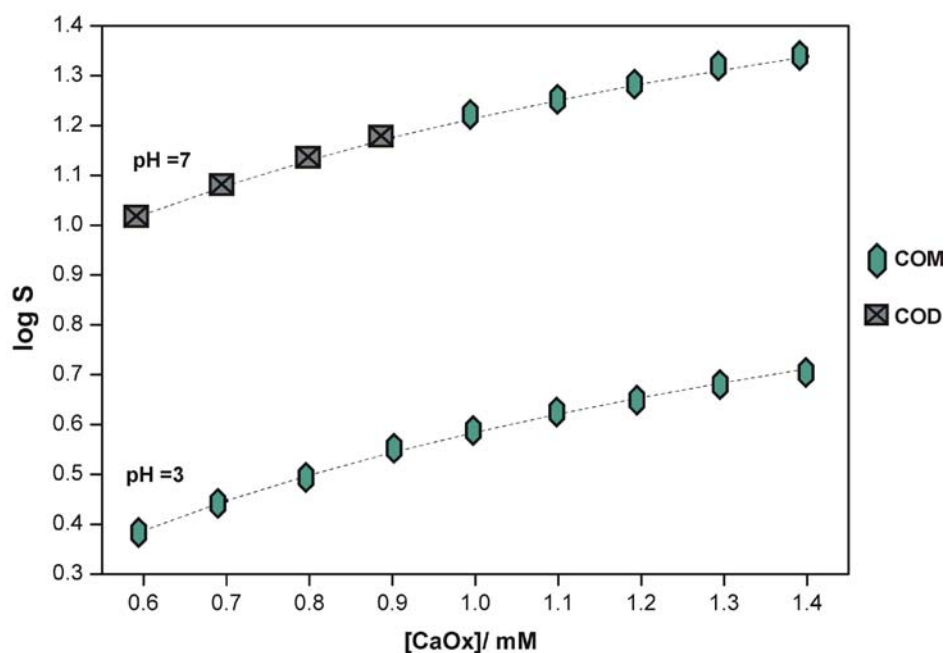


Fig. 3.1.2. Morphology and hydration state of calcium oxalates with respect to pH and supersaturation. The green coloured hexagon represents the six-sided platy morphology of COM even though most of the crystals formed were twinned, the ash coloured tetragon represents the tetragonal bipyramidal morphology of COD. At pH > 8, there is a dominance of COT. For the SEM images, refer to figure 3.1.3.

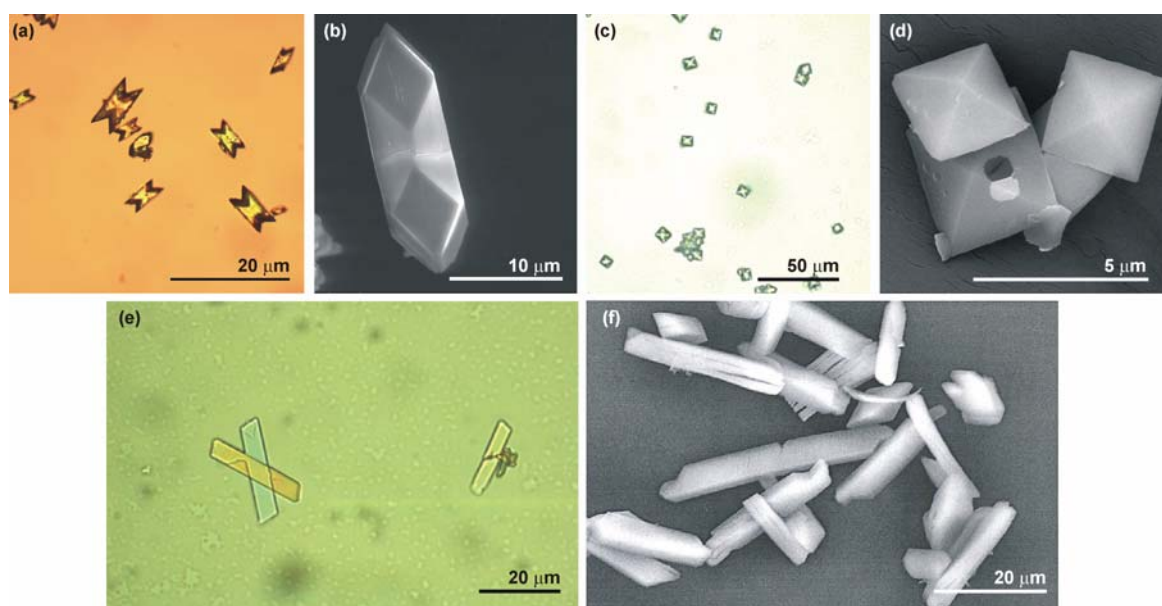


Fig. 3.1.3. Morphology of calcium oxalates grown from aqueous solutions without any additive. (a) light microscope image of twinned COM crystals, (b) SEM image of a single crystal of COM with six-sided platy habit, (c) light microscope image of tetragonal bipyramidal COD, (d) SEM image of tetragonal bipyramidal COD : note the damage of the sample under the electron beam. Light microscope (e) and SEM (f) images of COT with platy habit.

3.1.2 Characterization of calcium oxalate monohydrate (COM)

COM crystals (grown from 1mM calcium oxalate concentration at pH 6.5) were further characterized by chemical analysis, TG/DTA (Appendix Fig. 6.1) IR/Raman (Fig. 3.1.4) and XRD (Fig. 3.1.5). The chemical analysis indicated 27.60(\pm 0.16) wt.-% Ca, 16.48(\pm 0.08) wt.-% C, 1.52(\pm 0.03) wt.-% H and 57.3 wt.-% O in comparison to the calculated values of 27.43 wt.-%, 16.44 wt.-%, 1.38 wt.-% and 54.75 wt.-% respectively.

The IR spectrum in the region of 400 to 4000 cm^{-1} was recorded at room temperature. It is rather easy to assign the asymmetric and symmetric stretching modes of water molecules coordinated with COM as the five bands which appear above 3000 cm^{-1} . The most prominent bands in the spectrum of COM occurred at 1618, 519, 1317 and 780 cm^{-1} corresponding to ν_9 , ν_{10} , ν_{11} and ν_{12} [120-123]. The other bands in the FTIR and Raman spectra (Fig. 3.1.4 a,b) are assigned and recorded in table 3.1.1.

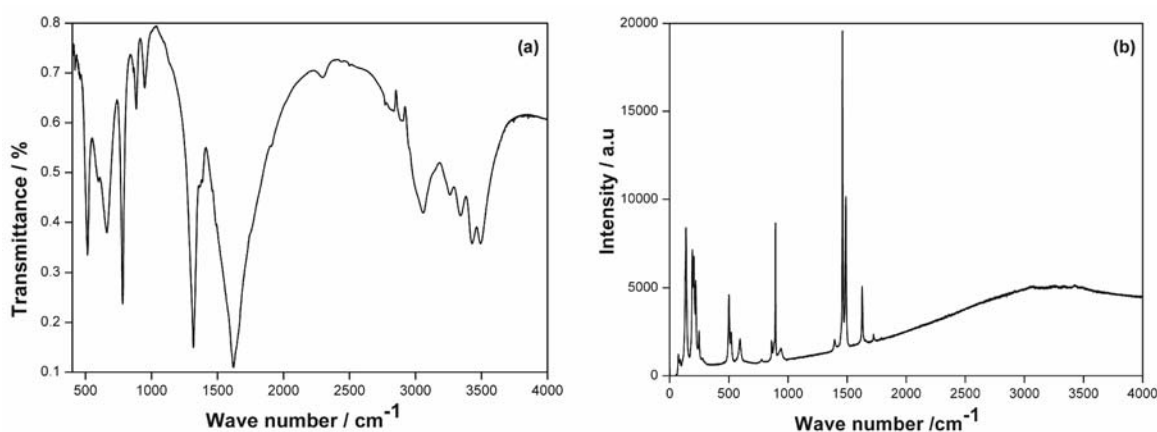


Fig. 3.1.4. (a) FT-IR and (b) Raman spectra of COM.

Table 3.1.1. IR and Raman vibration modes observed for COM and their assignments.

Vibration mode	IR (cm^{-1})	Raman (cm^{-1})
ν_1	1489	1461,1489
ν_2	-	882,894
ν_3	514	501,520
ν_5 ; ν_{as} (COO) _{out-of-plane}	1568 w	1627
ν_9 ; ν_{as} (COO) _{in-plane}	1618 vvs	1618
ν_{10} ; δ (OCO) _{out-of-plane}	519 s	476
ν_{11} ; ν_{sym} (COO) _{out-of-plane}	1317 vs	1393
ν_{12} ; δ (OCO) _{out-of-plane}	780 s	777
$\nu_1+\nu_{10}$; ν_{sym} (COO) _{in-plane} + ν (CC)	1385 sh	-

ν - stretching; δ - bending; as- antisymmetric; sym- symmetric; vs- very strong; w- weak; sh- shoulder; s- strong

A comparison of the observed XRD pattern with the pattern generated from the generally accepted crystal structure reported by Tazzoli and Domeneghetti [20] (Fig. 25) and the low temperature and high temperature phases of COM by Deganello and Piro [23-25] (Fig. 3.1.5) indicates that Tazzoli's structure more closely fits to COM. The lattice parameters for the as-prepared COM were refined using the crystal structure data program CSD as, monoclinic, $a = 6.2919(3) \text{ \AA}$, $b = 14.591(1) \text{ \AA}$, $c = 10.1193(3) \text{ \AA}$, $\beta = 109.455(4)^\circ$ and space group $P2_1/c$.

Analysis of the XRD patterns of the low temperature (ICSD 20-231) and high temperature (ICSD 14-768) phases of COM reveals that the intensity of the peaks which exclusively belong to the LT phase is extremely weak (reflections marked with * in figure 3.1.5). These reflections correspond to 2θ values, 15.92° , 16.12° , 20.5° , 26.16° , 26.9° , 27.6° , 28.28° , 29.02° , 32.8° , 33.92° , 34.14° and 35.06° .

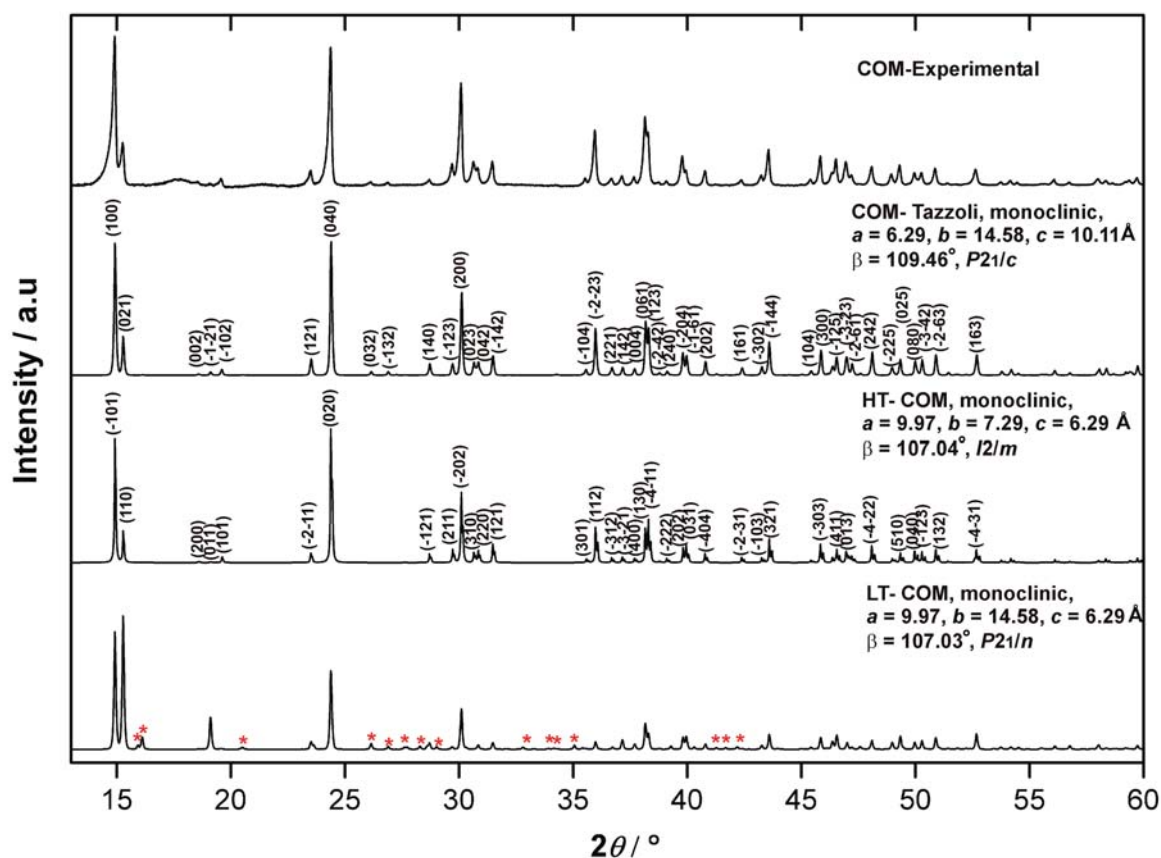


Fig. 3.1.5. Comparison of the XRD pattern of COM (experimental data measured using $\text{Cu } K\alpha_1$ - radiation) with the COM crystal structure proposed by Tazzoli [20] and the crystal structure of the low temperature phase of COM and the high temperature phase of COM proposed by Deganello and Piro [23-25]. The reflections marked with * are those occurring only in LT-COM and not in HT modification.

In order to check the transformation into the high temperature modification of COM, the as-prepared COM crystals were subjected to temperature dependent X-ray diffraction (STOE STADI P, Debye-Scherrer, linear PSD, Cu $K\alpha_1$ - radiation, Ge monochromator, High Temperature Attachment 0.65.3 of STOE). The COM powder was filled in Lindemann quartz capillary tubes with a diameter of 0.5 mm up to a length of 2-3 cm. The XRD pattern was recorded at temperatures ranging from room temperature to 300 °C with a scanning time of 460 seconds per step. The heating rate between the temperature steps was 5 °C/min. No significant change in the XRD pattern was recorded up to 125 °C and therefore the transformation to the high temperature modification of COM could not be observed (Fig. 3.1.6). Above 100 °C the onset of dehydration causes shifts in the reflections to lower 2θ values. One reason for the non detection of the HT phase could be that the low intensity peaks for the LT phase could not be recorded when the measurement was done using a quartz capillary. The low intensity peaks of the LT phase fall in the background noise of the measured pattern. The LT form exhibiting a primitive cell with a doubled b parameter in comparison with the HT phase is characterized by the presence of extremely weak superstructure reflections which are possible to track only *via* electron diffraction patterns [23]. X-ray powder methods are not sensitive enough to record these reflections thus disguising the doubling of b .

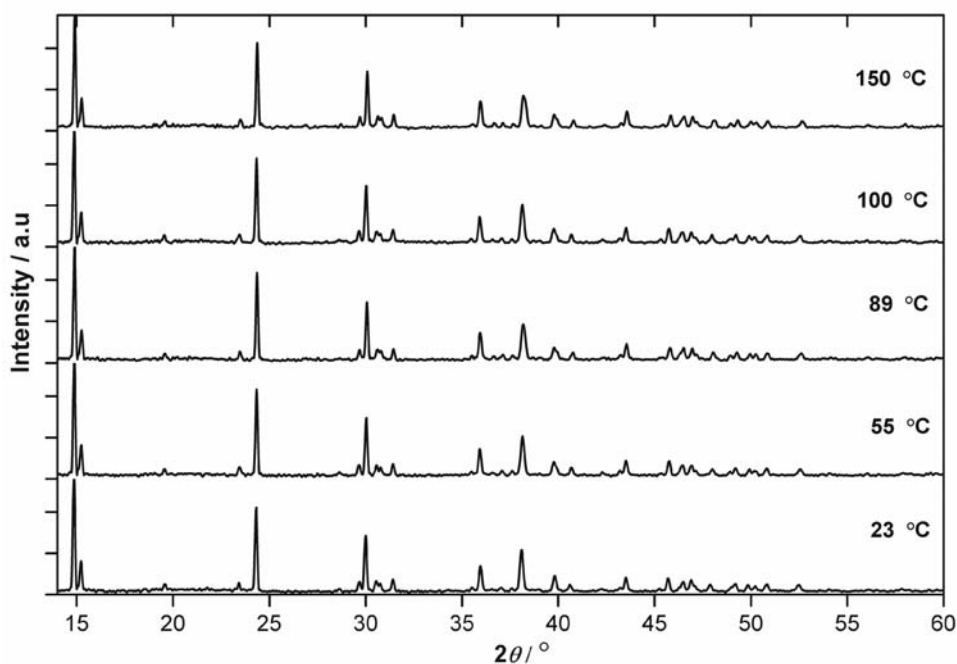


Fig. 3.1.6. XRD pattern of COM at various temperatures (measured using Cu $K\alpha_1$ - radiation). The patterns do not show any phase transition from the LT- to the HT-modification of COM.

Furthermore, the COM sample when analysed by DSC from -20 to 300 °C (heating rate 10 K/min) under argon atmosphere showed a minor endothermic peak at 81.5 °C (Fig. 3.1.7). In fact, the transition at 81.5 °C (absent upon cooling) belongs to the monohydrate form rather than the anhydrous form of calcium oxalate. The peak at 198.5 °C belongs to the dehydration of COM to form anhydrous calcium oxalate (COA).

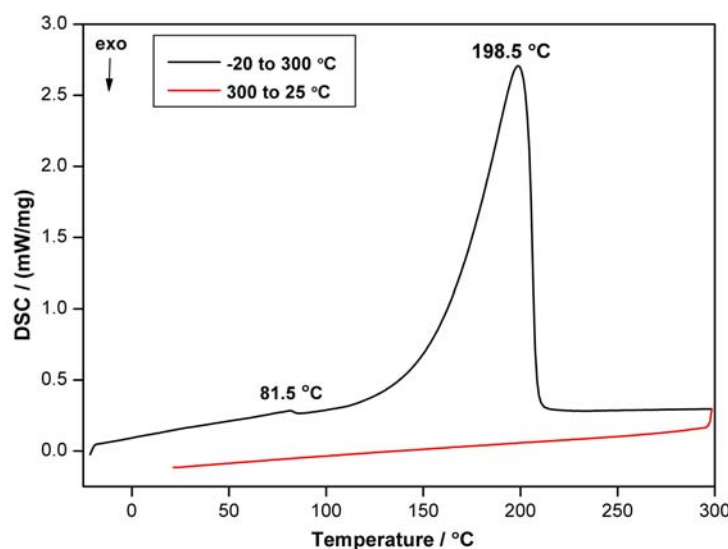


Fig. 3.1.7. DSC curve of COM from -20 to 300 °C. The small endothermic peak at 81.5 °C corresponds to the transition from the LT to HT phase of COM and the large endothermic peak at 198.5 °C corresponds to the loss of water molecule. Black curve represents the heating curve and the red curve represents the cooling curve.

This transition at 81.5 °C could be attributed to the low/ high temperature phase transition even though this temperature is not in good agreement with the XRD and Raman results which reported completion of this transition between 45 and 55 °C [120]. Differences in experimental set-up conditions may partly explain this discrepancy. Similar observations were reported by high temperature XRD measurements under different conditions by Gallagher *et al.* [124]. Again, the LT-/ HT -phase transition was not observed by variable-temperature Diffuse Reflectance Fourier Transform Infrared spectroscopy coupled with mass spectrometry (DRIFT/MS) by Ai *et al.* [121]. Even though, the XRD pattern does not show any evidence for the phase transition, the transition in DSC at 81.5 °C could be caused by the phase transition of COM. Nevertheless, this indicates that the LT- and HT- COM coexist in the present system up to 81.5 °C. Therefore, DSC measurements and electron diffraction patterns are more sensitive to track the phase transformation of COM.

3.2 Anhydrous calcium oxalate

3.2.1 Synthesis and characterization

The anhydrous calcium oxalate (COA) was prepared by thermal dehydration of calcium oxalate monohydrate (COM). For the preparation of COM, 8.5 mM (1.1g) of $\text{CaCl}_2 \cdot 2\text{H}_2\text{O}$ was added to 1000 ml of distilled water at 75 °C followed by drop-wise addition of 500 ml of 15 mM $\text{Na}_2\text{C}_2\text{O}_4$. The final concentration of calcium oxalate was approximately 5 mM. The solution was then stirred slowly for 1 hour at 75 °C and finally cooled to 25 °C under continuous stirring. The crystals obtained (15 to 20 μm in size) were separated from the mother liquor by centrifugation and thoroughly washed with distilled water. The reaction product was characterized as COM by elementary analysis and X-ray powder diffraction. In order to obtain the anhydrous form, the thermal dehydration was performed using a DTA/TG inside an argon filled glove box. Approximately 30 mg of COM were heated up to 370 °C with a heating rate of 2 °C/min in a corundum crucible. After isothermal storage of the sample for 5 hours at 370 °C it was cooled to room temperature with a rate of 2 °C/min (Appendix Fig. 6.1 right). The observed mass loss (12.51 wt.%) due to the thermal treatment matched the calculated mass loss according to equation 1 (12.3 wt.%). After thermal decomposition the resulting polycrystalline and hygroscopic COA was collected for further investigations. All preparations were done in an argon filled glove box (Braun).

Chemical analysis: The chemical analysis of COA obtained after thermal decomposition of COM was performed under inert atmosphere. The amounts (in wt.-%) of Ca $32.01 \pm 0.42\%$ (31.28) and C $18.38 \pm 0.38\%$ (18.75) were in good agreement with the calculated values (in parentheses), while the amount of oxygen $28.69 \pm 0.31\%$ (49.96) was not reliable. This may be due to the absorption of oxygen from the atmosphere during sample preparation and storing.

IR spectroscopy: The samples were prepared as KBr pellets (0.25 mg of the material under investigation dispersed in 150 mg KBr) inside an argon filled glove box. A comparison of the FT-IR spectra of the parent COM and the COA obtained by the thermal dehydration is shown in figure 28. Apart from the effects that can be attributed to the loss of water, the spectra of COM and COA are closely related (Fig. 3.2.1 a, Table 3.2.1). The strongest antisymmetric carbonyl stretching ν_{as} (C-O) occurs at 1618 cm^{-1} for COM and at 1625 cm^{-1} for COA. The secondary carbonyl stretching modes, the metal

carboxylate stretch, $\nu_{\text{sym}}(\text{C-O})$ occurs at 1317 cm^{-1} for COM and 1320 cm^{-1} for COA. The O-C-O antisymmetric in plane bending occurs at 519 cm^{-1} for COM and 524 cm^{-1} for COA. The out of plane bending of O-C-O groups occur at 780 cm^{-1} for COM and 787 cm^{-1} for COA. In order to separate the overlapping bands the spectral ranges $1400\text{--}1900\text{ cm}^{-1}$ were fitted with Pseudo-Voigt 1 distributions (Fig. 3.2.1 b). The fit has an R value of 0.99735 and the exact peak positions are $1625, 1638, 1703, 1710\text{ cm}^{-1}$. The peak at 1625 cm^{-1} with a shoulder at 1710 cm^{-1} is solely from COA. The band at 1710 cm^{-1} is a combination band produced by the low-frequency oxalate anion rotatory motion which could have been masked by the intense ν_9 absorption in COM [121].

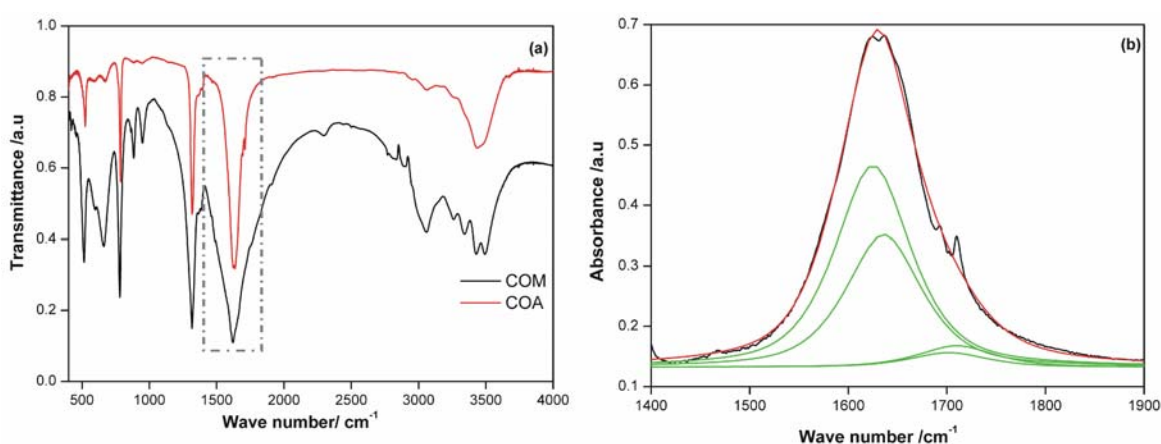


Fig. 3.2.1. (a) FT-IR spectra of COM and COA (dashed frames indicate the selected regions of the FT-IR spectrum fitted with Pseudo-Voigt 1 distributions for the bands from COA). (b) The experimental data for COA from the dashed frame is indicated by black lines. The red line is the resulting calculated spectrum and the green lines are the separated peaks.

Table 3.2.1. Comparison of the IR vibration modes for COM and COA produced by the thermal dehydration of COM.

COM	COA	Mode; description
1618 vvs	1625,1638	$\nu_9; \nu_{\text{as}}(\text{COO})$ in-plane
1568 w	NO	$\nu_5; \nu_{\text{as}}(\text{COO})$ out-of-plane
1385 sh	1397	$\nu_{1+} \nu_{10}; \nu_{\text{sym}}(\text{COO})$ in-plane + $\nu(\text{CC})$
1317 vs	1320	$\nu_{11}; \nu_{\text{sym}}(\text{COO})$ out-of-plane
780 s	787	$\nu_{12}; \delta(\text{OCO})$ out-of-plane
519 s	524	$\nu_{10}; \delta(\text{OCO})$ out-of-plane

ν - stretching; δ - bending; as- antisymmetric; sym- symmetric; vs- very strong; w- weak; sh- shoulder; s- strong

The reduction in band widths and the increase in intensity are characteristic for COA. These changes reflect the influence of lattice water molecules on the oxalate anion vibrations in COM. The loss of water molecules from COM results in larger stretching and bending force constants for the oxalate anions which is evident from the blue shifts.

Powder XRD: For XRD, the COA powder was filled in Lindemann glass capillary tubes with a diameter of 0.5 mm up to a length of 2-3 cm. Another capillary tube of lower diameter was inserted inside the first one to fix the powder and the ends of both the tubes were sealed with two component epoxy glue. The XRD pattern of COA (Fig. 3.2.2) matched with the JCPDS-database entry of the so-called β -modification (PDF: 18-296) of COA [39].

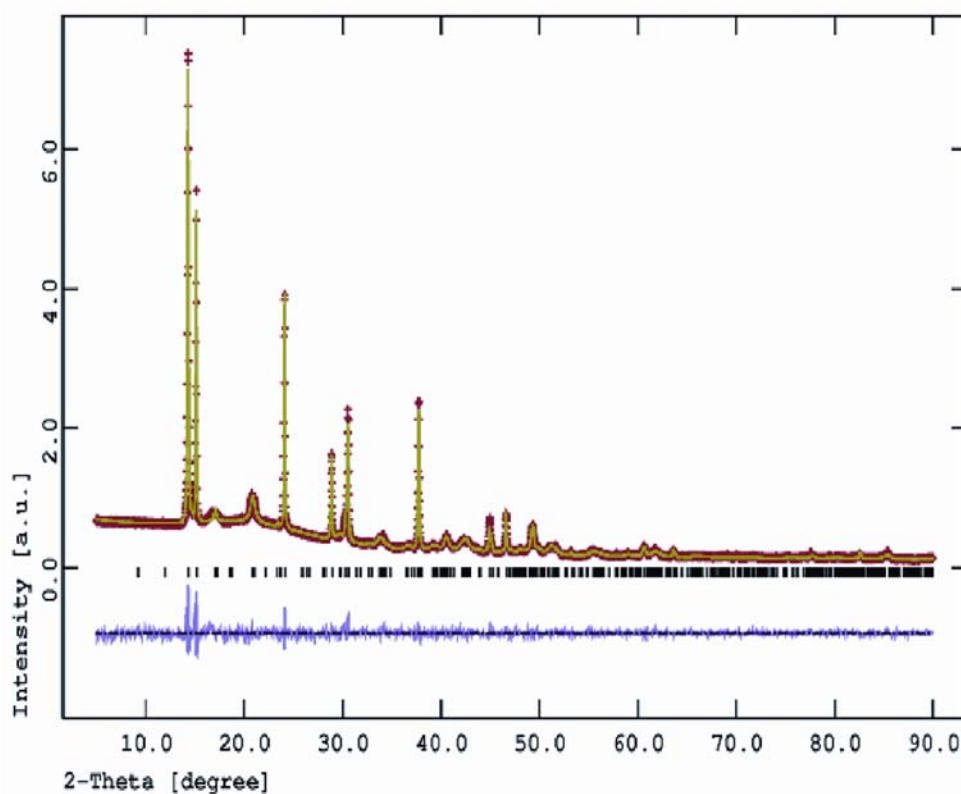


Fig. 3.2.2. Comparison of the measured (red) X-ray powder diffraction pattern with the calculated (green) pattern according to the Rietveld refinement. The difference plot of both is given in purple [134]. (Cu $K_{\alpha 1}$ radiation).

3.2.2 Crystal structure from a combination of atomistic simulations and rietveld refinements

Attempts for indexing the obtained X-ray powder pattern of COA by use of the indexing routines TREOR, ITO, DICVOL and MCMAILLE [125] failed. So, neither lattice parameters of the compound nor structure factors were accessible nor the well established techniques for solving a crystal structure from powdered samples – like *Direct-* or *Monte-Carlo-Methods* – were applicable [126]. In addition, no isotype or related structure is known, which could have been used as an initial model for the refinement. Therefore, *ab initio* molecular dynamics techniques were used to model the crystal structure of COA by *in silico* dehydration of COM. The simulations were

performed with the program SIESTA [127,128] applying the GGA functional with the PBE exchange-correlation [129]. The pseudopotentials for the core electrons of Ca, C, O and H were created within the Troullier-Martins scheme [130,131] (see [132,133] for details). The generated pseudopotentials were verified on the basis of test calculations on the crystal structure of COM. A cut-off of 200 Ry and a set of 9 k-points ensured total energy convergence.

For modelling the dehydration process, the unit cell of COM was first relaxed with a conjugated gradient (CG) scheme. Then the water molecules were removed from the structural model. After a structural optimization (CG) of this model, several simulated annealing cycles were performed in a temperature range between 100K and 800K. The resulting configurations with low total energies were optimized (CG) again. X-ray powder patterns of these promising structural models were calculated and compared with the experimental data [39]. The simulated XRD pattern of one of these models nicely resembled the experimental data. The lattice parameter of the calculated model for COA were monoclinic, $a = 6.247 \text{ \AA}$, $b = 15.028 \text{ \AA}$, $c = 9.653 \text{ \AA}$, $\alpha = 90.02^\circ$, $\beta = 89.99^\circ$, $\gamma = 89.99^\circ$ in comparison to COM (monoclinic, $P2_1/c$) $a = 6.290 \text{ \AA}$, $b = 14.583 \text{ \AA}$, $c = 10.116 \text{ \AA}$, $\beta = 109.46^\circ$. The program PLATON [134] was used to determine the space group of this calculated crystal structure model. This initial model was used for the Rietveld refinement with the GSAS software package [135]. The oxalate anions were treated as rigid bodies and the distances C-C and C-O as well as the angles C-C-O were optimized in the refinement.

Details on the XRD measurement, the crystallographic data and the Rietveld refinement are given in table 3.2.2. The atomic positions and isotropic thermal displacement parameters are given in table 3.2.3. A comparison of the observed and calculated X-ray diffraction pattern is shown in figure 3.2.2.

The crystal structures of COA and COM are closely related (Fig. 3.2.3 and Fig. 3.2.4). They contain layers consisting of Ca together with Ox1 (layer 1) and of Ox2 (layer 2), respectively, which are stacked along [100] in both structures. The oxalate ions (Ox1 and Ox2) are in two different structural environments: Ox1 is in a planar coordination by six calcium ions and Ox2 is surrounded by four calcium ions. In case of COM, two additional water molecules are connected *via* hydrogen bonds to the oxygen atoms of Ox2. While the local environment of Ox1 remains mainly unaffected by dehydration, the two coordinating water molecules around Ox2 are released. By this, a reorientation of Ox2 takes place in order to get closer contacts to the surrounding

calcium ions. This movement leads to an alternation in the orientation of all the oxalate groups and even the layers containing Ca and Ox1 (planar in COM) become puckered in COA.

Table 3.2.2. Crystallographic data and information about the X-ray powder measurement and Rietveld refinement of Ca[C₂O₄]. The underlined lattice parameters are from the initial model of the simulation. (Standard deviations in parentheses).

crystal system	monoclinic
space group	<i>P2/m</i> (No. 10)
lattice parameters <i>a</i> (Å)	6.1644(3) / <u>6.247</u>
<i>b</i> (Å)	7.3623(2) / <u>7.515</u>
<i>c</i> (Å)	9.5371(5) / <u>9.653</u>
β (°)	90.24(2) / <u>90.12</u>
volume of unit cell (Å ³)	432.83(4) / <u>453.127</u>
<i>Z</i>	4
temperature of measurement (°C)	25
diffractometer	STOE STADI P, Debye-Scherrer, linear PSD
radiation	CuK α
monochromator	germanium
θ range (°)	5 ≤ 2 θ ≤ 90
step width (°)	0.02
no. data points	3978
no. reflections	842
R _{wp}	0.081
R _p	0.054
Rietveld refinement system	GSAS [135]
background correction	function type 2, 10 parameters [135]
profile function	type 3 [135]
preferred orientation	spherical harmonics, cylindrical, 4 th order [135]

Table 3.2.3. Ca [C₂O₄]: atomic coordinates (underlined values are from the initial model of the simulation) and isotropic displacement factors U_{eq} (Å²) (standard deviations in parentheses).

atom	Wyckoff position	<i>x</i>	<i>y</i>	<i>z</i>	U_{eq}
Ca1	2n	0.407(2) / <u>0.41011</u>	0.5 / <u>0.5</u>	0.193(2) / <u>0.1763</u>	0.047
Ca2	2m	0.434(2) / <u>0.41018</u>	0 / <u>0</u>	0.318(2) / <u>0.32030</u>	0.031
C1	2j	0.5 / <u>0.5</u>	0.1081(7) / <u>0.1034</u>	0 / <u>0</u>	0.05 ^{a)}
C2	2l	0.5 / <u>0.5</u>	0.6081(7) / <u>0.6037</u>	0.5 / <u>0.5</u>	0.05 ^{a)}
C3	2n	0.0929(6) / <u>0.0658</u>	0.5 / <u>0.5</u>	-0.0577(4) / <u>-0.0684</u>	0.05 ^{a)}
C4	2m	0.0798(5) / <u>0.0658</u>	0 / <u>0</u>	0.5659(5) / <u>0.5685</u>	0.05 ^{a)}
O1	4o	0.5596(3) / <u>0.5479</u>	0.188(1) / <u>0.1796</u>	-0.1136(4) / <u>-0.1136</u>	0.05 ^{a)}
O2	4o	0.4636(1) / <u>0.4525</u>	0.688(1) / <u>0.6799</u>	0.3820(5) / <u>0.3864</u>	0.05 ^{a)}
O3	2n	0.0319(4) / <u>0.0335</u>	0.5 / <u>0.5</u>	-0.1869(9) / <u>-0.1821</u>	0.05 ^{a)}
O4	2n	0.290(1) / <u>0.2695</u>	0.5 / <u>0.5</u>	-0.0133(2) / <u>0.0532</u>	0.05 ^{a)}
O5	2m	0.0079(1) / <u>-0.0334</u>	0 / <u>0</u>	0.312(1) / <u>0.3179</u>	0.05 ^{a)}
O6	2m	0.285(1) / <u>0.2695</u>	0 / <u>0</u>	0.5404(4) / <u>0.5532</u>	0.05 ^{a)}

^{a)} not refined

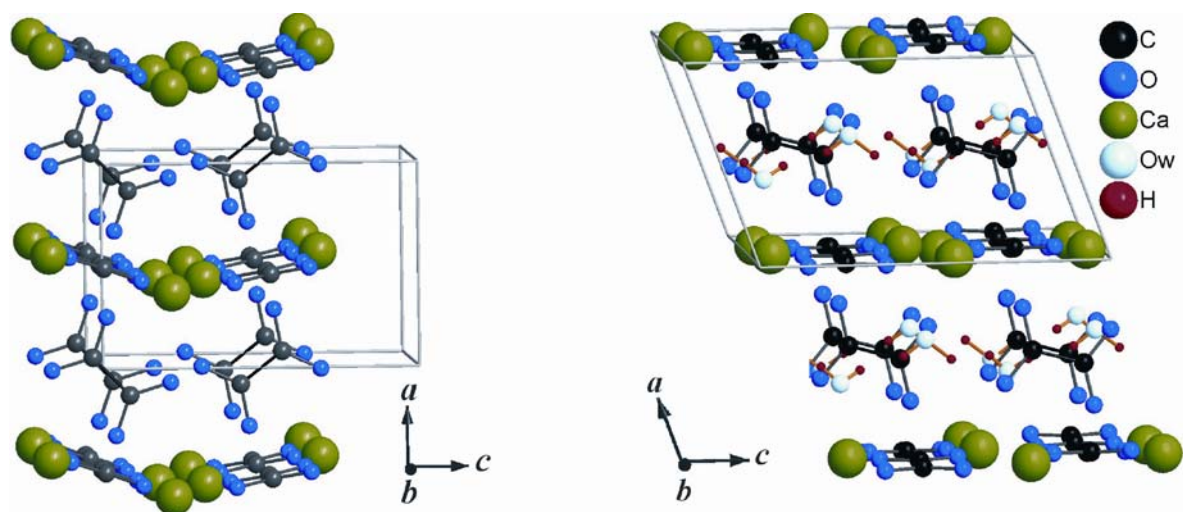


Fig. 3.2.3. The crystal structures of COA (left) and COM (right).

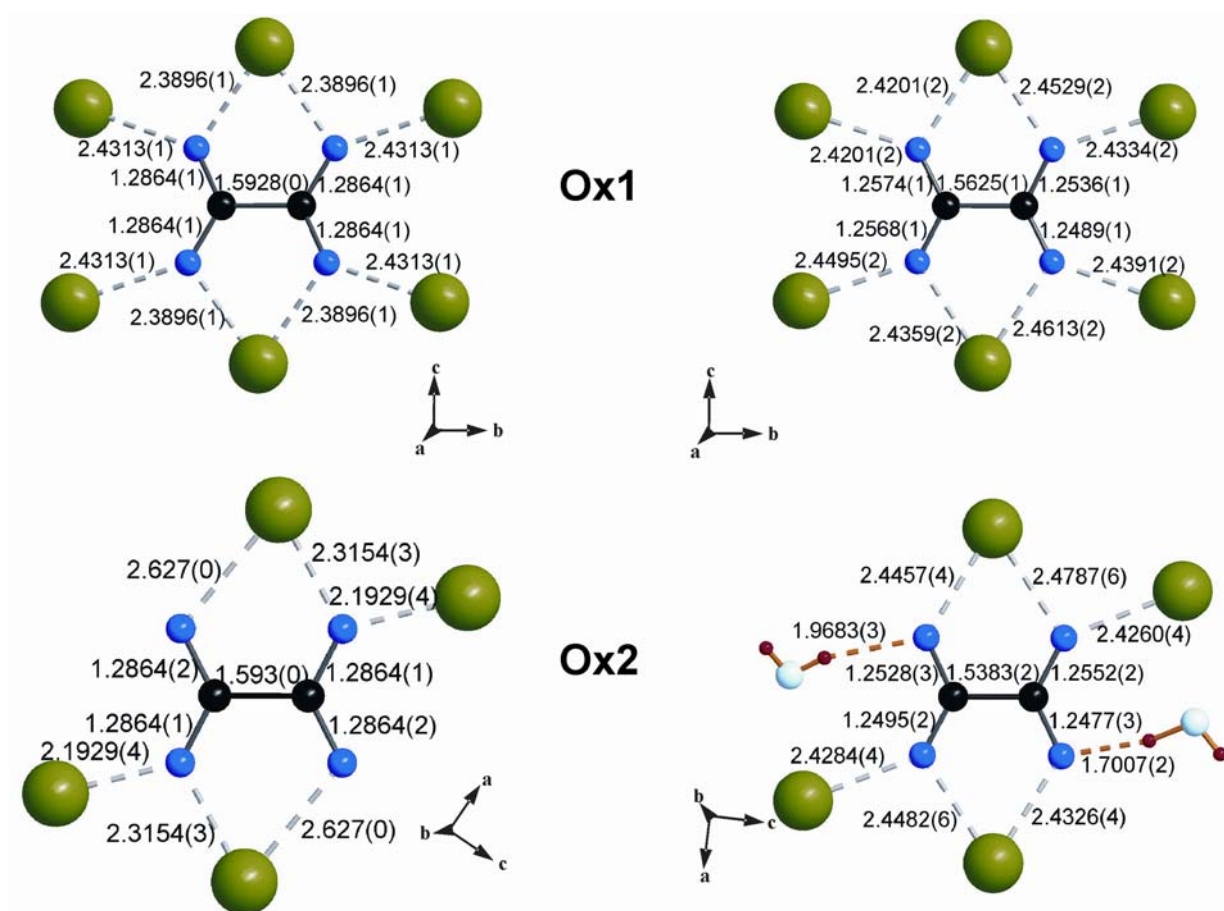


Fig. 3.2.4. Ca coordination around Ox1 and Ox2 of COA (left) and COM (right) [20]. Bond lengths are given in Å with standard deviations in parentheses.

HT XRD: Temperature dependent XRD investigations of the COA powder (performed in the range of 25–450 °C, Fig. 3.2.5) exclusively indicated the existence of the β -modification. At lower temperatures, the peaks from COM were detected due to the absorbance of moisture from atmosphere. XRD patterns from higher temperatures indicated the peaks from calcite. However, the α - and the γ - modifications of COA could not be detected in the high temperature XRD patterns of both COM and COA.

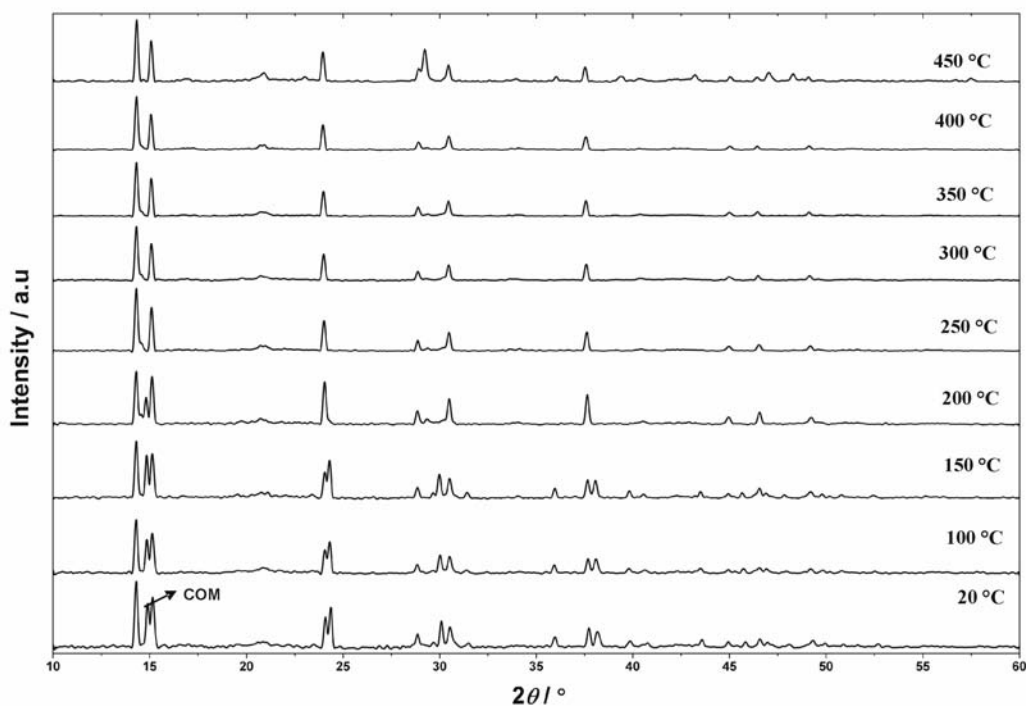


Fig. 3.2.5. HT XRD pattern of COA. The peaks from lower temperatures indicate the co-existence of COM with β -COA due to moisture absorbance.

No evidence for transformations from or to the α - or γ - modifications was found during our investigations. Several DTA/TG analyses were performed with different maximal temperatures and variations of the heating- and cooling-rates. It has been questioned about the occurrence of α - or γ - modifications by Shippey *et al.* and their studies could also reveal the occurrence of the β -modification only [42]. This supports our experiments which indicate the possibility of only the β -modification of COA.

3.3 Growth of calcium oxalates in the presence of PAA

3.3.1 The effect of pH and initial supersaturation

For the crystallization of calcium oxalates in the presence of PAA, the concentration of calcium oxalate was varied from 0.6 to 1.4 mM and the concentration of PAA was varied from 0 to 300 $\mu\text{g/mL}$ (Section 2.1.2, Appendix Fig. 6.3).

Effect of PAA on 1.2 mM CaOx: With the addition of 0.64 $\mu\text{g/mL}$ PAA to a 1.2 mM CaOx solution, COM was formed at pH of the stock solutions less than 5 and pH from 5 to 6 gave COD and pH greater than 6 gave COT. COM crystals formed in all the cases were twinned, COD crystals were tetragonal bipyramids and COT crystals were parallelogram-like platy crystals. The situation remained the same up to the addition of 10 $\mu\text{g/mL}$ PAA. The fraction of COD formed was found to increase with increase in concentration of COD. For example, figure 3.3.1 shows the SEM images of a mixture of COT and COD formed at pH 9 in the presence of 10 $\mu\text{g/mL}$ PAA. With increase in the concentration of PAA from 16 to 84 $\mu\text{g/mL}$, COM was obtained for $\text{pH} < 5$ and COD for $\text{pH} > 5.6$ and COT could be formed only above pH 8.

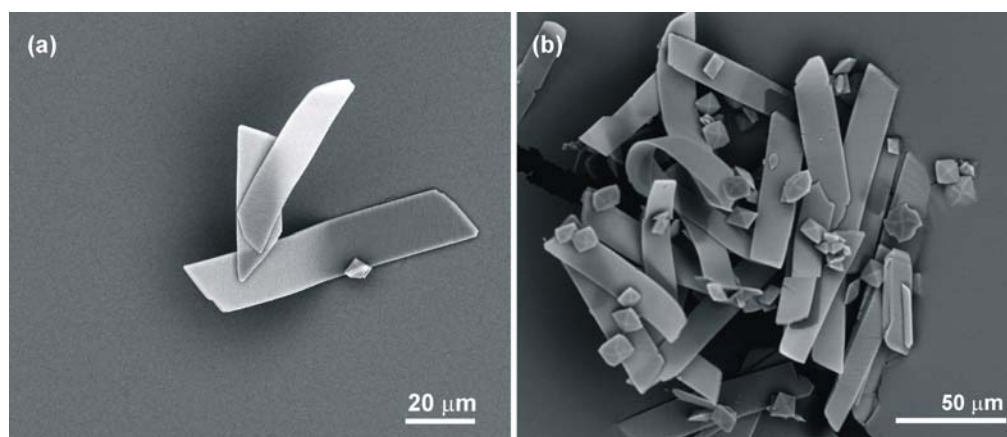


Fig. 3.3.1. (a,b) SEM images of the crystals obtained from 10 $\mu\text{g/mL}$ PAA and 1.2 mM CaOx at pH 9. The crystals with long platy morphology are COT crystals and the smaller tetragonal bipyramids are the COD crystals. The bending of the COT plates is caused by damage effects from the electron beam.

The morphology of COD crystals obtained was found to vary with increase in the concentration of PAA from tetragonal bipyramids (Fig. 3.3.2 a) to elongated tetragonal bipyramids with a combination of prism and pyramidal faces (Fig. 3.3.2 b) to tetragonal

bipyramidal prisms (Fig. 3.3.2 c,d) to dumbbells (Fig. 3.3.2 e) and finally to just-closed dumbbells or spheres with an equatorial notch (Fig. 3.3.2 f).

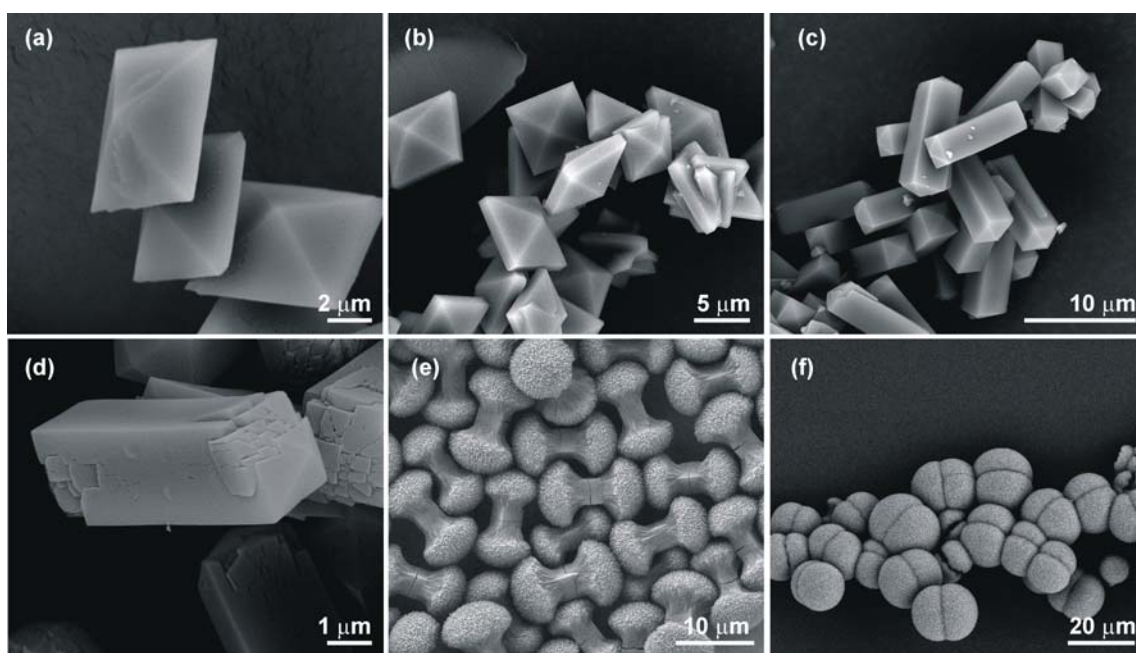


Fig. 3.3.2. SEM images of COD crystals produced in the presence of 1.2 mM CaOx and (a) 16, (b) 48, (c) 64, (d) 84, (e) 96 and (f) 110 $\mu\text{g/mL}$ PAA. These images show the morphological development of COD. (a) Tetragonal bipyramids, (b) elongated tetragonal bipyramids, (c) tetragonal bipyramidal prisms, (d) tetragonal prisms with “structuring” on the end faces, (e) dumbbells and (f) just-closed dumbbells or spheres.

In order to generate a morphology map, the experiments were conducted at a fixed initial concentration of 1.2 mM CaOx and varying concentrations of PAA added to both the stock solutions. The morphology and hydration states of calcium oxalates crystallized at different initial pH values of the stock solutions are summarized in figure 3.3.3. The pH of the start solutions turned out to be an important parameter for the control of the hydration states of calcium oxalates. While in the absence of PAA, COM crystals dominated at lower pH values and COT crystals at higher pH values, in the presence of higher concentrations of PAA ($>85 \mu\text{g/mL}$) no trace of COT was found even at higher pH values. However, the method under discussion here turned out to be an easy and reproducible route to synthesise COT. In the absence of PAA, a high pH of the stock solutions gives COT and in the other case a much lower concentration of PAA leads to COT.

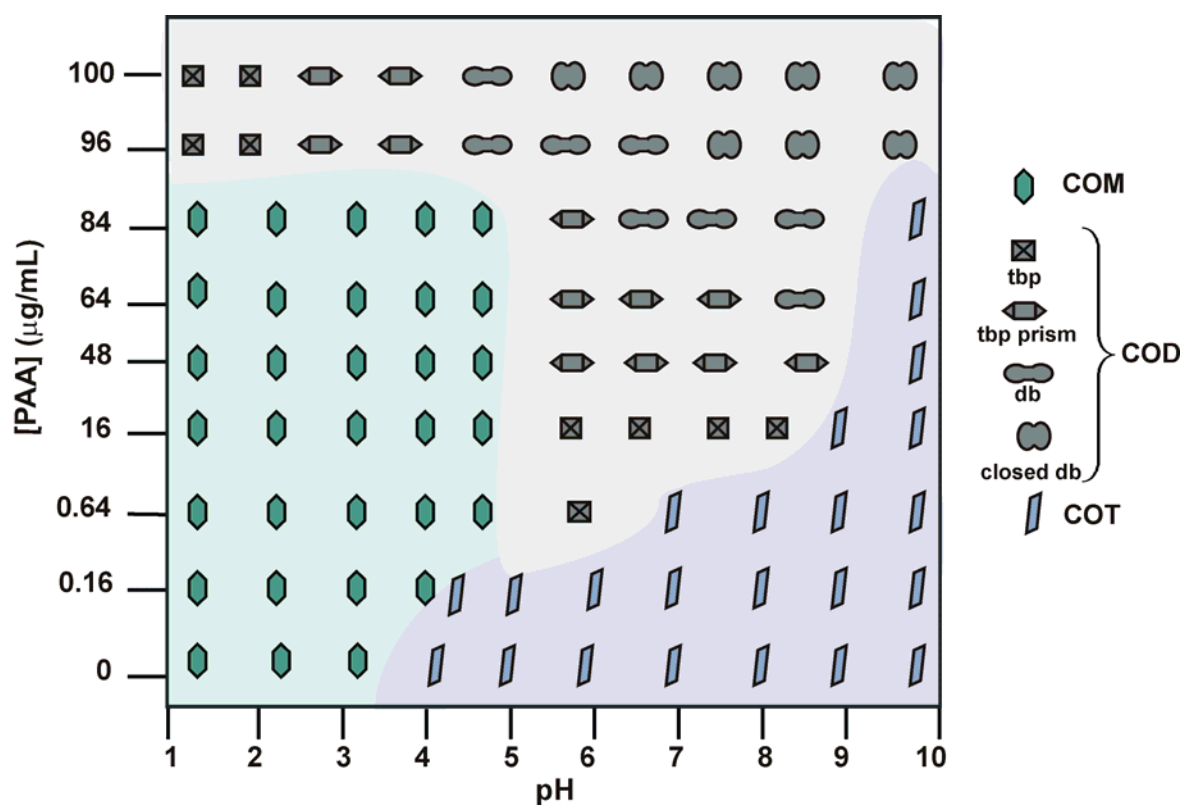


Fig. 3.3.3. Hydration state and morphology map of calcium oxalate crystals as a function of the concentration of PAA and pH values of 1.2 mM CaOx concentration. The reaction conditions corresponding to the green coloured region of the map give COM crystals (mostly twinned) and the blue coloured region gives COT crystals with platy habit. The reaction conditions corresponding to ash coloured region gives COD crystals with various morphologies depending on the concentration of PAA. The various morphologies are represented with the use of symbols. (tbp: tetragonal bipyramids, tbp prism: tetragonal bipyramidal prisms, db: dumbbells, closed db: just closed dumbbells).

Effect of PAA on 0.8 mM CaOx: The morphologies of COD formed at an initial concentration of 0.8 mM calcium oxalate was found to be the most reproducible and was studied extensively. Figure 3.3.4 shows the SEM images of the crystals obtained at 0.8 mM CaOx and different concentrations of PAA without any adjustment of the pH values of the solution. The morphologies of COD crystals have been found to vary with increase in the concentration of PAA from tetragonal bipyramids (Fig. 3.3.4 a) to elongated tetragonal bipyramids (Fig. 3.3.4 b,c) to tetragonal bipyramidal prisms (Fig. 3.3.4 d,e) to dumbbells (Fig. 3.3.4 h,i,j) and to just-closed dumbbells (Fig. 3.3.4 k). It is interesting to note that with even higher PAA concentrations, the morphologies are reverted back to tetragonal prisms and rod-like tetragonal prisms (Fig. 3.3.4 o,p). The dumbbells and the just-closed dumbbells are composed of aggregates of small tetragonal prismatic COD crystals (Fig. 3.3.5).

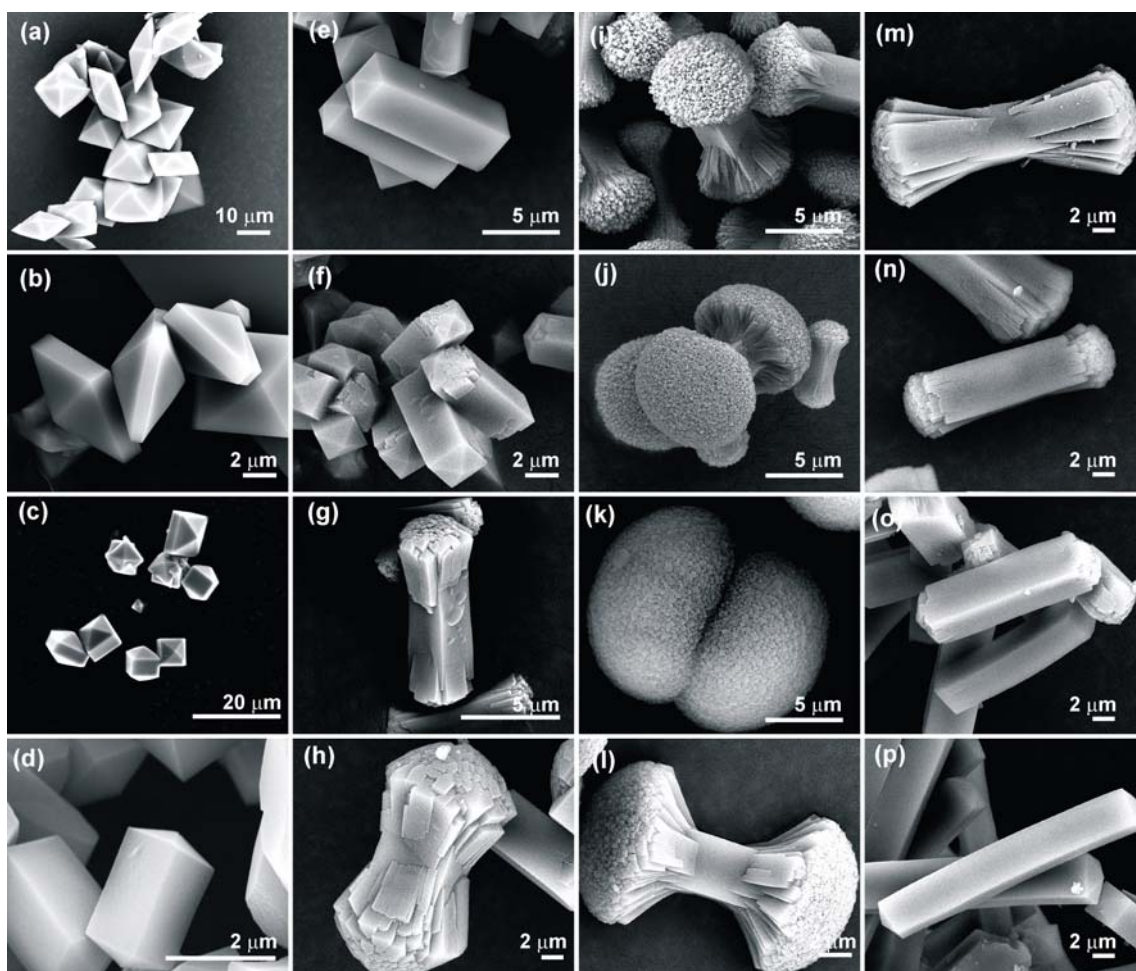


Fig. 3.3.4. SEM images of COD crystals grown in the presence of (a)3, (b)6, (c)7, (d)9, (e)11, (f)12, (g)14, (h)16, (i)32, (j)84, (k)96, (l)148, (m)168, (n)188, (o)200, (p)225 $\mu\text{g/mL}$ PAA and 0.8 mM CaOx.

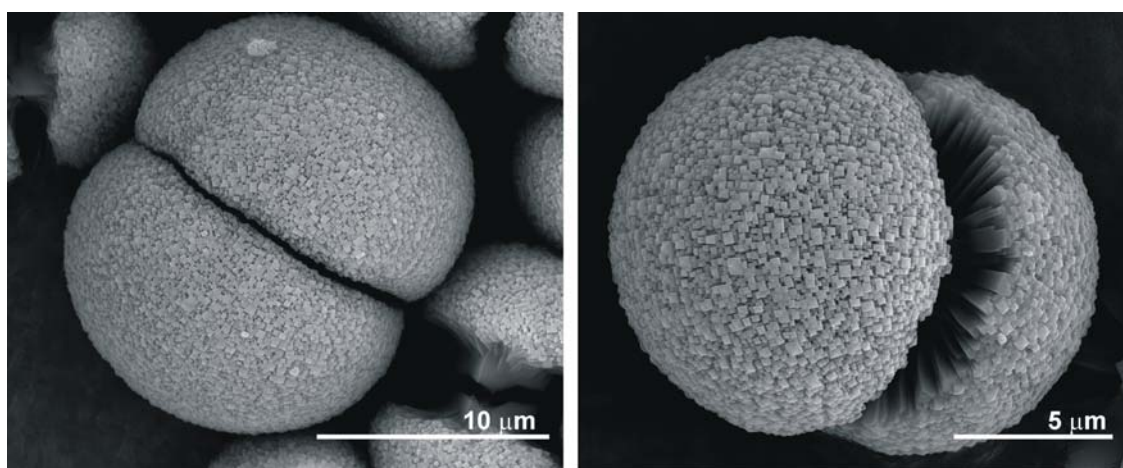


Fig. 3.3.5. SEM images of just-closed dumbbell aggregates consisting of tetragonal prismatic COD crystals grown from 0.8 mM CaOx and 96 $\mu\text{g/mL}$ PAA.

As already reported, an increase in the concentration of PAA results in elongation of tetragonal bipyramids with dominant (101) pyramidal faces, along the c -axis, resulting in tetragonal bipyramidal prisms, with dominant (100) prism faces [84]. A schematic

representation of the morphological influence of PAA on COD crystals is shown in figure 3.3.6, which is assumed to be caused by the preferential adsorption of PAA on the (100) faces of COD.

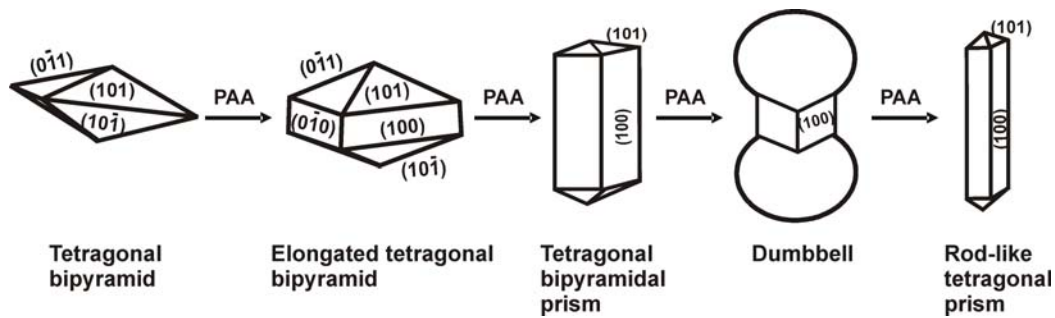


Fig. 3.3.6. Schematic representation of the influence of PAA on the morphologies of COD.

Further increase of the amount of PAA causes a crystal shape like a dumbbell, composed of two hemispheres connected with a rod with the hemispheres consisting of small tetragonal prismatic COD crystals. The short rod between the hemispheres is a COD crystal dominated by (100) faces elongated along [001]. These dumbbells when viewed by SEM often exhibit cracks at the centre of the tetragonal prism (Fig. 3.3.7 a). The view at one hemisphere of a dumbbell reveals that the aggregates are grown from a seed crystal with tetragonal cross-section (Fig. 3.3.7 b,c,d, Appendix Fig. 6.4).

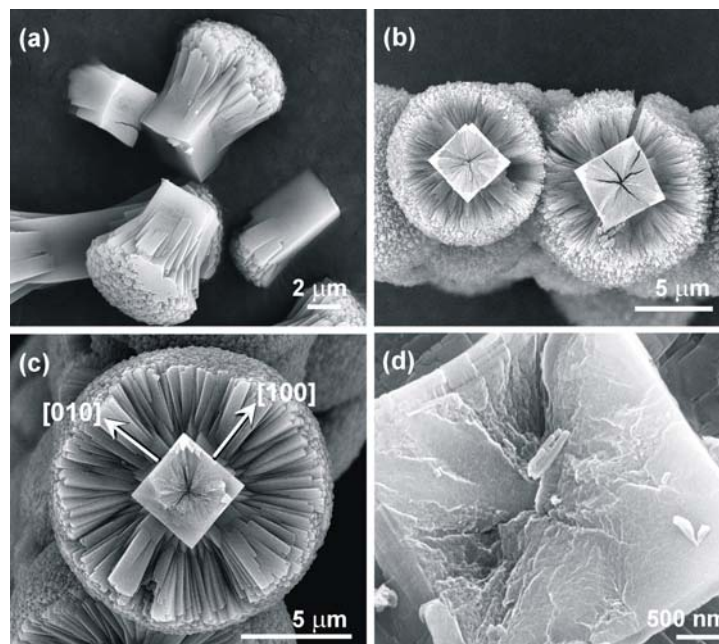


Fig. 3.3.7. SEM images of: (a,b) broken COD dumbbells showing the radial splitting at the ends and the tetragonal cross-section of the stem. (c,d) Cross-section of a COD dumbbell perpendicular to [001].

Powder XRD: The powder X-ray diffractograms (XRD) of the samples grown from 0.8 mM CaOx and various concentrations of PAA (6, 14, 32, 96, 168 and 230 $\mu\text{g/mL}$) are illustrated in figure 3.3.8. The positions of the measured peaks match with those of the calculated powder X-ray diffraction pattern of tetragonal COD ($a = b = 12.371(3)$ \AA , $c = 7.357(2)$ \AA , $\alpha = \beta = \gamma = 90^\circ$, $Z = 8$, $V = 1125.937$ \AA^3 and space group $I4/m$) [20]. The peaks are slightly broader as the concentration of PAA is increased up to 96 $\mu\text{g/mL}$. With further increase in the concentration of PAA, the peaks are sharper as in the case of low concentration of PAA.

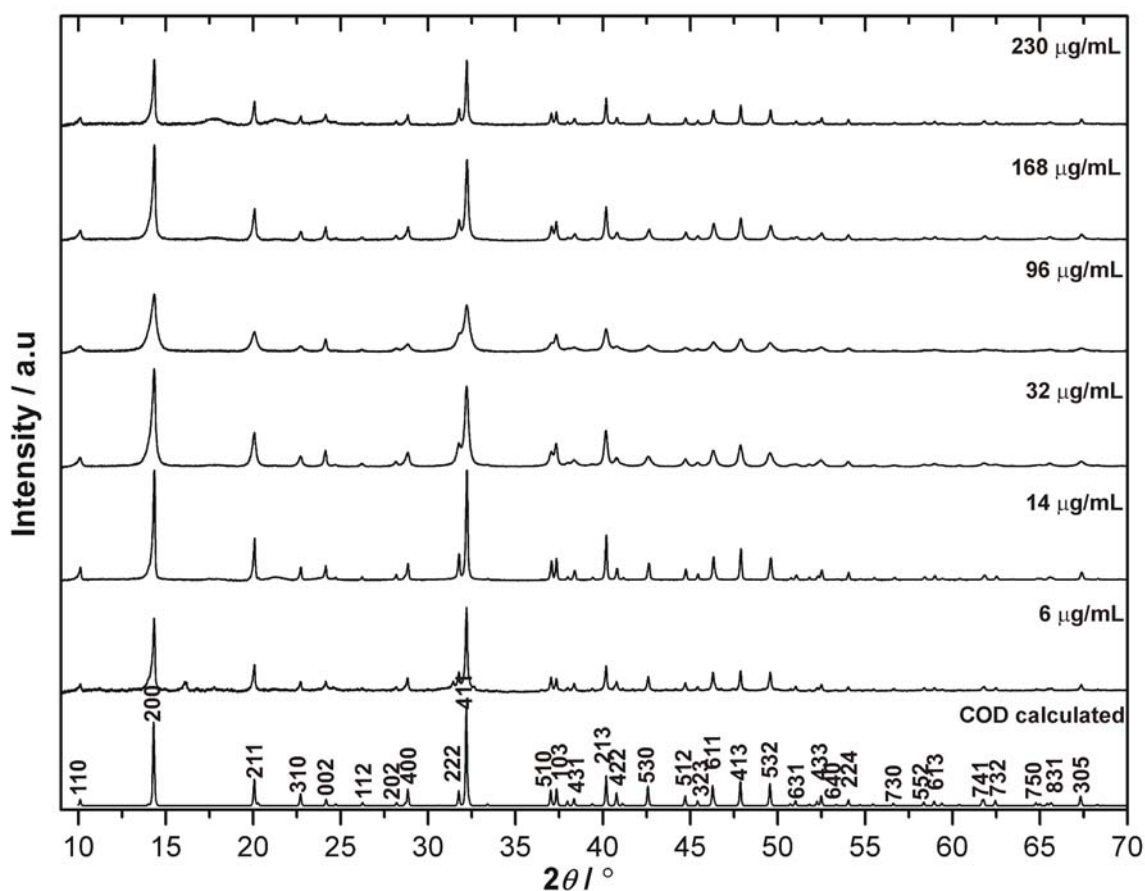


Fig. 3.3.8. XRD (measured using $\text{Cu } K\alpha_1$ - radiation) pattern of COD crystals grown from 0.8 mM CaOx and 6, 14, 32, 96, 168 and 230 $\mu\text{g/mL}$ PAA. COD grown from 6 $\mu\text{g/mL}$ PAA has tetragonal prismatic morphology and those from 14 to 96 $\mu\text{g/mL}$ PAA are COD dumbbells. COD grown from 168 $\mu\text{g/mL}$ PAA are dumbbells with structuring confined to the end faces and COD grown from 230 $\mu\text{g/mL}$ PAA are rod-like tetragonal prisms.

The lattice parameters of all the morphological variations of COD (grown from 0.8 mM CaOx and various concentrations of PAA) were calculated by least square refinements using LaB_6 (cubic, $a = 4.15692$ \AA) as internal standard and the program package WinCSD [115] (Fig. 3.3.9, Appendix table 6.3). Although there are slight

variations in the lattice parameters, they do not recognize any special trend emphasizing the fact that this macromolecule is too large to be incorporated into the crystal lattice.

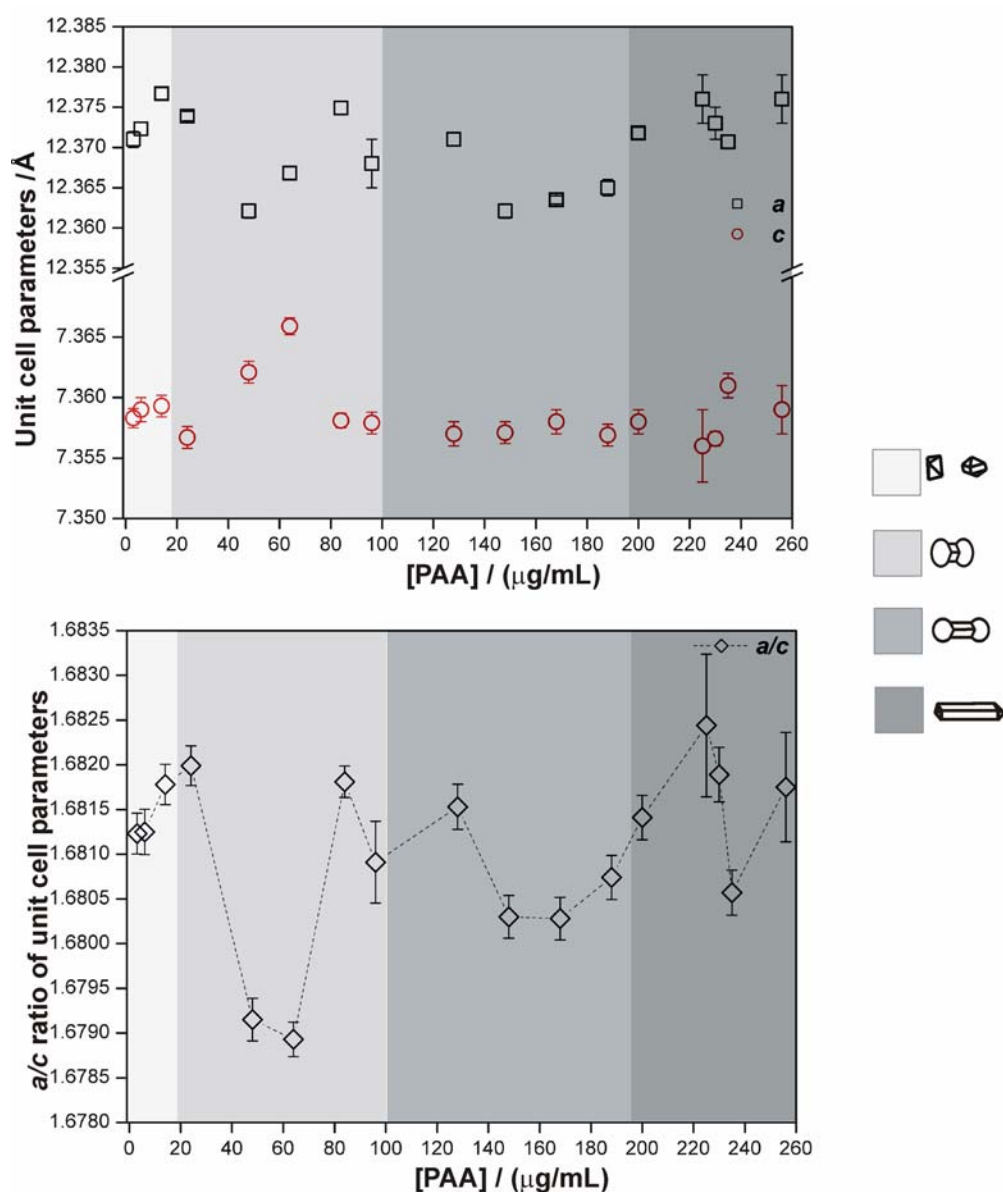


Fig. 3.3.9. Lattice parameters for COD crystals corresponding to different morphologies from 0.8 mM CaOx and various concentrations of PAA. Results from COD crystals with similar morphological trend are illustrated with the same colour.

In order to determine the influence of PAA on the size of the nano-subunits of COD, the coherence length of the nano-domains along their c - and a - axes were calculated from the Scherrer equation using the (002) and (200) reflections. Since the values obtained are semi quantitative because of the approximations in the used Scherrer equation and the possible contributions from stacking faults to the peak broadening, the use of coherence length ratios seems to be more relevant for the present case (Table 3.3.1).

The dimensions of the crystallites along [200] decrease as the concentration of PAA is increased up to 96 $\mu\text{g/mL}$. Conversely, the dimension along [002] is found to increase. As a result, the ratio of the coherence length ($L_{[002]}/L_{[200]}$) is increased. At concentrations greater than 96 $\mu\text{g/mL}$ PAA, the coherence length ratio ($L_{[002]}/L_{[200]}$) decreases. The crystallite dimensions are further used to calculate the mean crystallite volume (table 3.3.1). Up to 96 $\mu\text{g/mL}$ PAA, there is a sharp decrease in the mean crystallite volume. Furthermore, the yield of the products obtained was found to decrease with increase in concentration of PAA (table 3.3.1, Fig. 3.3.19 b). From the yield of the products formed and the mean crystallite volume, the number of crystallites per unit volume was determined [139]. It was found that up to 96 $\mu\text{g/mL}$ PAA, the number of crystallites per unit volume increases (table 3.3.1). This is in accordance with the classical nucleation theory that when the interfacial energy between the solution and the nucleus decreases, free energy of nucleation decreases, the critical nucleus size decreases and the nucleation rate increases. At PAA concentrations greater than 96 $\mu\text{g/mL}$ the observations are reverse.

Table 3.3.1. Crystallite dimensions of COD crystals calculated by means of Scherrer equation of the 200- and 002- reflections.

PAA ($\mu\text{g/mL}$)	$L_{[200]}$ (nm)	$L_{[002]}$ (nm)	$L_{[002]}/$ $L_{[200]}$	$\text{Vol}_{\text{cryst}}$ (nm^3)	Yield (g/L)	N_{cryst} (per Litre) ($\times 10^{14}$)
3	70	70	1	343000	0.11174	1.68097
6	64	67	1.04688	274432	0.106	1.99305
14	69	74	1.07246	352314	0.096	1.40601
32	49	52	1.06122	124852	0.1114	4.60401
84	48	55	1.14583	126720	0.0818	3.33084
96	28	54	1.92857	42336	0.06312	7.69314
128	50	52	1.04	130000	0.0402	1.59562
168	58	61	1.05172	205204	0.03368	0.846901
230	74	78	1.05405	427128	0.01724	0.208269
250	68	64	0.94118	295936	0.0044	0.0767187

In order to study the influence of PAA on the dimensions of the growing crystallites, the aggregates grown from 0.8 mM CaOx and 84 $\mu\text{g/mL}$ PAA were isolated at different time intervals and analyzed using XRD (Fig. 3.3.10, table 3.3.2). The value of $L_{[200]}$ increases steadily with increase in time where as $L_{[002]}$ almost doubles in 3 hours time. The value of $L_{[200]}$ is greater than $L_{[002]}$ initially but with evolution of time it is found that $L_{[002]}$ becomes greater than $L_{[200]}$.

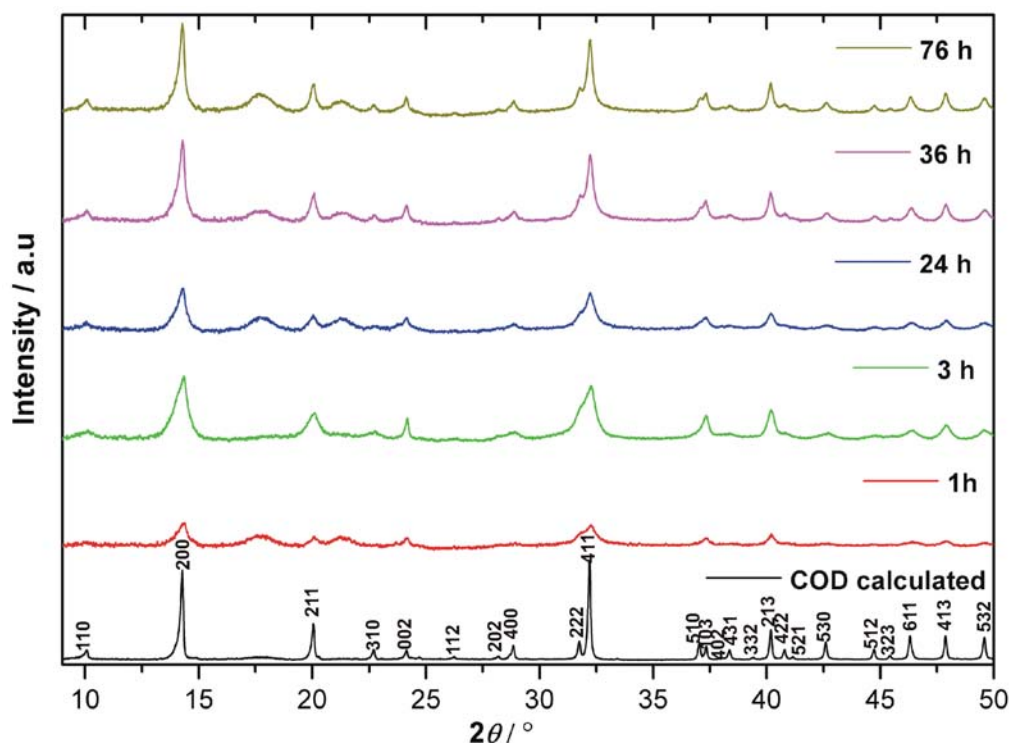


Fig. 3.3.10. Overlapped XRD pattern of COD grown from 0.8 mM CaOx and 84 $\mu\text{g/mL}$ PAA isolated at different time intervals (measured using Cu $K\alpha_1$ - radiation).

Table 3.3.2. Crystallite dimensions of COD crystals (grown from 0.8 mM CaOx and 84 $\mu\text{g/mL}$ PAA) with the evolution of time. The crystallite dimensions are calculated by means of Scherrer equation of the 200- and 002- reflections.

Time (hours)	$L_{[200]}$ (nm)	$L_{[002]}$ (nm)	$L_{[002]}/L_{[200]}$
1	26	23	0.88462
3	27	48	1.77778
24	28	30	1.07143
36	35	43	1.22857
72	37	47	1.27027

Theoretical calculations: In order to check the validity of the general assumption that the morphological development from tetragonal bipyramids to tetragonal prisms is caused by the adsorption of the polymer on the (100) planes of COD, atomistic simulations were performed to explore the interactions of a polyacrylate molecule with different faces of a COD crystal.

Based on empirical force-fields [136] and a recently developed algorithm for the identification of adsorption sites [137,138], a series of 100 independent adsorption experiments were performed for both the (100) and the (101) surfaces. While characteristic binding positions could be identified on the (100) faces (Fig. 3.3.11), polyacrylate association on the (101) faces was found to be unfavourable.

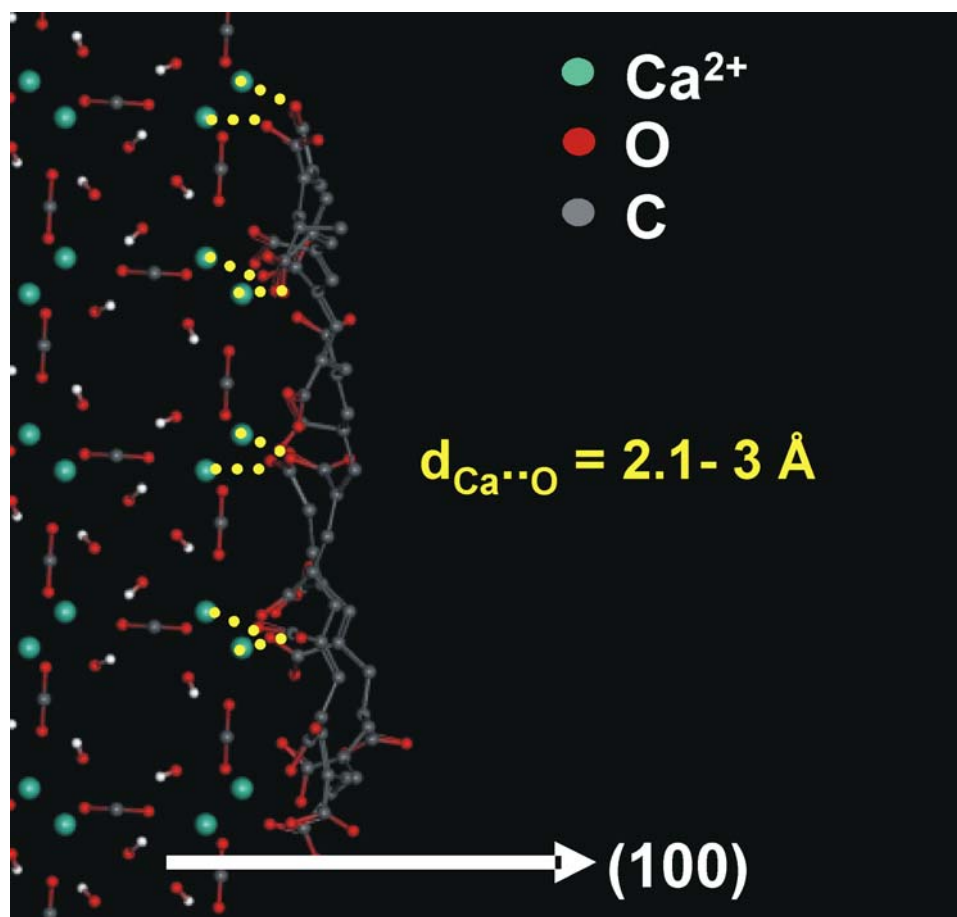


Fig. 3.3.11. Illustration of the interactions of a (100) surface of COD with an associated polyacrylate molecule (25 monomers). Almost each oxygen atom of the acrylate forms an electrostatic Ca···O bond as indicated by the yellow dotted lines in the upper left (for the sake of clarity, only a few bonds are illustrated for the rest of the polyacrylate molecule). In the vapour state, the average energy of adsorption was found to be -1500 kJmol^{-1} per monomeric unit. This corresponds to a factor of about 8 of the energy gain related to the association of an isolated water molecule.

An energetic scoring was obtained from comparing the average gain in potential energy resulting from the adsorption of isolated polyacrylate molecules (25 monomers) and water, respectively. For association to the (101) face, the COD-polyacrylate interactions per monomer unit were found to be weaker than the binding of a single water molecule. In aqueous solution, the (101) faces may hence be considered as free of polyacrylate molecules. On the other hand, for the (100) face the COD-polyacrylate interactions per monomer unit amounts to 8 times the association energy calculated for a water molecule. Sterically, each monomer unit requires the replacement of only about 2-4 COD-water contacts. Hence the (100) face experiences a strong tendency to polyacrylate association and its growth (along [100]) in aqueous solutions containing polyacrylate should be hindered considerably (Fig. 3.3.12).

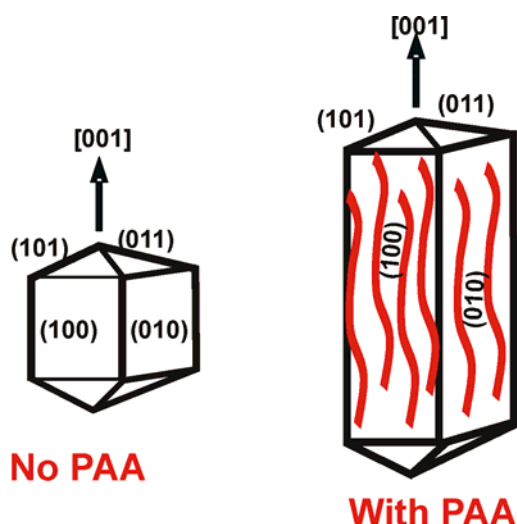


Fig. 3.3.12. Schematic illustration of the effect of the association of polyacrylate (PAA) ions to COD crystals. Selective coating of the (100) and (010) faces hinders crystal growth perpendicular to the [001] direction and leads to an elongated habit.

Thermal decomposition of the COD crystals grown in the presence of PAA: The decomposition processes of the COD aggregates crystallized in the presence of PAA with increasing temperature was investigated by means of TG/DTA/MS. The results obtained were used to determine the amount of PAA incorporated in each case. As an example, the thermally induced changes of COD dumbbells grown from an initial concentration of 0.8 mM CaOx and 96 $\mu\text{g/mL}$ PAA is explained here.

Before starting the measurements, the sample was ground well and washed several times in distilled water and dried at 40 $^{\circ}\text{C}$. The initial sample weight was 57.74 mg and heating was performed in an alumina crucible with a rate of 5 K/min up to 1300 $^{\circ}\text{C}$ in two steps. The first step was done in argon atmosphere with a heating rate of 5 K/min up to 220 $^{\circ}\text{C}$ and a holding time of 6 hours to ensure complete removal of water (as indicated by the straight line in Fig. 3.3.13 top). Then, the sample was heated up to 1300 $^{\circ}\text{C}$ in oxygen atmosphere with a heating rate of 5 K/min (Fig. 3.3.13). The residual mass obtained after TGA when subjected to chemical analysis showed the presence of pure CaO without traces of other elements.

A representative TG/DTA of COD dumbbells (grown from 0.8 mM CaOx and 96 $\mu\text{g/mL}$ PAA) clearly indicates the stepwise mass losses of 23.12, 19.15 and 25.54 wt.-% at 160–211 $^{\circ}\text{C}$, 227–452 $^{\circ}\text{C}$ and 460–803 $^{\circ}\text{C}$ (Fig. 3.3.13, table 3.3.3). The temperature ranges of decomposition were similar for all types of COD crystals with slight variation in the mass losses which is used for the detection of incorporated PAA.

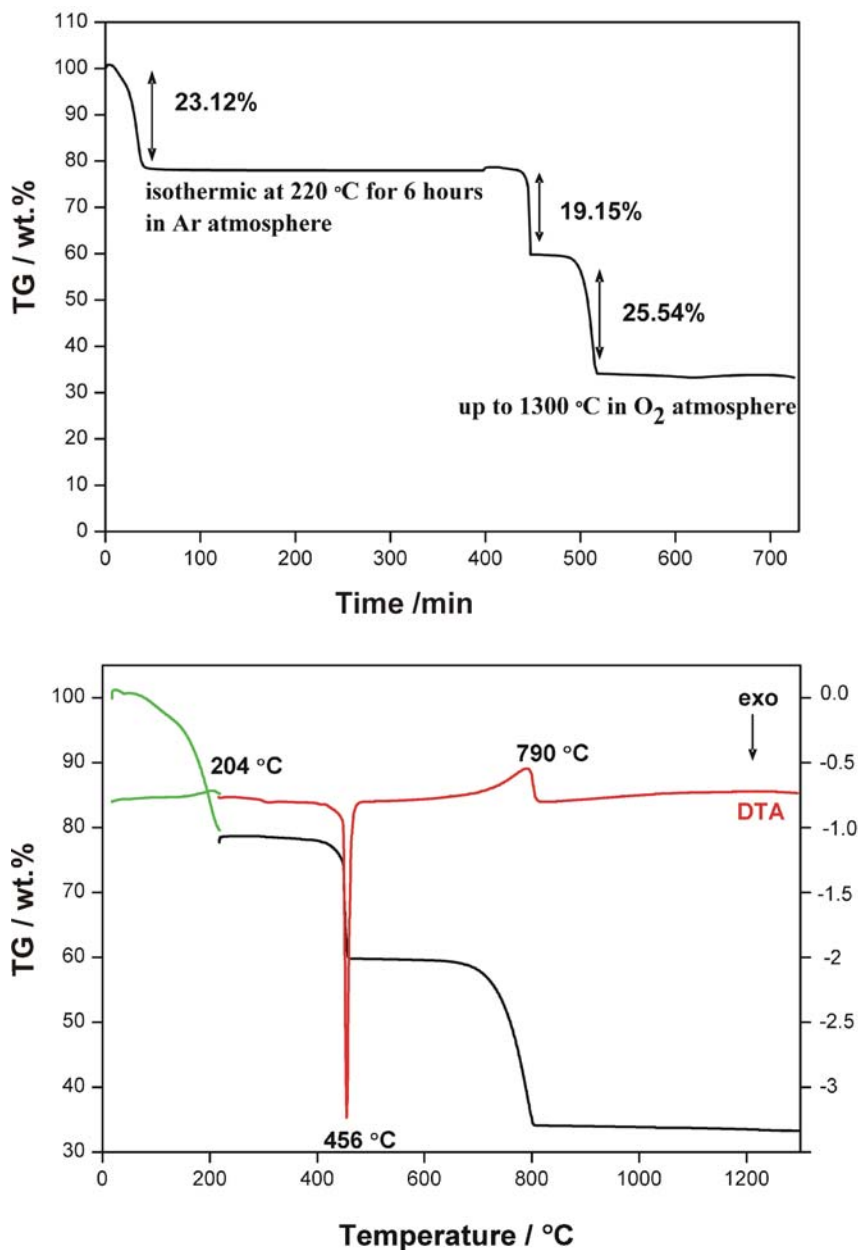


Fig. 3.3.13. TG of COD dumbbells (grown from 0.8 mM CaOx and 96 $\mu\text{g/mL}$ PAA). (Top) The x- axis with time is shown here to point out the complete removal of water as indicated by the straight line after step 1. (Bottom) TG/DTA of COD dumbbells grown from 0.8 mM CaOx and 96 $\mu\text{g/mL}$ PAA. The green line corresponds to the measurement performed under argon atmosphere. All the other lines are the result of measurements performed under oxygen atmosphere (black- TG, red- DTA).

Pure COD also undergoes thermal degradation in three steps and the proposed mechanism [33,38,140,141] is shown in table 3.3.3. TG/DTA investigations under the same conditions were also performed for pure PAA (Fig. 3.3.14, table 3.3.3). PAA also shows a three-step mass loss. The first step with a weight loss of 19.5 wt.-% (endothermic peak at 111 °C in DTA) corresponds to the dehydration of PAA and the formation of the anhydride by intramolecular cyclisation of carboxyl groups (Fig. 3.3.15)

[142-144]. The second step with a weight loss of 37% (exothermic peak at 419 °C with a shoulder at 381 °C) is due to the decarboxylation (COO) of the anhydride followed by fragmentation of the modified back bone. A third mass loss of 32.14% (endothermic peak at 865 °C) can be attributed to the fragmentation of the modified back bone.

Table 3.3.3. Thermal decomposition of pure COD, pure PAA and COD dumbbells grown from 0.8 mM CaOx and 96 µg/mL PAA.

Component	Temperature range	Processes	Mass loss (wt.-%)
COD	110-215 °C	$\text{CaC}_2\text{O}_4 \cdot 2\text{H}_2\text{O} \rightarrow \text{CaC}_2\text{O}_4 + 2\text{H}_2\text{O}$	21.6
	210-515 °C	$\text{CaC}_2\text{O}_4 \rightarrow \text{CaCO}_3 + \text{CO}$	17.4
	500-800 °C	$\text{CaCO}_3 \rightarrow \text{CaO} + \text{CO}_2$	26.8
PAA	room temperature to 200 °C	dehydration	19.5
	200-480 °C	decarboxylation	37
	480-1200 °C	fragmentation of back bone	32.14
COD dumbbells	160-211 °C	release of water	23.12
	227-452 °C	formation of calcite and pyrolysis of PAA	19.15
	460-803 °C	decomposition of calcite and removal of residual organics	25.54

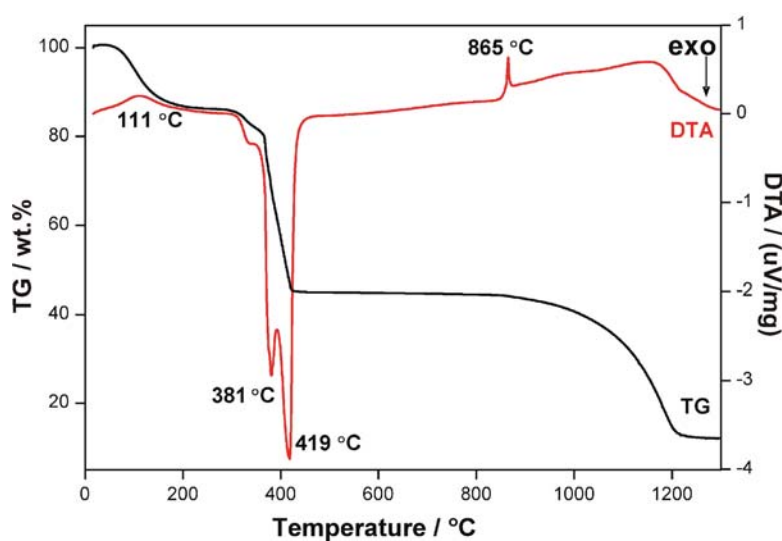


Fig. 3.3.14. TG/DTA of pure PAA showing three-step mass loss. For further details refer to table 3.3.3.

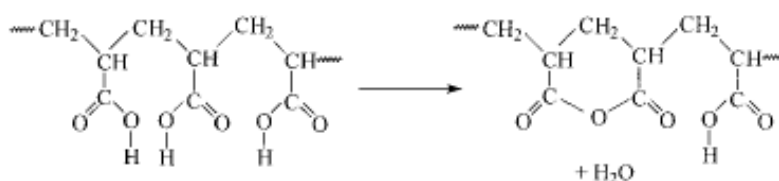


Fig. 3.3.15. Scheme for the dehydration of PAA and subsequent anhydride formation.

All the peaks are overlapping for pure COD and pure PAA due to the same COO functionality in both. This made the analysis concerning the possible amount of the organic component within the aggregates difficult. The thermally induced transitions in the aggregates are very complex, involving overlapping reactions with the release of several gaseous species. It is not possible to resolve the reactions from the TG curves alone; additional informations were obtained from DTA combined with mass-spectroscopy (MS) which allows a better correlation of the mass loss to specific degradation products and reactions. The respective MS diagram of the thermal decomposition of COD dumbbells grown from 0.8 mM CaOx and 96 $\mu\text{g/mL}$ PAA is given in figure 3.3.16 (a-d).

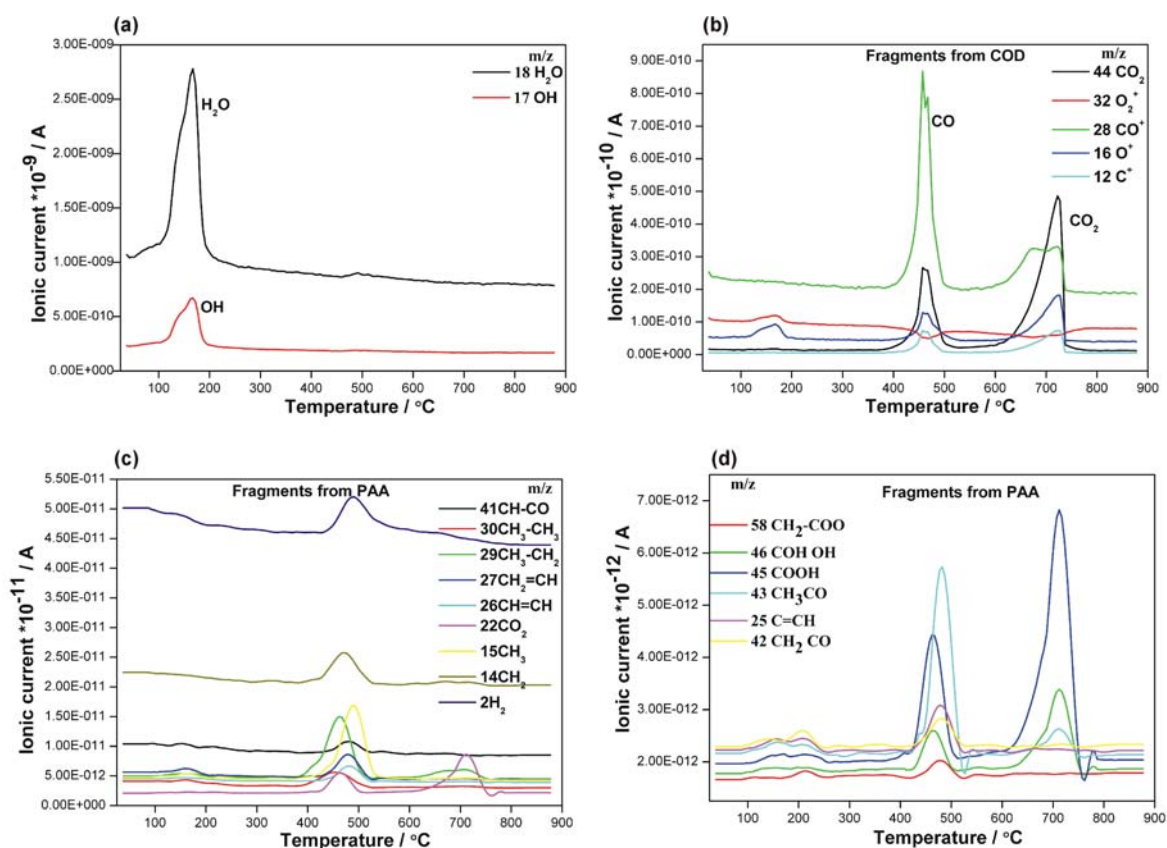


Fig. 3.3.16. Mass spectra of COD dumbbells grown from 0.8 mM CaOx and 96 $\mu\text{g/mL}$ PAA. As a prototype, only the mass spectra of the COD dumbbells are shown as the spectra are quite similar for all the morphological variations of COD grown under the experimental conditions adopted in the present study.

The first step with a weight loss of 23.12% starting at room temperature is finished at 211 $^{\circ}\text{C}$ and is related to the release of crystal water from the aggregates ($m/z = 17, 18$, Fig. 3.3.16 a). The endothermic peak in the DTA curve corresponding to the desorption of water appears at 204 $^{\circ}\text{C}$. The second step (227–452 $^{\circ}\text{C}$) is more complex

and is characterized by the release of the main fragments with molecular masses of 28 and 44, corresponding to CO and CO₂, respectively (Fig. 3.3.16 b). It shows a weight loss of 19.15% and can be attributed to the exothermic peak in DTA at 456 °C. The strong and sharp exothermic peak at 456 °C (maximum) corresponds to the thermal degradation and pyrolysis of PAA. The third step starts around 460 °C and ends at 803 °C and is associated with the final thermal decomposition of residual organics and the whole removal of organics from the composite [141,144]. This process is also indicated by the endothermic peak in the DTA curve at 790.2 °C (maximum). To sum up, a combined analysis of TG/DTA/MS shows that the three steps correspond to the release of H₂O (forming anhydrous calcium oxalate), CO (forming CaCO₃) and CO₂ (forming CaO) form COD.

For the estimation of the amount of organic components in these aggregates, the weight of the sample after each step of thermal decomposition was determined. From figure 3.3.16 it is evident that after step 1, the complete removal of water causes the existence of a residue consisting of CaC₂O₄ and PAA. PAA is completely pyrolysed in step 2 and step 3. From the weight of the pure CaO finally left, the amount of calcium oxalate present in the starting aggregates is calculated and compared with the weight remaining after step1; the difference in weight gives the amount of PAA. From the above investigations the amount of organic component in the COD dumbbells was calculated to be 3.6 wt.-%. The measurements were repeated for samples prepared under different initial concentration of PAA. It is estimated that the COD dumbbells have a PAA content of 3.0 to 3.5 wt.-%, the tetragonal bipyramids and the tetragonal prismatic COD have approximately 2 wt.-% and the rod-like tetragonal prisms, 0.6 to 1.2 wt.-% (Fig. 3.3.17, table 3.3.4).

Table 3.3.4. Amount of PAA in the COD aggregates with respect to initial amount of PAA used for the growth from 0.8 mM CaOx solution.

PAA (µg/mL)	Wt.-% of PAA in the COD aggregate
6	2.1(3)
14	2.5(2)
32	2.6(1)
84	3.16(7)
96	3.45(8)
168	2.5(3)
200	1.2(2)
230	0.6(2)

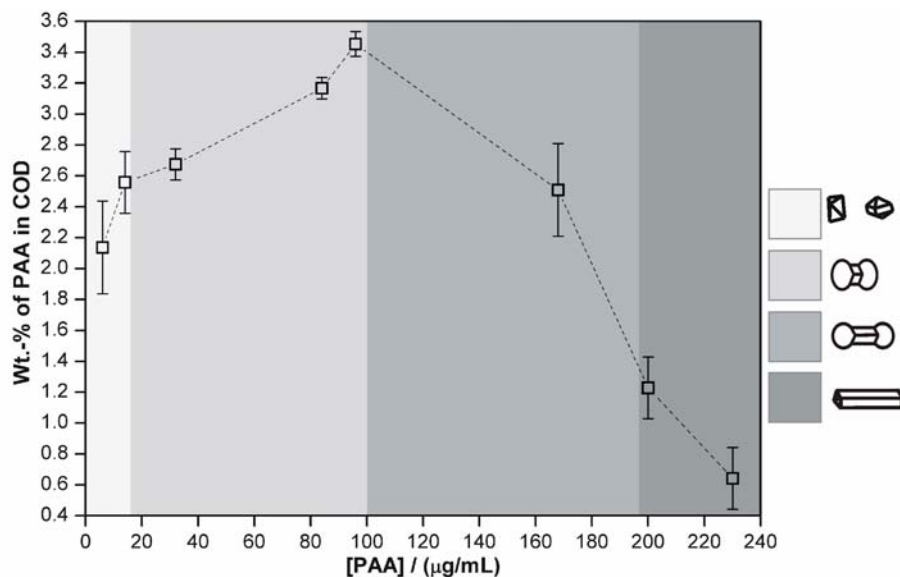


Fig. 3.3.17. Amount of PAA in the COD crystals with respect to morphology and initial concentration of PAA used for the growth from 0.8 mM CaOx solution. The results obtained for the crystals with similar morphology are illustrated with the same colour.

From the theoretical calculations, it becomes evident that PAA is adsorbed on the (100) crystal faces of COD. Combining the results from XRD and TG/DTA analyses it is clear that for samples with PAA content of about 2 wt.-% (having tetragonal prismatic morphology) the coherence length ratio increases slightly along the long axis. Almost the same trend was observed for the dumbbell shaped aggregates having 3 to 3.6 wt.-% PAA. COD dumbbells with a maximum amount of 3.5 wt.-% of incorporated PAA shows the maximum elongation of the nanocrystallites along the c -axis. However, the elongation of the nano-subunits could not be confirmed by HRTEM (High Resolution TEM) due to the destruction of the sample under electron beam. But it is in agreement with our TEM (conventional TEM) and SEM observations that the composite ‘core’ is composed of small elongated subunits with preferred crystallographic orientation along [001] (discussed in proceeding sections).

Furthermore, our TGA results show that the rod-like tetragonal prisms (grown from 0.8 mM CaOx and PAA concentrations $> 200 \mu\text{g/mL}$) have the lowest PAA content (0.6 to 1.2 wt.-%). This is reflected from the fact that the coherence length along the a -axis ($L_{[200]}$) is slightly greater than $L_{[002]}$ or in other words, the elongation of the crystallite along c -axis due to the adsorption of PAA is not prominent in these crystals.

The effect of pH: The results obtained for pH 3 and pH 7 of 0.8 mM CaOx solutions at different concentrations of PAA were also compared (table 3.3.5, Fig. 3.3.18). The crystals grown at pH 3 were bigger in size when compared to the crystals obtained at pH 7. Furthermore, the aspect ratios (ratio of the length of the crystal along [001] to the width along [100]) of the crystals formed at pH 3 were smaller than that of pH 7.

At pH 3 of CaOx solutions, only COM crystals were formed up to a concentration of 13 $\mu\text{g/mL}$ PAA. A mixture of COM and COD were formed for PAA concentrations as high as 168 $\mu\text{g/mL}$. There was no trace of COT at any of the concentrations of PAA. COD with tetragonal bipyramidal morphology were formed only at a concentration of PAA as higher as 48 $\mu\text{g/mL}$ and tetragonal prisms for PAA concentrations up to 168 $\mu\text{g/mL}$ (Fig. 3.3.18 a,b). COM was also precipitated along with COD. COM formed under these conditions exhibited flat and round faces (see Appendix Fig. 6.5). COD dumbbells with “structuring” on the pyramidal faces were formed at PAA concentrations $>188 \mu\text{g/mL}$ (Fig. 3.3.18 c,d).

Table 3.3.5. Summary of the morphological changes of CaOx grown at pH 3 and 7 of 0.8 mM stock solutions and different concentrations of PAA.

pH	[PAA] ($\mu\text{g/mL}$)	Morphology	Size (μm)		Aspect ratio
			along [001]	along [100]	
3	1 to 13	COM	15-20		
3	14 to 96	COM + COD- tbp [‡]	7.7	7	1.1
3	100 to 128	COM + COD- tbp elongated	18	17.5	1.02
3	148 to 168	COM + COD- tetragonal prism	22	9	2.4
3	188 -250	COD- db*	9	3	3
7	1 to 4	COT+COD- tbp	10	10	1
7	5 to 13	COD- tbp prism	2.8	0.88	3.5
7	14 to 96	COD- db	10	2	5
7	100 to 188	COD- db elongated COD- rod-like	15	2	7.5
7	200 to 250	prism	16	1.5	9

[‡] tbp: tetragonal bipyramids, *db: dumbbells

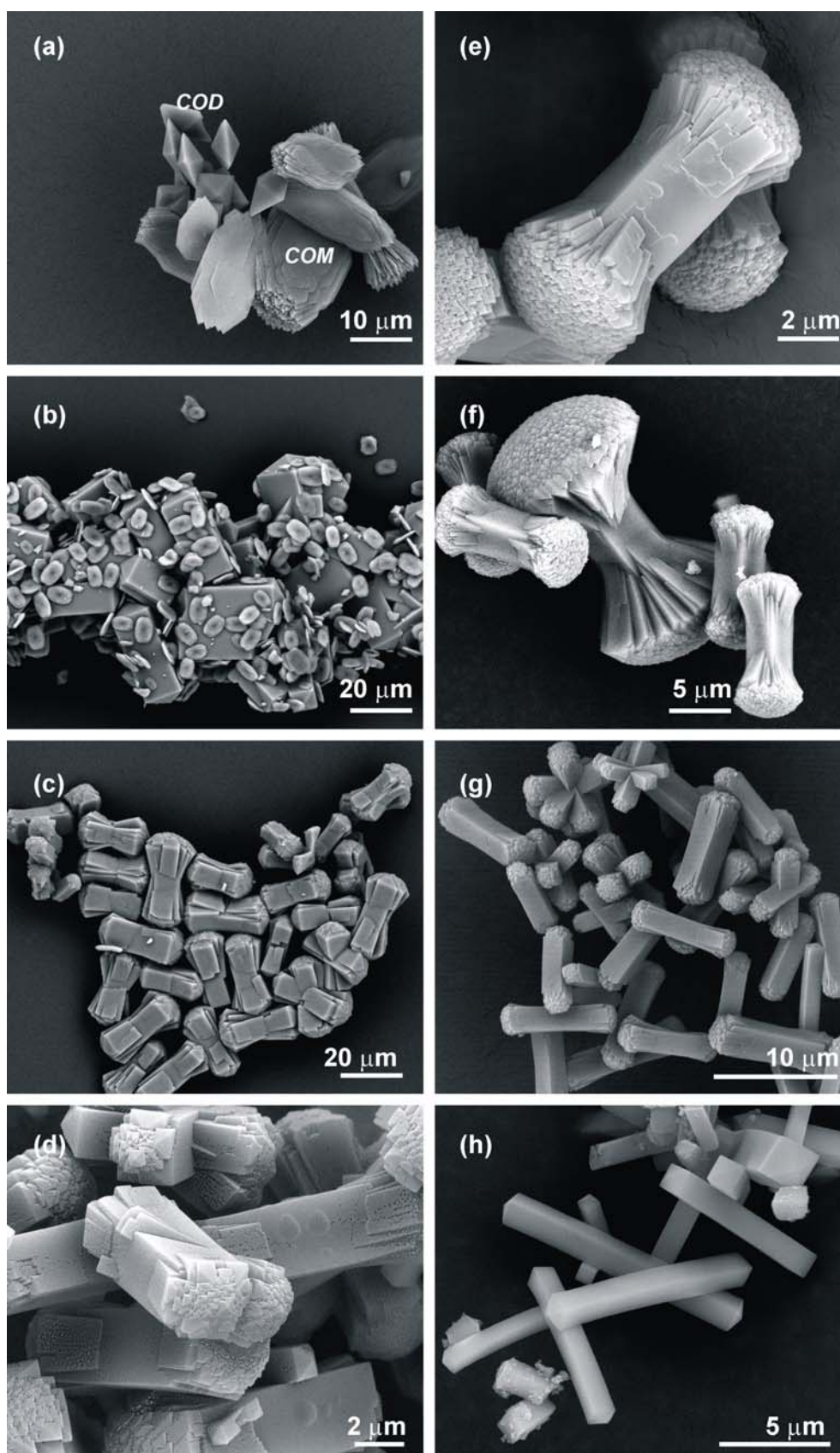


Fig. 3.3.18. SEM images of the morphologies of COD crystals grown in the presence of 0.8 mM CaOx at (a,b,c,d) pH 3 and (e,f,g,h) pH 7. The initial concentrations of PAA are (a,e) 48 μg/mL, (b,f) 168 μg/mL, (c,g) 188 and (d,h) 220 μg/mL. The flatter aggregates in (a) and (b) are COM.

COM is always formed at lower pH values. This may be due to two reasons. As already stated in section 3.1.1, the morphology and hydration state of the crystals are affected by CaOx supersaturations and the supersaturation is decreased at lower pH values. COM is preferably formed at lower supersaturations. Another reason for the formation of COM even at higher concentrations of PAA (and pH 3) may be due to the inefficiency of PAA to behave as a polyanionic chain at lower pH values. As a result the formation of COM is not inhibited. This is because, the dissociation constants (pK_a) for poly-carboxylic acids are around 4.5 ($pK_a = pH - (\log[A^-]/[AH])$) which means, at $pH > 5$, PAA is in the form of a polyanionic chain, resulting in strong interactions between PAA and the growing calcium oxalate to form COD. So, the inhibition effect on COM (by blocking the active growth sites on crystal surfaces) becomes weaker with decreasing pH. At pH 2 to 3, PAA forms neutral chains resulting in weak interactions between PAA and the growing calcium oxalate to form COD. Additionally, it was observed that the induction time (first appearance of crystals observed with the aid of an optical microscope) increased greatly at pH 3 (Fig. 3.3.19 a). This supports the fact that solution supersaturation is decreased and CaOx nucleation is retarded.

At pH 7, it was observed that the induction time is small for very low concentrations of PAA but increases with increase in concentration of PAA. The same polymer which acts at very low concentrations as nucleation agent inhibits primary nucleation at higher concentrations. The increase in induction time with increase in concentrations of PAA means that solution supersaturation is not affected by the addition of PAA. If PAA was to increase the supersaturation, we would have observed decrease in induction time. This is further supported by the fact that the yield of the product formed is decreased with increase in PAA concentration (Fig. 3.3.19 b). The induction time increase steadily starting from PAA concentration of 24 $\mu\text{g/mL}$ which suggests that a considerable amount of CaOx is kept stable in solution and only COD is grown through a slow crystallization process and inhibition of growth of specific crystal face by PAA becomes effective. The approximate aspect ratios of the crystals increase with increase in concentration of PAA which further support the hindrance to crystal growth along [100] and the observation of increase in the induction time (Table 3.3.5).

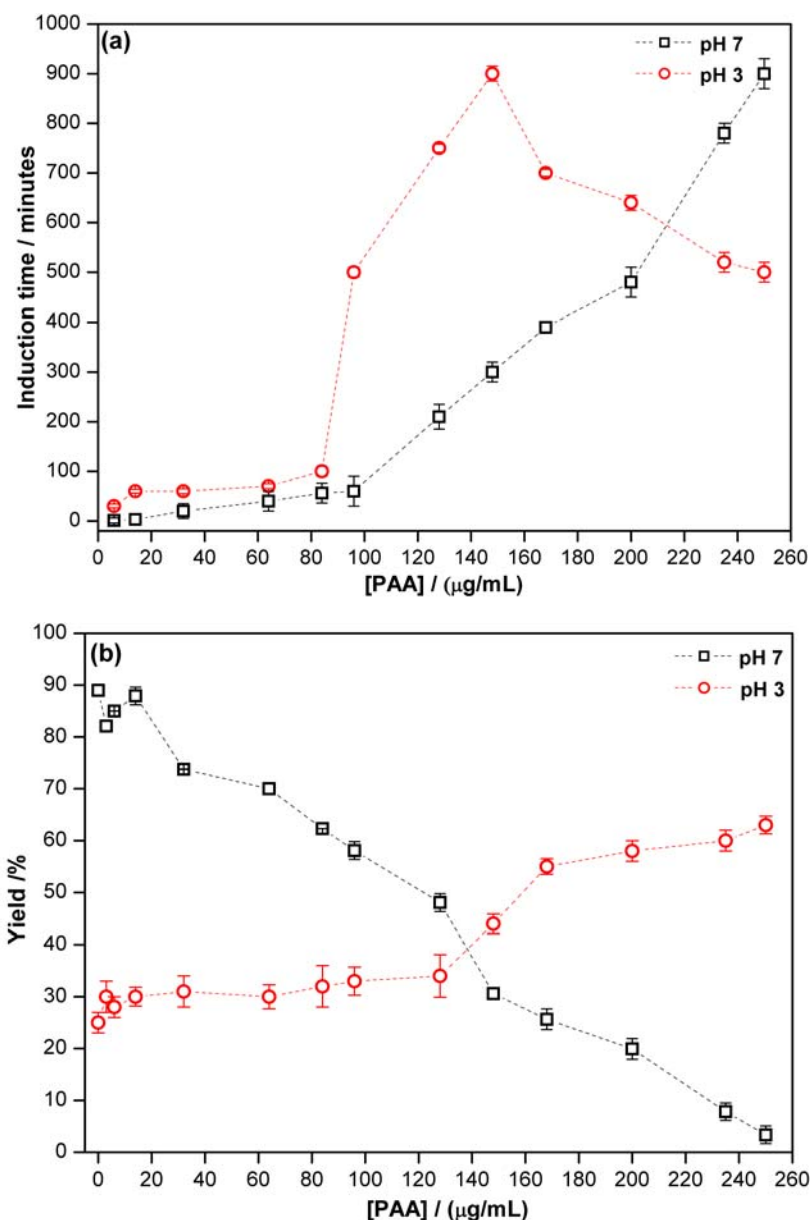


Fig. 3.3.19. (a) Plot of induction time (in minutes) for 0.8 mM CaOx and different concentration of PAA at pH 3 and 7. (b) Yield of the products formed from 0.8 mM CaOx and different concentrations of PAA at pH 3 and 7. Each data symbol represents an average of 6 determinations.

Our observations and calculations suggest that a limiting amount of PAA (at pH 7) kinetically inhibits COD nuclei and gives rise to crystallization of COT. COT formed first may be transforming readily and irreversibly to COD by a solvent mediated process. This is in accordance with the classical nucleation theory that sub critical nuclei of all potential polymorphs are stochastically formed and dissolved, and just those nuclei which pass a critical size (defined by crystallization enthalpy and interface energy) can continue to grow. If a polymer lowers the interface energy of a specific polymorph (and the interface energy is lowered already below the critical surface coverage), it is this

polymorph which is specifically nucleated. It is evident from the calculations that PAA decreases the interfacial energy of (100) faces of COD and so it can be assumed that during the induction time, the most of the active growth sites of COM are poisoned by PAA and favour the growth of COD.

The yield (Fig. 3.3.19 b) of the crystals formed at low pH was low in comparison to the yield formed at higher pH values. This is also because the interaction of PAA with calcium oxalate is low at lower pH values. In the case of pH 7 there was a steady decrease in the yield with increase in concentration of PAA. This reflects the inhibitory effect of PAA on calcium oxalate crystal growth. Even though the yield increases slightly at low concentration of PAA, it decreases sharply afterwards. At pH 3, the yield is even lower. This may be attributed to the decrease in supersaturation of CaOx at low pH values. Nevertheless, at pH 3, the yield increases after a PAA concentration of 148 $\mu\text{g/mL}$ when COD dumbbells begin to form. PAA concentration of 84 $\mu\text{g/mL}$ gives dumbbells at pH 7 where as it gives only tetragonal bipyramidal crystals at pH 3. This may be because crystallization control by PAA is more efficient than primary nucleation is slowed down by the adsorption of PAA on the crystal planes while secondary nucleation is completely suppressed [9]. The dumbbells are formed by a combination of primary and secondary nucleation (discussed in the proceeding sections). At low pH, the morphologies are rather simple while at high pH values dumbbells are formed easily. This shows that not only primary nucleation but also secondary nucleation is affected by the pH value. Prisms are obtained when the primary nucleation is slowed down by the adsorption of PAA and when secondary nucleation is suppressed.

In order to examine the effect of initial CaOx supersaturation, the crystallization experiments were repeated at various initial calcium oxalate concentrations (0.6 to 1.4 mM) and PAA concentrations (0 to 300 $\mu\text{g/mL}$), without fixing the pH. The morphology of COD crystals obtained was more or less the same at different initial concentrations of calcium oxalate (except for slight shifts in the corresponding PAA concentration, Appendix Fig. 6.3). Therefore, it becomes clear that the relative proportion of the polymer and calcium oxalate concentrations is more relevant for determining the polymorph and the morphology of the produced particles rather than the “absolute” concentrations of PAA [9,13,145]. In general, a very low concentration of PAA leads to COT, medium concentrations of PAA results in COD and very high concentrations of PAA inhibits the crystallization of calcium oxalate. In all the cases at very low PAA concentrations COT is formed (Appendix Fig. 6.3).

3.3.2 Morphological control of COD

Growth of calcium oxalate in the presence of 0.8 mM CaOx and < 5 µg/mL PAA: Formation of COD with tetragonal bipyramidal habit

While up to a concentration of 3 µg/mL PAA, mixtures of tetragonal bipyramidal COD and platy COT are formed, concentrations from 3 to 5 µg/mL PAA leads to the growth of tetragonal bipyramidal COD of approximately 8 µm in size (Fig. 3.3.20 a).

To get an insight into the inner architecture, the samples were subjected to conventional TEM analyses. Thin sections from these samples for TEM analyses were obtained by the Focused Ion Beam (FIB) technique in a scanning electron and ion microscope (dual SEM/SIM).

Thin sections were made parallel to (100) crystal plane. The SEM/SIM/TEM images of tetragonal bipyramidal COD crystals are shown in figure 3.3.20. The arrangement of the crystallites as seen from TEM is shown in a model sketch as the picture quality is low (Fig. 3.3.20 c). The crystallites appear to diverge from a single point in the centre. The blue lines in the model sketch indicate crystallites whose orientation is more bent than the crystallites indicated with green lines which have nearly straight orientation. All the crystals happened to have an eye-like area in the exact centre (Fig. 3.3.20 h). A highly magnified TEM image shows that the centre is not empty but consists of a weak area of low density (or less crystalline) which is suspected to be filled with organics or can be a defect region (Fig. 3.3.20 g, indicated with red arrow). Such an enclosure of organic material can be suggestive of the development of a close association between the organic and the inorganic constituents, very early during the crystallization process.

From TG analyses, the amount of PAA in these aggregates were calculated to be approximately 2 wt.-%. X-ray measurement showed that these crystals are not single crystalline. From the powder X-ray diffraction pattern, the crystallite dimension is calculated to be 70X70 ($L_{a^*} \times L_{c^*}$) nm. This means that these COD crystals are composed of nano crystallites with almost the same size along the *a* and *c*- axes. After exposure to the electron beam for a long time, the central area opens up to form a crack (Fig. 3.3.20 i). This happened to be the case for all the COD crystals obtained from PAA. Therefore, the nanostructuring, if present for these crystals could not be confirmed. Radiation damage made it difficult to investigate the crystals under higher magnification.

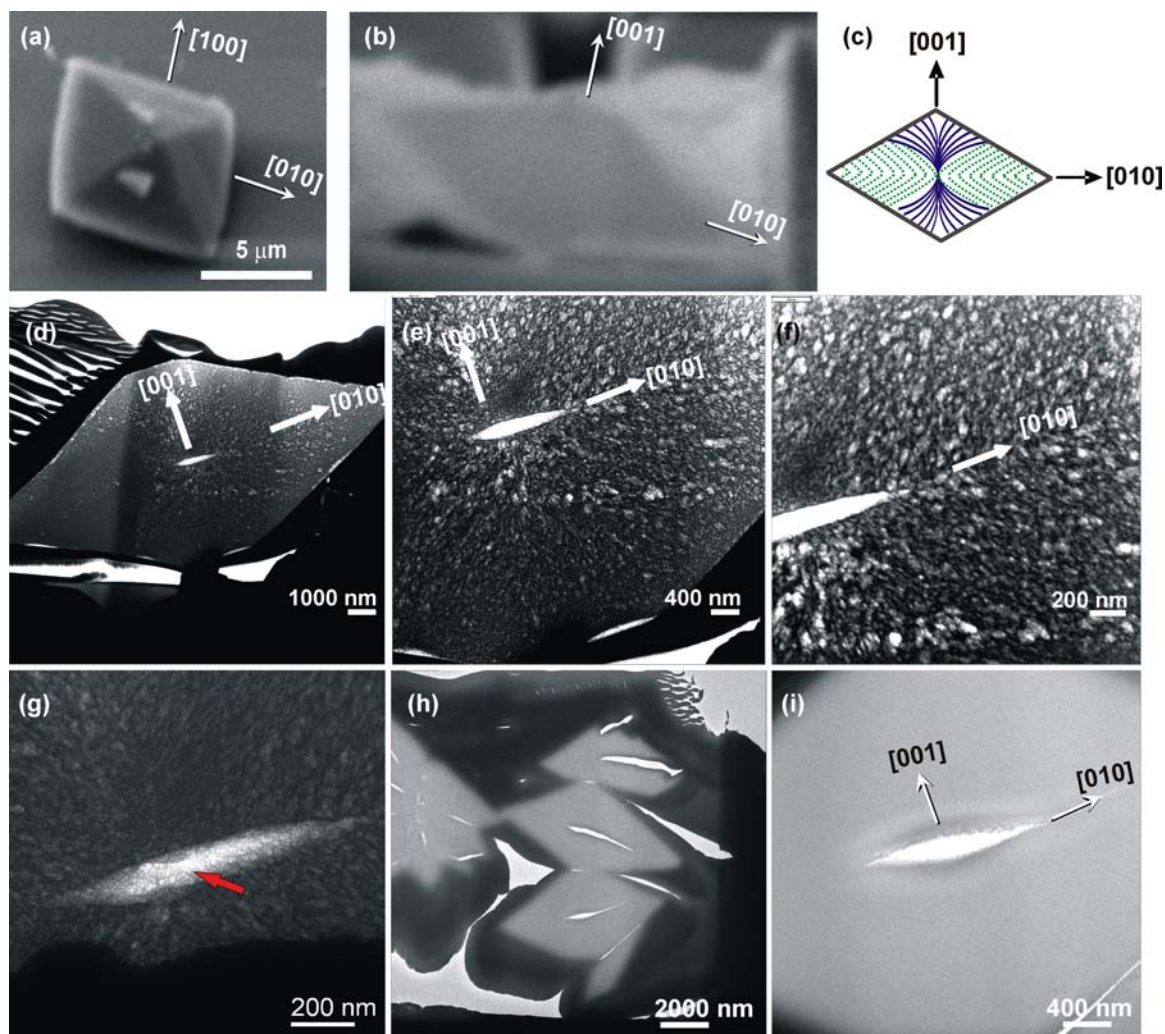


Fig. 3.3.20. (a) SEM image of a tetragonal bipyramidal COD crystal grown from 0.8 mM CaOx and 3 $\mu\text{g/mL}$ PAA with the crystallographic axes indicated. (b) SIM image of the same crystal after FIB treatment: [100] cross-section. (c) Model sketch of the inner architecture as seen from TEM. (d,e,f) TEM images indicating the arrangement of the crystallites along the [100] cross-section inside the crystal. (g) A magnified TEM image of the eye-like area showing that it is not empty (indicated with red arrow). (h,i) Bright field TEM images with the eye-like area opened up to form a crack in the centre of the crystal.

Growth of calcium oxalate in the presence of 0.8 mM CaOx and 5 to 14 $\mu\text{g/mL}$ PAA: Elongated tetragonal bipyramids and tetragonal bipyramidal prisms of COD

In this range of concentration, “elongated tetragonal bipyramids” and “tetragonal bipyramidal prisms” are formed. The structuring on the pyramidal faces was observed for some of the tetragonal prisms. The elongated tetragonal bipyramids (Fig. 3.3.21 a, grown from 7 $\mu\text{g/mL}$ PAA) are in fact tetragonal bipyramids with a combination of pyramidal (101) faces and prism (100) faces. The aspect ratio (ratio of length along [001] to width long [100]) is approximately 0.6 and the amount of PAA in the aggregate as estimated from TGA is *ca.* 2.13 wt.-%. The tetragonal bipyramidal prisms (Fig. 3.3.21 b,

grown from 9 $\mu\text{g/mL}$ PAA) with aspect ratio of *ca.* 3.5 have PAA content of 2.55 wt.-%. The increase in aspect ratio clearly indicates considerable elongation of the crystal along the *c*-axis and the morphology of these crystals reveals well-developed tetragonal (100) prism faces with increase in concentration of PAA. The theoretical calculations confirm that PAA is adsorbed preferably on the (100) faces compared with the (101) faces, as PAA decreases the surface energy of the (100) faces. The preferable adsorption of PAA is assumed to have caused by the higher number of Ca^{2+} on the (100) planes ($0.04395 \text{ ions}/\text{\AA}^2$) compared with (101) ($0.0213 \text{ ions}/\text{\AA}^2$) [84,85,106].

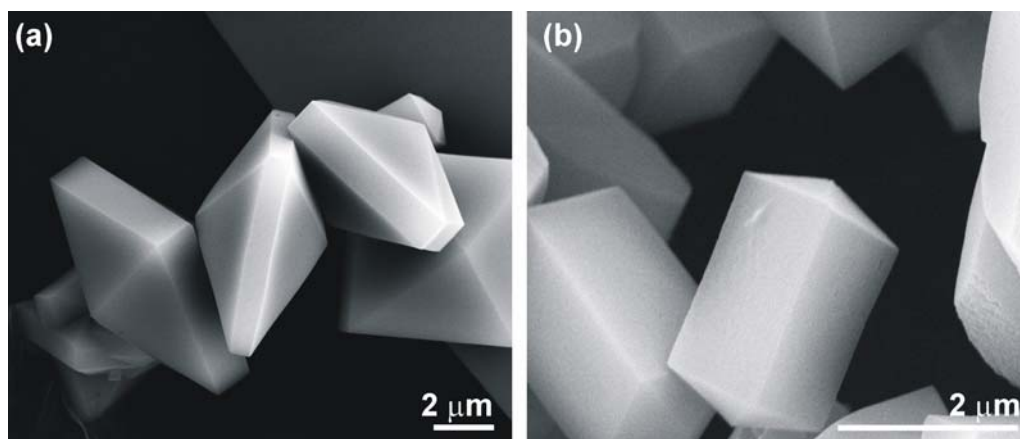


Fig. 3.3.21. SEM images of: (a) elongated tetragonal bipyramids grown from 0.8 mM CaOx and 7 $\mu\text{g/mL}$ PAA and (b), tetragonal bipyramidal prisms grown from 0.8 mM CaOx and 9 $\mu\text{g/mL}$ PAA.

TEM investigations of the elongated tetragonal bipyramidal COD crystals were also performed after FIB cutting along the [100] cross-section (Fig. 3.3.22). The inner architecture shows thinner crystallites (indicated with blue lines in the model sketch) diverging from the centre of the crystal towards the pyramidal faces. It also shows a mosaic-like arrangement of the crystallites (indicated with green dots) in the waist area of the crystal, extending towards the prism faces.

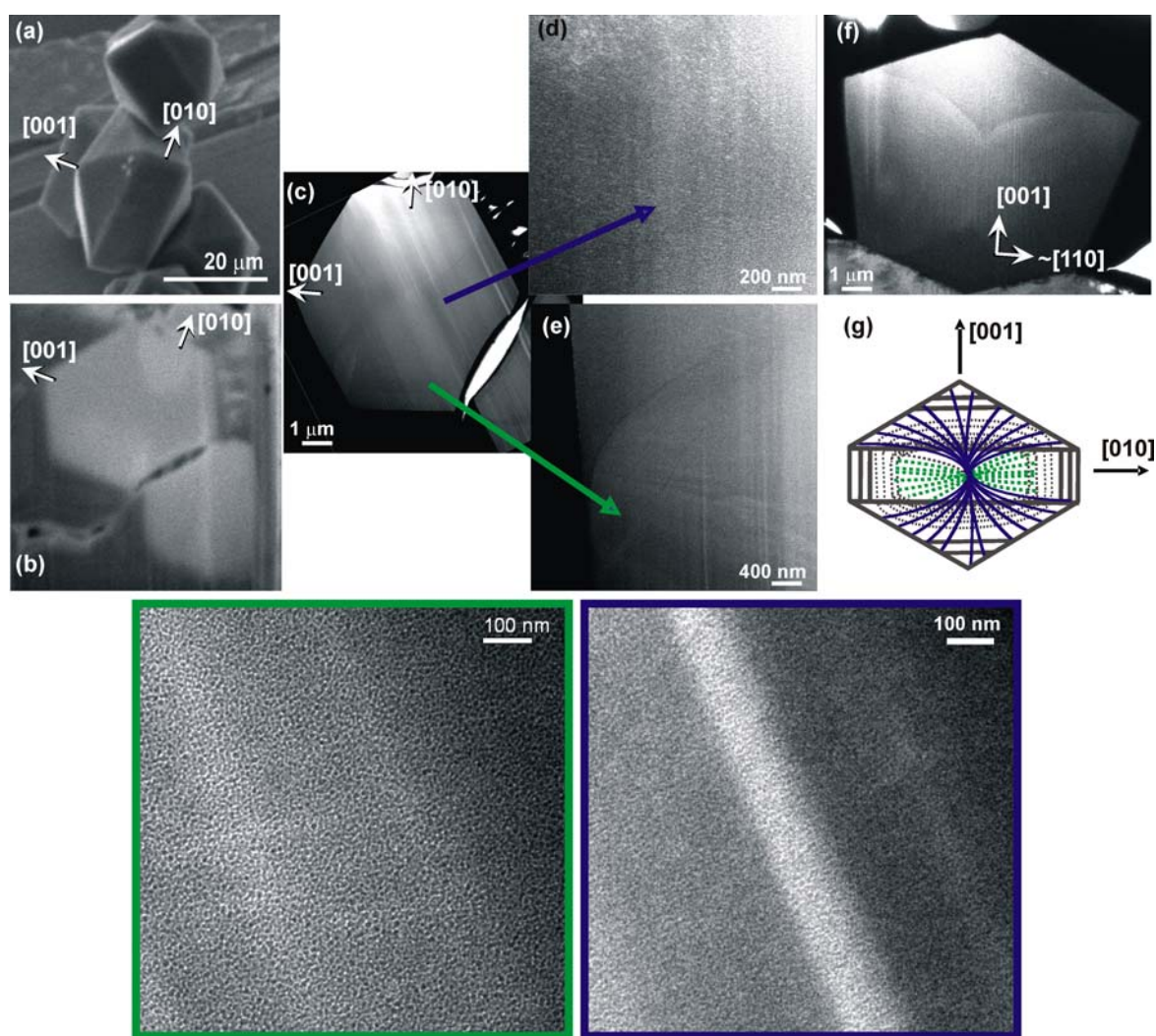


Fig. 3.3.22. (a) SEM image of an elongated tetragonal bipyramidal COD, (b) SIM image after the FIB treatment along $[100]$ cross-section. (c,d,e) TEM images indicating the inner architecture. (f) TEM image of a COD crystal cut along $[100]$ half cross-section. The region indicated with blue arrow is further magnified and shown with blue frame. The area indicated with green arrow is shown with green frame. (g) Model sketch of the inner architecture (blue lines indicate the arrangement of the crystallites from the centre towards the pyramidal faces and the green broken lines indicate the mosaic-like arrangement of the crystallites extending towards the prisms faces with less bent orientation).

In order to gain additional evidence on the growth of these crystals, the products were isolated at specific time intervals after mixing the reactant solutions and analyzed by SEM. The relevant morphological developments of aggregates grown from 0.8 mM CaOx and 7 $\mu\text{g/mL}$ PAA are given in figure 3.3.23. It shows the development of disc-like aggregates (Fig. 3.3.23 a) into elongated tetragonal bipyramids (Fig. 3.3.23 d) *via* a “cushion-like” morphology (Fig. 3.3.23 b,c). Such cushion-like morphologies are also observed for copper oxalate crystallized in the presence of HPMC (hydroxypropylmethyl cellulose) [139]. A closer look at the crystals isolated after 6 hours from solution

containing 7 $\mu\text{g/mL}$ PAA (Fig. 3.3.24) shows rounded edges and corners for the (101) and (100) faces.

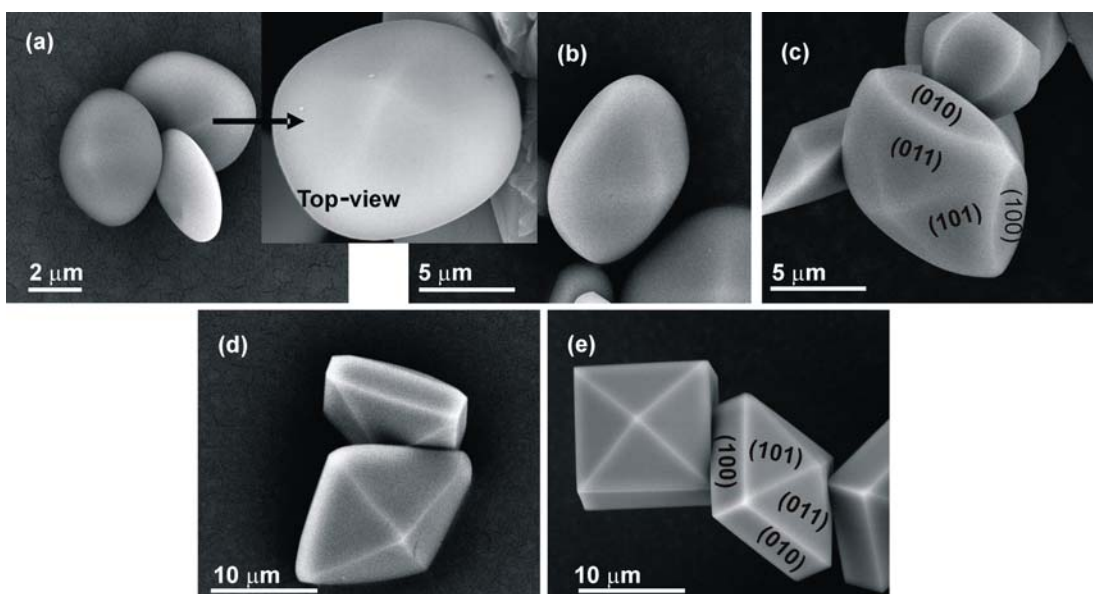


Fig. 3.3.23. SEM images of COD crystals isolated from 0.8 mM CaOx and 7 $\mu\text{g/mL}$ PAA. (a) Soon after mixing the reactant solutions, (b) after 30 minutes, (c) after 3 hours, (d) after 6 hours and (e) after 2 days.

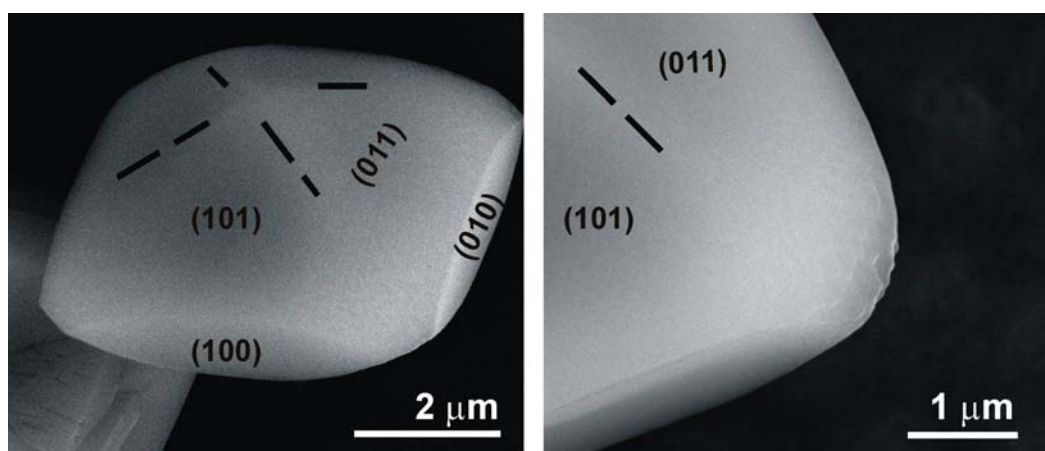


Fig. 3.3.24. SEM images of “early” crystals (isolated after 30 minutes) with rounded edges and corners obtained in the presence of 7 $\mu\text{g/mL}$ PAA.

Apart from this, the TEM image of a [100] cross-section of a “cushion-like” COD (isolated after 2 hours) indicated three regions of different arrangement of the crystallites (Fig. 3.3.25 a). However, these samples were extremely destructed under high electron beam which made them inefficient to study under higher magnifications. The three regions may be as follows: the central weak area of poor crystallinity, the middle region (later described as core) and an outer region of good crystallinity (later described as shell). However, this could not be confirmed from the [001] cross-section of

another crystal isolated under the same conditions which indicated just the uniform arrangement of the crystallites (Fig. 3.3.25 b).

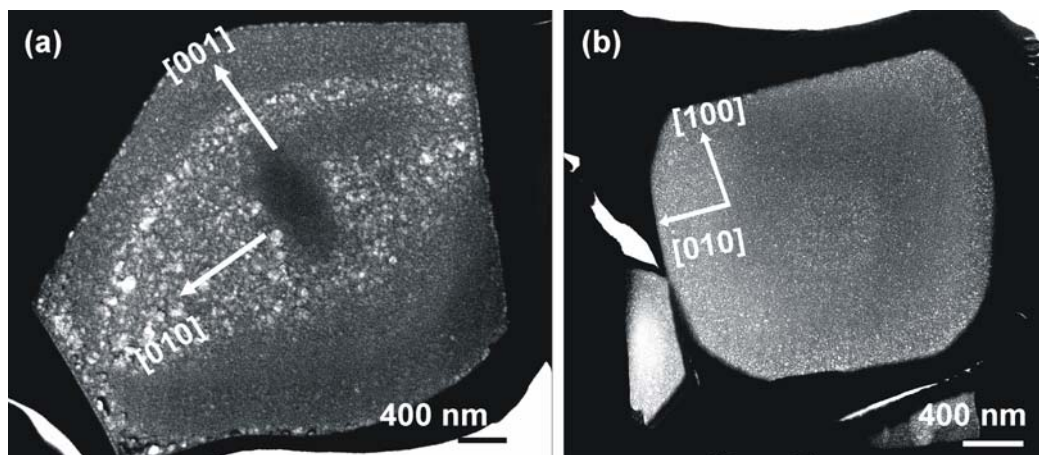


Fig. 3.3.25. TEM images of COD crystals isolated after 2 hours from solutions containing 0.8 mM CaOx and 7 $\mu\text{g}/\text{mL}$ PAA. (a) Cross-section along [100]. The pores in the sample are caused by the electron beam. (b) Cross-section along [001].

COD aggregates were isolated also from solutions containing 0.8 mM CaOx and 9 $\mu\text{g}/\text{mL}$ PAA at specific crystallization times. Even though the induction time is slightly increased, a mixture of disc-like and rod-like crystals were observed immediately after the solution became cloudy (Fig. 3.3.26 a). These rod-like aggregates already expressed (100) prism faces with definite edges. The pyramidal faces/caps were rounded without well-defined edges. The rod-like aggregates separated after 2 hours indicated the formation of edges between their (101) faces (Fig. 3.3.26 b). However, the crystallization of COD was so fast that it was difficult to clearly distinguish between different stages occurring during nucleation, growth and aggregation.

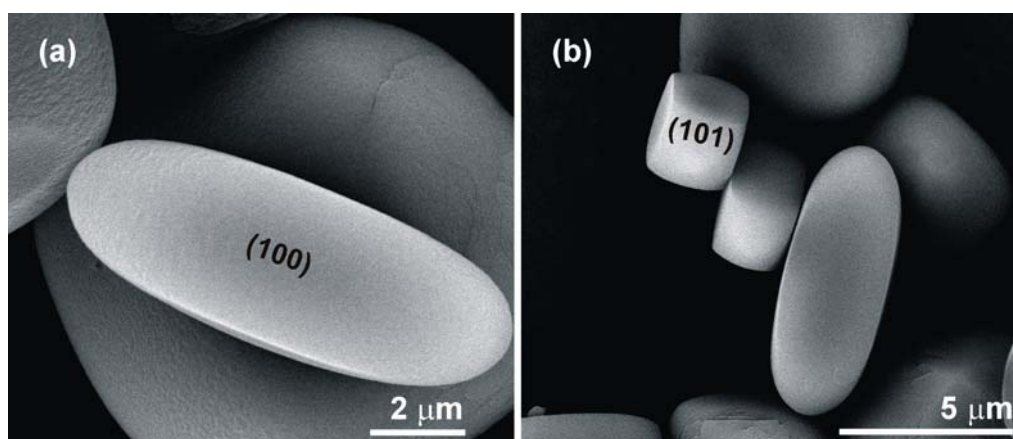


Fig. 3.3.26. SEM images of COD aggregates isolated from solutions containing 0.8 mM CaOx and 9 $\mu\text{g}/\text{mL}$ PAA after: (a) 30 minutes, (b) 2 hours. Note that the prism faces are already showing the edges between the (100) faces while the pyramidal faces are rounded.

COD crystals isolated from solutions containing still higher concentration of PAA at shorter time intervals also showed that the (101) faces with well-defined edges evolve slowly than (100) faces (Fig. 3.3.27).

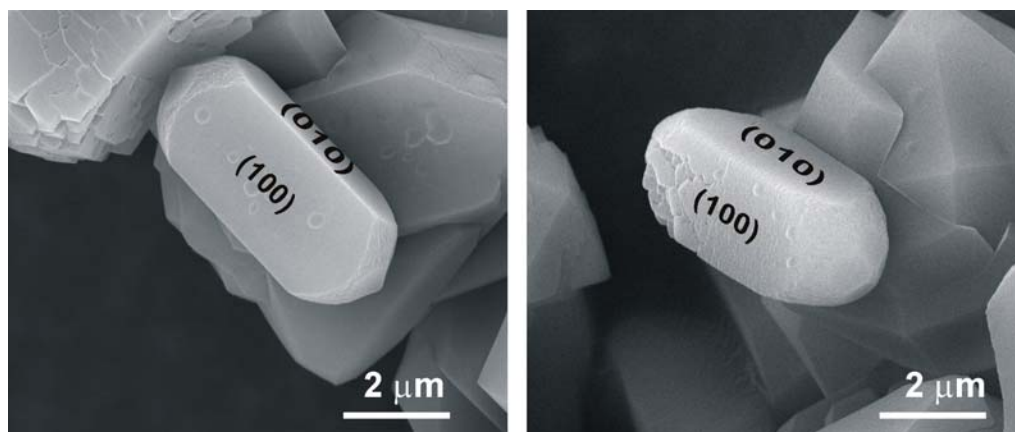


Fig. 3.3.27. SEM images of COD aggregates isolated from solutions containing 0.8 mM CaOx and 12 $\mu\text{g/mL}$ PAA after 30 minutes. The prism faces are almost completely developed while the pyramidal faces are incomplete.

In general, the morphology of a growing crystal is determined by the relative growth rates of its faces. The faster the growth rate in the direction perpendicular to a particular face, the smaller that face appears. If an effective growth inhibitor adsorbs on some crystal faces, but not on others, it will retard crystal growth in the direction perpendicular to that face. The affected face will appear larger than in non affected crystals and, as a result, crystal morphology will change. Thus, those faces which grow slowly will control the final growth morphology. Our calculations reveal that PAA adsorbs more on the (100) faces which means that the PAA backbone which is not adsorbed on the (100) faces acts as a fence on the crystal surface, thus forming an obstacle for propagating steps that lead to further crystal growth. It can be assumed that PAA will be attached at each growth step leading to smoothing of rough crystal faces and this in turn may lead to decreased entropic states and surface energies and evolution of prism faces with well-defined edges.

Morphological changes of COD crystals from tetragonal bipyramidal prisms to rod-like tetragonal prisms in the presence of poly(ethyleneglycol)-block-poly(methacrylic acid) were also reported by Zhang *et al.* [85]. However, the mechanism of the morphological changes remained elusive. Similar morphological changes of copper oxalate from cubes to rods in the presence of HPMC were explained in terms of perfect alignment of nanoparticles to form a “mesocrystal” [76,139]. As for copper

oxalate, PAA seems to influence the nucleation, growth and aggregation of nano crystallites by face selective interactions as shown in the model sketch in figure 3.3.28.

General considerations and Hypothesis: The influence of PAA on the morphogenesis of calcium oxalate seems to be closely related to its crystal structure with two types of faces, (100) and (101). It can be assumed that soon after mixing the reactant solutions, poorly crystalline primary particles are formed (Fig. 3.3.28-1) which aggregate to form secondary particles with facets (Fig. 3.3.28-2). The specific adsorption of PAA on the (100) facets happens and even though there is an inhibition of crystal growth by adsorption of PAA, the growth resumes when the polymeric agents provide covering when the degree of supersaturation increases around the surface.

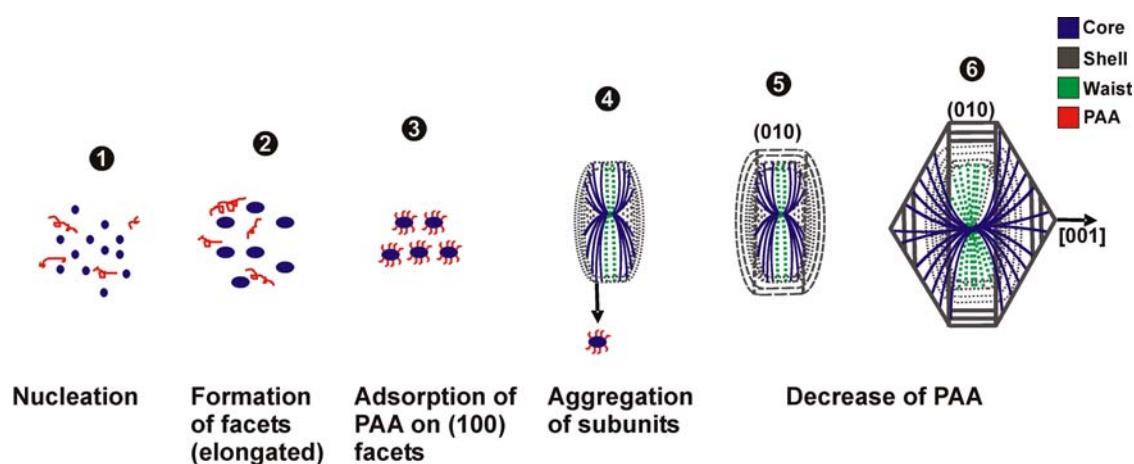


Fig. 3.3.28. Schematic representation of morphogenesis of elongated tetragonal bipyramidal COD with a specific inner architecture of the crystallites as indicated from TEM analyses. Blue dots and red coils represent CaOx and PAA respectively. The blue lines from step 4 onwards represent elongated calcium oxalate crystallites (as in step 3) coated by PAA. These crystallites extend from the centre towards the pyramidal faces. The green dots represent the mosaic-like arrangement of the crystallites in the waist area extending towards the prism faces. The outer thicker lines correspond to the lastly formed layer of calcium oxalate crystallites.

As a result of adsorption of PAA on the (100) facets, nanocrystallites which are slightly elongated along the *c*-axis are formed (Fig. 3.3.28-3). This is confirmed from the calculation of coherence length of the domains from the powder X-ray diffraction pattern (Table. 3.3.1). It is generally assumed that such a situation of dispersed nanocrystallites is apparently not favourable for the system and the nanocrystallites decrease the overall free energy of the system by aggregation (Fig. 3.3.28-4). When such crystallites with (100) surfaces coated with PAA approach, a weakly adsorbed polymer layer may be depleted as proposed in the case of copper oxalate-HPMC system [139]. Hence, the

osmotic pressure becomes unbalanced, resulting in an attraction of neighbouring crystallites. Thus, the major part of polymer would consequently be depleted from the crystallites' surface as they aggregate while the remaining amount in solution surrounding the so-formed polycrystalline particles would still interact with the external surface. The aggregation takes place layer by layer to form tetragonal particles with rounded faces (Fig. 3.3.28-4). The model in figure 3.3.28-5 can be correlated to the product isolated within 30 minutes after mixing the reactant solutions (Fig. 3.3.24). After this initial increase of supersaturation, the crystal growth occurs at moderate supersaturation of active calcium and oxalate ions in the solution which ultimately results in elongated tetragonal bipyramidal crystals (Fig. 3.3.28-6).

For the tetragonal bipyramidal prisms, the growth mechanism could be similar to the above case but the (100) crystal faces are kept more stable by the adsorption of PAA and the (101) faces are formed at a later stage (Fig. 3.3.27). The TEM image of an approximately [100] cross-section of a tetragonal prismatic COD crystal obtained from 0.8 mM CaOx and 14 $\mu\text{g}/\text{mL}$ PAA indicates a similar arrangement of crystallites with the divergence starting from a common point in the centre of the specimen (Fig. 3.3.29). The crystallites diverging from the centre and extending towards the pyramidal faces are thinner or needle-like. The arrangement of such thinner crystallites ultimately represents a dumbbell-like arrangement (indicated by blue lines in the model sketch in Fig. 3.3.30-5). In these crystals also, the crystallites constituting the waist area appear different (indicated in green colour). Furthermore, an outer crown-like layer is conspicuous in this case (indicated with thick darker lines).

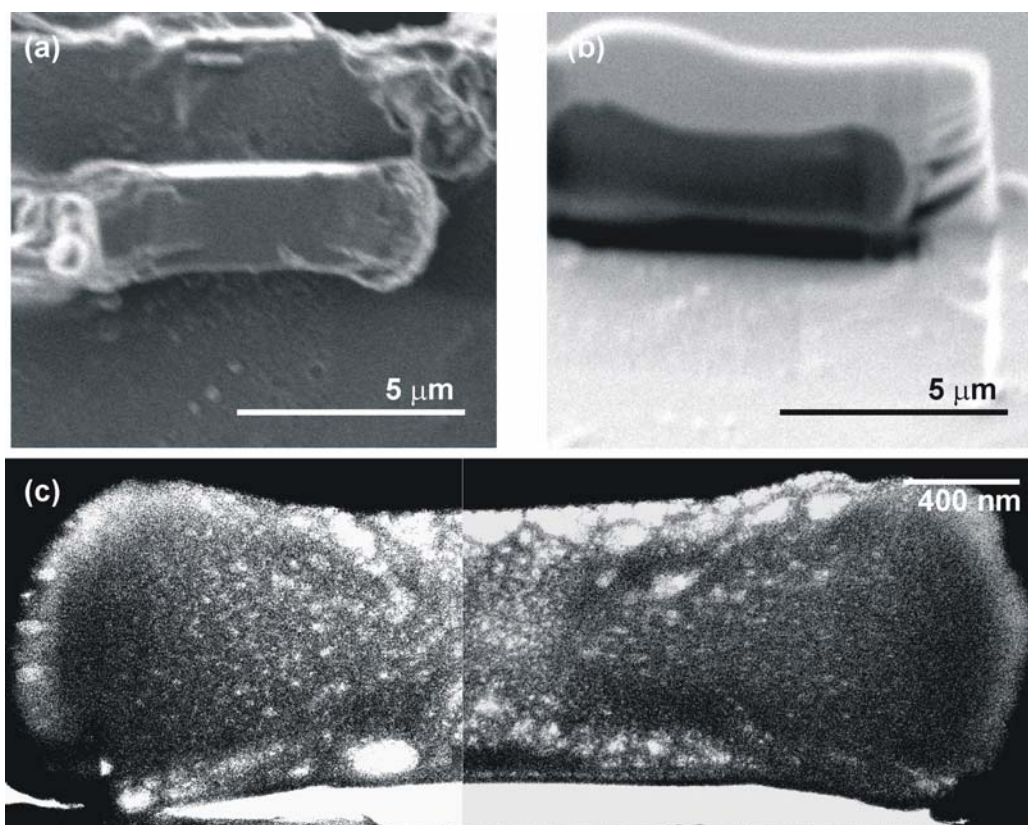


Fig. 3.3.29. Series of SEM (a), SIM (b), TEM (c) images of tetragonal prismatic COD. The TEM image of the (100) cross section shows the arrangement of the crystallites from the centre towards the pyramidal faces.

Therefore, the morphogenesis of a tetragonal prismatic COD also proceeds as in the case of elongated tetragonal bipyramids with nucleation, growth and aggregation (Fig. 3.3.30). The crystallites formed are more elongated than the latter case due to the presence of more PAA. This is evident from the coherence length ratio and the amount of PAA in these crystals. As a result, the aggregation of the such elongated crystallites form COD aggregates with well-developed (100) faces (Fig. 3.3.30-4).

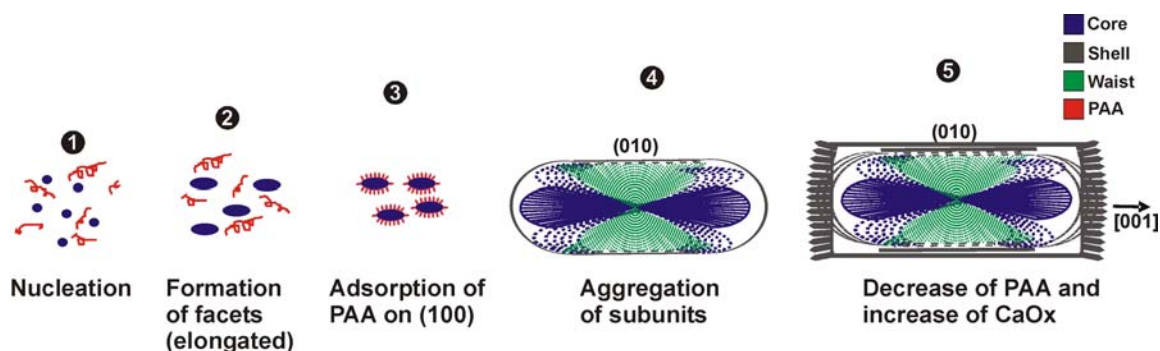


Fig. 3.3.30. Schematic representation of the morphogenesis to form tetragonal prismatic COD crystals with the inner architecture of the crystallites as indicated from TEM analyses. Step 4 may be correlated with figure 3.3.26.

Growth of calcium oxalate in the presence of 0.8 mM CaOx and 15 to 188 $\mu\text{g/mL}$ PAA: Formation of COD dumbbells

For PAA concentrations in the range 15 to 96 $\mu\text{g/mL}$, COD dumbbells with aspect ratio ranging from 3.5 to 5 are formed. The amount of PAA as detected from TGA analyses are 2.5 to 3.5 wt.-% respectively (Table 3.3.4). For PAA concentration in the range of 100 to 188 $\mu\text{g/mL}$, “elongated”-dumbbells (with structuring/splitting at the pyramidal faces) with aspect ratio approximately 7 and amount of PAA *ca.* 2.5 wt.-% are formed (Fig. 3.3.31 b).

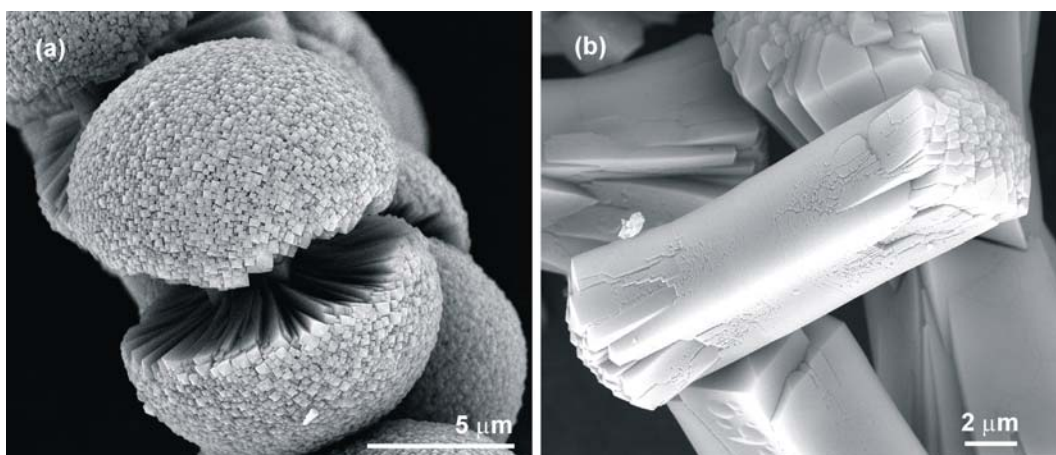


Fig. 3.3.31. SEM images of: (a) COD dumbbell grown from 0.8 mM CaOx and 96 $\mu\text{g/mL}$ PAA. (b) A COD crystal grown from 0.8 mM CaOx and 168 $\mu\text{g/mL}$ PAA. For the sake of convenience such crystals are addressed as “elongated” dumbbells, which is actually an elongated tetragonal prism with smaller tetragonal crystals formed on the pyramidal faces.

It was found that with increase in concentration of PAA, the length of the tetragonal seed crystal along [001] increases and the structuring starts closer to the pyramidal faces rather than on the prism faces (Fig. 3.3.31 b, note the sequence from l to o in Fig. 3.3.4). The powder XRD patterns of these samples were matching well with that of the calculated COD pattern although the peaks were slightly broader (Fig. 3.3.8). The crystallite dimensions calculated using the Scherrer equation showed that the elongation of the domain along *c*- axis reached a maximum for COD dumbbells grown from solution containing 96 $\mu\text{g/mL}$ PAA (Table. 3.3.1). This can be correlated with the fact that the amount of the adsorbed PAA is higher in this case (*ca.* 3.5 wt.-%). This means the crystallites are sufficiently coated with PAA on their (100) faces and as a result, the coherence length along [001] is greater than that along [100]. The number of crystallites formed per litre (calculated using the yield of the sample formed under these conditions

and the volume of the crystallite formed) was also found to be a maximum (Table 3.3.1) [139].

The COD dumbbells grown from 0.8 mM CaOx and 96 $\mu\text{g/mL}$ PAA were cut parallel to the (100) plane of the tetragonal prism and TEM investigations were performed with (Fig. 3.3.33) and without (Fig. 3.3.32) staining the lamellar sections by 1% uranyl acetate. As in the case of tetragonal bipyramids and tetragonal prisms, the TEM images of the dumbbells also clearly indicate the arrangement of smaller crystallites diverging from the centre and extending towards the pyramidal faces (Fig. 3.3.32, Appendix Fig. 6.6, 6.7, 6.8). These crystallites were smaller and much more elongated along the [001] direction as compared to the case of tetragonal prism. This inner region consisting of smaller crystallites are called as “core” here onwards (also indicated with blue colour in all the sketches). Additionally it was found that there is a region of bigger crystallites outside the core. This region made up of bigger crystallites is called “shell” and there exists a boundary between the core and the shell which is called “front of the core”. In this case also, the crystallites constituting the waist area appeared to be different (see Appendix Fig. 6.7).

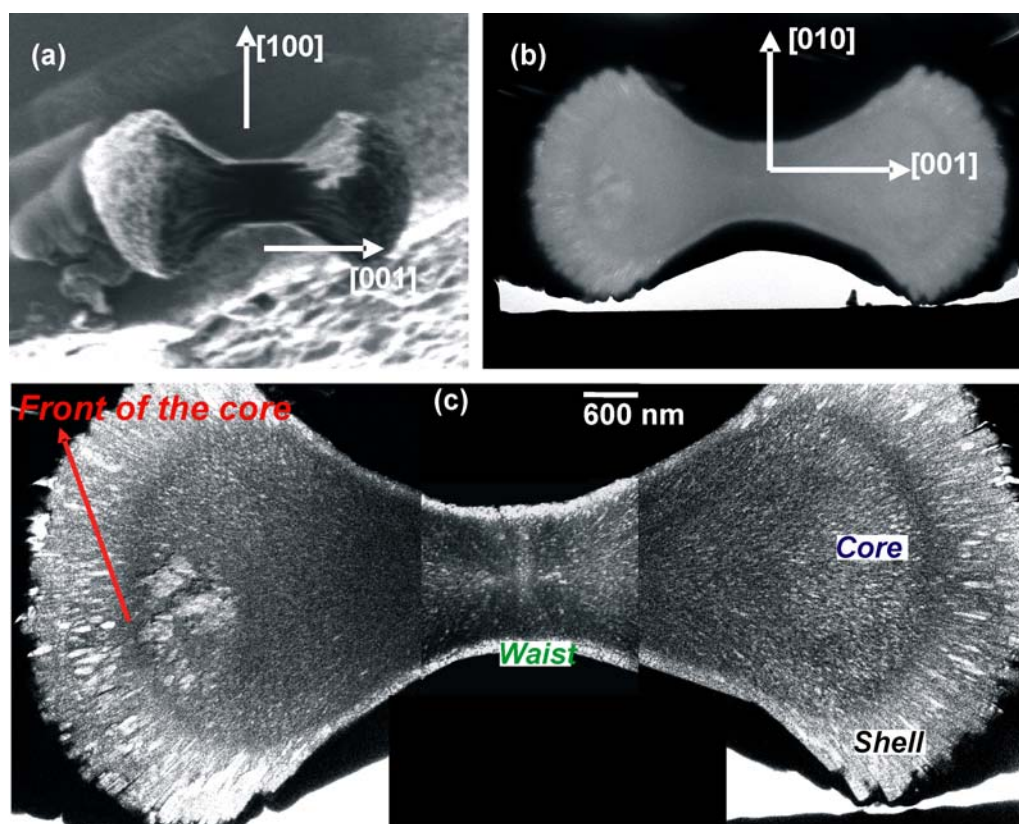


Fig. 3.3.32. SEM (a), SIM (b) images of a COD dumbbell (grown from 0.8 mM CaOx and 96 $\mu\text{g/mL}$ PAA). (c) Overlapped TEM images of a [100] cross-section. Note that specific regions inside the dumbbells are called core, waist and shell.

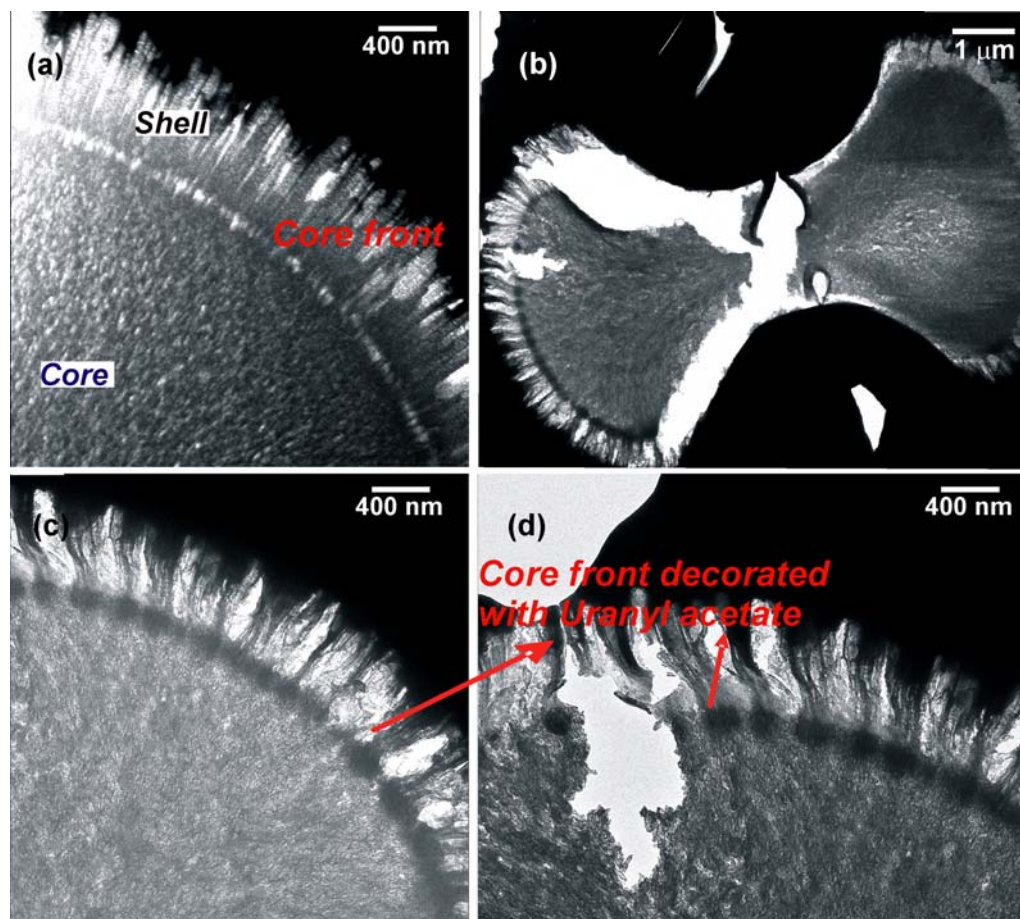


Fig. 3.3.33. TEM images of a section from a COD dumbbell. (a) Unstained section, (b,c,d) stained with uranyl acetate indicating the core front enriched with organic material.

The TEM investigations were again performed after staining the thin sections from the [100] cross-section of COD dumbbells with 1% uranyl acetate. Then it became apparent that the boundary between the core and the shell, the so-called front of the core is enriched with organic material (Fig. 3.3.33). Although the staining with uranyl acetate causes the dehydration of the sample and a subsequent shrinking effect, the core front is nicely decorated with uranyl acetate and convinces the presence of organic material inside these dumbbell shaped COD aggregates. Also, the core area seems to contain organic material and the crystallites constituting the core are embedded in the organic material.

Dissolution behaviour of the inorganic part of the aggregates: For decalcification, the COD dumbbells (grown from 0.8 mM CaOx and 96 μg/mL PAA) were treated with 0.25 N EDTA (pH = 4.5). The aggregates were totally decalcified within 15 minutes. PAA could not be obtained as a residue due to its solubility in water. The SEM images of the

decalcified samples further confirm that the “core” itself is dumbbell shaped and the “shell” is made up of tetragonal prismatic COD crystallites (Fig. 3.3.34).

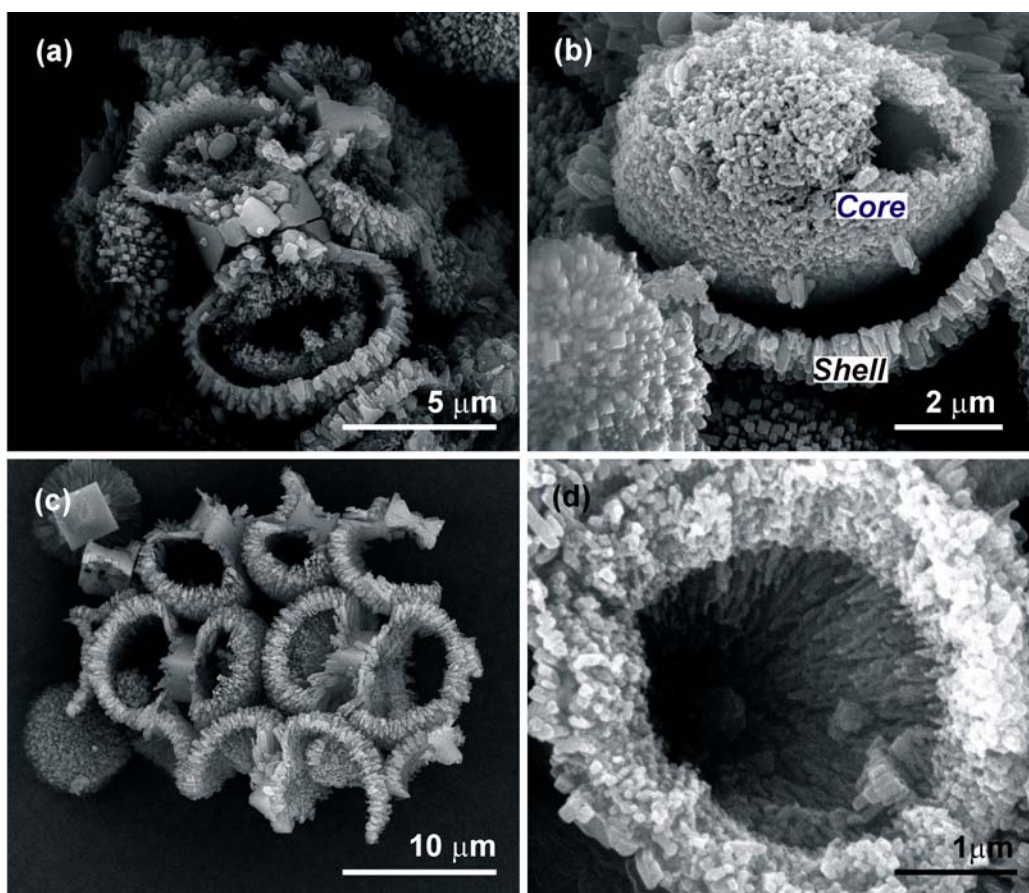


Fig. 3.3.34. SEM images of the dumbbells of COD (grown from 0.8 mM CaOx and 96 μg/mL PAA) after treatment with EDTA. (a,b) partially decalcified dumbbells with crown removed and some of the core and the shell area remaining. (c,d) Almost completely decalcified core.

A partially decalcified sample shows that the rate of decalcification is different for the core and the shell areas (Appendix Fig. 6.9). The prism faces of the central tetragonal seed connecting the two hemispheres were the last to be decalcified (Fig. 3.3.34 c). Demineralization is faster in the core area as it is composed of smaller crystallites than the shell. Demineralization by EDTA therefore leads to hollow dumbbells (Fig. 3.3.34 c,d). These images clearly support the notion that the shell is formed as part of a secondary growth mechanism. After partial decalcification, some of these dumbbells formed a gap between the core and the shell areas (Fig. 3.3.34 a,b). This region is made up of smaller crystallites and covers the caps of the dumbbells like a “crown”.

The core-shell architecture is further supported by the SEM images of partly broken dumbbells grown from 0.8 mM CaOx and 96 $\mu\text{g/mL}$ PAA (Fig. 3.3.35, Appendix Fig. 6.10). The core seems to be made up of elongated or needle-like crystallites with preferred crystallographic orientation along [001]. These crystallites, (approximately 50-70 nm long and 20-30 nm thick, Appendix Fig. 6.8) seem to be arranged layer by layer with significant bent orientation to constitute the dumbbell shaped core (as indicated by blue lines in Fig. 3.3.36 a). The tetragonal prisms forming the shell area protruding from the core area are approximately 1 μm in length.

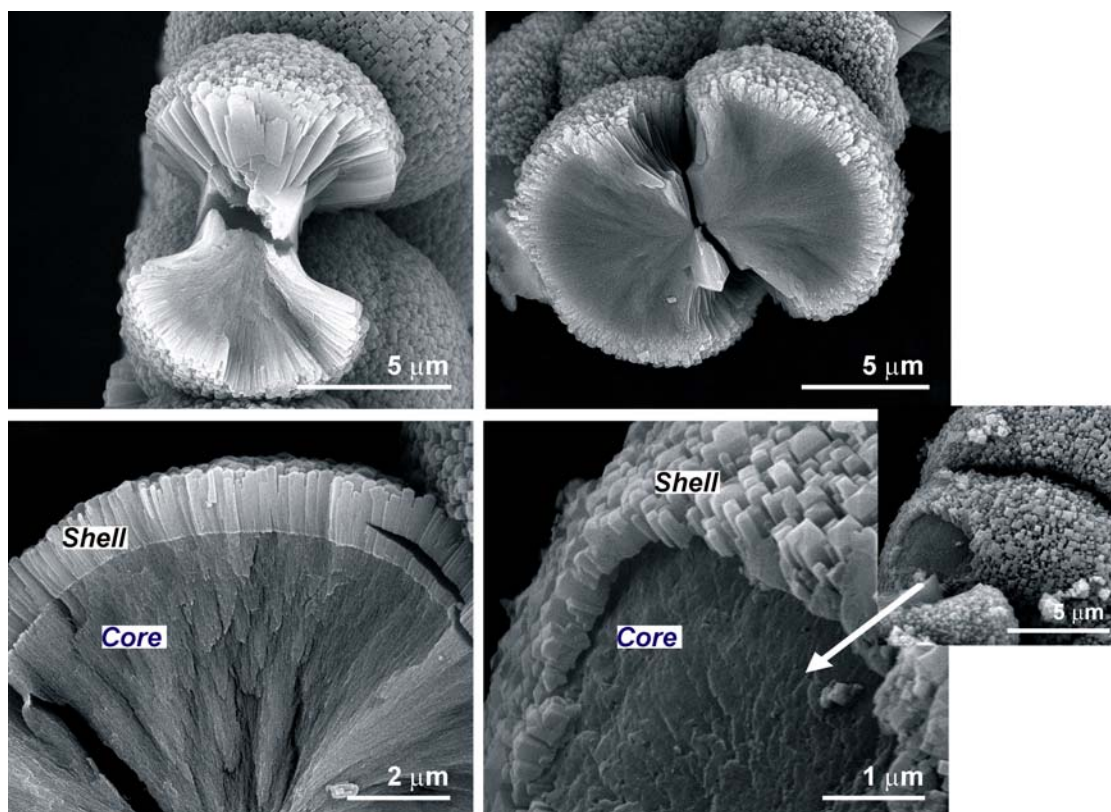


Fig. 3.3.35. SEM images of broken COD dumbbells indicating a core made up of smaller crystallites and a shell of bigger tetragonal prismatic crystals. Also note the perfect boundary between the core and the shell.

Therefore, a completely developed COD dumbbell consists of a “*core-crown-shell*” architecture (Fig. 3.3.36 d). The less or only “partially crystalline” core is composed of small needle-like or rod-shaped crystallites diverging from the centre and extending symmetrically towards the pyramidal faces (region 1 in Fig. 3.3.36 d). The crown is composed of tetragonal prismatic crystallites arranged around the caps of the core (region 2 in Fig. 3.3.36 d) and the shell is composed of larger tetragonal prismatic

COD crystals starting from the central tetragonal seed crystal protruding outwards (region 3 in Fig. 3.3.36 d).

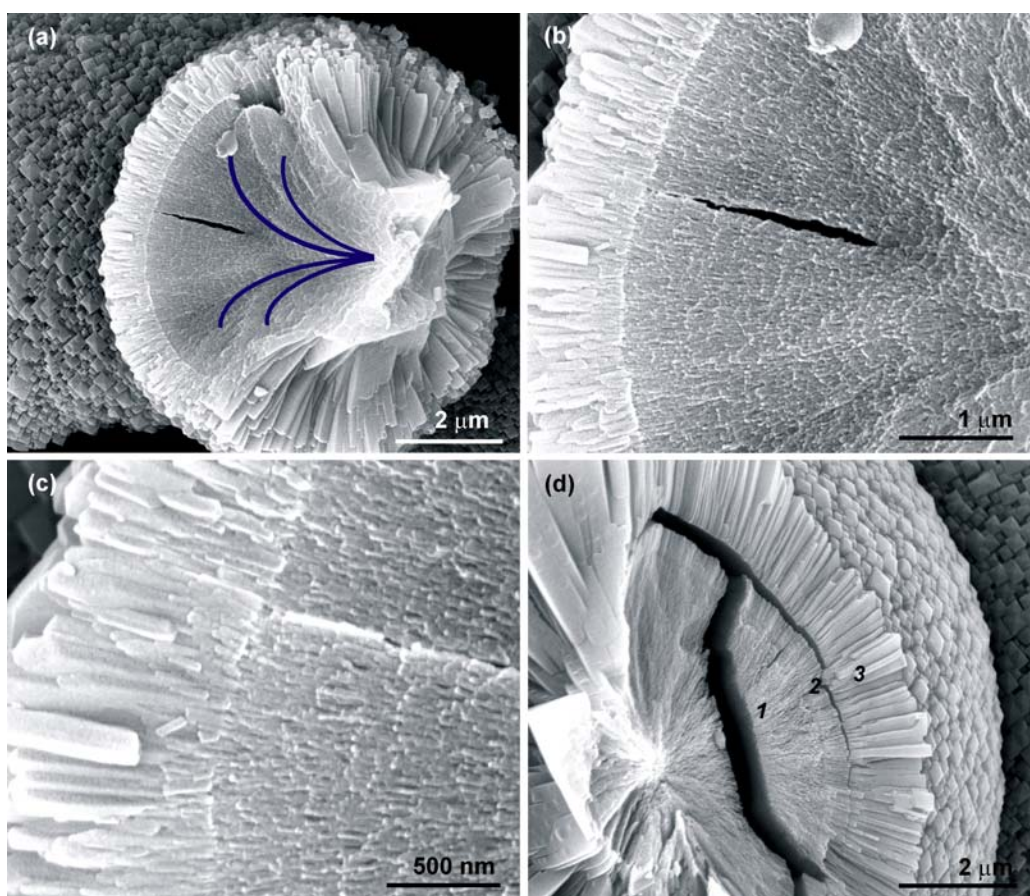


Fig. 3.3.36. (a,b,c) SEM images of the dumbbells of COD broken along their long axis. Note the crystallites constituting the core diverge from the centre and extend towards the pyramidal faces as indicated with blue lines. These crystallites are arranged in layer by layer fashion. (d) A broken dumbbell with region1 (core), region2 (crown) and region3 (shell).

The radial and continuous arrangement of the crystallites is evident from the TEM images of a half dumbbell (Fig. 3.3.37). These dumbbells represent an early growth stage without shell formation. The damage of the sample under the electron beam produced lacunae inside the sample which can be taken as an indication of the poorly crystalline or the more “composite” nature of the core region. These crystallites constituting the core were approximately 10 to 20 nm in thickness and appear well-spaced (Appendix Fig. 6.8). The space between the nano subunits may be filled with organic material. However, highly magnified images from these samples were not possible as they decomposed too rapidly under the electron beam.

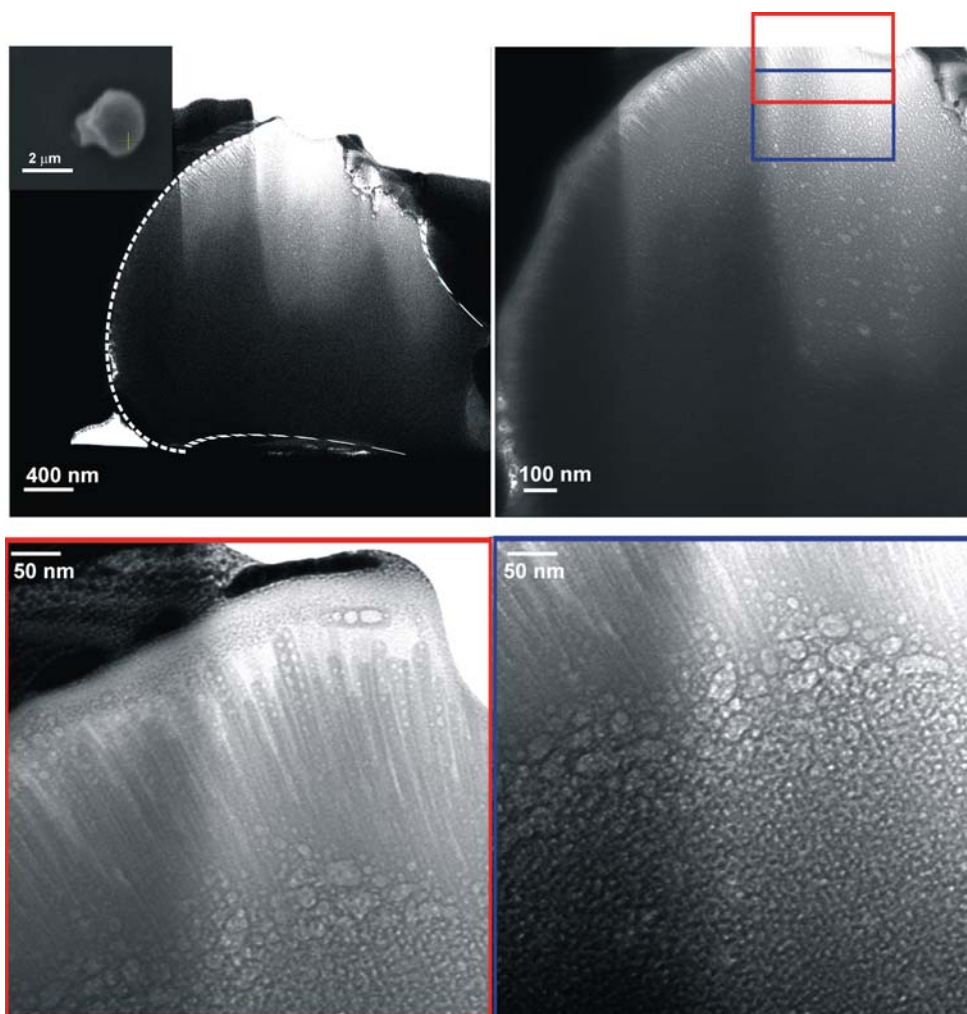


Fig. 3.3.37. (Top) TEM images of a half dumbbell of COD (inset-SEM image) with radial and continuously arranged nanocrystallites. (Bottom) Enlarged TEM images from the coloured frames areas. Also see figure 6.8 in appendix.

To gain additional information on the morphogenesis, the COD dumbbells formed from 0.8 mM CaOx and 96 μg/mL were isolated at specific crystallization times and analyzed by SEM. It was observed that the solution became cloudy after 30 minutes. However, the dumbbell shaped aggregates were formed as early as after 10 minutes from mixing the reactant solutions (Fig. 3.3.38 a). These early species were highly damaged under the electron beam. These images plainly indicate a polymer layer glued to these aggregates which remained even after repeated washing (Fig. 3.3.38 a). Such a residual polymer layer was observed also by Manne *et al.* [105]. Dumbbells isolated after 30 minutes already showed tetragonal prism faces, but instead of pyramidal faces they showed a rounded cap made up of small needle like crystallites (Fig. 3.3.38 b,c). After 1 hour, the smaller units on the caps are transformed to smaller tetragonal crystallites with well defined edges (Fig. 3.3.38 d,e,f). A closer look at some of the products obtained after 1 hour shows the formation of loose rod-shaped specimens. These elongated

particles (400-600 nm) (Fig. 3.3.39) might be the precursor with which the core is finally made up of.

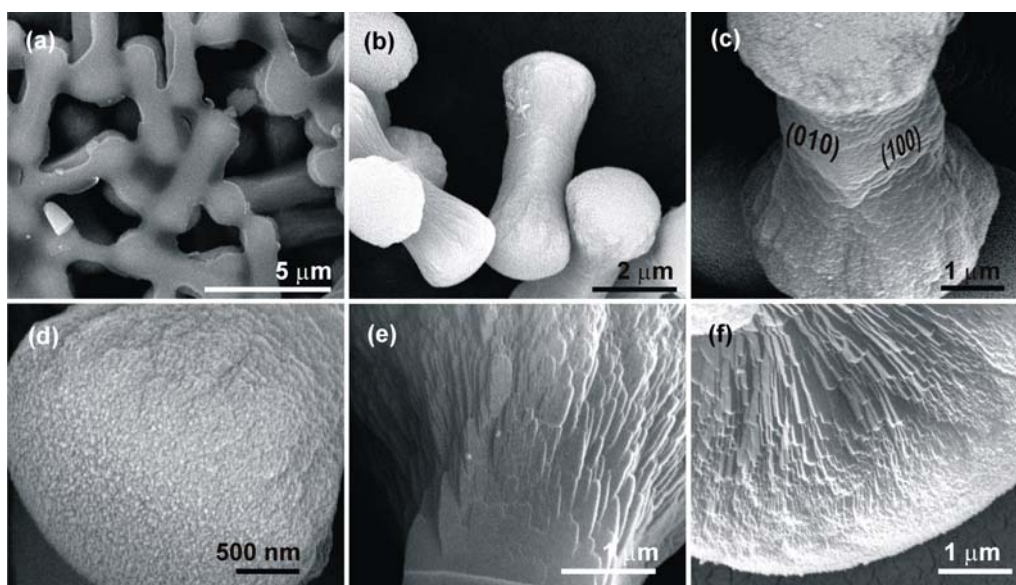


Fig. 3.3.38. SEM images of the aggregates formed from 0.8 mM CaOx and 96 µg/mL PAA after (a) 10 minutes (b) 30 minutes (c,d) 1 hour (e,f) 6 hours. These aggregates have dumbbell shape as early as 10 minutes. The small needle-like subunits formed after 1 hour (d) is getting transformed into small tetragonal prisms as time evolves (e,f).

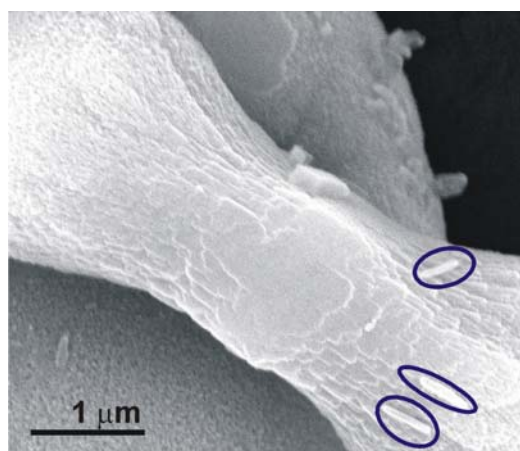


Fig. 3.3.39. Rod shaped products found (circled with blue colour) along with the aggregates isolated from solutions containing 0.8 mM CaOx and 96 µg/mL PAA after 1 hour.

The XRD pattern of all these early isolated aggregates matched well with the calculated pattern of COD (Fig. 3.3.10). The crystallite sizes were calculated from the Scherrer equation. It was found that the coherence length of the nanodomain along the *c*-axis almost doubles in 3 hours time.

Products isolated at various time intervals from solutions containing 0.8 mM CaOx and PAA concentrations of 16 and 24 µg/mL were also analysed by SEM (Fig. 3.3.40 and Fig. 3.3.41). The aggregate formed after 10 minutes from solution containing

0.8 mM CaOx and 16 $\mu\text{g/mL}$ PAA appeared elongated and rounded (for the sake of convenience it may be called cylindrical) with additional growth stages appearing near to the caps (Fig. 3.3.40 a). After 30 minutes, the specimen develops into a tetragonal prismatic crystal with structuring on the pyramidal faces (Fig. 3.3.40 b,c). The products isolated after 30 minutes from solution containing 0.8 mM CaOx and 24 $\mu\text{g/mL}$ PAA (Fig. 3.3.41) already looked like the ones obtained from 96 $\mu\text{g/mL}$ PAA in 1 hour. This is because the crystallization is faster in the presence of lower concentrations of PAA.

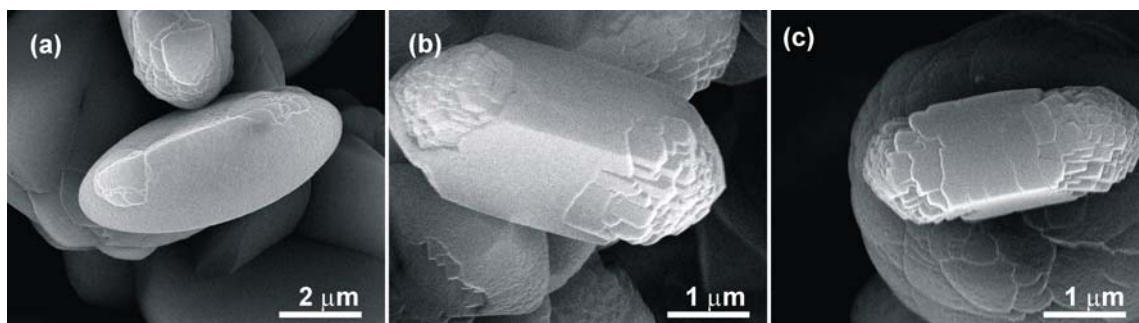


Fig. 3.3.40. SEM images of COD aggregates formed from 0.8 mM CaOx and 16 $\mu\text{g/mL}$ PAA after (a) 10 minutes (b,c) 30 minutes.

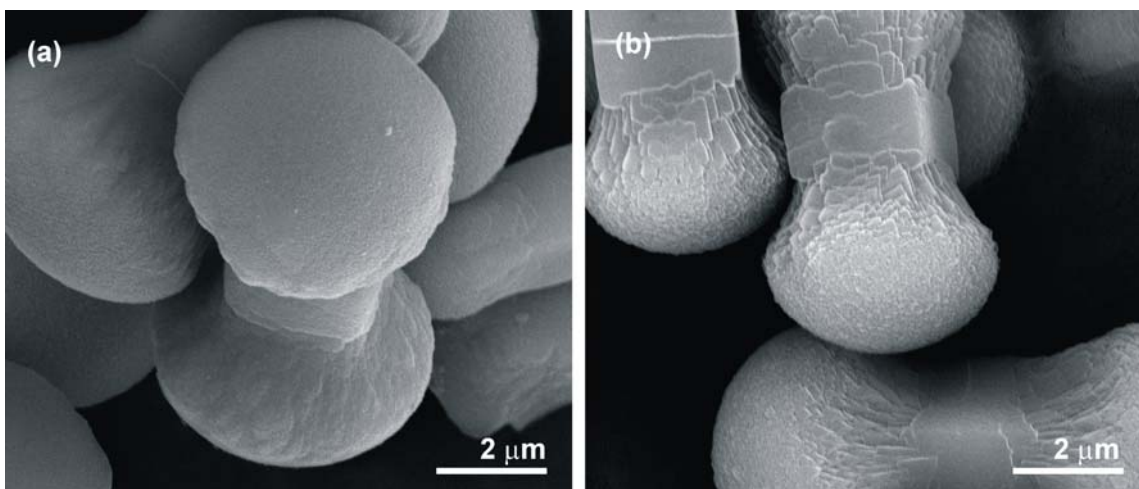


Fig. 3.3.41. SEM images of COD specimens obtained from solutions containing 0.8 mM CaOx and 24 $\mu\text{g/mL}$ PAA after (a) 30 minutes (b) 1 hour.

It can be assumed that the dumbbell shaped core in fact is the tetragonal seed crystal with dominant prism faces ((100) faces) and bulbous caps (instead of pyramidal faces, (the (101) faces)). The core is made up of small needle-like crystallites. From the time series experiments it is clear that the shape developments happening in shorter time scales for high PAA concentrations can be tracked out from the events happening during longer time scales for low PAA concentrations.

The investigations of the cross-section of the dumbbells obtained at shorter intervals of time confirms that the dumbbell shaped core has a tetragonal cross-section which appears to be rather smooth (Fig. 3.3.42 a,b). With evolution of time, radial striations on the tetragonal cross-section starting from the exact centre appear due to the progressive growth of the aggregate (Fig. 3.3.42 c,d).

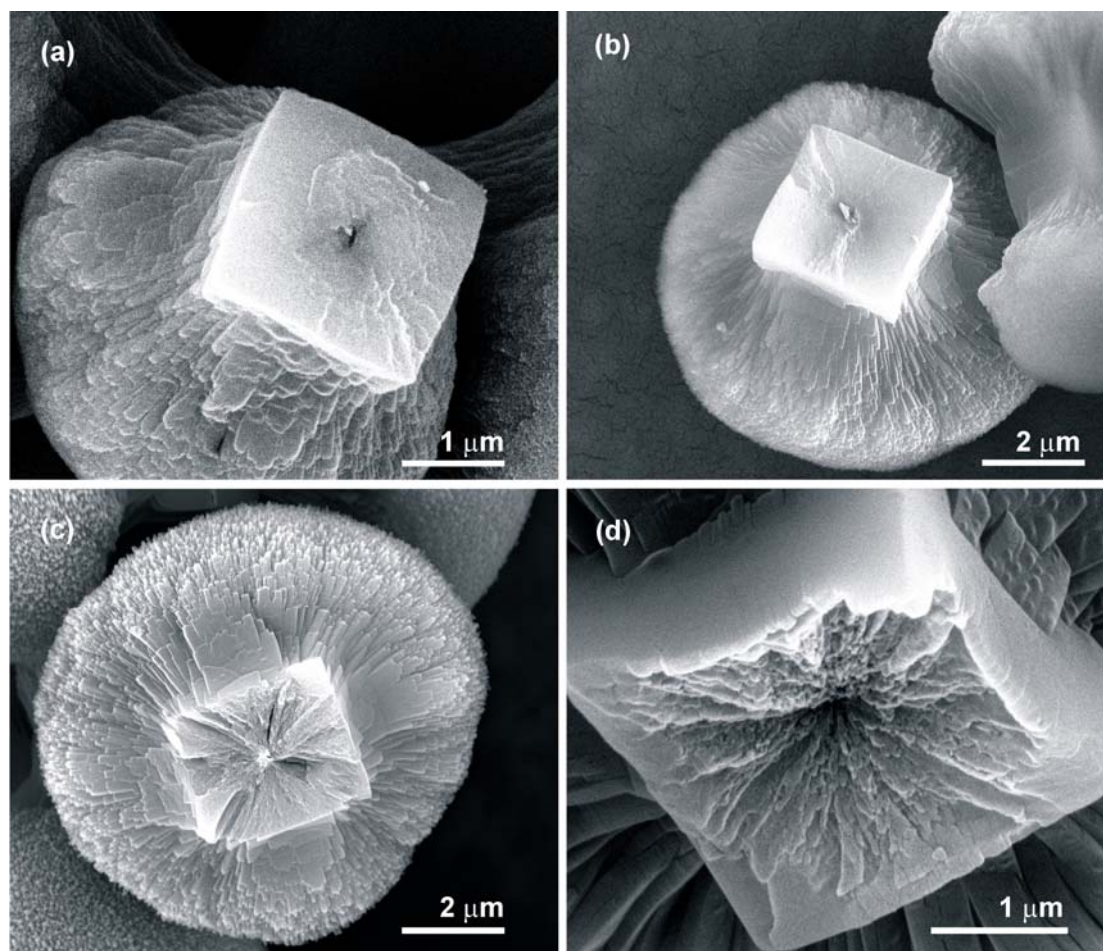


Fig. 3.3.42. SEM images of cross-section of the COD dumbbells grown from 0.8 mM CaOx and 96 μg/mL PAA after (a,b) 4 hours, (c) 9 hours and (d) 3 days. The radial striations of the tetragonal cross-section increases with evolution of time.

General considerations concerning the development of COD dumbbells: The above observations suggest that the COD dumbbells are composed of a dumbbell shaped core formed *via* primary nucleation processes, a crown of tetragonal COD prisms on the cap of the core enriched in organic material and a shell formed by secondary nucleation processes. This assumption is confirmed by the following SEM images of a dumbbell after partial decalcification with EDTA (Fig. 3.3.43).

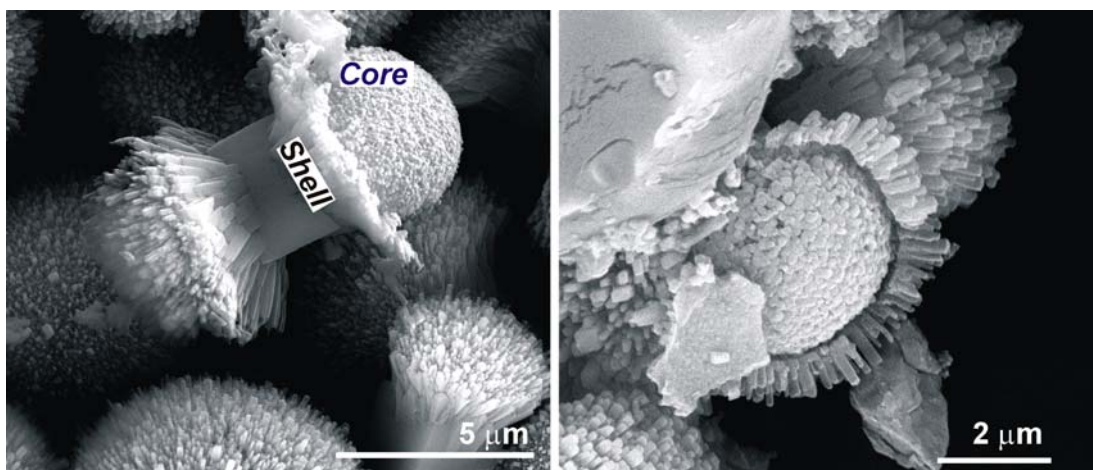


Fig. 3.3.43. SEM images of partly decalcified dumbbells of COD with the core-shell structure retained after the dissolution of the crown crystallites. Compare the similarity of the core with the specimens in figure 3.3.38.

Therefore, the morphogenesis of COD dumbbells may be beginning with the primary crystallization of the tetragonal prisms. Instead of the formation of a well developed tetragonal prism a cylindrical shaped particle is formed (Fig. 3.3.40 a, also see Fig. 3.3.26 a). The constituent crystallites form bulbous caps at the ends of the tetragonal prisms instead of pyramidal faces. A possible reason for the emergence of bulbous caps instead of well-developed tetragonal pyramidal faces can be that these edges are sites of high surface energy [146]. In other words, a loss of edges between the pyramidal faces of a tetragonal prismatic seed crystal would lead to the formation of a dumbbell shaped core.

A specific relative proportion of the concentration of CaOx and PAA is required for the formation of COD dumbbells (supported by experiments conducted with different concentration of calcium oxalate, Fig. 6.3 in Appendix). At this concentration there is a subtle balance between the inhibition and promotion of crystal growth by PAA. It is not an abrupt change of tetragonal bipyramids into tetragonal prisms, but a slow evolution of faces by the attachment of the polymer and a competition between supersaturation and inhibition of crystal growth. The scheme for the morphogenesis of COD dumbbells is illustrated in figure 3.3.44.

It can be assumed that the carboxylate groups of coiled PAA in aqueous solution direct the growth of calcium oxalate (Fig. 3.3.44-1) and forms nanometer sized rod-like crystallites (Fig. 3.3.44-2,3) which then aggregate and align parallel to form the dumbbell shaped core (Fig. 3.3.44-4). The rod-like crystallites with PAA adsorbed on the (100) facets aggregate only in the directions free to grow. It grows in the direction where

the crystallization hindrance is the weakest as in the case of rod-like tetragonal prisms formed from solutions containing only low concentrations of PAA. Progressive stages of self-organized growth of these smaller crystallites lead to dumbbell-shaped core.

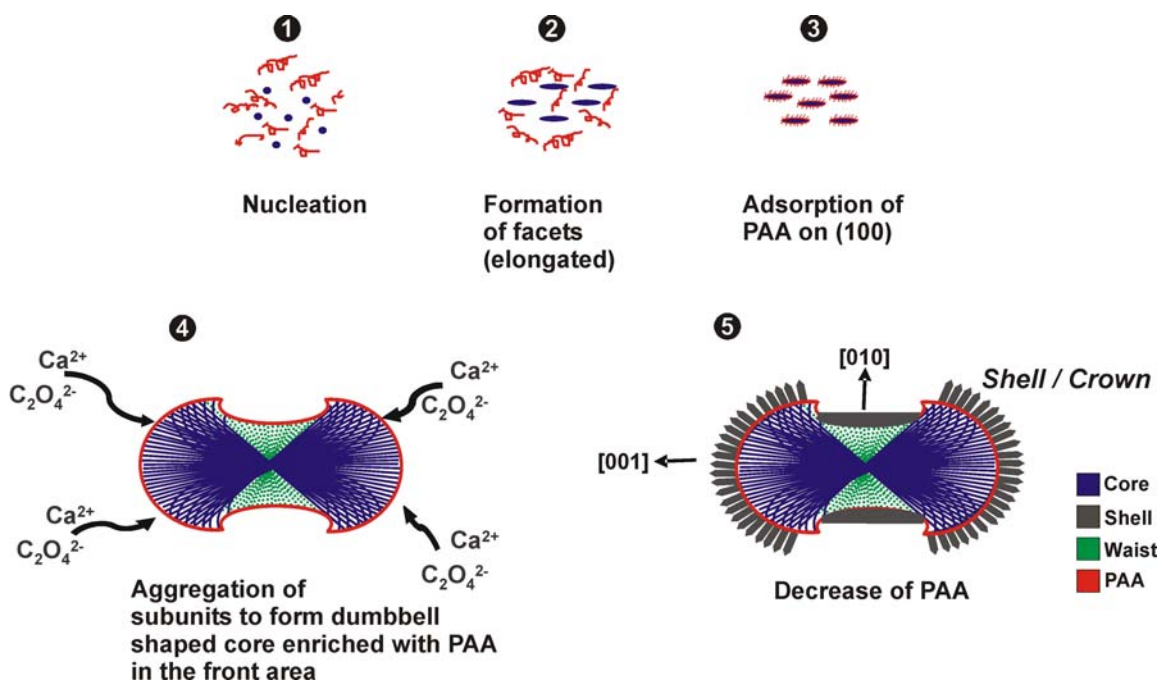


Fig. 3.3.44. Schematic representation of the morphogenesis of COD dumbbells in the presence of PAA (concentrations $> 16 \mu\text{g/mL}$). Step 1 represents nucleation of CaOx (blue dots) in the presence of PAA (red coils). Step 2 represents smaller crystallites with facets. The (100) facets of these crystallites are coated with PAA in step 3. Such elongated crystallites aggregate and form dumbbell shaped core enriched with PAA on the exterior faces (step 4). The green dots are CaOx crystallites in the waist area which are poorly coated with PAA and hence less elongated (refer to Appendix Fig. 6.7). Secondary nucleation of COD (shown with ash colour) takes place by the incorporation of Ca and Ox ions from the solution and by utilizing PAA (red) depleted from the crystallites constituting the core.

The second growth stage is characterized by the formation of elongated tetragonal prismatic calcium oxalate units with nearly parallel orientation on top of the core. The dumbbell-shaped core (Fig. 3.3.44-4) with more PAA on the exterior surfaces acts as nucleation centre for the growing shell. The secondary nucleation starts from the cap because of unstable interface and richness in organic material (Fig. 3.3.45). For crystals growing in solutions the entropy change is usually large, resulting in fast-growing faces which are unstable, while the faces growing slowly growing are stable. So, for a tetragonal prismatic COD crystal, it can be assumed that the apex or the cap provides an unstable interface which can induce further crystal growth if the conditions are favourable. The tetragonal prismatic COD has more PAA adsorbed on the (100) plane than (101) plane and the polymer backbone acts as barriers preventing further

growth along [100]. Under such a situation, the cap ((101) faces) which is enriched with organic material causes further growth to produce dumbbell-shaped core.

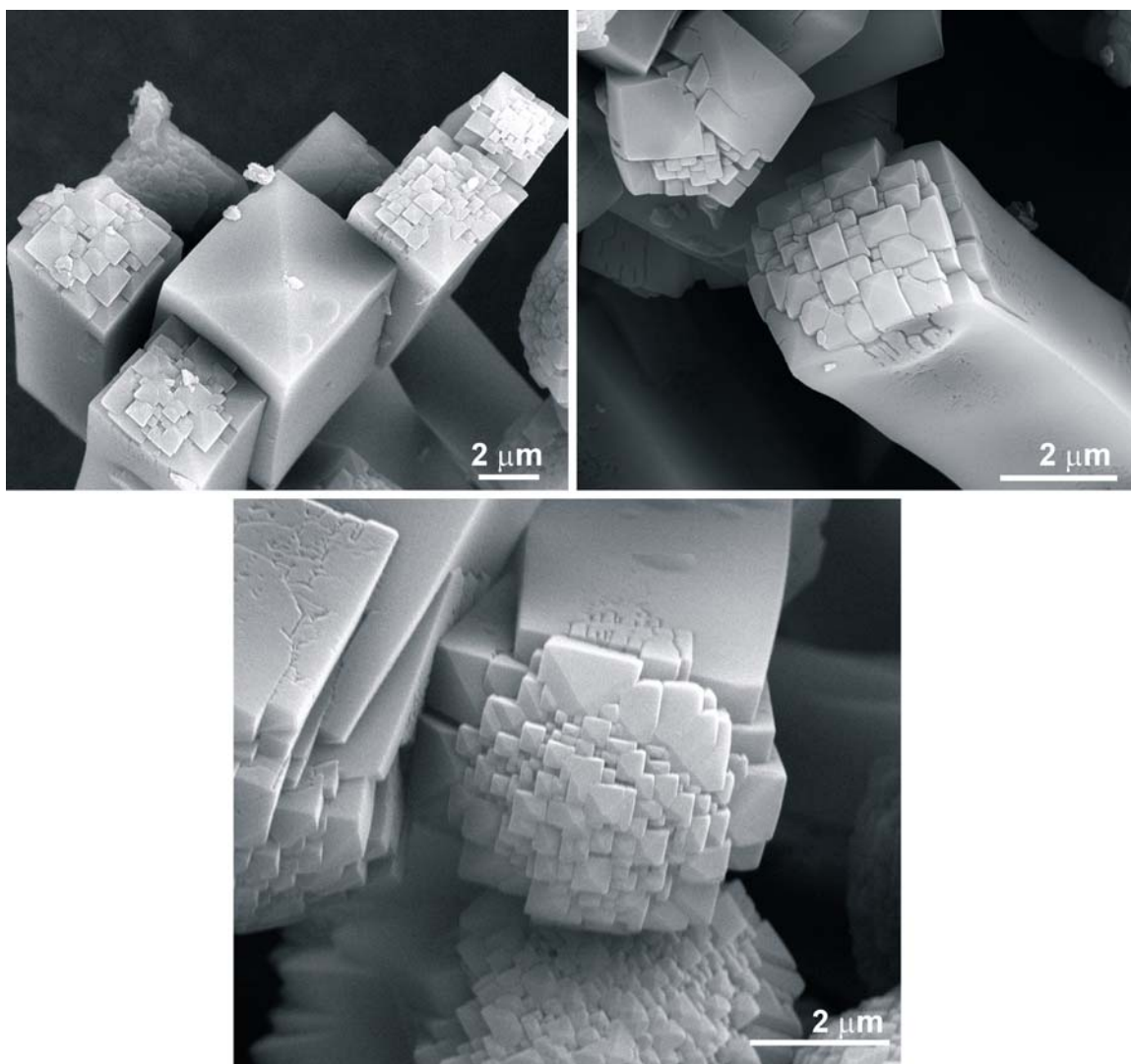


Fig. 3.3.45. SEM images of tetragonal prismatic seed crystals of COD with structuring on the pyramidal faces. These images support the fact that secondary nucleation events are more prominent on the pyramidal faces than on the prism faces.

So, the secondary nucleation of calcium oxalate starts from the cap of an elongated COD crystal. The growth components (Ca^{2+} and $\text{C}_2\text{O}_4^{2-}$ ions) from the bulk solution arrive at the rough interface (cap) of the main seed and are immediately attached/ incorporated. In such a situation the rate of crystal growth is controlled not only by surface phenomena, but by the diffusion of the growth components from the bulk solution to the crystal surface. Later, the outgrowth of calcium oxalate from the core surfaces takes place in such a way that the prism faces of the secondary COD crystals develop by utilizing the residual PAA. This suggests that the carboxylate group of PAA has a significant interaction on the primary as well as on the secondary crystal growth

processes [76,139]. The tetragonal prisms protruding from the main seed are larger than the crystallites constituting the core as the supersaturation is lowered. From the SEM images of broken dumbbells it becomes clear that the needle-like crystals are preferentially oriented along [001] (Fig. 3.3.36). And these needle-like aggregates are arranged layer by layer or in a brick by brick fashion which could be the result of decreasing supersaturation of the medium which in turn leads to ordering of the aggregates (Fig. 3.3.36 c).

When the dumbbells which are formed from high and low concentration of PAA are compared, it can be seen that the length of the bridge connecting the hemispheres increases which plainly suggests more probability of secondary nucleation events on the caps (Fig. 3.3.46).

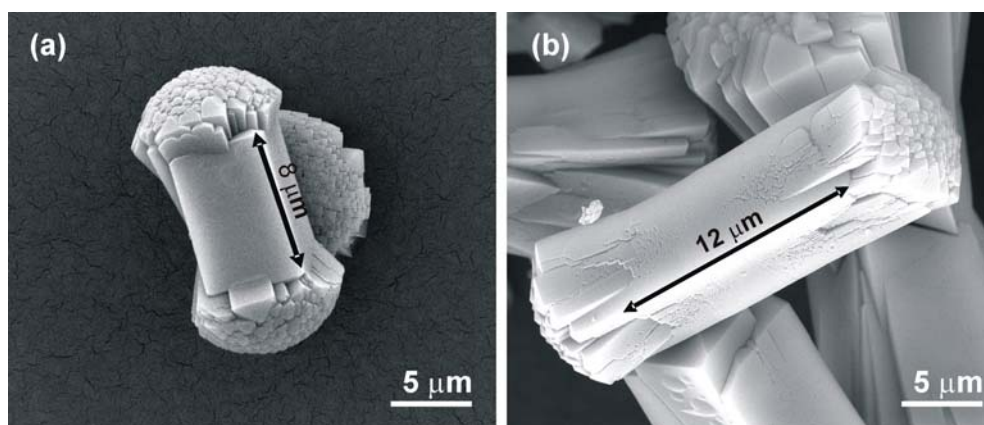


Fig. 3.3.46. SEM images of tetragonal prisms with structuring on the pyramidal faces obtained from 0.8 mM CaOx and: (a) 48 μg/mL PAA and (b) 168 μg/mL PAA.

The dumbbell shaped core could have been formed by the gradual outward bent orientation of the nanocrystallites on both the ends of the tetragonal prismatic seed by the growth of new crystallites in the space between the existing crystallites (Fig. 3.3.36 c). If no nucleation occurs on the caps of the seed, the crystallites will only attach to each other end by end resulting in rod-like or oval shaped particles [9,139]. Therefore, it becomes clear that such a bending orientation of the crystallites can be achieved only by the effect of PAA. The carboxylate group of PAA may be attached to the crystallites and the non adsorbing PAA chain might be playing the role of a spacer which is present between the growing crystallites pushing one another. This would cause the outward bending of the crystallites favouring the formation of dumbbell-shaped cores.

**Growth of calcium oxalate in the presence of 0.8 mM CaOx and > 200 µg/mL PAA:
Formation of rod-like tetragonal prisms**

At PAA concentrations greater than 200 µg/mL, rod-like tetragonal COD crystals with aspect ratios ranging from 8 to 10 are formed (Fig. 3.3.47 a). The tetragonal cross-section of these crystals appear relatively smooth than that of COD dumbbells (Fig. 3.3.47 b).

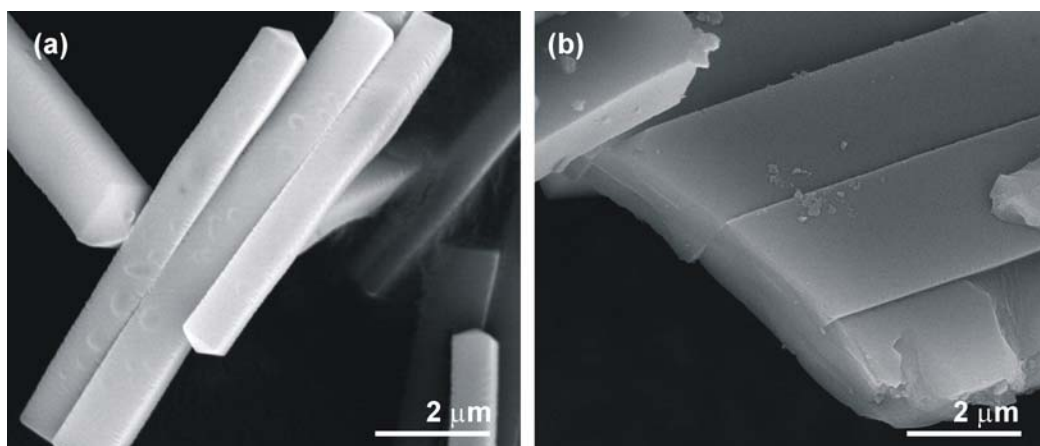


Fig. 3.3.47. (a) SEM image of rod-like tetragonal prismatic COD grown from 0.8 mM and 250 µg/mL PAA, (b) broken crystals indicating the tetragonal cross-section.

Under these conditions, the amount of incorporated organic material is found to decrease with increase in initial concentration of PAA (Table. 3.3.4). For example, the tetragonal prisms grown from solutions containing 0.8 mM CaOx and 200 µg/mL PAA contains *ca.* 1.2 wt.-% PAA while those grown from 0.8 mM CaOx and 230 µg/mL PAA contains *ca.* 0.6 wt.-% PAA. The yield of the samples obtained was also lowered with increase in concentrations of PAA. A high induction time reflects the fact that the inhibitory effects of PAA on calcium oxalate crystal growth becomes stronger under these conditions and the primary nucleation is much delayed (Fig. 3.3.19 a). This can be ascribed to the decrease in the number of nucleation events at high PAA concentrations due to the fact that most of the ions for nucleation and growth are blocked by PAA. Decrease in crystal nucleation is also evident from the decrease in the number of crystallites formed per litre (Table. 3.3.1).

The XRD patterns of these samples were matching well with that of the calculated pattern of COD (Fig. 3.3.8). The calculation of coherence length of the domains using Scherrer equation shows that the crystallite dimensions are larger than the case of COD dumbbells. Not only this but also, the length of the domain along the *c*-axis

(L_{c^*}) is slightly lower or almost equal to the crystallite thickness (L_{d^*}). This is confirmed by the fact that amount of incorporated PAA is lower in this case. If the crystallites were sufficiently coated with PAA, the coherence length along [001] would have been larger than that along [100].

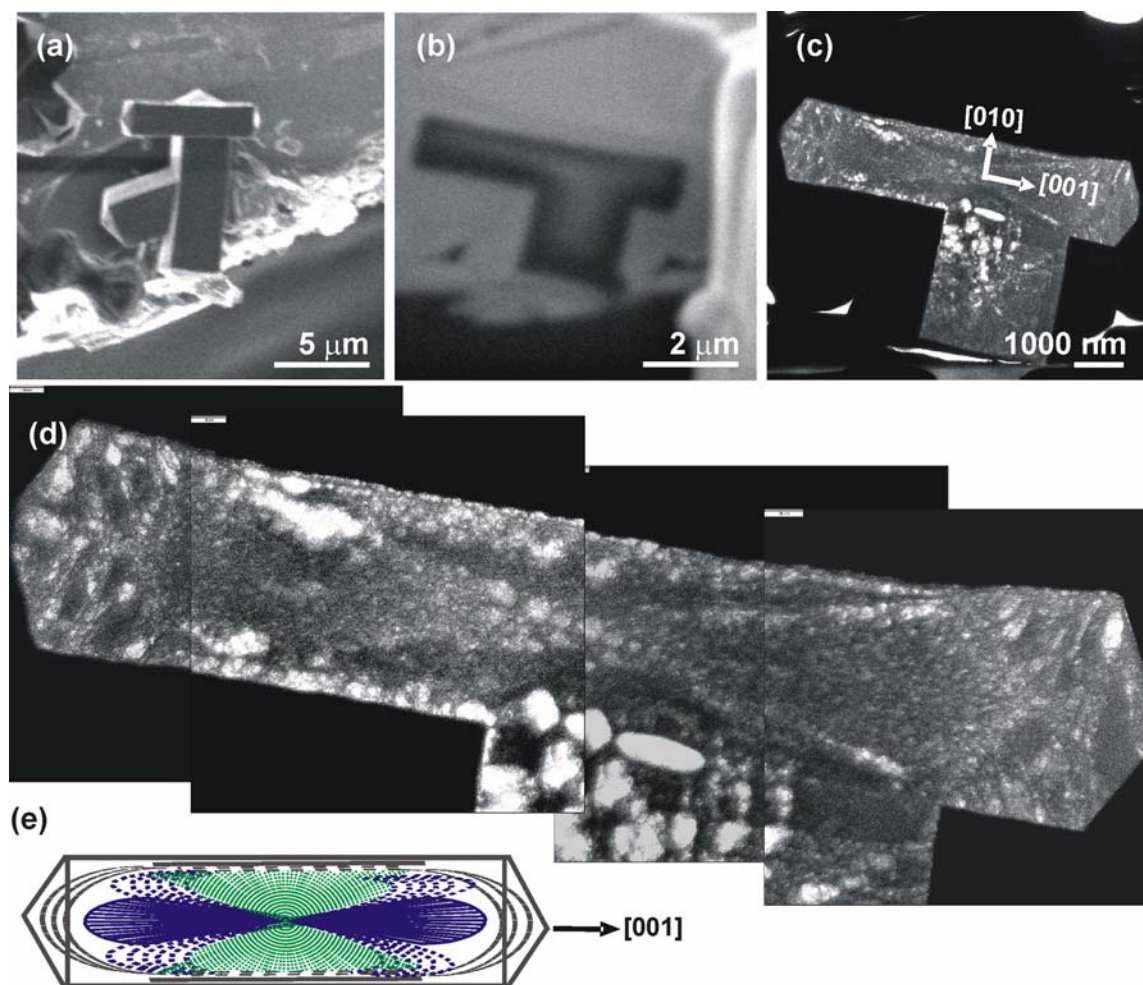


Fig. 3.3.48. Series of SEM (a), SIM (b), TEM (c,d) images of COD grown from 0.8mM CaOx and 200 µg/mL PAA, with the model sketch of the [100] cross-section (e). Blue lines indicate the arrangement of the crystallites from the centre towards the pyramidal faces and the green broken lines indicate the mosaic-like arrangement of the crystallites in the waist area extending towards the prisms faces.

TEM images of the (100) cross-section of the rod-like tetragonal prismatic COD crystals grown from 0.8 mM CaOx and 200 µg/mL PAA indicate a complex inner pattern/architecture (Fig. 3.3.48). However, in this case also, the arrangement of needle-like crystallites diverging from the exact centre and symmetrically extending towards the pyramidal faces is observed. They have an ultimate two cones joined at the base-like

arrangement. This patterning becomes clearer in the case of aggregates grown at higher concentration of 225 $\mu\text{g/mL}$ PAA (Fig. 3.3.49).

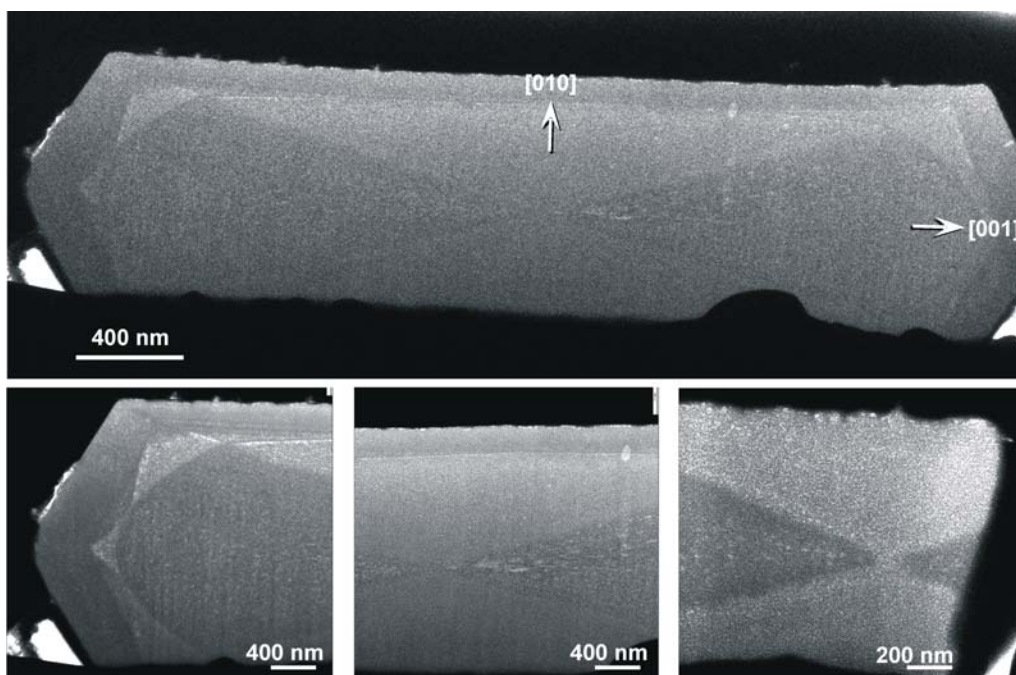


Fig. 3.3.49. TEM images of rod-like tetragonal prismatic COD grown from 0.8mM CaOx and 225 $\mu\text{g/mL}$ PAA along (100) cross-section (top). (Bottom-left) enlarged image from the cap. (Bottom middle and right) magnified images from the centre.

It is generally stated that the behaviour of PAA in water depends on the concentration or ionic strength, concentration of added salt and the degree of neutralization [147-152]. When PAA is dissolved in water the carboxylic groups are fully ionized. In general, at low ionic strength it exists as random coils in water and at high ionic strength, the coil is expanded due to repulsion and it exists as rigid rods parallel to each. However, when the chains are highly extended by electrostatic interactions they are generally regarded as worm-like chains [151]. This conformation is a plausible intermediate between the flexible random coil and fully extended rod. But under the conditions discussed here, the behaviour of PAA chain cannot be predicted without further experiments. Hence, for the time being it is reasonable to assume that a delayed nucleation results in the formation of such elongated COD crystals. Although the concentration of PAA is higher, dumbbells are not formed further due to the lack of active calcium and oxalate ions in comparison to PAA in solution.

3.3.3 Summary

The inner architecture of all the morphological variations of COD grown in the presence of increasing concentration of PAA appears similar. They are characterized by a core, a waist area and a shell. The dumbbell-like (or two cones joined at the base-like) arrangement of crystallites constituting the core is common in all the COD crystals (indicated with blue lines in figure 3.3.50). The core made up of thin elongated calcium oxalate crystallites has incorporated PAA and a crown/shell region is formed as part of secondary nucleation processes after the decrease of initial supersaturation. In all the cases, the crystallites forming the outer region are found to be different in size and crystallinity than those forming the core. Hence, the assumption is that those crystallites forming the outer layer have relatively less amount of PAA.

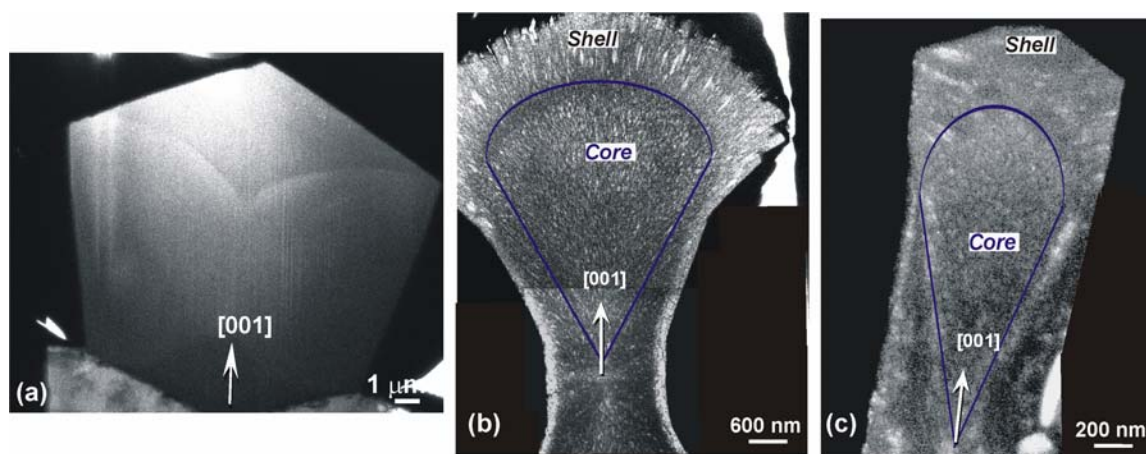


Fig. 3.3.50. TEM images (100) cross-sections of COD crystals grown from 0.8 mM CaOx and (a) 7, (b) 96 and (c) 200 $\mu\text{g/mL}$ PAA with half of the core region outlined with blue lines. All the COD crystals have the typical core/shell architecture.

Therefore the morphogenesis of these aggregates generally described by the mechanisms of nucleation, growth and aggregation should also be similar as shown schematically in figure 3.3.51. The major difference in morphology arises from the arrangement of the nanocrystallites constituting the core which in turn depends on the relative proportion of PAA and CaOx concentrations. The core acts as a template for the next steps of growth which corresponds to the self-organization and alignment, generating a final COD particle having a poorly crystalline core and a polycrystalline shell. Our assumptions could not be confirmed due to the rapid decomposition of these samples by electron beam irradiation. However, there is a good correlation between the amount of PAA incorporated and the elongation of the nanocrystallites along the *c*-axis.

Therefore, it can be considered that PAA directs the crystal growth in all these aggregates which may be considered as a special case of classical crystallization.

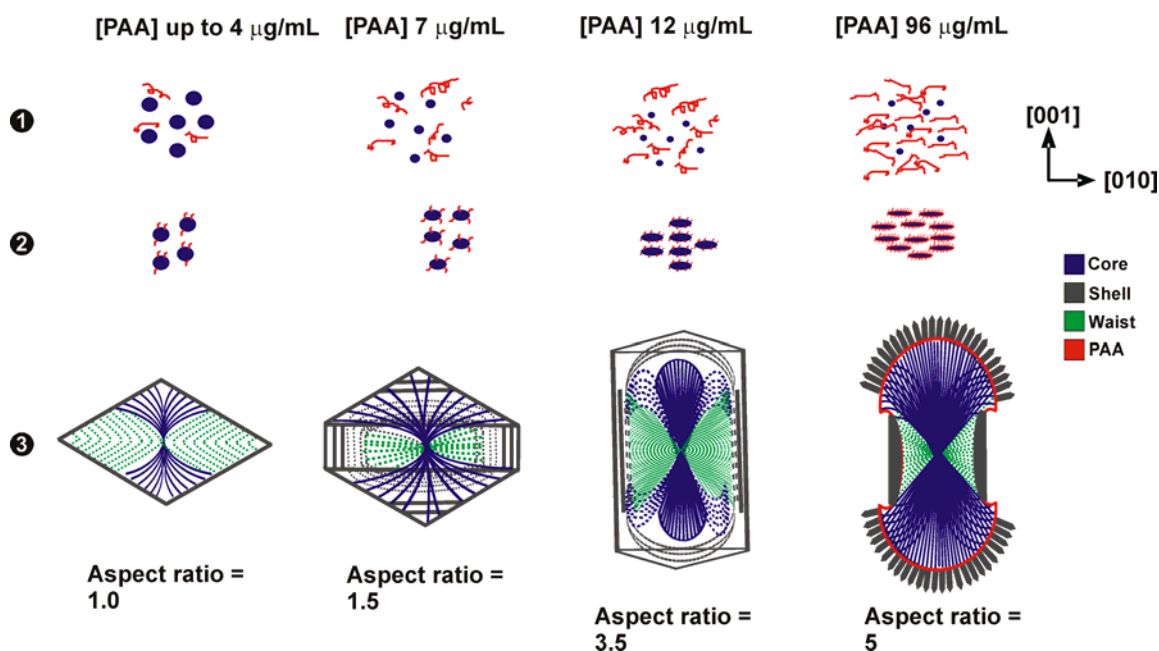


Fig. 3.3.51. Schematic illustration of the influence of PAA on the morphology of COD crystals. The crystallites constituting the core are depicted with blue lines diverging from the centre of the crystal. These blue lines should be considered as PAA (red) coated calcium oxalate crystallites (blue) as shown in step 2. The green dots are crystallites with less or without coated PAA which forms the waist area. The ash coloured framework of bigger crystallites is formed at a later stage or formed as part of secondary nucleation processes.

3.4 Biomimetic approach towards Calcilogenesis: The double diffusion technique

3.4.1 Morphological aspects of calcium oxalates grown in agar gel

3.4.1.1 The effect of concentration of agar

For the double diffusion experiments, agar gels were used at different concentrations and different pH values. First, the results obtained in agar gels of different concentrations (at same pH) are compared.

Synthesis: The stock solutions (0.05 M of both $\text{CaCl}_2 \cdot 2\text{H}_2\text{O}$ and $\text{Na}_2\text{C}_2\text{O}_4$) pre-adjusted to the physiological pH of 7.4 with tris (hydroxymethyl) methylamine/ HCl were allowed to diffuse into agar gel from opposite sides.

Agar gels with concentrations ranging from 0.5 to 4 wt.-% were used. The required amount of agar was added slowly to water at 90 °C and stirred until a clear solution was formed. After cooling to room temperature, a white coloured gel was formed with a pH of 5. The entire set-up was kept in a water bath at 37 °C. After a period of 5 days, the white coloured aggregates formed inside the gel were separated and washed five times in hot distilled water, centrifuged and finally dried at 40 °C.

The aggregates were formed in a single band in the middle of the gel. With increase in concentration of the gel, the aggregates were formed more towards the oxalate reservoir. The pH of the stock solutions before and after the double diffusion and yield of the products obtained are documented in appendix table 6.4. The yield of the products obtained was found to decrease with increase in concentration of the gel due to the decreased diffusion of the ions through highly concentrated gels.

The morphology of the aggregates grown in agar gels of varying concentrations is shown in figure 3.4.1.

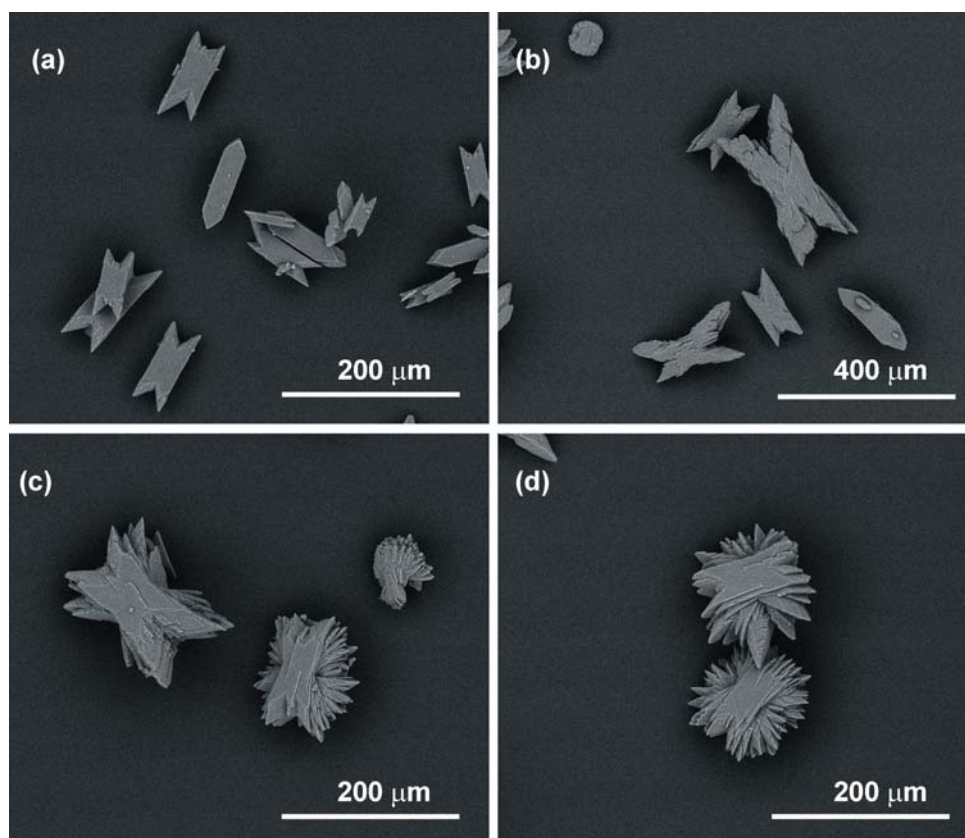


Fig. 3.4.1. SEM images of COM aggregates grown from (a) 0.5 wt.-%, (b) 1 wt.-%, (c) 2 wt.-% and (d) 4 wt.-% agar gels at pH 5. The aggregation of crystallites increases with increase in concentration of agar gel.

All these aggregates belong to COM as indicated from the powder X-ray diffraction pattern (Fig. 3.4.2). Only the XRD pattern of the aggregates grown from 0.5 wt.-% and 4 wt.-% agar gels are shown for the sake of simplicity. The XRD analysis of these aggregates shows four main XRD diffraction peaks located at 0.59308, 0.36456, 0.29654, and 0.23480 nm, corresponding to the (-101), (020), (-202) and (-4-11) planes of COM according to the structure proposed by Deganello and Piro [23-25]. The XRD pattern fits more closely to the HT modification of COM [25]. There was no trace of COD or COT in these aggregates.

With increase in concentration of the gel, the aggregation of smaller crystallites was found to increase. For example, COM grown from 0.5 wt.-% agar gels (Fig. 3.4.1 a) were mainly twinned crystals of COM (size ranging from 50 to 100 μm). As the concentration of agar gel was increased to 4 wt.-% rosette-type COM crystals were formed with many smaller crystallites attached on the (-101) faces a COM twinned crystal (Fig. 3.4.3, for face indexing refer to Fig. 1.5).

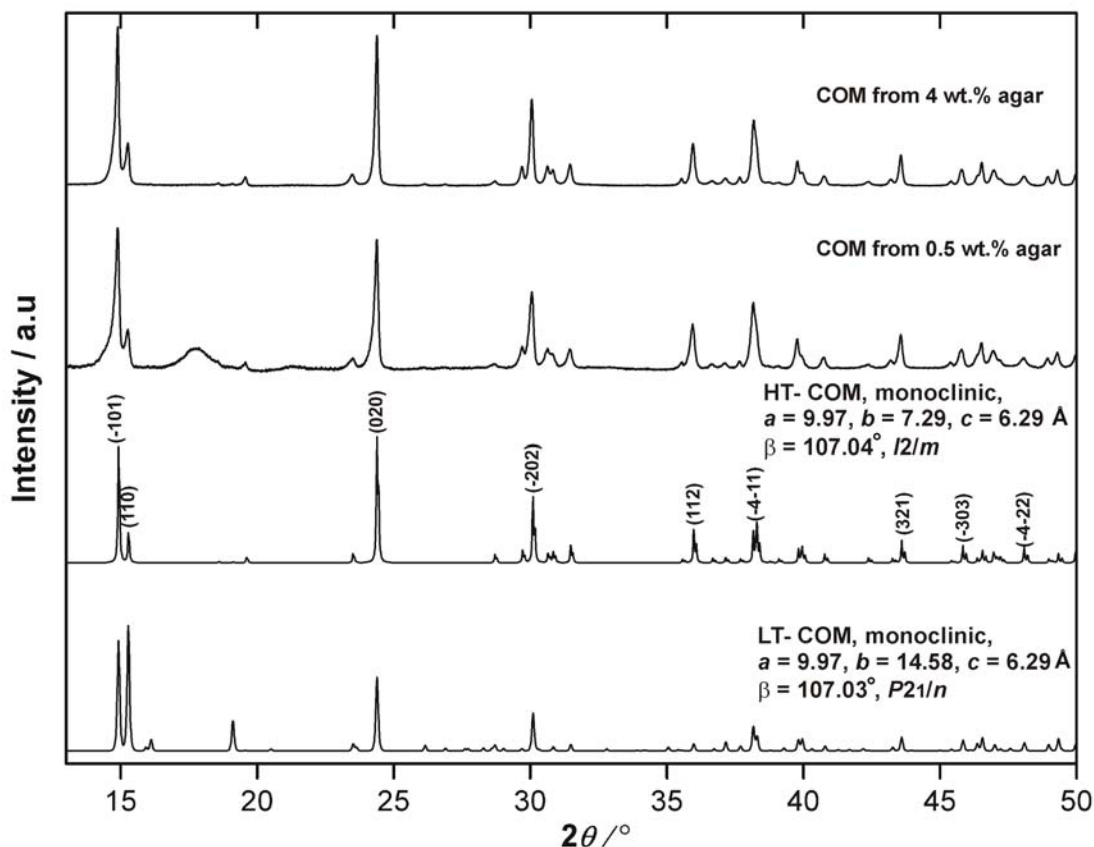


Fig. 3.4.2. Comparison of the XRD pattern of COM (grown from 0.5 wt.-% and 4 wt.-% agar gels at pH 5) with the crystal structure of the low temperature and the high temperature modifications of COM proposed by Deganello and Piro [23-25]. The experimental patterns are measured using $\text{Cu } K\alpha_1$ -radiation.

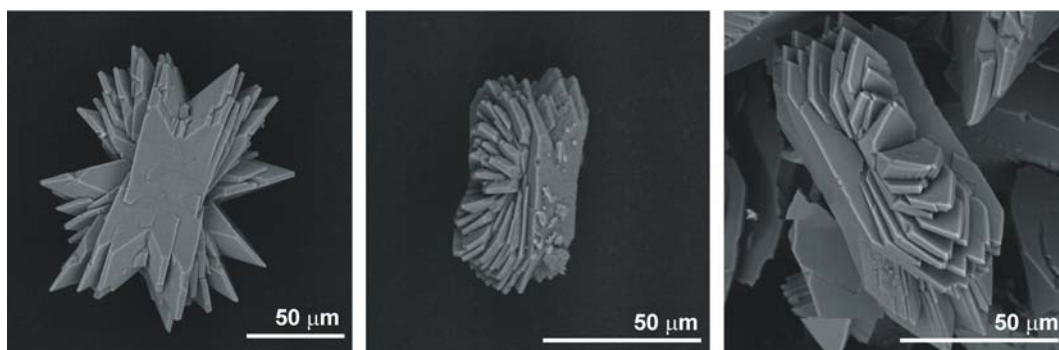


Fig. 3.4.3. SEM images of rosette-like COM aggregates formed in 2 wt.-% agar gel of pH 5. Note the formation of new crystals on the (-101) face of the original crystal.

Such crystals of COM with rosette morphology have been reported previously [89,93] and are classified as crystals with split tips characteristic of growth poisoning [67, Section 1.2.5]. The splitting of whewellite along (-101) is common in nature. The rosette-type crystals are assumed to have formed by the nucleation of new crystals on the (-101) faces of an original COM crystal. The new crystals reach similar size by subsequent

regular crystal growth. Therefore, from these observations, it is evident that agar promotes the nucleation of new crystals on the crystal faces of COM crystals.

The morphology of these crystals appears much similar to the “druse” crystals formed in plants with many facets radiating from a central core [19,153]. Whewellite druses are sharp enough to lacerate the mouths of marauding insects and often classified by their acute tips and general star-like shape (Fig. 1.12 a).

3.4.1.2 The effect of pH

Double diffusion experiments were performed in 2 wt.-% agar gel at different pH values. The hydration state and the morphology of calcium oxalates formed were found to change with the pH value of the gel.

3.4.1.3 Agar gel of pH 8.5

Preparation of 2 wt.-% agar gel of pH > 8.0: The required amount of agar (2 wt.-%) was added to water at 95 °C. After the solution became clear, 2N NaOH was added while stirring to obtain the desired pH. Further heating resulted in change of the colour of the solution from clear to yellow to brown (Fig. 3.4.4 I). After cooling down to room temperature a brown coloured gel was formed. It is assumed that the hydrolysis of agar using NaOH at elevated temperatures causes the brown coloration.

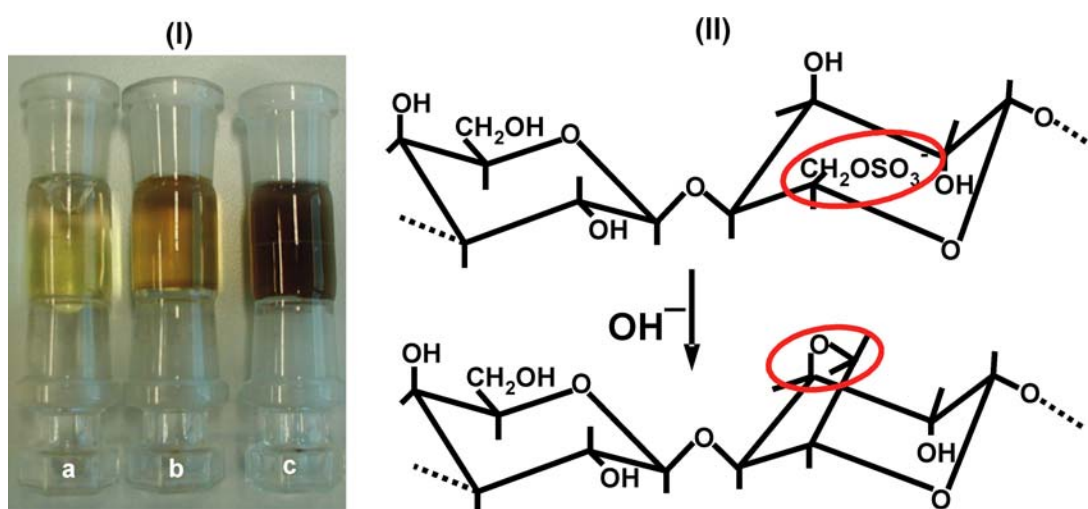


Fig. 3.4.4. (I) Colour change of 2 wt.-% agar gel (pH 8.5) with increased heating time: (a) Immediately after adding NaOH (at 95 °C), (b) after 10 minutes (at 95 °C), (c) after cooling to room temperature. (II) Transformation of the precursor of agarose to agarose. Alkali treatment can eliminate the sulphate group at C-6, and form 3,6-anhydro rings resulting in enhanced gel strength due to increased capability of forming double helices [95].

As already stated (Section 1.3.2) agar is generally considered to be a mixture of agarose and agarpectin. Idealized agarose is a polymer with alternating 3-linked β -D-galactosyl residues and 4-linked α -3,6-anhydro-L-galactosyl residues, and gelation is generally assumed to arise by the formation of double helices between agarobiose units [95]. Agar generally contains a number of agarose precursor units, where the 4-linked residues contain L-galactose 6-sulphate. These 6-sulphate residues cannot form double helices, and hence when these units arise in agar, it is generally assumed that helix formation is limited. Accordingly, the resultant gel is a large interwoven network. If there are too many L-galactose-6-sulphate units, the amount of double helix structure is small, and the gel strength weakens. The L-galactose-6-sulphate units can be converted to anhydro galactosyl units by treatment with alkali. Closure of the ring to form the 3,6-anhydrode, and elimination of the C-6 sulphate group makes the chain straightened and leads to great regularity in the polymer, resulting in enhanced gel strength due to increased capability of forming double helices (Fig. 3.4.4 II). Alkali treatment of agar, or agar bearing seaweeds, is commonly practiced in order to decrease the amount of sulphate and thus improve the gel strength [154].

Idea for the use of hydrolyzed agar: The formation of urinary stones in living systems is (also) caused by high urinary pH and diabetes. Agar gel is stable at higher pH values whereas agarose, gelatine and carrageenan are not. It has been reported that refined carbohydrates can influence urinary electrolyte excretion in such a way that there may be an increased risk of over-saturation with calcium oxalate [155]. Both, proteins and carbohydrates are known to alter urinary electrolyte excretion, particularly the rate of calcium excretion [156,157]. Alkaline treatment of agar produces agarose in fairly good amounts. The study of the influence of agar is important because carbohydrates are more rapidly assimilable and therefore more likely to show a demonstrable effect on renal excretion. The biomimetic crystallization of calcium oxalate was studied at 37 °C in order to get deeper insight into the effects of this “green” polysaccharide on the calcium oxalate crystallization. A series of experiments were carried out to investigate the influence of the Ca:Ox molar ratio on the crystallization in agar gel. Faster growth was observed in the presence of excess oxalate.

2 wt.-% agar gel of pH 8.5 (Ca:Ox=1:3): Since faster growth rates were observed for higher concentrations of oxalate ions, the stock solutions used to diffuse through 2 wt.-% agar gel at pH 8.5 were 0.033 M $\text{CaCl}_2 \cdot 2\text{H}_2\text{O}$ (pH = 12) and 0.1 M $\text{Na}_2\text{C}_2\text{O}_4$ (pH = 8). The

pH values of the stock solutions were held at a high level in order to maintain the overall supersaturation high and subsequently to get phase pure solids.

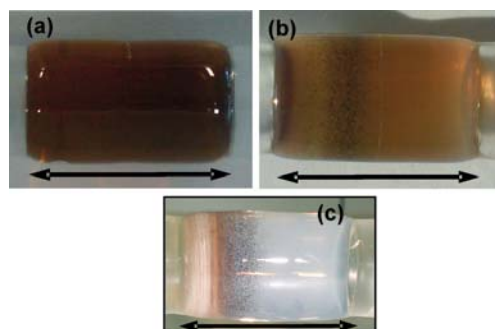


Fig. 3.4.5. 2 wt.-% agar gel at pH 8.5: (a) before the diffusion of the stock solutions and after the double diffusion reaction: (b) 1 day (c) 3 days. (Scale bar corresponds to 30 mm).

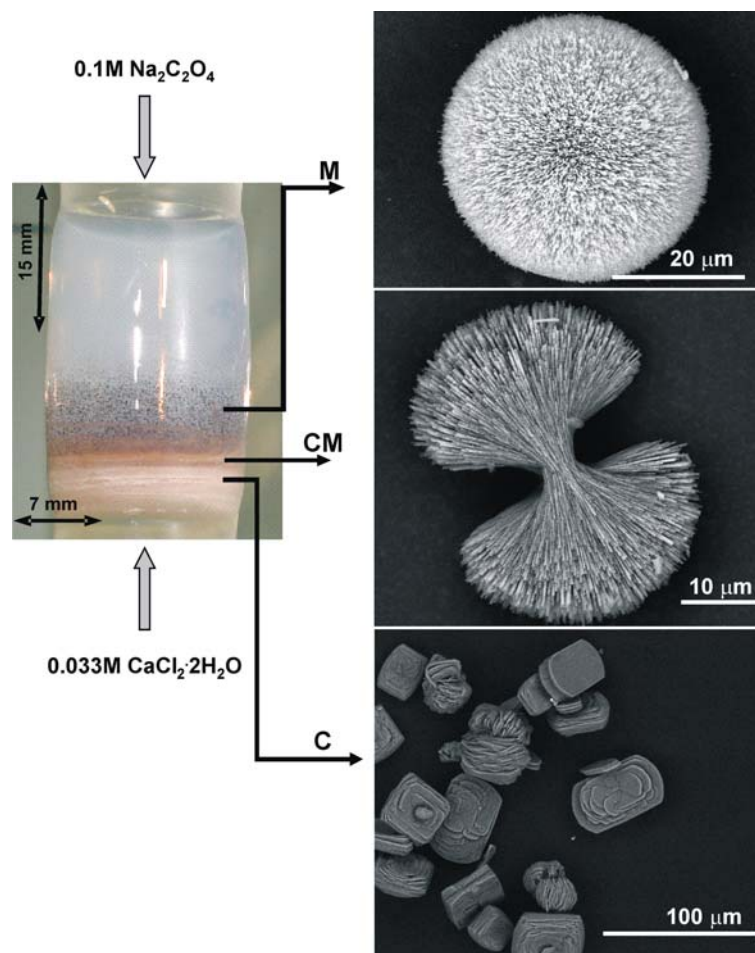


Fig. 3.4.6. Band assignments and SEM images of COM aggregates formed by double diffusion in 2 wt.-% agar gel at pH 8.5 after 3 days.

Three (Liesegang) bands were observed at 37 °C over a period of 3 days. The band assignments in terms of distance from the calcium source for all the experiments in the present study are shown in appendix figure 6.11. In the present study, a scattered M

(middle) band formed first (Fig. 3.4.5 b) consisted of COM spheres (major) and COD dendrites (minor). The CM band formed adjacent to the middle band, but towards the Ca reservoir, consisted of mainly COM dumbbells and the C band (near to the Ca side) consisted of COM ovals and twins (Fig. 3.4.5 c, 3.4.6). The band assignments and the overall morphology of the aggregates formed are shown in figure 3.4.6. The order of appearance of these bands in the present study is such that, M bands are formed first, which is followed by CM bands and the last to form, are the C bands.

Factors promoting the fraction of COD in agar gel

Influence of the pH value of 2 wt.-% agar gel on the formation of COD: A minor fraction of COD was formed along with COM in hydrolyzed agar gels. Since agar is a natural product, single phase products of calcium oxalates were not usually observed.

In order to estimate the factors promoting the formation of COD, equal volumes of 0.05 M calcium and oxalate solutions adjusted to a pH of 8 with tris buffer was allowed to diffuse through 2 wt.-% agar gel of increasing pH value (Fig. 3.4.7). The reactions were allowed to proceed at 37 °C for 3 days. The aggregates in the M and O bands were isolated and analyzed by XRD.

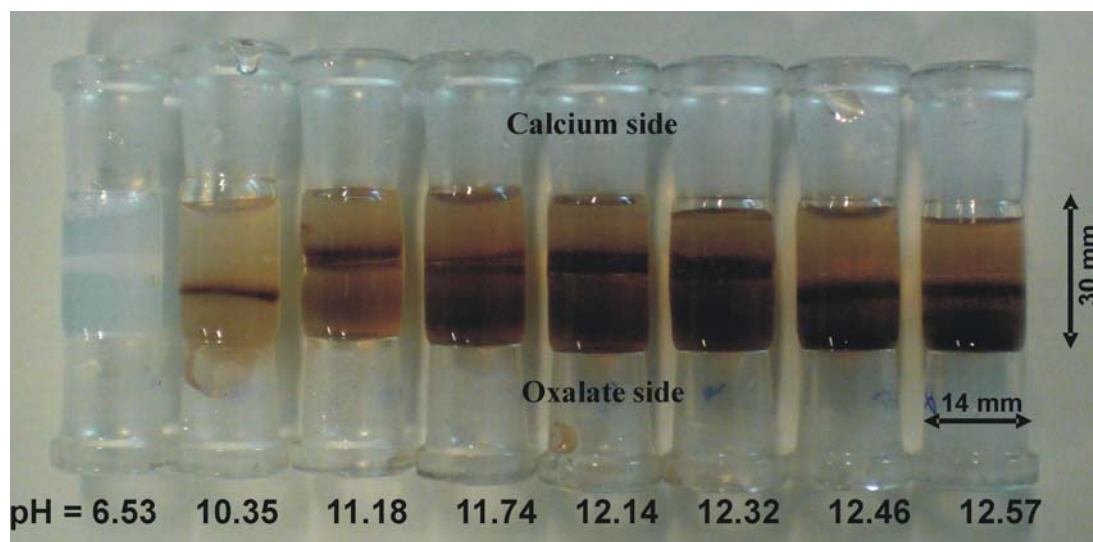


Fig. 3.4.7. Photograph of 2 wt.-% agar gels with increasing initial pH values (indicated at the bottom of each gel) after the double diffusion reaction at 37 °C for 3 days.

The XRD patterns confirmed the increase in occurrence of COD (marked with * in Fig. 3.4.8) in the M band with increasing pH of the 2 wt.-% agar gel. A dramatic increase

in the intensity of the (100) peak of COD ($2\theta = 14.31^\circ$) was observed with increasing pH value of the gel.

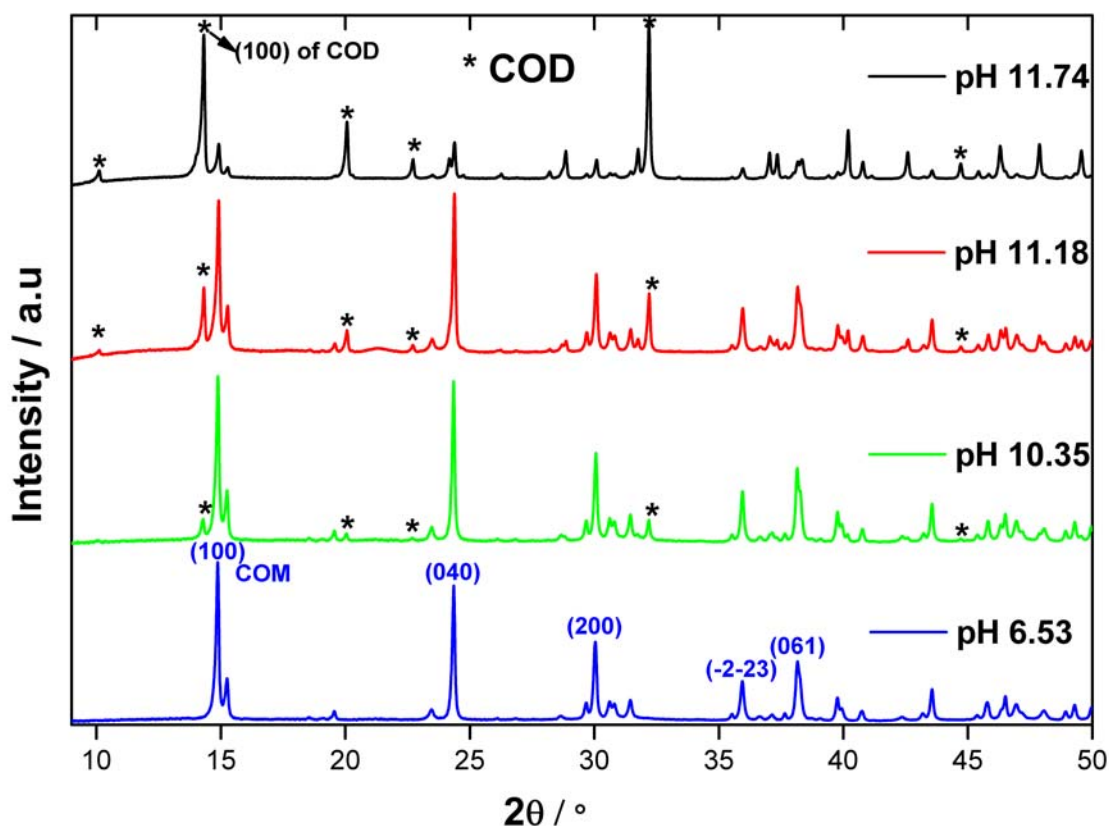


Fig. 3.4.8. XRD patterns (measured using $\text{Cu } K\alpha_1$ - radiation) of calcium oxalate aggregates obtained from the M band of 2 wt.-% agar gel with different pH values. Reflections from COD are marked with *. (Indexing with blue colour in the bottom corresponds to COM).

The phase composition of the calcium oxalates formed was estimated from the intensity ratio of the major X-ray diffraction lines of COM (I_{COM}), COD (I_{COD}) and COT (I_{COT}) respectively, as shown in eq. (3.4.1) [158].

$$(3.4.1) \text{ Estimated \% COD} = I_{\text{COD}} / (I_{\text{COM}} + I_{\text{COD}} + I_{\text{COT}})$$

Accordingly, the fraction of COD in the M band is calculated from the major XRD peak intensities and plotted in figure 3.4.9. The COD aggregates formed in the M band support the fact that a higher concentration of any of the reactants favours the formation of COD [119,159]. After a certain level of high pH (around 11.7), the fraction of COD in the M band decreases and more COD is formed in the O band (just adjacent to the M band but towards oxalate reservoir). It is assumed that COD is kinetically favoured when the supersaturation is higher. The fraction of COD formed in the O band could not be checked

for all the gels because of difficulty in separating the M and O bands formed in gels of pH less than 11. Other factors which have been found to promote the fraction of COD during the experiments are the increase of the pH value in the sodium oxalate stock solution.

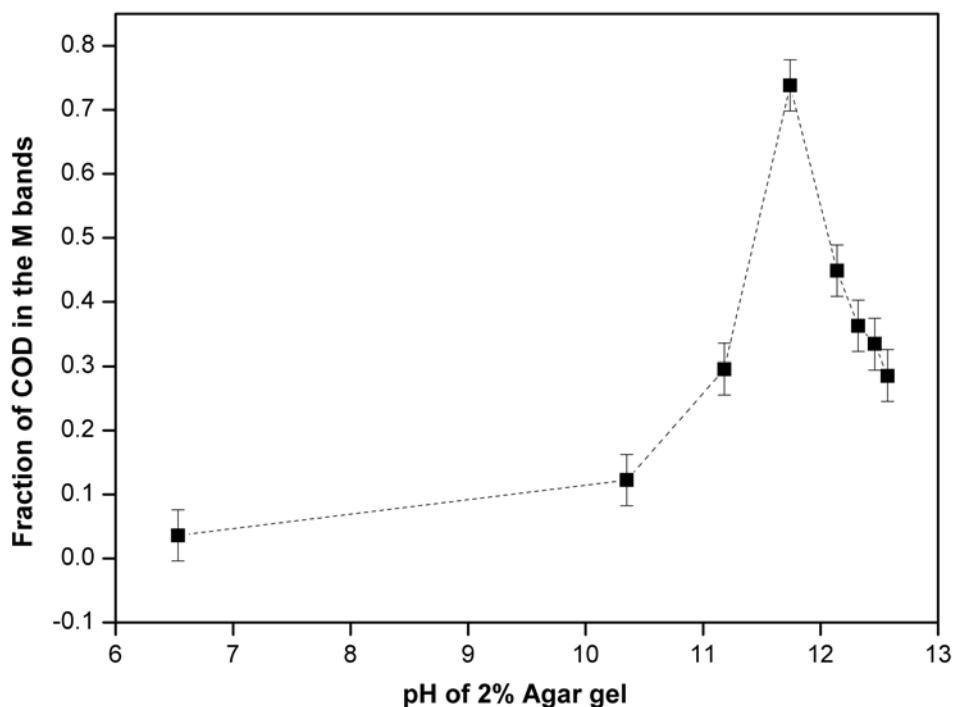


Fig. 3.4.9. Plot of the fraction of COD in the M bands as a function of the initial pH value of the 2 wt.-% agar gel.

Factors promoting the fraction of COD in mixed gels of agar and gelatine:

2 wt.-% Agar + (0.1-5) wt.-% Gelatine of pH 8.5: Equal volumes of 0.05 M of stock solutions adjusted with tris buffer to a pH of 8 were allowed to diffuse through the mixed gels consisting of 2 wt.-% agar + (0.1-5) wt.-% gelatine of identical pH value (8.5). The reaction was allowed to proceed at 37 °C for 3 days. The aggregates in the M and O bands were isolated and analyzed by XRD. Three very close Liesegang bands were formed up to 0.5 wt.-% gelatine, which reduced to two bands for 1 wt.-% and 2 wt.-% gelatine. 2.5 to 5 wt.-% gelatine produced only one band (Fig. 3.4.10). The fraction of COD formed during these experiments were at maximum for 1.5 wt.-% gelatine and further increase in the gelatine content resulted in a decrease in the fraction of COD (Fig. 3.4.11). For 5 wt.-% gelatine, COM was predominantly formed which indicates that the presence of polysaccharides is required for the inhibition of COM.

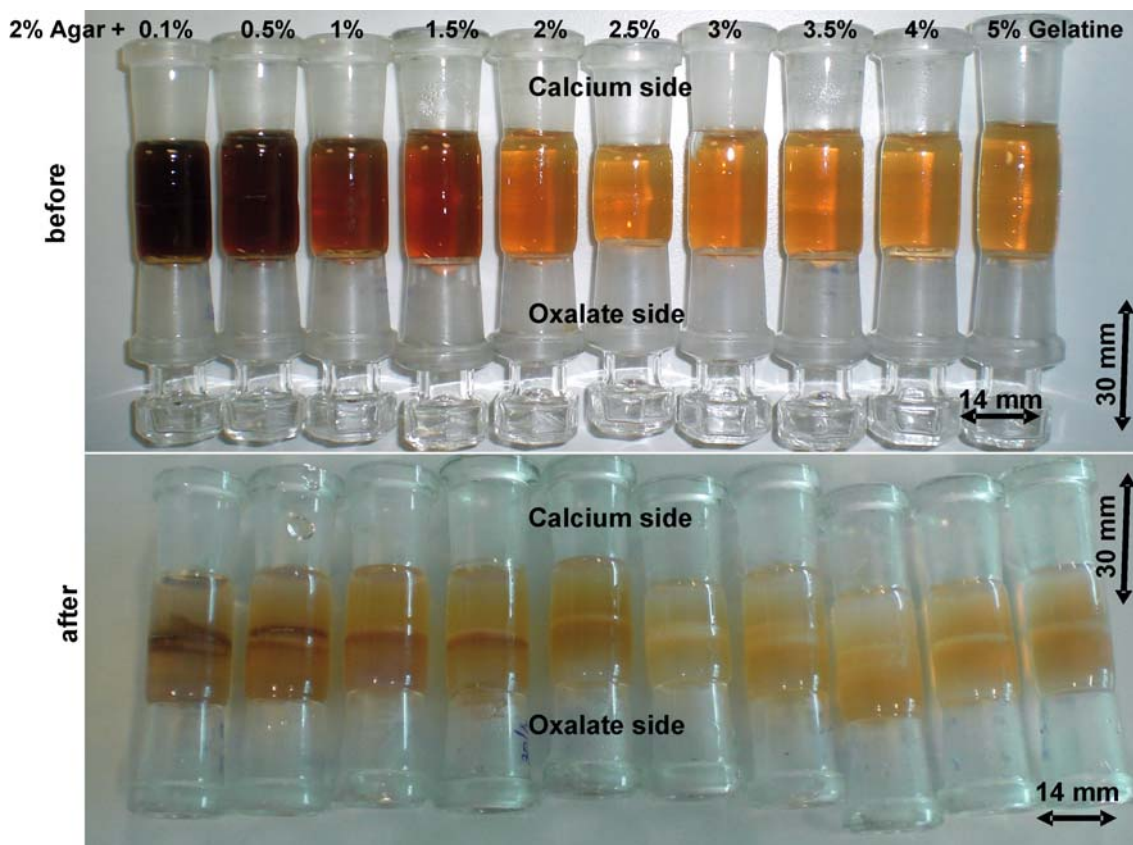


Fig. 3.4.10. Photographs of agar-gelatine gels before and after the double diffusion reactions.

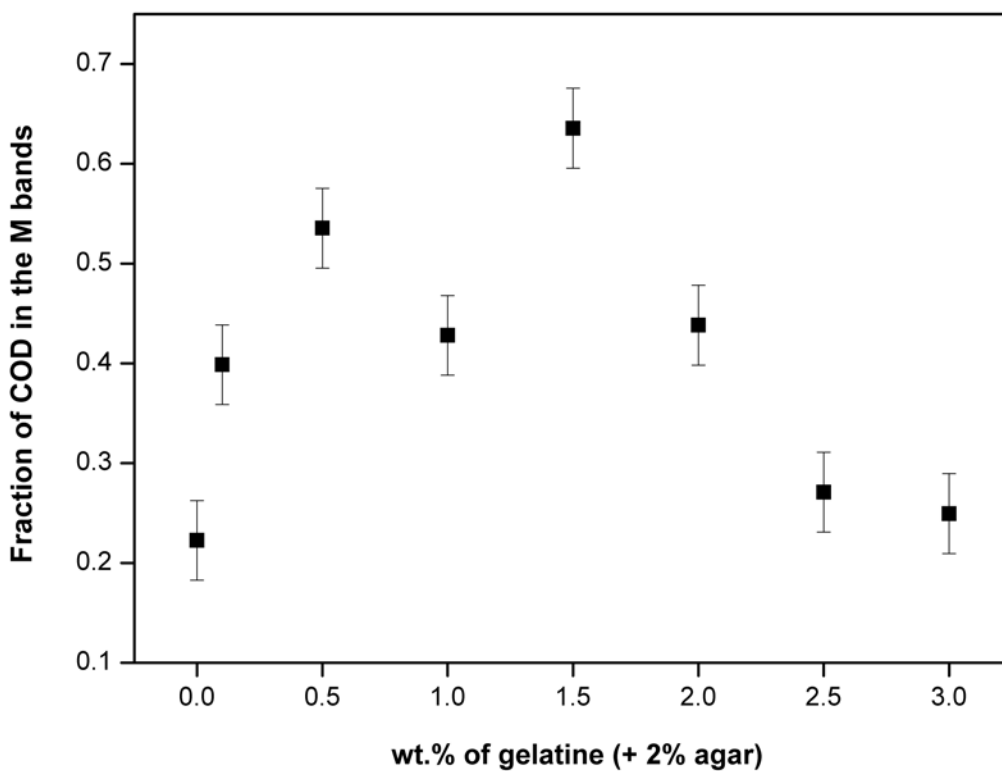


Fig. 3.4.11. Fraction of COD formed in the M bands of mixed agar-gelatine gels. All gels had an initial pH of 8.5.

Morphological aspects of COM aggregates formed in 2 wt.-% agar gel of pH 8.5 (Ca:Ox = 1:3)

Aggregates formed in the CM band: COM dumbbells

The morphology of the COM aggregates formed in the CM bands is shown in figure 3.4.12 (Appendix Fig. 6.12). These aggregates consist of nearly rectangular plate-like crystallites which are piled up, one over the other resulting in an overall dumbbell or sheaf of wheat morphology (size 60 to 80 μm).

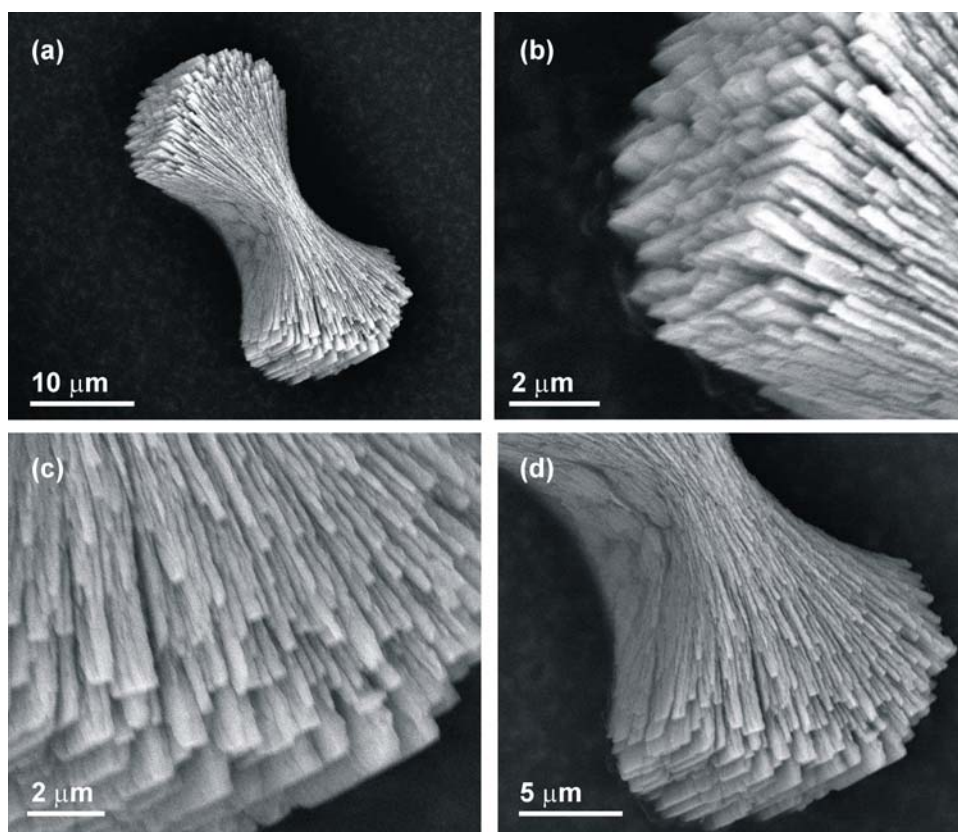


Fig. 3.4.12. (a) SEM images of a COM aggregate with dumbbell/sheaf of wheat morphology formed in the CM band of 2 wt.-% agar gel of pH 8.5. (b,c,d) Magnified images from the same aggregate.

It is interesting to note that the morphology of a single COM crystal constituting the dumbbell is changed from the normal “six-sided” platy morphology of COM (Fig. 1.5) to “rectangular” COM with serrated edges and surface pittings (Fig. 3.4.13). Normally, the COM crystals grown from high ionic strength solutions reflect their monoclinic symmetry and are comprised of three face types, (-101) , (010) and (-120) . The individual rectangular plate-like crystals grown in the presence of agar appear to have well-developed (-101) faces but the apical planes ($\{120\}$ faces) are almost missing.

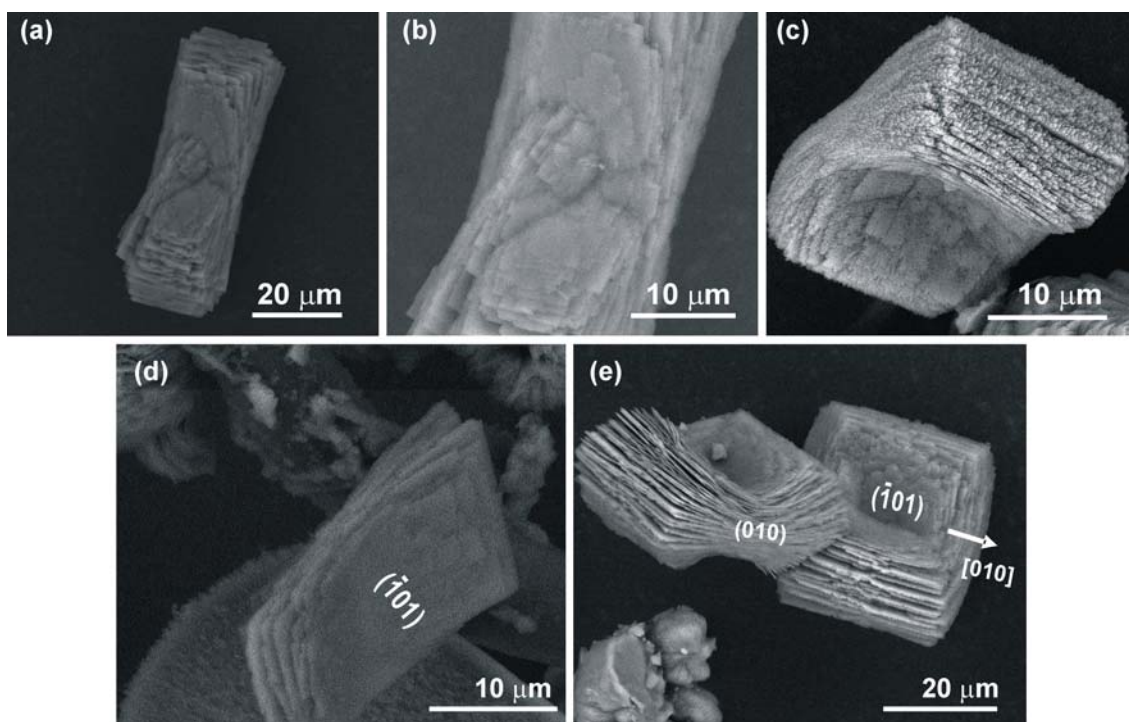


Fig. 3.4.13. SEM images of less aggregated COM stacks obtained from the CM band of 2 wt.-% agar gel of pH 8.5. Note the piling of rectangular platy crystallites.

These images already give the impression that the two dimensional (2D) aggregation of crystallites resulting in dumbbells occur by the stacking of rectangular plate-like crystallites on the (-101) faces of a central COM crystal. When viewed along [010], these aggregates exhibit the sheaf of wheat morphologies.

In order to investigate the crystallographic orientation of the COM plates, a single plate was detached mechanically and was analyzed by TEM. The electron diffraction pattern (ED) taken from the plate oriented approximately along the [100] zone axis corresponds to monoclinic COM with lattice parameters, $a = 10 \text{ \AA}$, $b = 7.3 \text{ \AA}$, $c = 6.3 \text{ \AA}$, $\beta = 107^\circ$ with space group $I2/m$ which corresponds to the high temperature (basic) phase of COM. (Fig. 3.4.14). Accordingly, these plates are (-101) dominant plates which are probably elongated along the a - axis. This means that agar promotes the preferential development of (-101) faces.

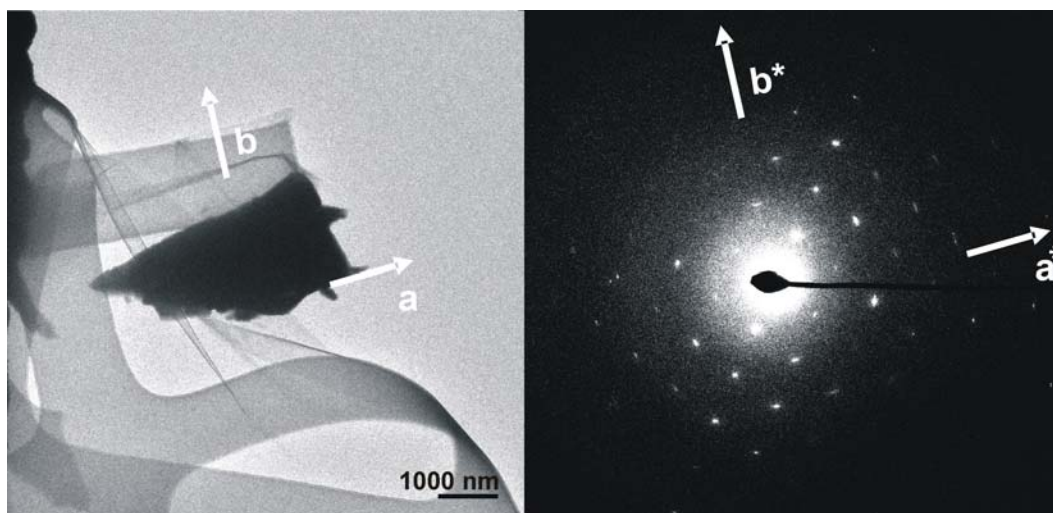


Fig. 3.4.14. (Left) Fragment of a single plate detached from a COM dumbbell and (right) the corresponding electron diffraction pattern from an approximate [100] zone axis. These plates corresponds to HT-COM with monoclinic, $a \sim 10\text{\AA}$, $b \sim 7\text{\AA}$, $c \sim 6\text{\AA}$, $\beta \sim 107^\circ$ and space group $I2/m$.

Similar to agar, GAGs (glycosaminoglycans) and several dicarboxylates (malonate, malate, and maleate) have been reported to change the morphology of COM from a six-sided plate to a rectangular plate [111,112]. Likewise, COM grown in the presence of nephrocalcin has been reported to undergo a phase change to high temperature (basic) form with increase in concentration of nephrocalcin [161]. The general explanation for such a morphological change is that the macromolecule shields the (-101) plane by adsorption, thus inhibiting crystal growth in a direction perpendicular to that face. As a result the (-101) face shows increased surface area by growing along [010] (Fig. 3.4.15). It has been proved by measuring the adhesion forces at the crystal faces of COM or COD with carboxylate modified AFM tips that the (-101) faces of COM and the (100) faces of COD exhibit maximum adhesion forces [59,109,162-165]. COM with their extended (-101) faces adhere strongly to biological macromolecules and cell membranes surfaces [166-168].

Therefore, it is worth to assume that hydrolyzed agar strongly interacts with the (-101) faces of COM and blocks its growth perpendicular along [-101] and simultaneously stabilizes this face. As a result the (-101) face increases in surface area by its preferential growth along [010] (Fig. 3.4.15). It has been confirmed that the {120} faces of COM are the fastest growing and the {-101} faces are the slowest [160]. The absence of apical planes for the rectangular platy crystals grown in the presence of agar may be due to the increased supersaturation in the gel which enhances the crystal growth rate.

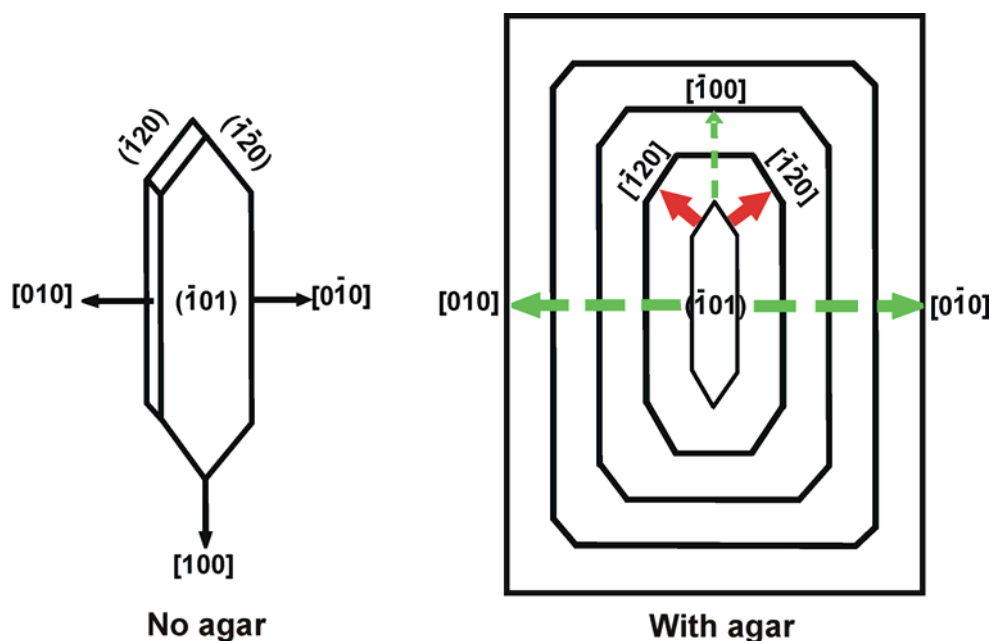


Fig. 3.4.15. COM crystal habit in the absence (left) and in the presence of agar (right). Transformation of the morphology from six-sided platelet to rectangular platelet. The macromolecules adsorb on the (-101) planes and eventually results in the disappearance of the fast growing apical planes (red arrow). Slower growth of the (-101) faces results in increased surface area (green arrow) and preferential growth along $[010]$.

It is known that the (-101) face of COM is calcium rich and has a slight positive charge whereas the (010) face is nearly neutral and contains an alternate arrangement of calcium and oxalate ions [27,169]. The atomic arrangements on the (-101) and (010) faces of HT COM are shown in figure 3.4.16. The calculated calcium densities are 0.04 and 0.03 ions/ \AA^2 for (-101) and (010) faces respectively. Similar to many other cases, the adsorption processes of agar can also be assumed to take place in two steps. First, the macromolecule may be adsorbing on the (-101) planes and eventually disordering the bonding situation between the calcium ions and the oxygen atoms from the C(2)-C(2) oxalate groups (Fig. 3.4.16 A). Second, the side chains of the macromolecule may be emerging from the (-101) planes to interfere with the C(1)-C(1) oxalate groups and the network of the water molecules. Such an interaction is highly destructive since the C(1)-C(1) groups inter-link the (-101) planes and the water molecules form hydrogen bonds with adjacent CaO8 polyhedra. As a consequence, the (-101) layers can no longer align properly along the $[-101]$ direction and this results in structural destabilization and growth inhibition. Furthermore, the macromolecule by adhering to the crystal face from one side may also be acting as nucleation centres by using the remaining radicals to nucleate new crystals on an already formed crystal which results in piling up of crystals on over the other [54,108-110,170].

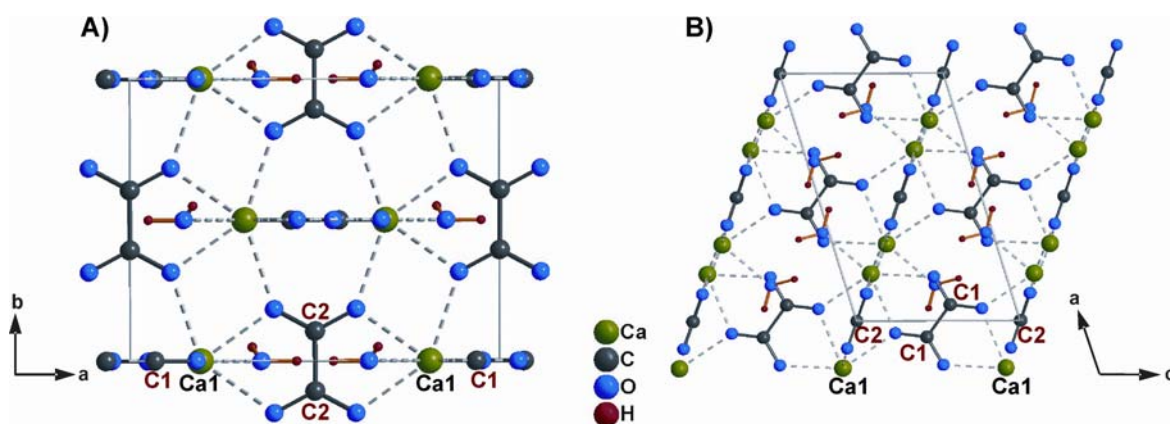


Fig. 3.4.16. (A) (-101) face and (B) (010) face of HT COM [23-25].

As the aggregation increases, the end faces almost touch to form two-dimensional (2D) spherulites with the so called “double-eye” (Section 1.2.5) as shown in figure 3.4.17.

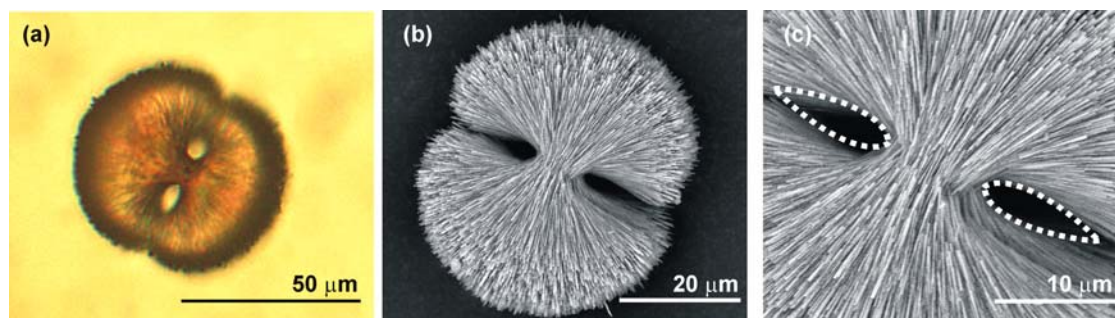


Fig. 3.4.17. 2D spherulites of COM grown from the CM band of 2 wt.-% agar gel at pH 8.5. (a) Light microscope image, (b,c) SEM images showing the characteristic “double-eye” morphology (highlighted with white dots).

As the aggregation increases further, the individual crystallites appear more needle-like than platy and the double-eye is only hardly visible (Fig. 3.4.18 a, Appendix Fig. 6.13). TEM examinations of such a highly aggregated species (Fig.3.4.19 right) confirmed that the individual crystallites have the near-rectangular but needle-like habit (Fig.3.4.19 left). Furthermore, from the ED pattern it was found that the rectangular needle-like crystals belong to the LT modification of COM (Appendix Fig. 6.15).

Although, the dumbbell-shaped COM aggregates with constituent plate-like crystals and with constituent needle-like crystals are isolated from the same band, the ones with needle-like crystallites are formed more towards the M band. As in the present system, the M bands are formed faster than the CM bands; it means that the rectangular needle-like crystallites are formed earlier than the flatter rectangular plates when the supersaturation was higher. It is known that agglomeration usually proceeds faster in a

system containing higher concentration of calcium oxalate and fast agglomerated crystallites are needle-like resulting in a spherulitic shape.

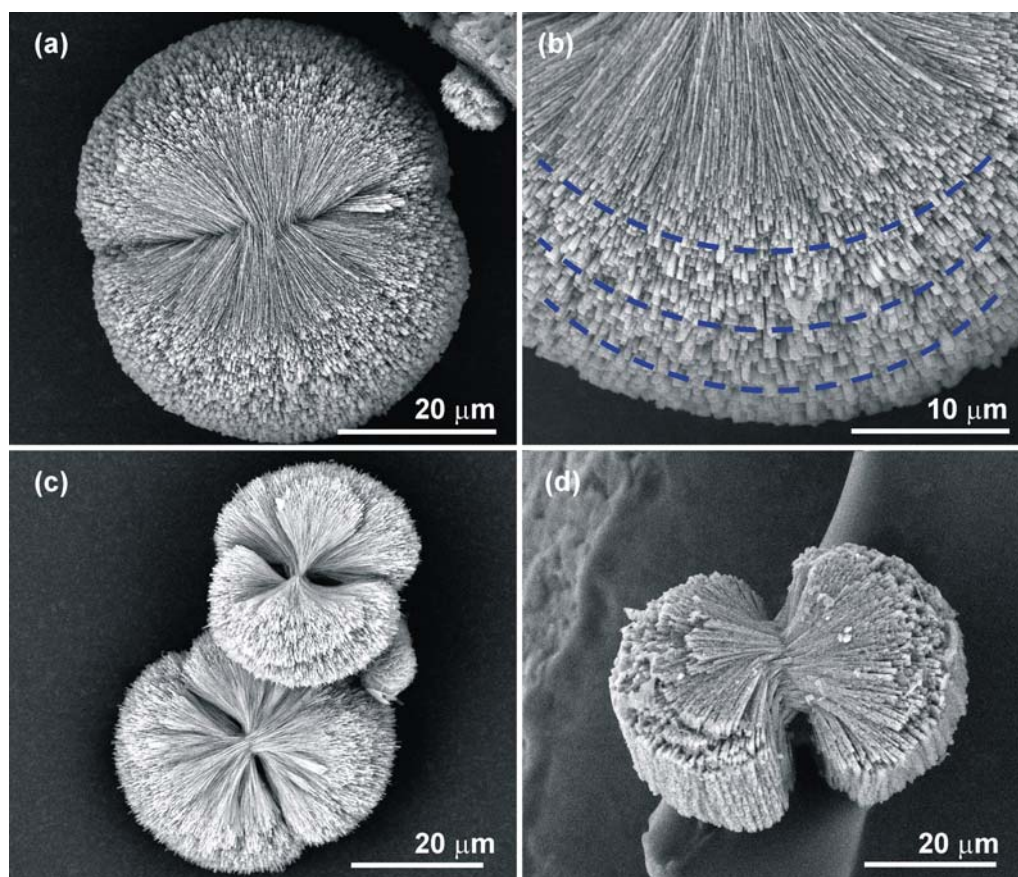


Fig. 3.4.18. SEM images of COM aggregates obtained from the CM band of 2 wt.-% agar gel of pH 8.5. These are formed by the aggregation of needle-like crystallites. Note that after the formation of a 2D dumbbell (c,d), the aggregation takes place on top and bottom and results in a 3D spherulite. This results in layer by layer appearance as indicated with blue lines (b).

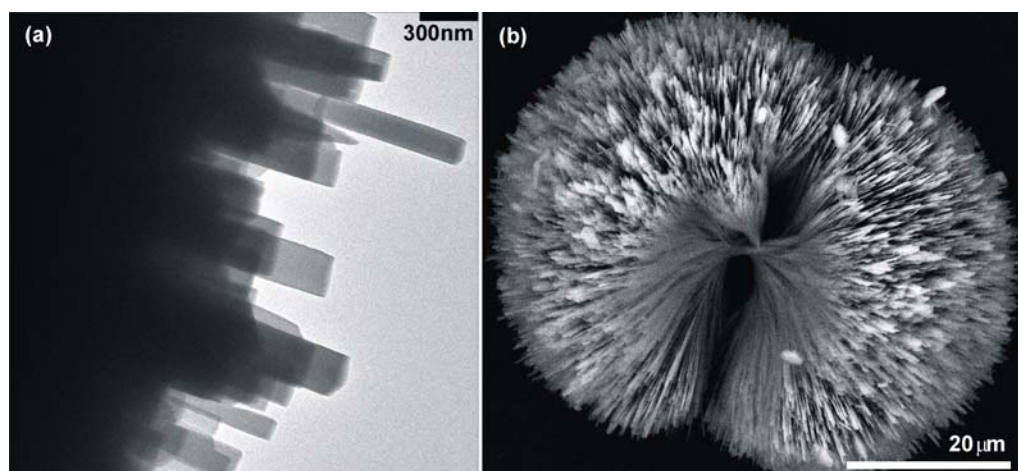


Fig. 3.4.19. (Left) TEM image of the outer crystallites from a COM dumbbell (right) indicating the near-rectangular shape of outer crystallites.

The rectangular plate-like crystallites have an approximate aspect ratio (ratio of length along [100] to width along [010]) of 5:1 while that of rectangular needles is *ca.* 13:1. Such a fineness of the individual rectangular plates might be a consequence of increased supersaturation of the system and faster growth. The images in figure 3.4.18 give the impression that, after the formation of a 2D dumbbell, 3D aggregation starts by formation of new crystallites on top and bottom of such a 2D dumbbell. This is evident from the curved layer by layer appearance of the stacks as indicated by blue lines in figure 3.4.18 b (Appendix Fig. 6.14). The 3D aggregates appear to be formed by nucleation of new crystallites on the (010) faces of the crystallites of the first formed bundle (Fig. 3.4.18 c,d).

In the 2D dumbbell, the crystal growth along [-101] direction was blocked by the adsorption of agar on the (-101) faces of COM. As a result the growth could take place only along [010] and [100]. In the case of needle-like crystals, the aspect ratio is enhanced which proves that the crystal growth along [010] is also retarded and the crystal grows as much as it can along [100] direction. This means that at initial higher supersaturations, agar hinders the crystal growth along both [010] and [-101]. This is possible only if agar is adsorbed on (010) and (-101) faces. As the adsorbed agar on the (-101) faces causes the stacking of new crystallites along [101] and the adsorbed agar on the (010) faces may be causing the nucleation of new crystals along [010]. As a result crystals are nucleated on the (010) faces of already formed crystal stacks. Such a nucleation of new crystallites on the (010) faces of the crystallites constituting an already formed dumbbell results in the formation of 3D aggregates.

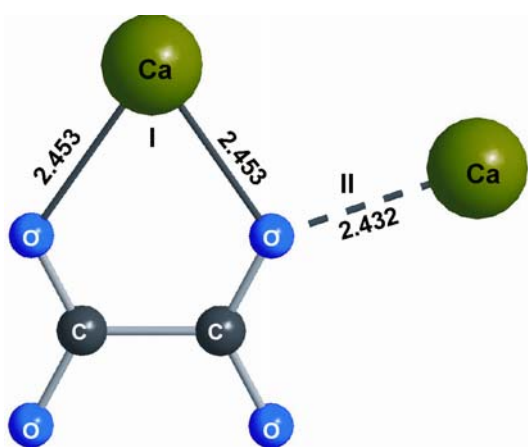


Fig.3.4.20. Oxalate-Ca interactions: Oxygen atoms from oxalate forms chelate bond with Ca1 (indicated with full lines). Bond length are in Å units.

The interpretation given by Millan [27,54,170] on the development of a needle-like shape of COM at stages of higher supersaturation is due to the strong tendency of

oxalate ions to form chelate-chains with Ca ions. In the crystal structure of HT COM (Figs. 3.4.16 and 3.4.20) the calcium ions occupy two different positions in the first coordination sphere of oxalate ions. Ca^{2+} ions at position (I) are in a close distance to two oxygen atoms forming a chelate bond with the oxalate group. The second position (II) corresponds to a single contact. Each Ox1 ion binds six coplanar Ca^{2+} ions, two of them by chelating, and the other four by single bond. Each Ox2 ion binds four Ca^{2+} ions, two of them by chelate bonds and the other two by single contacts (Section 1.2.1).

The structure of oxalate double salts with divalent and alkaline metal ions usually consist of linear polymeric chelate complexes of the divalent metal with oxalate ions surrounded by the alkaline metal ions. At high supersaturations, complexes of this type may be present in solutions forming more linear structures rather than spherical ones. A random condensation of these linear structures could explain the spherulite formation of the needle-like crystals which are typical in precipitation reactions by fast mixing of concentrated reactant solutions.

Biological relevance: There is a striking similarity between the dumbbells biomimetically grown in agar gel and the COM dumbbells found in human crystalluria [56,168] (Fig. 3.4.21). Also, the dumbbell morphology of COM is commonly found in the urine of individuals suffering from intoxication with ethylene glycol, a metabolic precursor of oxalate, and in mice fed with glyoxylate [171-173].

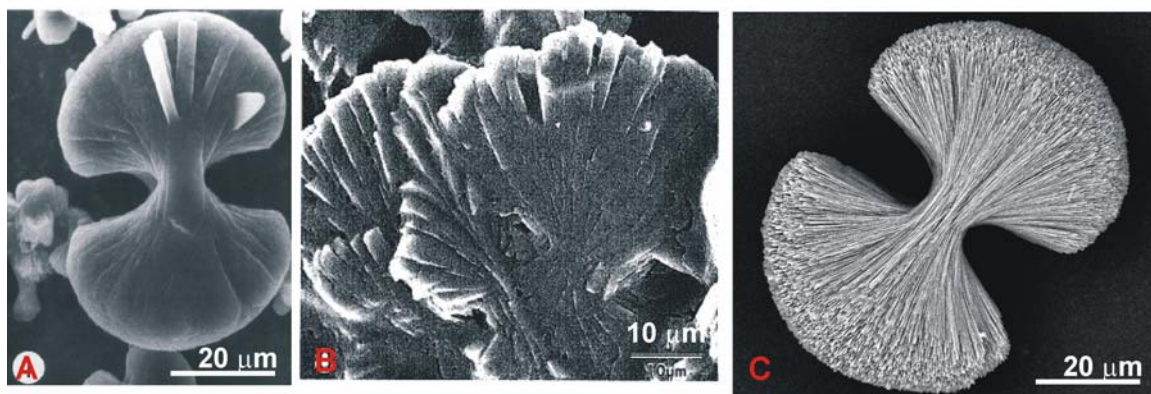


Fig. 3.4.21. (A) SEM image of a dumbbell shaped COM formed under *in-vivo* conditions by glyoxylate intoxication in rats [172]. These dumbbells are formed by stacking of COM crystallites of platy habit. (Oxalate is an end-product of the glyoxylate metabolism. Its primary pathway of excretion is through the kidney. Oxalate is excreted into the urine together with calcium, thus creating the potential for precipitation of calcium oxalate). (B) A fan-like human urinary stone [56], (C) Biomimetic COM aggregate grown from 2 wt.-% agar gel of pH 8.5 at 37 °C.

Thermal decomposition of COM dumbbells isolated from CM bands of 2% agar gel of pH 8.5: The decomposition processes of COM dumbbells from the CM band were investigated by means of TG/DTA/MS. The ground sample was copiously washed with distilled water and dried before starting the measurement. Heating was performed in alumina crucibles with a rate of 5 K/min up to 1300 °C in two steps (Ar and O₂ atmospheres) as already previously discussed for COD dumbbells grown from PAA (Section 3.3.1). The TG/DTA of COM aggregates (Fig. 3.4.22 a) clearly indicate step-wise mass losses of 14.58 wt.-% (165-202 °C), 18.54 wt.-% (450-476 °C) and 29.75 wt.-% (697-790 °C).

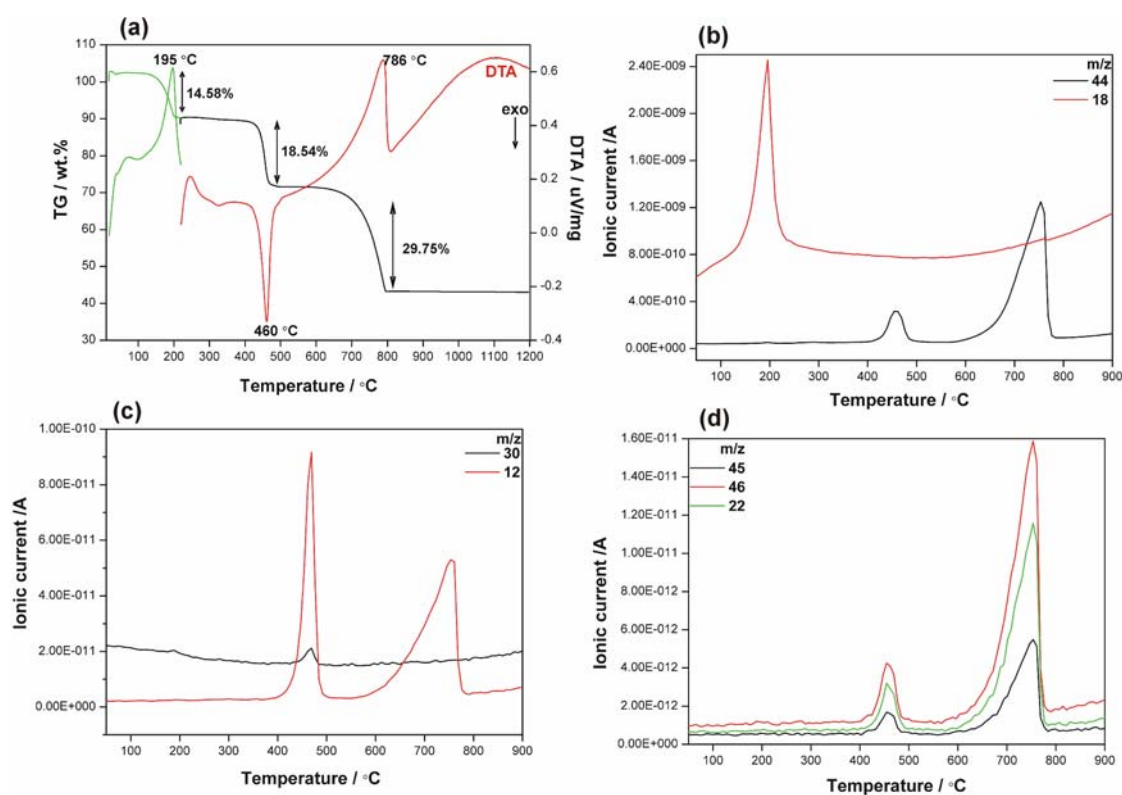


Fig. 3.4.22. (a) Thermogravimetric analysis of COM dumbbells isolated from CM bands of 2 wt.-% agar gel of pH 8.5. The green lines correspond to the measurement performed under argon atmosphere. All the other lines are the result of measurements performed under oxygen atmosphere (black- TG, red- DTA). (b-d) Mass spectra of COM dumbbells isolated from CM bands of 2 wt.-% agar gel of pH 8.5.

A combined TG/DTA/MS analysis ensures the complete removal of water in the first step (Fig. 3.4.22 b, $m/z = 18$). The endothermic peak in DTA corresponding to the release of water appears at 195 °C. The second step corresponding to an exothermic peak at 460 °C is characterized by the release of minor fragments with molecular masses 12(C^+), 22 (CO_2^{2+}), 30 (further reaction of CO), 44 (CO_2), 45 ($C_2H_5O^+$) and 46 (further reaction of CO_2) (Fig. 3.4.22 c,d). The final thermal decomposition takes place in a third

step corresponding to an endothermic peak at 786 °C. From the TGA, the mass release of organic material in the sample was detected to be 1.5 (± 3). The presence of such a small fraction of organic component in the COM aggregates makes the quantitative analysis of the organic component difficult even by mass spectroscopy. Higher molecular mass fragments are not detected in the mass spectrum in contrast to that of pure agar (Figs. 3.4.23 and 3.4.24).

The thermal decomposition of pure agar takes place in two steps at 95 and 285 °C with mass losses of 5.86% (72.9–126.9 °C) and 65.20% (251–445 °C) (Fig. 3.4.23).

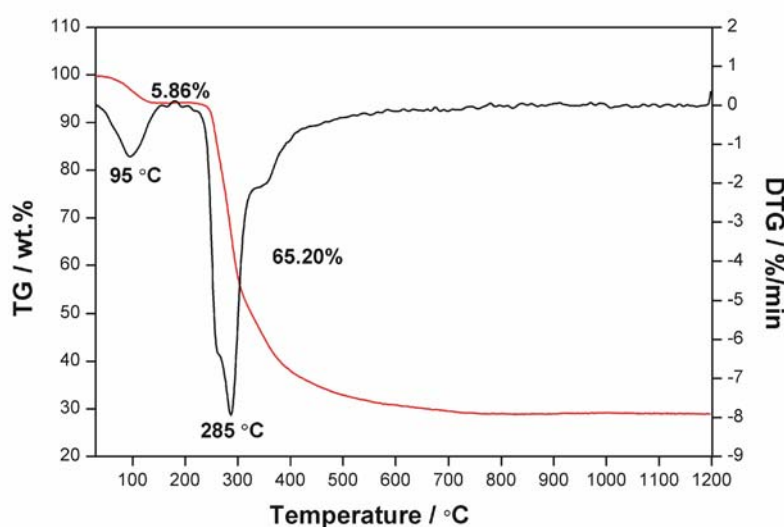


Fig. 3.4.23. TG/DTG of pure agar. For further details see text.

MS analyses of the evolved gases show that water is evolved at 109 °C (maximum). The second step (200 to 400 °C) is more complex with the release of main fragments with molecular masses of 18 and 44 corresponding to H₂O and CO₂ respectively (Fig. 3.4.24 a,b). Small amounts of fragments with molecular masses 12, 15, 22, 31, 45, 53, 69 (Fig. 3.4.24 c,d) indicate the release of products of partial decomposition and simultaneous oxidation of agarose (C⁺, CH₃⁺, CO₂²⁺, CH₃O⁺, C₂H₅O⁺, C₄H₅⁺, C₄H₅O⁺) [97,174].

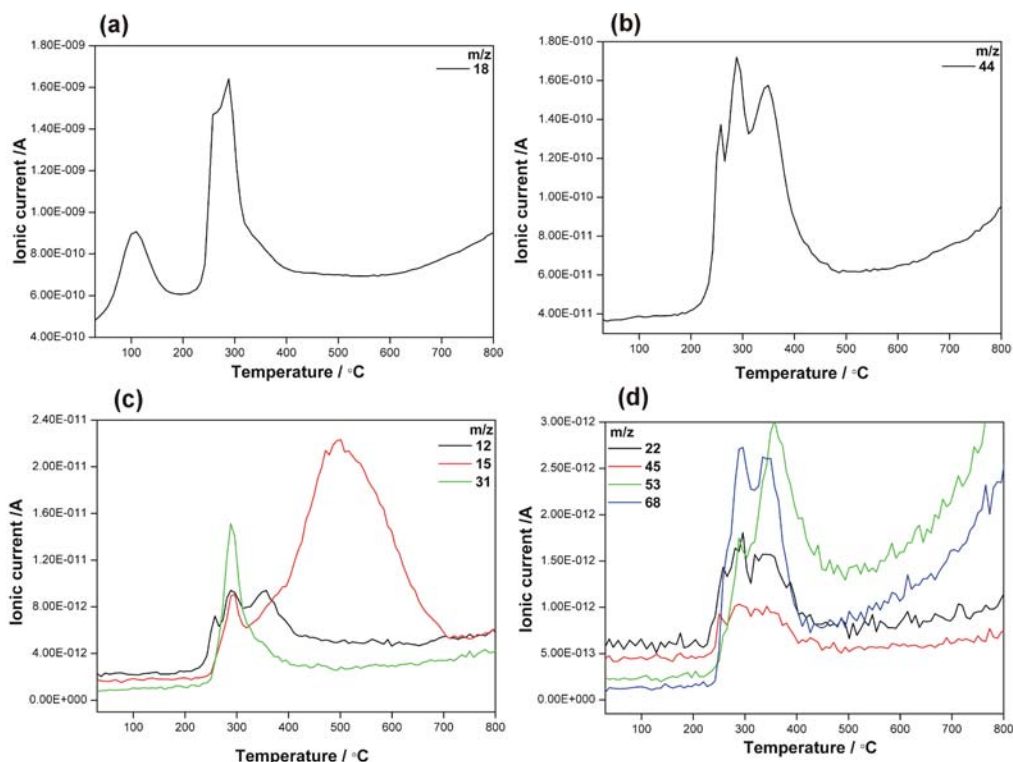


Fig. 3.4.24. Mass spectra of pure agar. For further details see text.

Aggregates formed in the M band of 2 wt.-% agar gel of pH 8.5: COM spherulites

The aggregates isolated within 3 days from the M band (1st formed band) of 2 wt.-% agar gel of pH 8.5 were COM spherulites (70 to 80 μm) consisting of randomly arranged small platy crystallites (Fig. 3.4.25).

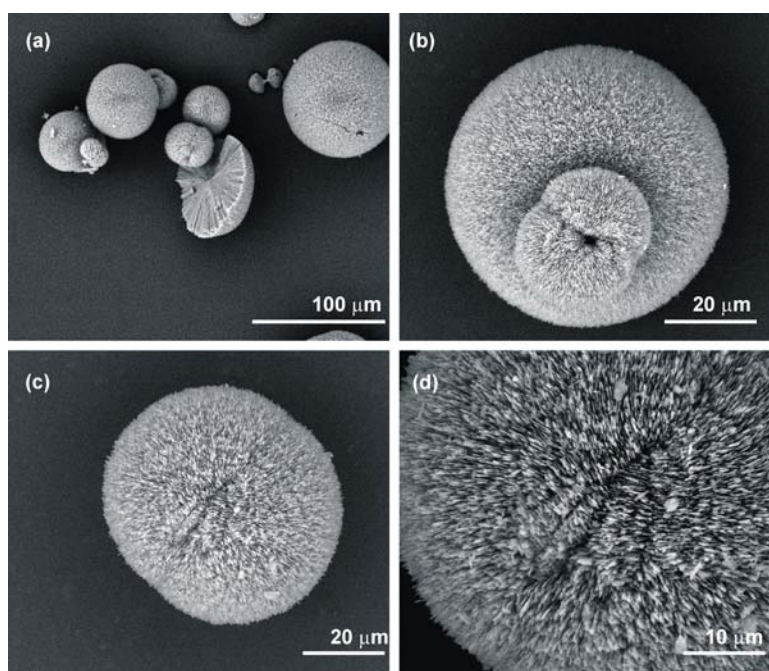


Fig. 3.4.25. SEM images of COM spherulites formed in the M band of 2 wt.-% agar gel of pH 8.5 at 37 °C.

The spherulites isolated after 1 day from the M band suggest that these are formed by stacks of crystallites arranged in layers (Fig. 3.4.26, Appendix Fig. 6.16). It is reasonable to assume that under initial high supersaturation conditions, rectangular needle-like COM crystallites aggregate together to form such spherulites with dense stacking. As opined before, the first formed stack of crystallites may be adding up more crystallites on the (010) faces to finally give spherulitic aggregates. Such a notion is supported by the presence of an equatorial notch in these spherical aggregates (Fig. 3.4.26).

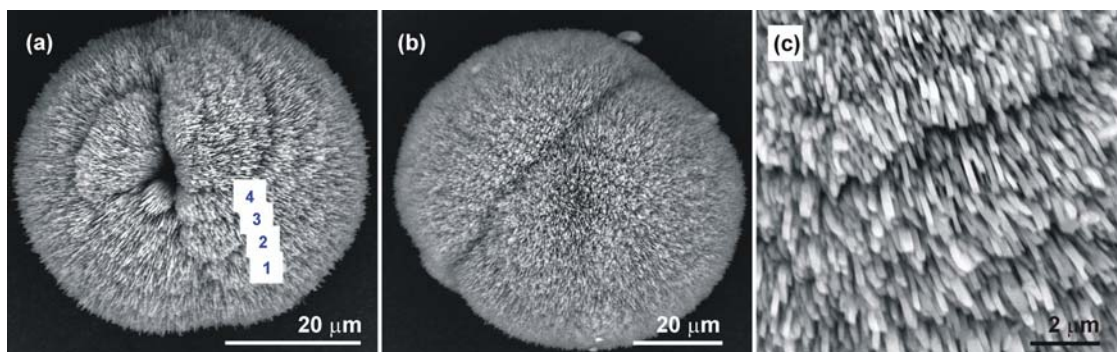


Fig. 3.4.26. (a,b) SEM images of COM spherulites isolated after 1 day indicating layer by layer arrangement of stacks. Each layer (1,2,3,4) consists of stacks or bundles of rectangular needle-like crystallites. (c) Surface of the spherulite clearly indicating layered pattern.

The cross-section of these spherulites shows radial striations with the characteristic “double-eye” in the centre (Fig. 3.4.27). However, the radial striation is more confined to the outer region. Such radial striation is due to the needle-like habit of individual COM crystallites.

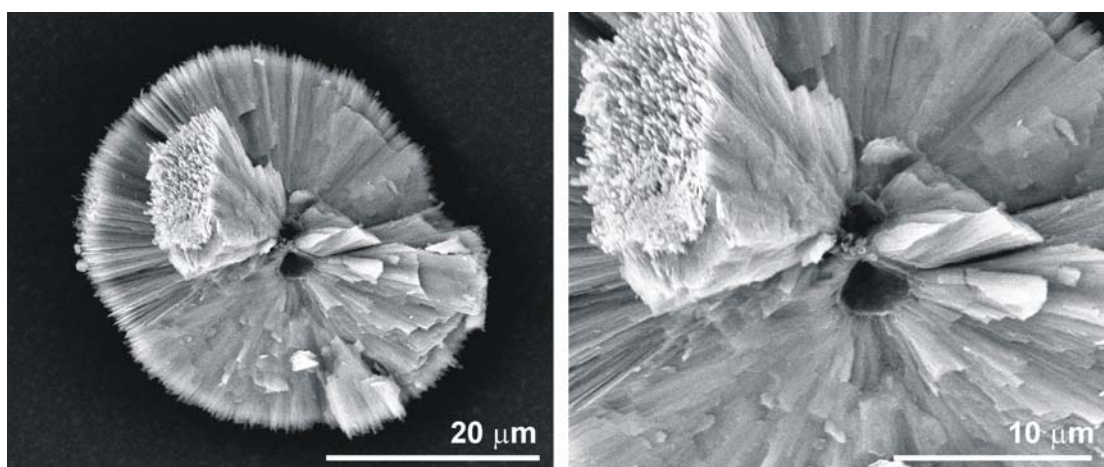


Fig. 3.4.27. SEM images of cross-section of a COM spherulite with the characteristic double-eye (section 1.2.5).

The SEM images of these spherulites decalcified with 0.25N EDTA (pH 4.5) shows that the inner region is decalcified faster than an outer layer of randomly oriented rectangular needle-like crystallites (Fig. 3.4.28, Appendix Fig. 6.17). As a matter of fact, such images give the assumption that these spherulites consist of an inner layer (core) and an outer layer of randomly oriented platy crystallites.

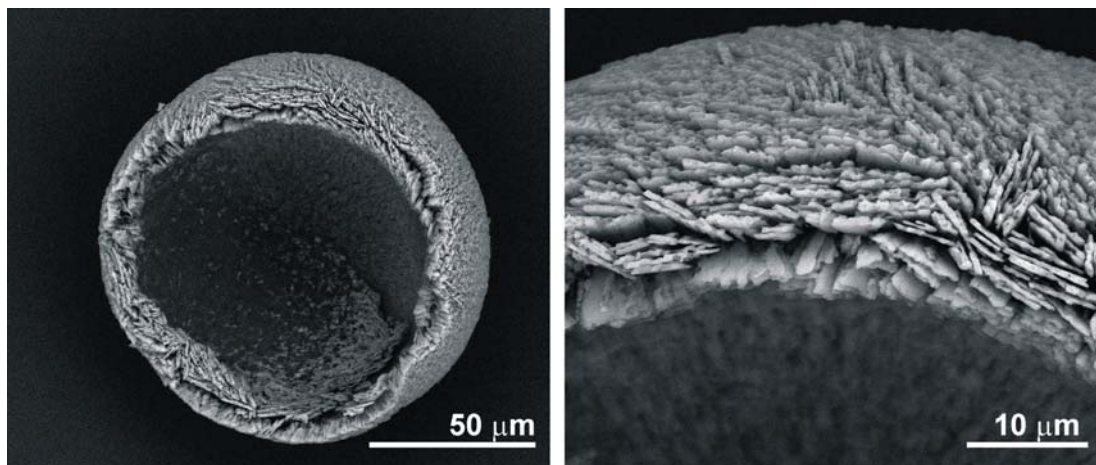


Fig. 3.4.28. SEM images of COM spherulite after partial decalcification with EDTA. The inner region is decalcified faster than an outer region of randomly oriented crystallites.

Some of the COM spherulites isolated from the M band (Fig. 3.4.29 a) showed a more compact inner layer with the double-eye hardly or not at all visible (Fig. 3.4.29 b). Here also the radial striation is prominent towards the outer region of the sphere.

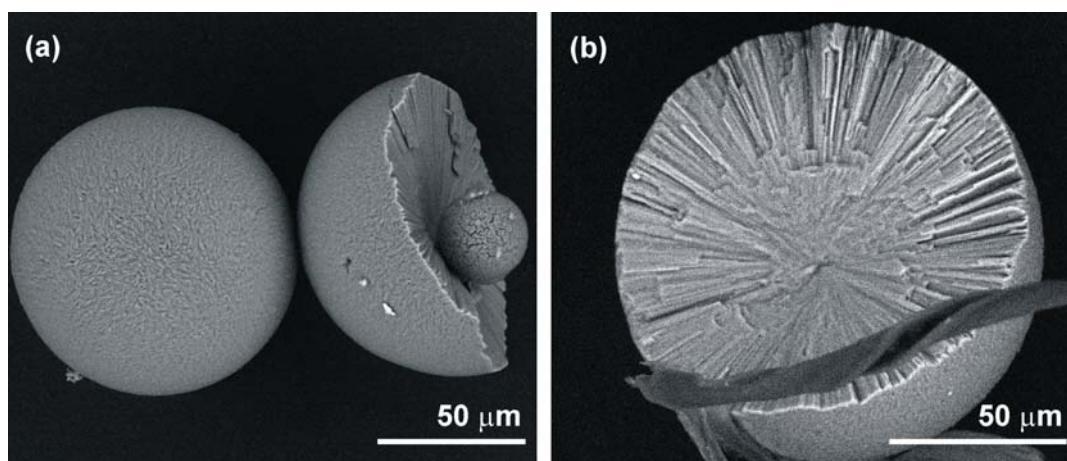


Fig. 3.4.29. SEM images of completely developed COM spherulites obtained after 5 days from the M band of 2 wt.-% agar gel of pH 8.5. The inner region appears compact and the outer region shows radial striations.

A possible reason in this observation could be the fact that the smaller crystallites were too tightly aggregated leaving no space in between. Another explanation would be

that, the cavities are filled by later growth processes. Such a completely developed COM spherulite was subjected to decalcification with 0.25N EDTA of pH 4.5. It clearly indicates the presence of a core region with a narrow double-eye and an outer layer shell consisting of elongated needle-like crystallites in a radial arrangement (Figs. 3.4.30 and 3.4.31). Therefore, a completely developed COM spherulite is characterized by core-shell architecture. The needle-like or columnar crystallites constituting the shell are arranged layer by layer in concentric fashion. Such columnar arrangements of crystallites have been identified on the surface of COM biogenic stones [175-177, refer to Fig. 1.13].

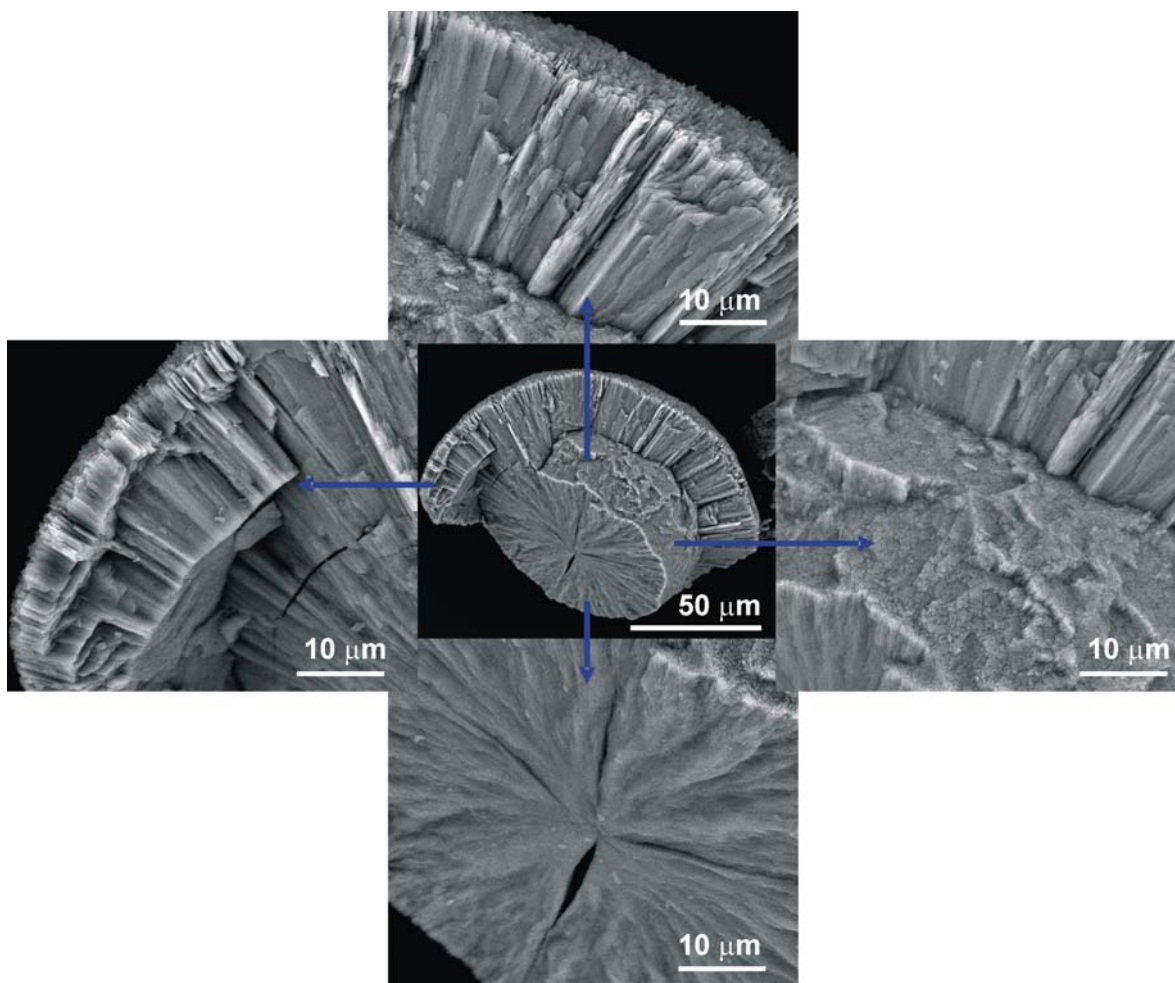


Fig. 3.4.30. SEM images of completely developed COM spherulites (obtained after 5 days from the M band of 2 wt.-% agar gel of pH 8.5) after partial decalcification with 0.25 N EDTA solution. Specific regions indicated with arrows from the same sample are enlarged. The columnar arrangement of the crystallites constituting the shell is evident.

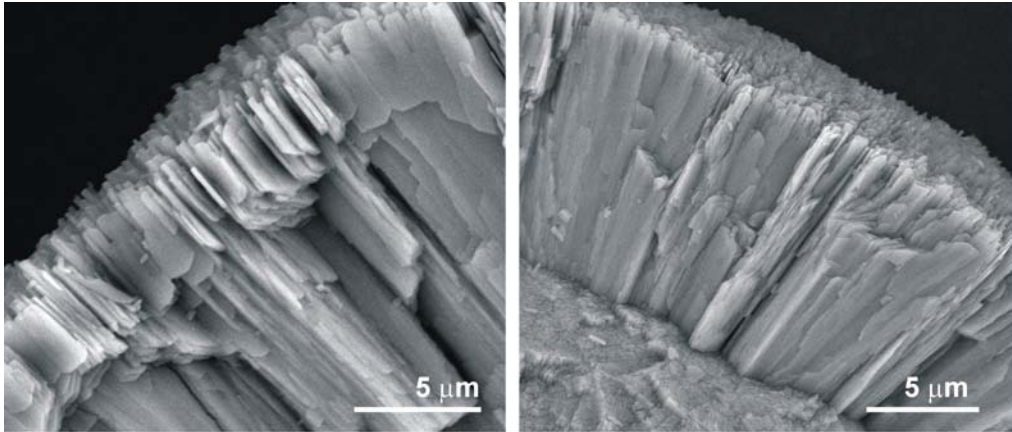


Fig. 3.4.31. The outer region of a completely developed COM spherulite (from the M band of 2 wt.-% agar gel of pH 8.5) after partial decalcification with 0.25 N EDTA. The layer by layer arrangement of columnar platy crystallites results in concentric laminations.

All these spherulites were brown coloured in appearance which is assumed to be caused by agar. Such brown colouration of the COM aggregates can be taken as an indication of the presence of organics in them (Fig. 3.4.32 a). The completely developed spherulites appear darker, an observation from which is assumed to be correlated with the presence of large amounts of organics in between the crystallite layers compared with the less developed spherulites (which shows equatorial notch and the double-eye is visible in the cross-section) (Fig. 3.4.32 a). However, all these spherulites show interference patterns under crosser polarizer (Fig. 3.4.23 b). The completely developed spherulites consist of a high density of crystallites and therefore do not always show interference patterns (Fig. 3.4.33 b). Usually, a complete radial spherulite shows lower birefringence than the crystals from which it is made up [68,178].

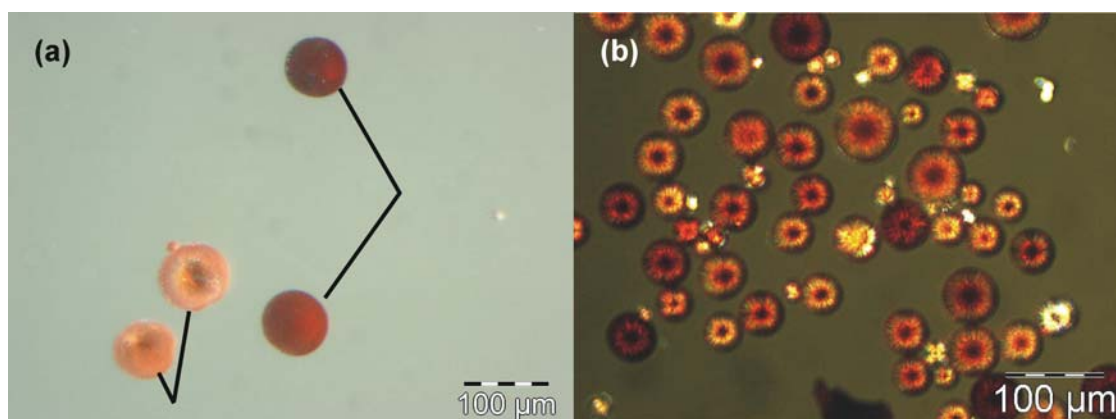


Fig. 3.4.32. Light microscope images of (a) COM spherulites from the M band of 2 wt.-% agar gel of pH 8.5. The connected spherulites belong to the same type. For example, spherulites which appear darker are completely developed spherulites (b) Image of these spherulites under crossed polarizers showing interference patterns.

In an attempt to check the presence of organic material within the spherulites, the COM spherulites obtained from the M band of 2 wt.-% agar gels were decalcified with 0.25N EDTA (Fig. 3.4.33 c). The decalcification resulted in a residue consisting of the EDTA insoluble organic material which maintained the shape but did not show any interference pattern. This means that the decalcified residue is isotropic. There is no orientational correlation between the organic and inorganic material and the organic material is just an inclusion. Figure 3.4.34 shows the sequence for decalcification for a less-developed COM spherulite. Figure 3.4.35 shows the sequence for decalcification for a completely developed COM spherulite consisting of a higher density of smaller crystallites.

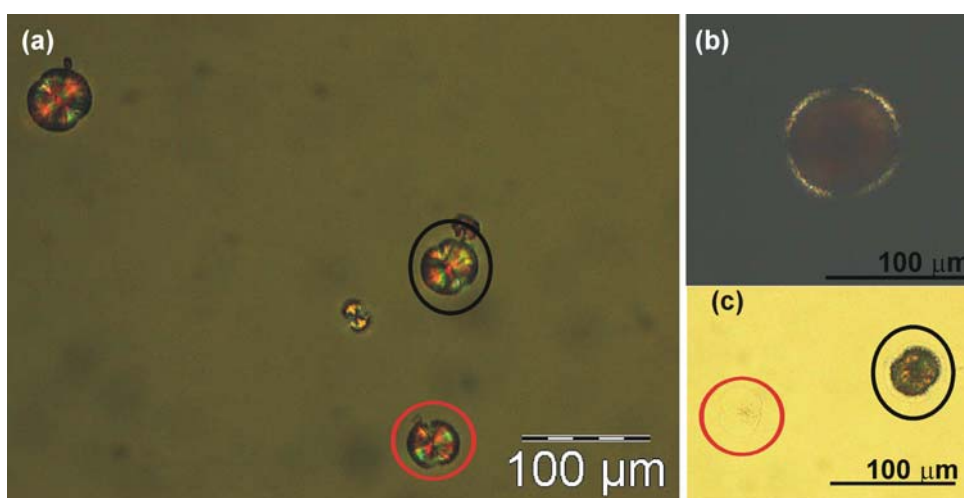


Fig. 3.4.33. Light microscope image under crossed polarizer: (a) spherulites in EDTA solution, (b) a complete spherulite, (c) agar residue of decalcified COM spherulites circled with red and black in (a). Note that the agar residue although maintains the spherical shape, does not show any interference pattern.

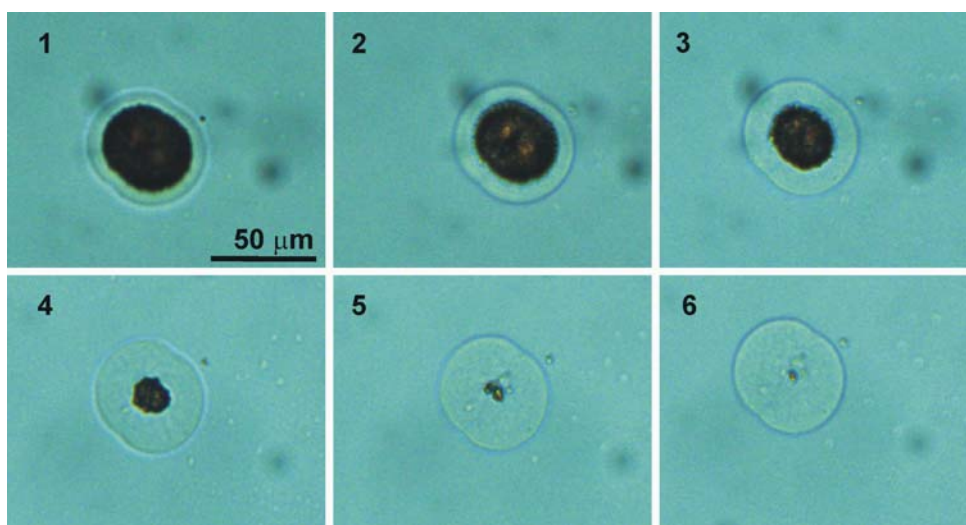


Fig. 3.4.34. Light microscope images of the sequence of the decalcification processes of a less developed COM spherulite in 0.25N EDTA solution. Complete decalcification takes place in about 2 hours.

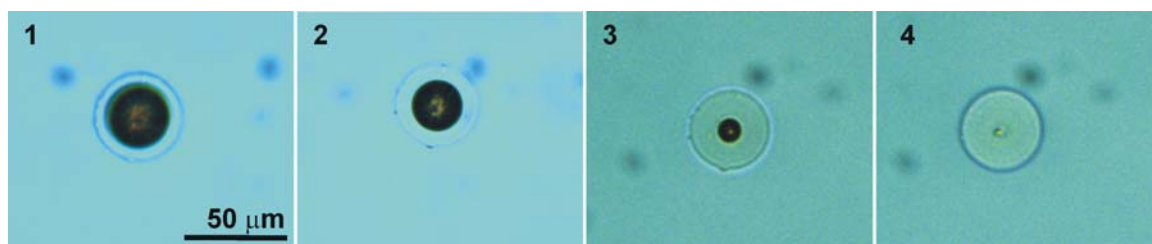


Fig. 3.4.35. Light microscope images of the sequence of decalcification of a completely developed COM spherulite in 0.25N EDTA solution. Complete decalcification takes place during 5 hours. In all the spherulites, the agar ghost remains after decalcification.

Biological relevance: The results obtained give a good correspondence between *in vitro* experiments and *in vivo* observations [45,50]. COM spherulites with radial striations and concentric laminations are the characteristic crystallization products in the supersaturated medium which typically exists in the kidney [179-181]. The spherulitic morphology is considered as a normal product of crystallization on a “split” seed crystal which grows further by epitatic intergrowth and aggregation with the aid of macromolecules [45,182,183]. Agglomeration is recognized as an important step in renal stone development [53,179,180]. A combination of primary agglomeration of crystals forming stones and the nucleation of new crystals on a mucoprotein layer partially covering their surface constitutes the possible mechanism of biogenic stone development [181]. During further growth of the stones, the mucinous layer is incorporated into the crystalline material, thus becoming the organic matrix of the calculus [50,157]. However, the role of the organic material is not yet defined. The assumptions are that the organic material may take part in epitaxy or may act as a cementing material where epitaxy does not play a role.

A great variety of forms is obtained in agar gel. Nevertheless, spherulitic structures which represent fundamental forms of crystallization under conditions of slow reactions in viscous media are frequently associated with biomineralization [62,178,184, Section 1.2.5]. The very first work of this kind was performed by Peter Harting in 1872 who showed the morphological complexity of calcium carbonate crystals grown by double diffusion technique in oyster marrow [185]. The various morphologies obtained are shown in figure 3.4.36. These drawings highlight the absence of clear faces and the appearance of curvatures, properties that are classically not attributed to crystalline matter.



Fig. 3.4.36. CaCO_3 crystals obtained by double diffusion experiments in Oyster marrow [185].

The morphology of the particles formed in agar gel suggests that they form at least to some extent *via* self-organization processes (Fig. 3.4.37). However, the mechanisms of such self-organized growth processes cannot be explained without further investigations. Generally, crystal growth in gel media takes place under very high supersaturations [66,184,186] and the aggregation of individual crystallites appears to be a general feature of crystallization at high supersaturations. The driving force of the aggregation remains ambiguous. It has already been found that some minerals tend to grow into unusual sheaf structures. It is believed by mineralogists that the sheaf structures and the spherulites may be formed by crystal splitting during their growth [67] (Fig. 3.4.37 A).

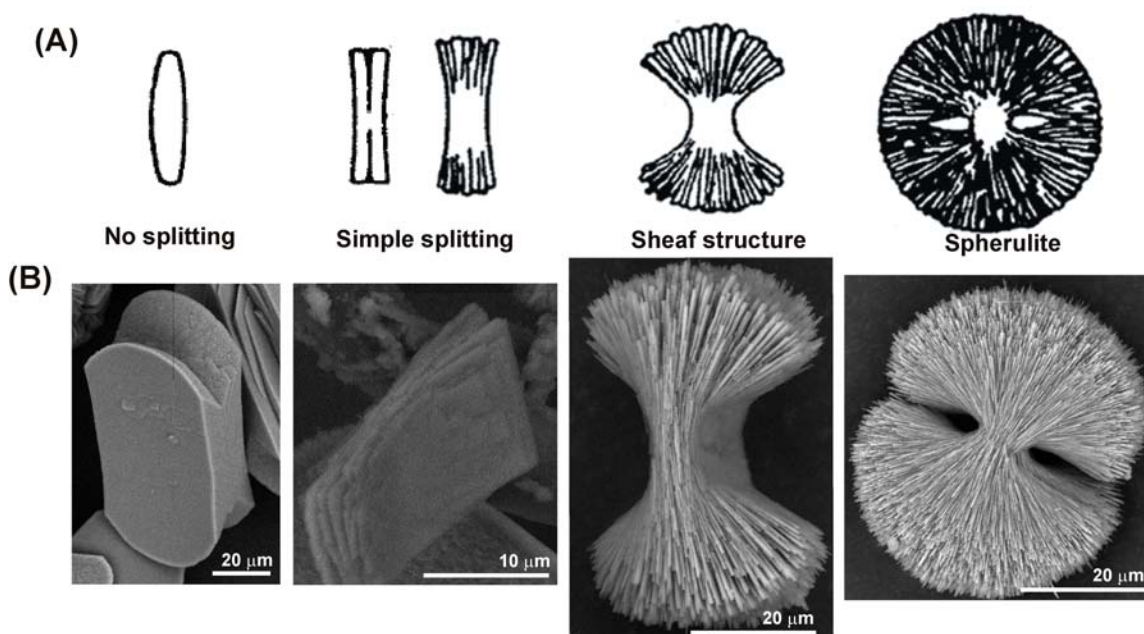


Fig . 3.4.37. (A) Concepts for the formation of spherulite with unidirectional and low angle branching [67,187]. (B) SEM images of different forms of COM grown from 2 wt.-% agar gel of pH 8.5 at 37 °C.

Generally speaking, splitting is associated with fast crystal growth which strongly depends on the supersaturation of the solution. Putnis *et al.* suggested that splitting is only possible if the super saturation exceeds a certain “threshold” level, which is specific for each mineral under the given conditions [186]. Other factors that have been found to cause crystal splitting are *mechanical splitting* and *chemical splitting*. Depending on the level of supersaturation or impurity concentration (which can change during growth), minerals can take on different degrees of splitting, resulting in a number of sub-forms of split crystals (Section 1.2.5).

As already stated, a minor fraction of COD was always associated with COM in the M band. The COD crystals obtained along with COM in the M band (formed first) were large dendrites 200-400 μm in size (Appendix Fig. 6.18). These dendrites appeared to be only poorly crystalline at the base (Appendix Fig. 6.19). An initial high pH value must be causing a high level of supersaturation when the nucleation begins, also indicated by the appearance of the kinetically favoured COD. This means a high metastability level should be expected. In case of COD, the metastability range is smaller since its solubility is higher than that of COM. These dendrites appear to have formed by stacking of smaller tetragonal crystallites. Dendrites of COD are often formed if the Ca:Ox molar ratio is skewed from unity. It is known that dendrites of COD are formed at higher sugar concentrations and high temperatures [31]. In general, very fast growth rates lead to the formation of dendritic crystals [188].

Finally, COM crystals are formed in the C band. These crystals are oval in shape and mainly twinned with dominant (-101) faces (Fig. 3.4.38). As these crystals are formed in the latest formed band, the supersaturation is decreased which results in less aggregated units. The light microscope images show that these specimens are relatively transparent in appearance when compared to the spherulites which may be an indication of less organic content in these crystals. On the other hand, spherulites which appear dark and consist of many stacks of smaller crystallites shed light into the organically assisted aggregation. Therefore, the crystals formed in the C band are poor in their organic content and hence are less aggregated.

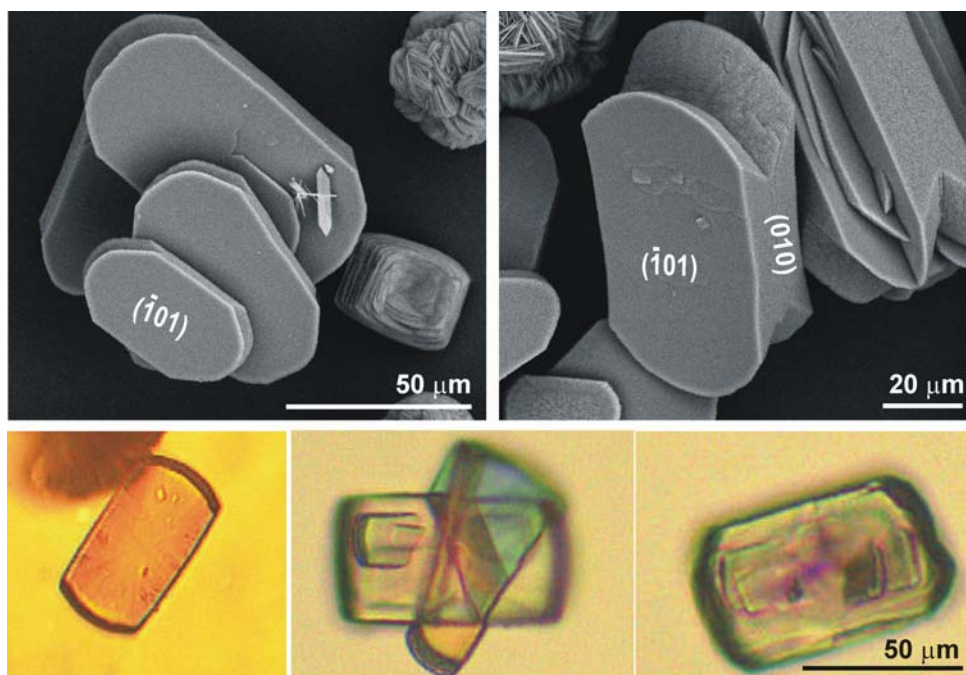


Fig. 3.4.38. (Top) SEM images of COM aggregates obtained from the C band of 2 wt.-% agar gel of pH 8.5 at 37 °C after 3 days, (Bottom) light microscope images (same scale bar for all).

3.4.1.4 Agar gel of pH 11.5

The stock solutions, 0.033 M $\text{CaCl}_2 \cdot 2\text{H}_2\text{O}$ (pH = 12) and 0.1 M $\text{Na}_2\text{C}_2\text{O}_4$ (pH = 8) were allowed to diffuse into a 2 wt.-% agar gel of pH 11.5 at 37 °C over a period of 3 days. Two bands were generated during that time. The one formed near to the oxalate reservoir (O band) was composed of dumbbell shaped COD aggregates (Fig. 3.4.39) and the second band (extending from CM to C bands) consisted of tetragonal prismatic and tetragonal bipyramidal COD (Fig. 3.4.40). The COD dumbbells were found to be unsymmetrical when compared to those formed in the presence of PAA with either one half-dumbbell bigger in size than the other one.

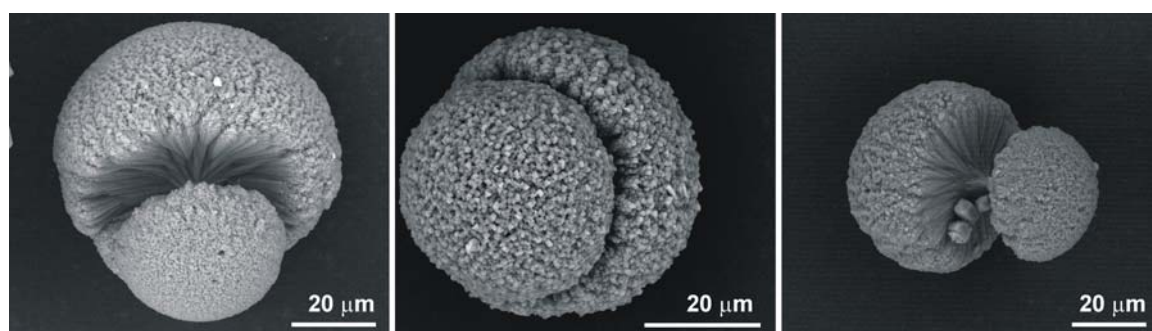


Fig. 3.4.39. SEM images of the less symmetric COD dumbbells composed of rod-like tetragonal prisms obtained from 2 wt.-% agar gel of pH 11.5 at 37 °C.

These SEM images indicate that the dumbbells are formed by the aggregation of rod-like tetragonal prismatic COD crystals. The broken dumbbells do not show the tetragonal cross-section that was clearly evident in the case of COD dumbbells formed in the presence of PAA (Fig. 3.4.40). Magnified SEM images from the broken dumbbells indicate that each half dumbbell is composed of colonies of very small rod-like tetragonal prisms (Fig. 3.4.40 d, Appendix Figs. 6.20 and 6.21). Nevertheless, these results prove that PAA is not unique in controlling the morphology of COD and agar gel at a specific pH value is also able to control the hydration state as well as the morphology of calcium oxalates.

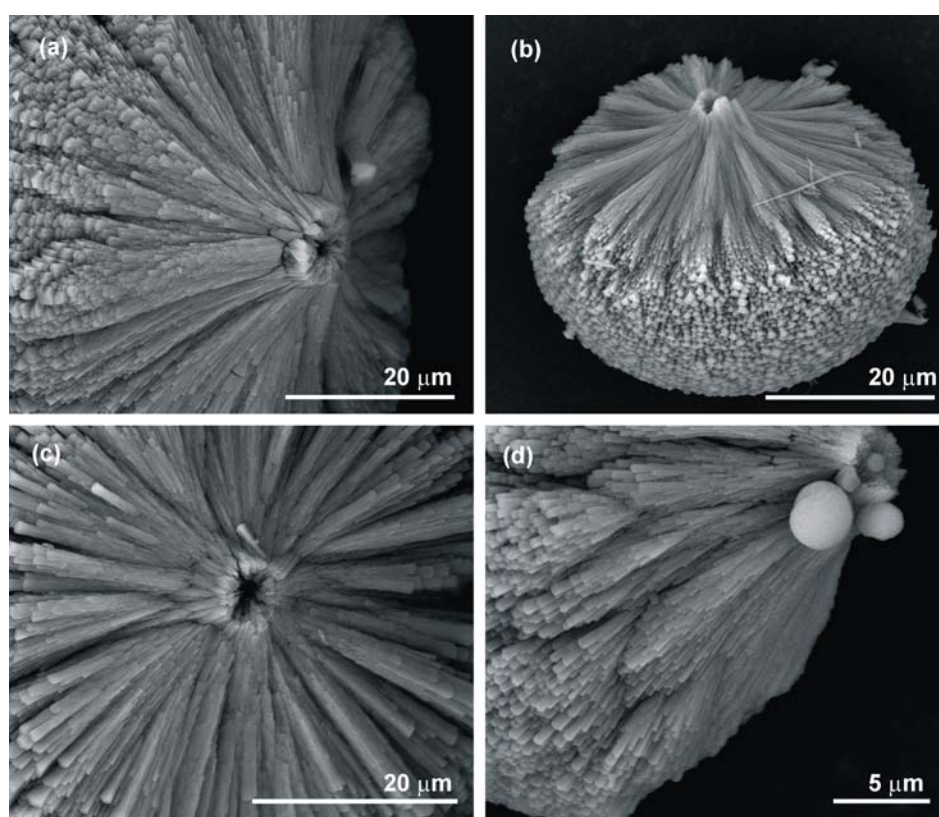


Fig. 3.4.40. SEM images of half dumbbells of COD grown from 2% agar gel of pH 11.5 at 37 °C. These images reveal that the dumbbells are composed of smaller tetragonal prismatic COD crystals. For more pictures see appendix figures 6.20 and 6.21.

The organic content in the dumbbells is estimated from the thermogravimetric analysis as 1.8 ± 3 wt.-%. A representative TG/DTG/DTA of the as-prepared COD dumbbells is shown in figure 3.4.41 which clearly indicates stepwise mass losses at temperatures specific for COD. The TG/DTG of COM aggregates (Fig. 3.4.41 top) clearly indicate stepwise mass losses of 20.28 wt.-% (40-228 °C), 15.67 wt.-% (230-520 °C) and 26.96 wt.-% (528-780 °C).

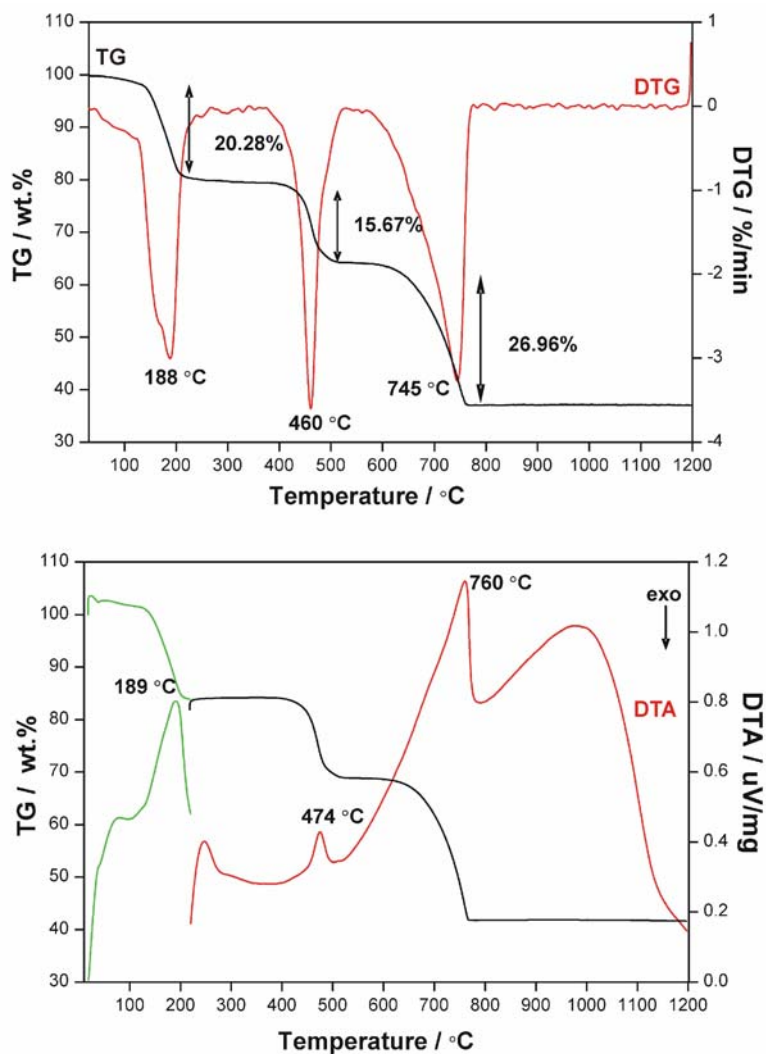


Fig. 3.4.41. (Top) TG-DTG and (b) TG-DTA of COD dumbbells grown in 2 wt.-% agar gel of pH 11.5. (Bottom) The green lines correspond to the measurement performed under argon atmosphere. All the other lines are the result of measurements performed under oxygen atmosphere (black- TG, red- DTA).

The COD dumbbells appear to have formed by the aggregation of smaller tetragonal crystallites which is also evident from the less aggregated forms obtained from the same band (Fig. 3.4.42).

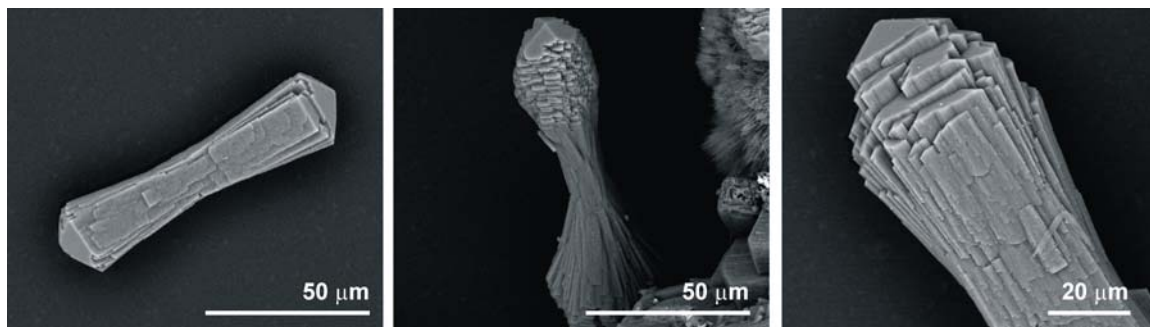


Fig. 3.4.42. SEM images of tetragonal prisms with only small number of aggregated crystallites.

The aggregates formed near the Ca source side consisted of tetragonal bipyramids and tetragonal prisms (Fig. 3.4.43). From the SEM images, it is evident that stacking of the crystallites takes place on the (100) faces of COD rather than on the (101) faces. The (101) faces appear relatively smooth during all the observations. These images just give the idea that the adsorption of the macromolecule on the (100) faces of COD and further nucleation of new crystallites results in the final formation of dumbbells (Figs. 3.4.43 and 3.4.44).

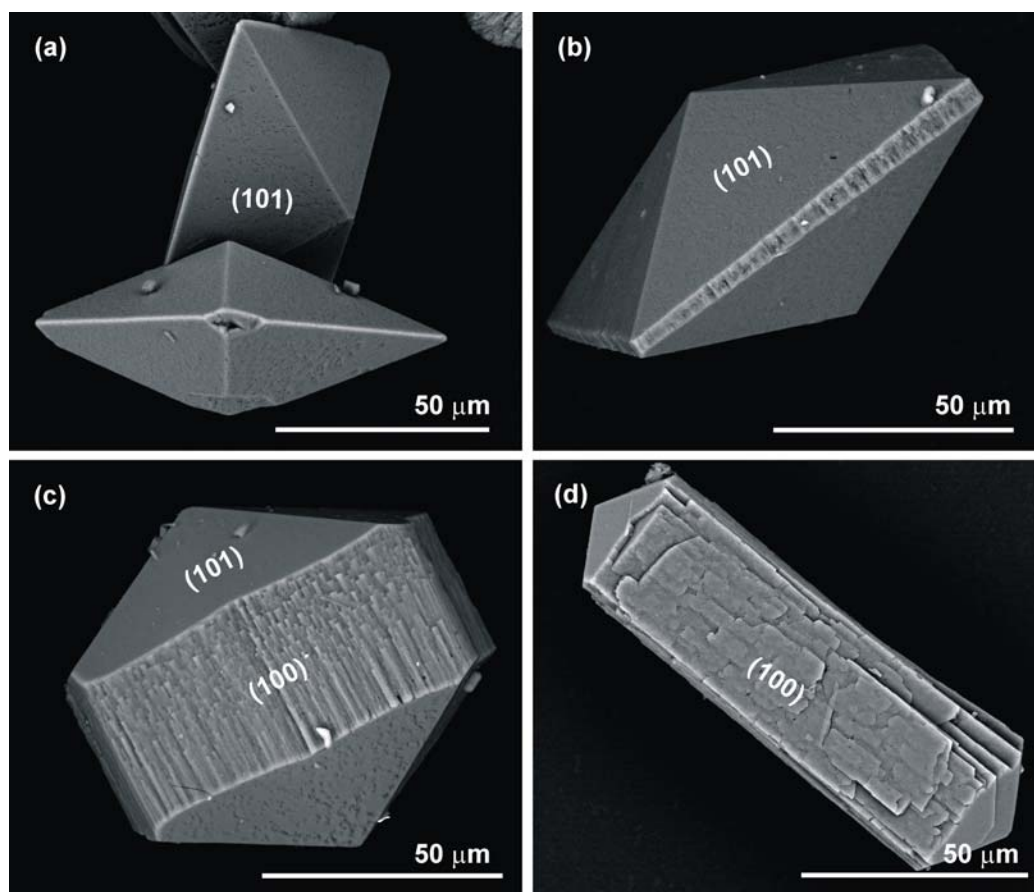


Fig. 3.4.43. SEM images of COD crystals formed at low supersaturation in 2 wt.-% agar gel of pH 11.5. (a) Tetragonal bipyramids. (b) Tetragonal bipyramids with a combination of (101) pyramidal faces and (100) prism faces. (c) Elongated tetragonal bipyramidal prism. (d) Tetragonal prism. All the aggregates show preferential structuring on the (100) faces.

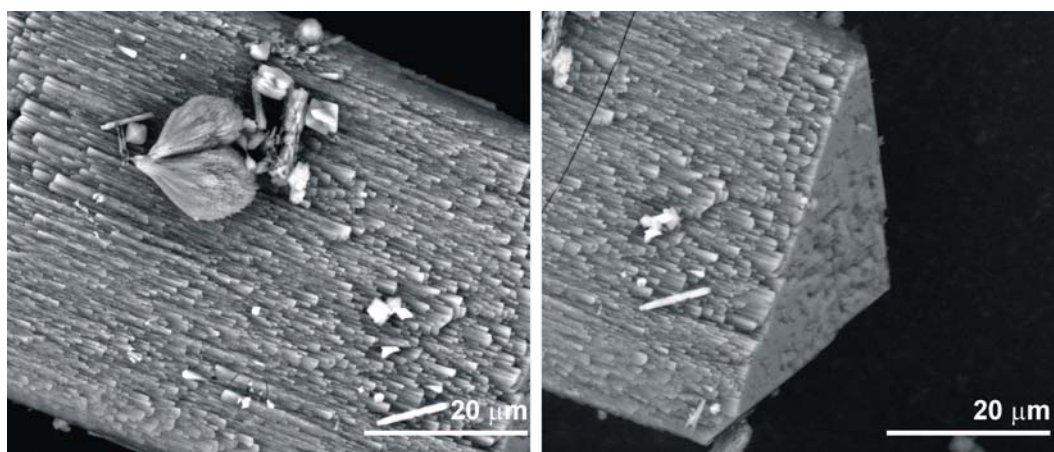


Fig. 3.4.44. Magnified SEM images of tetragonal prisms of COD with thin elongated crystallites aggregated with parallel orientation on the (100) faces and with relatively smooth (101) pyramidal faces.

The double diffusion experiments were also repeated with 3 wt.-% agar of pH 11.5 as an increase in concentration of agar should promote the fraction of COD. Under these conditions the COD dumbbells generated appear to be soft and made up of thinner crystallites (Fig. 3.4.45). The pyramidal cap of the central seed crystal (tetragonal prismatic COD) was visible in this case. The pyramidal faces of such a central seed were never observed for COD grown in the presence of PAA. For COD grown from PAA, the assumption was that even before the development of pyramidal faces of central tetragonal prism, the secondary growth processes start which cover the core like a shell. Such core-shell architecture was not observed for COD dumbbells grown in the presence of agar.

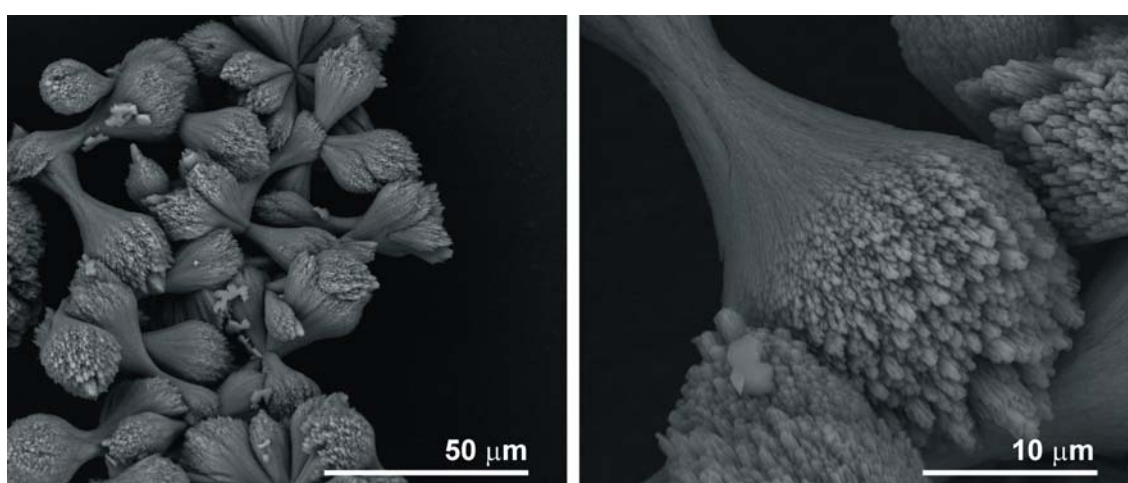


Fig. 3.4.45. SEM images of COD dumbbells generated in 3 wt.-% agar gel of pH 11.5 at 37 °C.

To sum up, in a 2 wt.-% agar gel of pH 8.5, COM spherulites (3D) are formed at high supersaturations, COM dumbbells at moderate supersaturations (2D) and less aggregated COM crystals at low supersaturations. Dumbbells and tetragonal crystals of COD were formed at pH 11.5 of 2 wt.-% agar gel (Fig. 3.4.46). These results support the fact that whether COM or COD, the crystals formed in agar gel are aggregated suggesting that this medium has “some” effect in stacking the crystallites together.

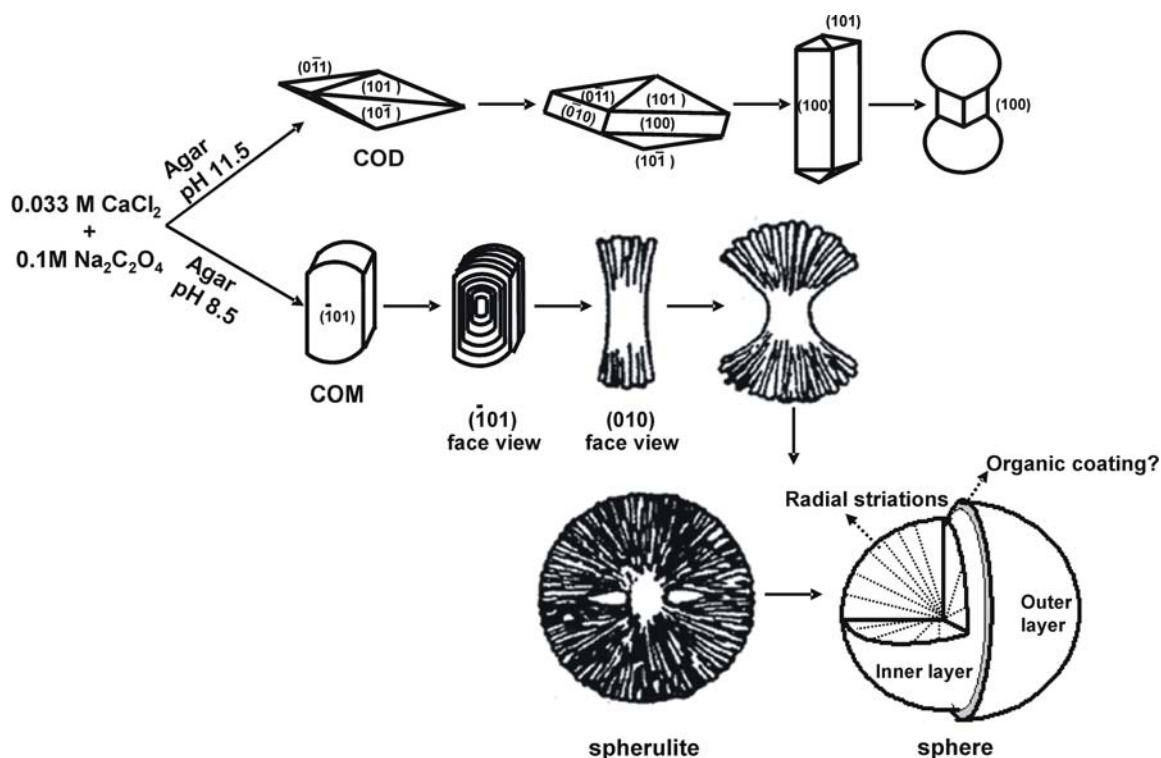


Fig. 3.4.46. Schematic representation of morphological and phase change of calcium oxalate with varying pH value of 2 wt.-% agar gel [67].

2 wt.-% agar gel of pH 11.5 (Ca:Ox = 1:1)

The double diffusion experiments were also performed in 2 wt.-% agar gel of pH 11.5 with equal concentration of 0.05 M of stock solutions (instead of Ca:Ox = 1:3). Under these conditions, the COD dendrites with flower-like appearance were formed instead of COD dumbbells in the M bands (near to oxalate reservoir). These dendrites were composed of thin and elongated tetragonal prisms aggregated randomly (Fig. 3.4.47 a,b,c). The dendrites isolated after 6 hours from the gel were needle-like which may be attributed to the presence of organic material (Fig. 132d, Appendix Fig. 6.22).

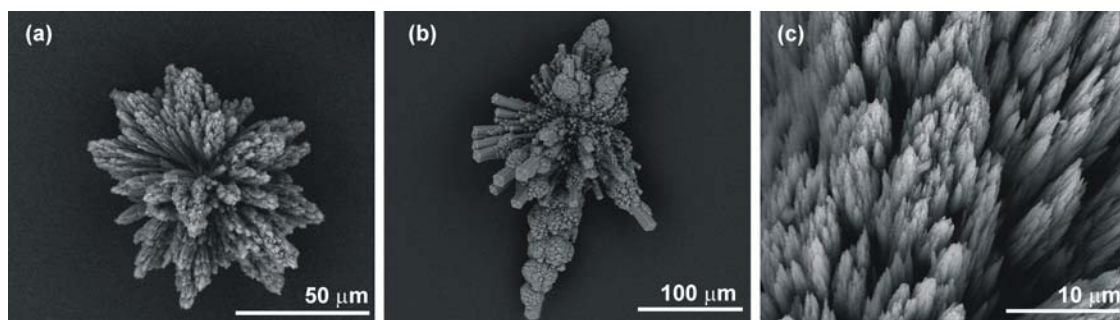


Fig. 3.4.47. (a,b) SEM images of COD dendrites isolated from the M band of 2 wt.-% agar gel of pH 11.5 and 0.05M of the stock solutions at 37 °C after 3 days. (c) Magnified view of a COD aggregate isolated after 6 hours.

Under the same conditions, COM spheres were formed in the M band (Fig. 3.4.48-top). But the surface of these COM spheres (110 to 130 μm in diameter) appeared different from each other with the presence of randomly oriented tubular crystallites of different sizes.

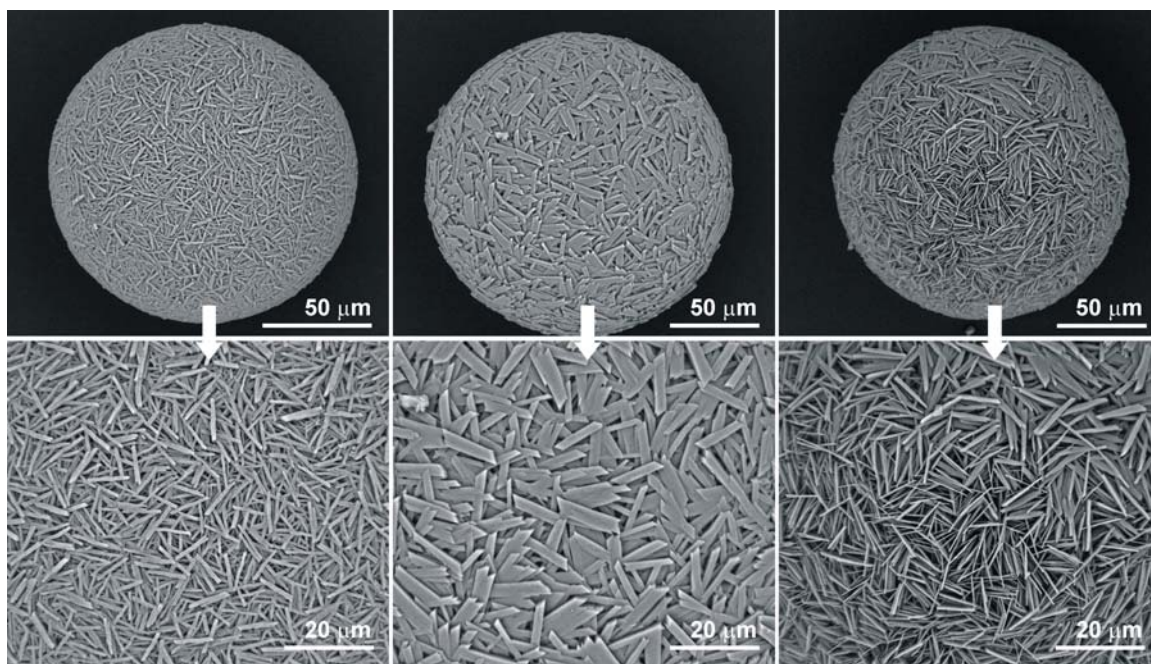


Fig. 3.4.48. (Top) SEM images of COM spheres isolated from the M band of 2 wt.-% agar gel of pH 11.5 and 0.05M of the stock solutions at 37 °C after 3 days. (Bottom) The surface of these spheres consists of crystallites of varying size and shape.

An accidentally broken sphere indicated a softer inner layer (core) and the random array of outer tubular crystallites (Fig. 3.4.49, Appendix Fig. 6.23).

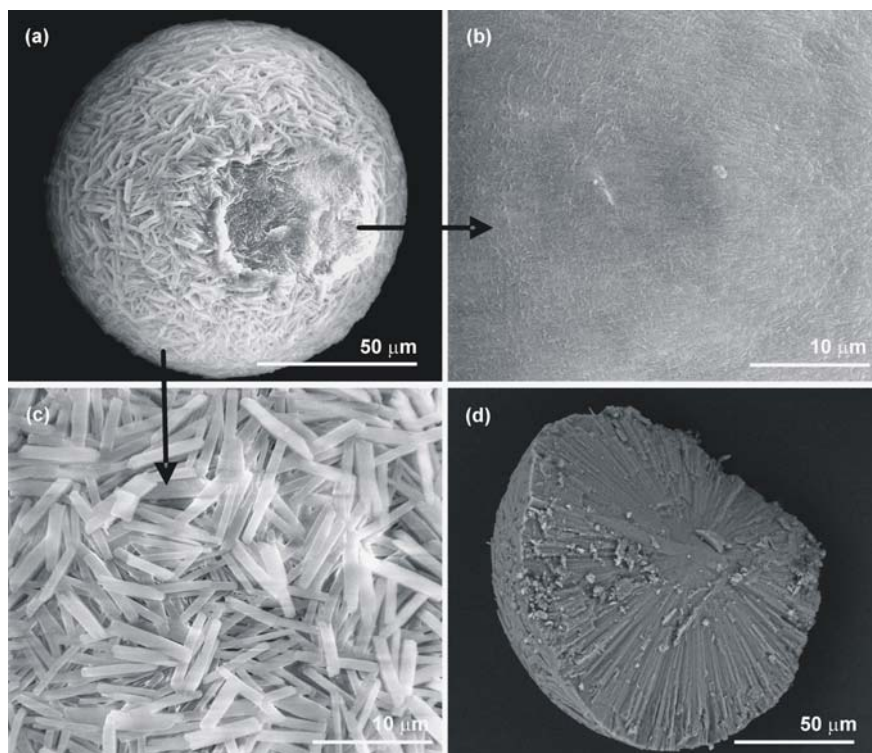


Fig. 3.4.49. (a) SEM image of a COM sphere isolated from the M band of 2 wt.-% agar gel of pH 11.5 and 0.05M of the stock solutions at 37 °C after 3 days. (b) Enlarged view of a fracture area indicating a compact core. (c) Randomly oriented platy crystallites on the surface of the same sphere. (d) Cross-section of the sphere showing the columnar arrangement of crystallites in the outer region.

Decalcification of the COM spheres by using 0.25N EDTA (pH 2) indicated a faster decalcification of the inner region and retention of the outer layer of crystallites (Fig. 3.4.50). In general, all the COM spherulites formed in agar gel consist of a core, a shell of radially arranged crystallites and an outermost region of randomly arranged crystallites. It is reasonable to assume that the crystallites which constitute the outer layer of a COM sphere are formed at relatively lower supersaturation than the core and the habit of the crystallites which make the outer layer are strongly influenced by the local supersaturation. The crystal growth rate influencing the morphology of the outer crystallites of these COM spheres is different, making some thinner and some thicker.

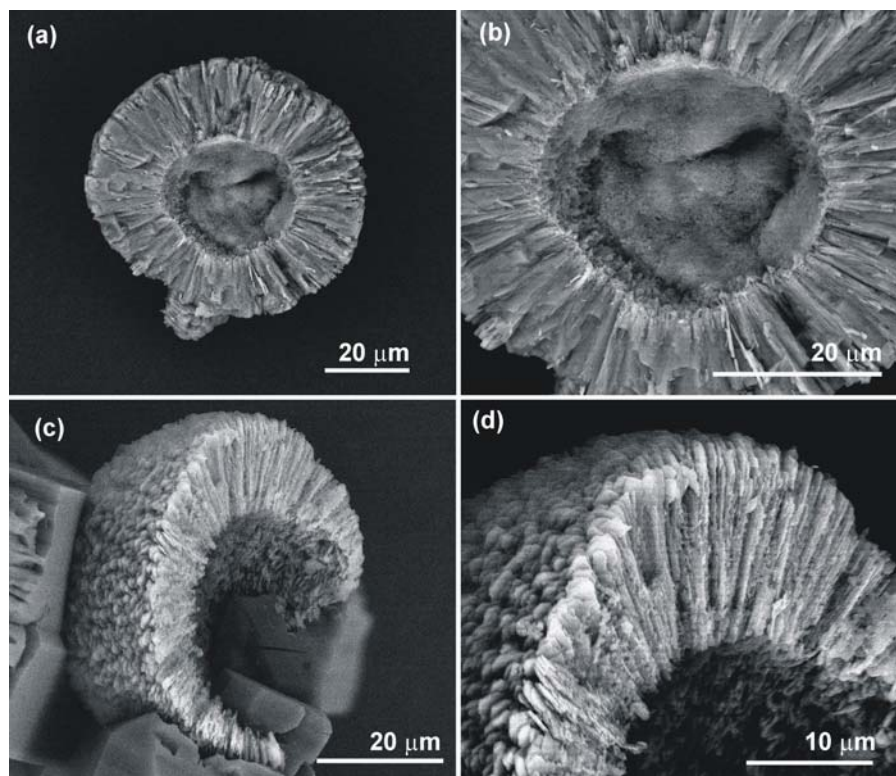


Fig. 3.4.50. SEM images of COM spheres after immersing in EDTA solution. (a,b) The inner layer partly removed (c,d) core completely removed with the outer layer of radially arranged platy crystals remaining.

In the CM band, two types of COM dumbbells are observed. One set consists of nearly rectangular platy crystals (Fig. 3.4.51). The second type of dumbbells (and spheres) appear smooth and seem to have included more organic material (Fig. 3.4.52). The more crystalline dumbbells (Fig. 3.4.51) could have been formed after a decrease in supersaturation as the individual platelets show well-defined edges and are larger in size.

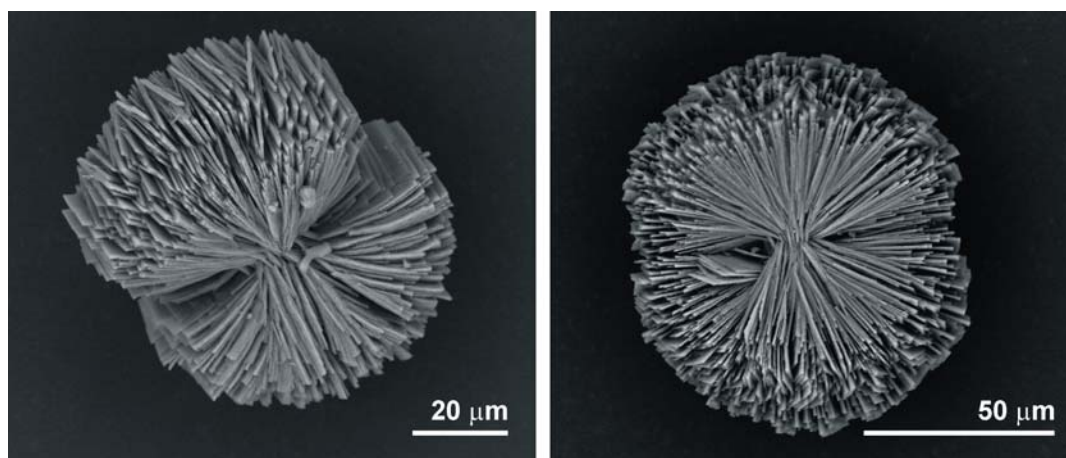


Fig. 3.4.51. SEM images of COM aggregates formed in the CM band of 2 wt.-% agar gel of pH 11.5 and 0.05M of the stock solutions at 37 °C after 3 days. These are characterized by the stacking of bigger rectangular platy crystals.

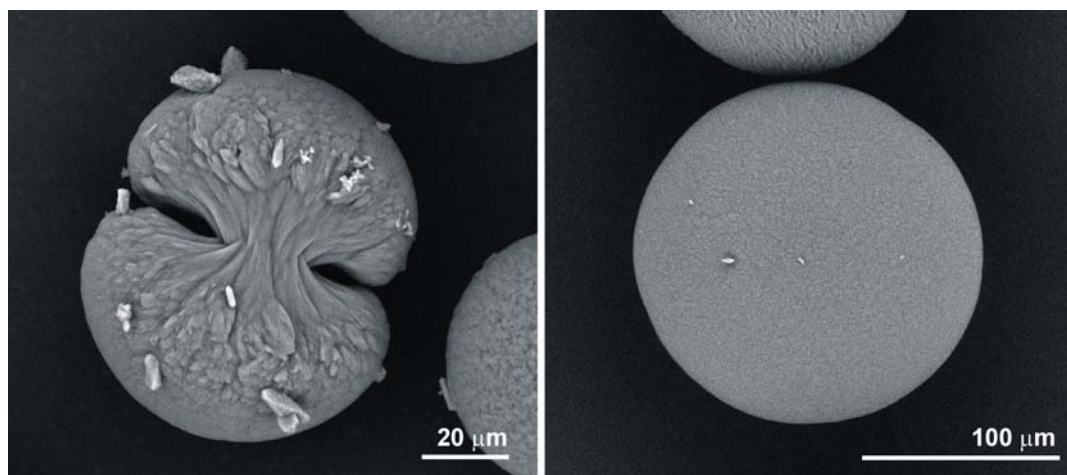


Fig. 3.4.52. SEM images of COM aggregates formed in the CM band of 2 wt.-% agar gel of pH 11.5 and 0.05M of the stock solutions at 37 °C after 3 days. Both the dumbbell-shaped COM (left) and the spherical COM (right) appear soft.

These smoother COM spheres appear to have formed from a dumbbell-shaped aggregate as shown in figure 3.4.53.

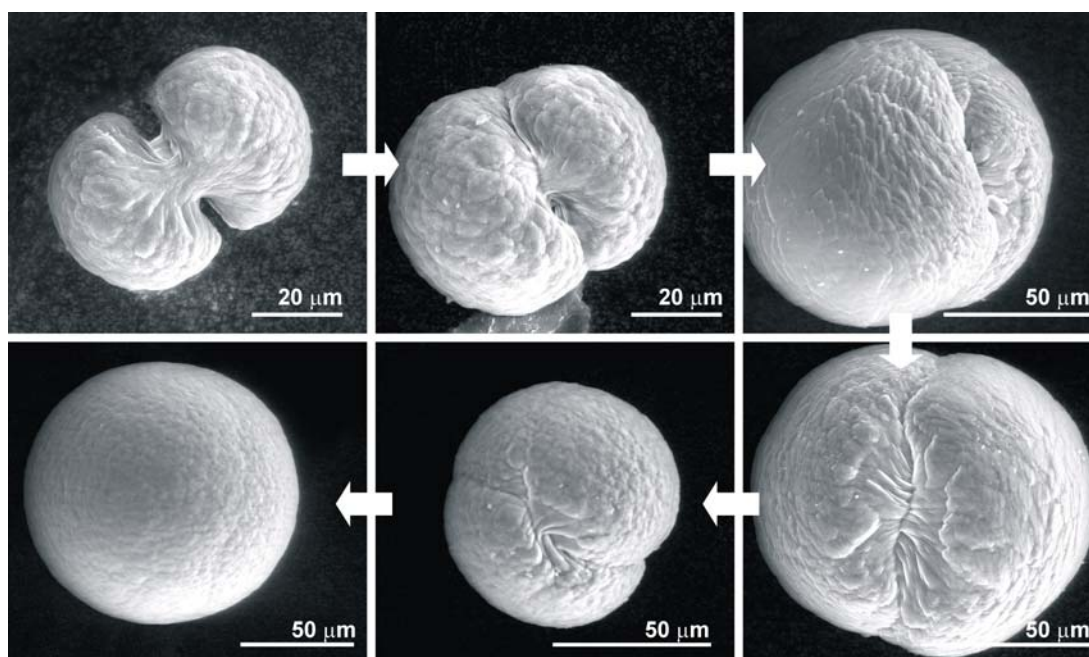


Fig. 3.4.53. Sequence (SEM images) of COM sphere formation *via* dumbbell morphologies. Arrows indicate the sequence.

It was also observed that some of the smooth COM spheres were sites for secondary nucleation processes. The spheres are then covered by a layer of radially grown lamellar crystallites (Fig. 3.4.54). After the formation of a smooth sphere, the decrease in supersaturation results in the formation of platy crystallites which get

aggregated on the surface of the sphere, thereby favouring the outer layer. These images confirm the core/shell architecture of all the COM spheres formed in agar gels.

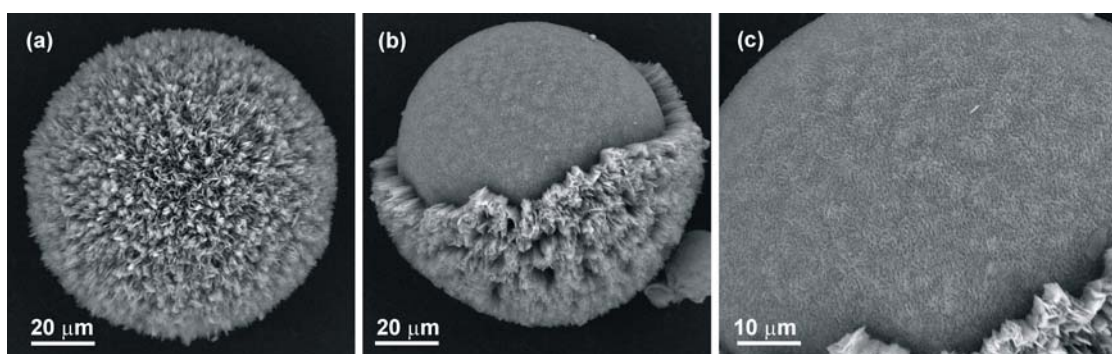


Fig. 3.4.54. (a) SEM images of a COM sphere formed in the CM band of 2 wt.-% agar gel of pH 11.5 and 0.05M of the stock solutions at 37 °C after 3 days. (b) a partially decalcified sphere with the enlarged core surface (c).

The COM spherulites formed in agar gels are similar to the biogenic COM stones. It has been reported that the biogenic COM stones contain a core consisting of small discrete particles, sometimes even of amorphous material buried in organic component and a shell of sheet-like COM crystallites interwoven with organic matter [189].

Up to now sheets of columnar COM crystallites which are common in urinary calculi were not produced under *in vitro* conditions. In a study of concretions developed on urinary catheters, it was found that the surface of the catheter was covered by a layer of organic matter on which a columnar layer of plate-like COM crystallites were grown [190]. Based on this observation, it was explained that intense nucleation process starting from the organic layer covering the core generates a large number of randomly orientated columnar COM crystals constituting the stone surface. Such columnar packed structures can be only formed due to the platy habit of COM crystals. The unusual platy habit of COM crystal is a consequence of the presence of urinary macromolecules that are preferentially adsorbed on the (-101) crystal faces. It was also claimed that COM columnar structures would be formed when a non-renewed/non-protected solid surface is in contact with urine containing normal calcium concentrations and with non physiological urinary pH values (physiological pH is between 5.5 and 6.5). This explanation seems adequate for the observation of radially orientated sheet-like crystals in the spheres formed in agar gel at all non-physiological pH values.

Finally, COD spheres were formed in the same gel close to the Ca side of the gel after 2 days (Fig. 3.4.55 top). These COD spheres are relatively low in yield and size (maximum 50 μm) and are always associated with a surface coating of the gel (Fig. 3.4.55 bottom). A thin layer of the gel remains even after repeated washing. These COD spheres show the typical Brewster-cross pattern (of centrosymmetric and radially oriented crystallites) when viewed with an optical microscope under crossed-polarizer (Fig. 3.4.55 right). These COD spheres were decalcified in 0.25N EDTA within 5 minutes. However, the residual agar gel coating retains the spherical shape after decalcification but does not show the Brewster-cross pattern.

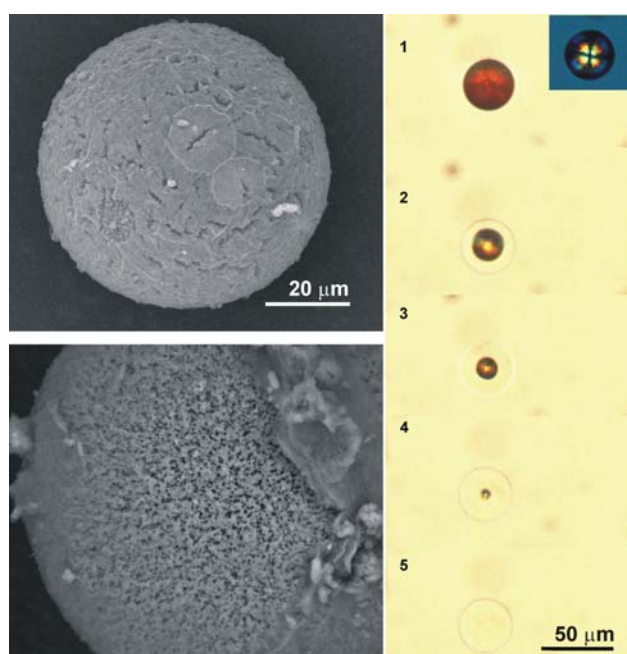


Fig. 3.4.55. (Top, bottom) SEM images of COD spheres from the C band of 2 wt.-% agar gel of pH 11.5 and 0.05 M of the stock solutions at 37 °C. (Right) Sequence of decalcification of a COD sphere in 0.25N EDTA solution. (Inset) A COD sphere under crossed- polarizers showing the characteristic brewster-cross.

3.4.1.5 Summary and discussion of results

The purpose of the investigations described in this chapter was to study the selective effect of agar on the growth and aggregation of calcium oxalates. Agar not only affects phase formation, but also the morphology. An increase of pH value of agar suppresses the growth of COM and favours the growth of COD. The hydrates formed depend on different parameters such as concentration of reactants, pH of the gel, temperature *etc.* In principle agar gel is a versatile gel which by adjusting the pH gives the possibility to tune the hydration state as well as morphology of calcium oxalates formed.

The results obtained in agar gel are summarized in the map presented in figure 3.4.56. At low pH values, agar gel produces COM rosettes which resemble the druse crystals of plants. At pH 8.5 COM spherulites and dumbbells are formed similar in morphology to urinary calculi. At higher pH values (11 to 12.5) tetragonal prisms and dumbbells of COD are formed. There is a striking relationship between the medium viscosity and the phase that forms. COM is crystallized in rigid gels (pH 5) when the rate of precipitation was low. COD is grown when the gel was less rigid. Also, at pH 5, COM crystals were formed towards the middle of the gel while at pH 11.5, the COD aggregates are formed more towards the oxalate source. This means a higher availability of oxalate leads to crystallization of COD.

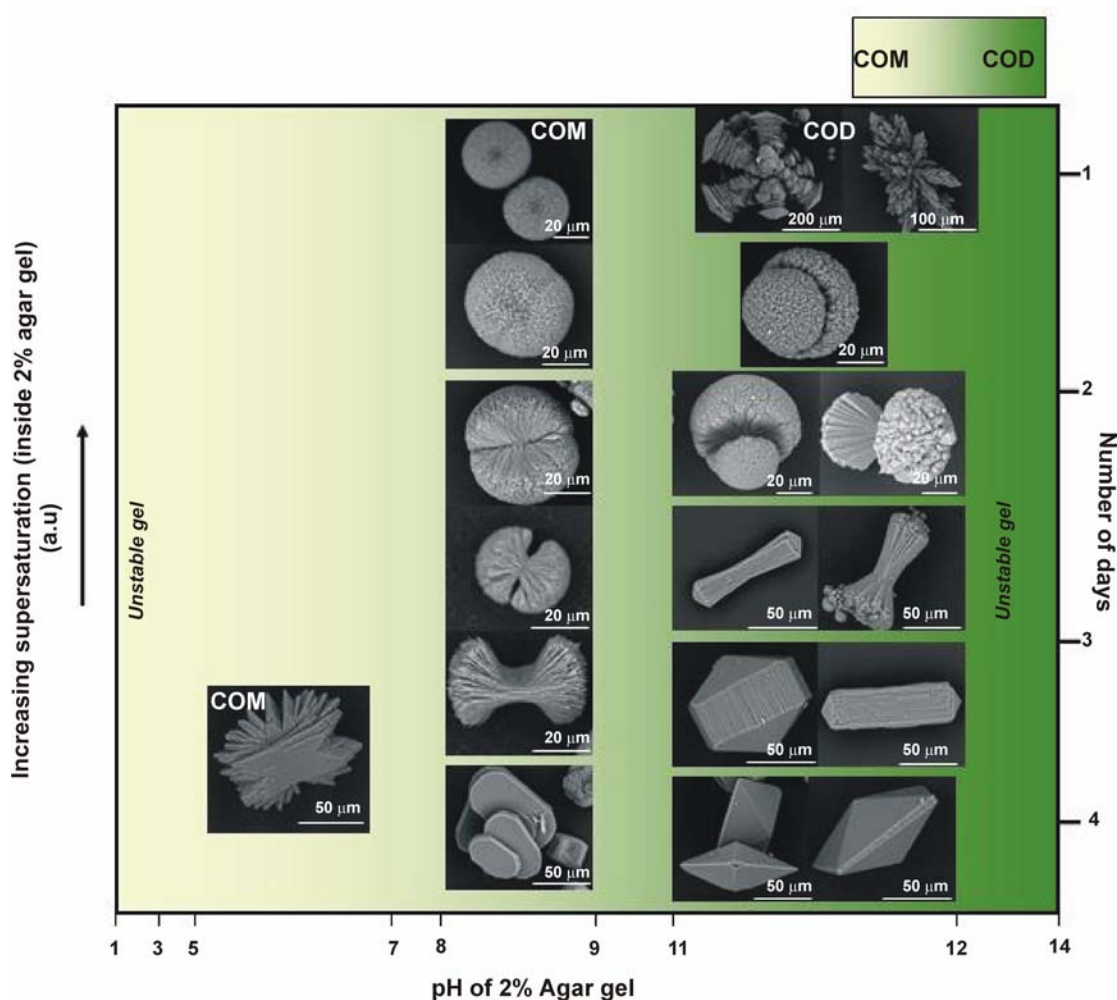


Fig. 3.4.56. Morphology and hydration state map of calcium oxalate aggregates grown in 2 wt.-% agar gels at different pH values.

The results obtained in 2 wt.-% agar gel of pH 8.5 are complicated. It can be arbitrarily summarized as shown in figure 3.4.57 based on the position and time of appearance of aggregates. The red curve represents the occurrence of COD and the black

curve, COM aggregates. The first crystals formed are always dendrites of COD. Sometime after the nucleation of COD, spherulites of COM are formed. In the CM band, dumbbells and sheaf of wheat morphologies of COM and all intermediate forms appear. The sequence ends in the C band with formation of COM twinned crystals. In general, the COM spherulites occupy the region close to the oxalate source and COM twins occupy the region close to the calcium source. All the intermediate morphologies are distributed between these two extremes.

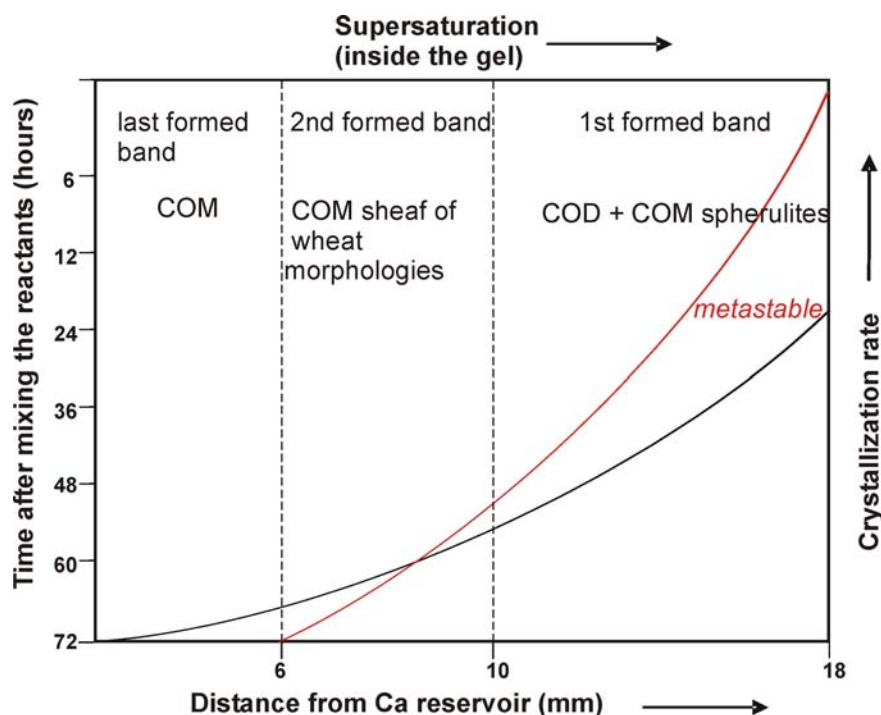


Fig. 3.4.57. A plot of the results obtained in 2 wt.-% agar gel of pH 8.5. First formed band is the M band. It is formed under the highest supersaturation conditions and consists of COM spherulites. Together with COM spherulites, a minor fraction of COD dendrites are also formed. The second formed band (CM band) consists of COM dumbbells. The third formed band (C band) is formed more towards Ca reservoir and consists of less aggregated crystals of COM. These results show that there is a gradient of supersaturation inside the gel which causes the development of these morphologies. The product obtained under the red curve is a mixture of COM and COD, while under the black curve it is only COM (thermodynamically stable phase).

It is evident that the development of morphology of COM crystals is related to changes in supersaturation inside the gel. The diffusion of ions through the gel forms gradients of pH and concentration along the gel column. Appearance of kinetically favoured COD (dendrites) among the aggregates formed in the M band suggests a high value of supersaturation attained by the system in this region. Fraction of COD formed in each of these bands is evidenced from the XRD patterns (Appendix Fig. 6.25). This means that a high metastability level is to be expected for this system. Or in other words,

the early growth stages of calcium oxalate crystals take place in the instability regions. The surface adsorption of agar is also evident from the change in COM crystal habit from six-sided platelet to rectangular platelets and needles.

According to classical theory of homogeneous nucleation, the term “critical supersaturation” is used to define the supersaturation value above which the nucleation rate rapidly increases (Fig. 3.4.58). Critical supersaturation is the boundary between metastable and the labile state. As the critical supersaturation increases different morphologies develop as described in section 1.2.5. However, in diffusing reactant systems, as in the present case, the pH, the concentration of the ions and thus the supersaturations change continuously. For such inhomogeneous systems, the concept of “threshold supersaturation” has been developed [66, 186]. This is a dynamic concept of supersaturation and none other than the metastability level. In a gel column, different levels of metastability can be reached.

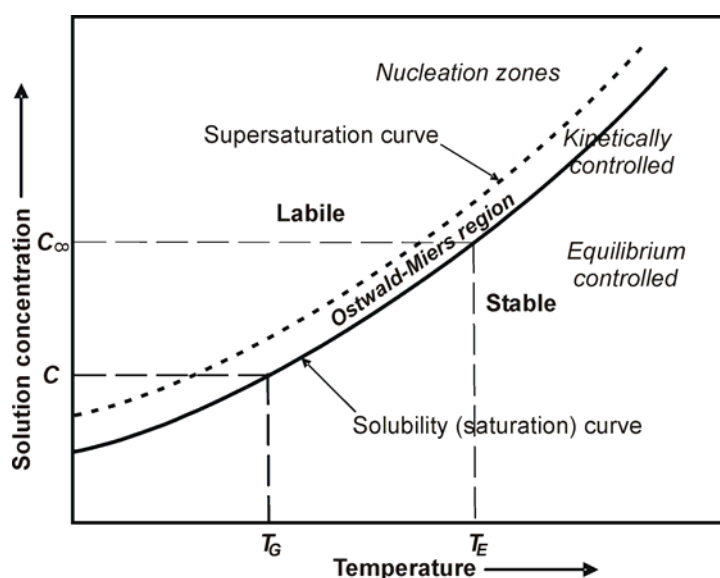


Fig. 3.4.58. Solubility curve (solid line, equilibrium curve) and the Ostwald-Miers region (metastable zone, the region where spontaneous nucleation and growth hardly occur). The driving force (supersaturation) relates to the difference between the dotted line and the solubility curve. C_∞ is the concentration at the equilibrium temperature T_E and C is the concentration at the growth temperature, T_G [61].

In the present case, it is assumed that the supersaturation is increased as the distance from the calcium source is increased. As a result, the metastability level is also increased. This can explain the appearance of metastable COD in the regions close to the oxalate source. Later, progressive decrease in supersaturation causes the rest of the morphologies of COM. The supersaturation is still maintained higher which is evidenced

from the appearance of spherulites. Hence, the surface adsorption of agar together with higher supersaturation causes the morphological variations in this case.

It is interesting to note that at pH 11.5, the factors favouring the formation of COM are suppressed and hence COD is favoured. Or in other words, inhibition of COM by agar reaches a maximum at pH 11.5. It was found that, as the pH of the gel was increased to pH 11.5, the gel was fragile and therefore may be causing faster diffusion of ions. The aggregates are formed more towards the oxalate source in this case. This also means a high oxalate ion concentration in this range and therefore an enhanced ion activity and hence an increased supersaturation. In this case also, the adsorption of agar on the crystal faces of COD is evident from the structuring seen on the (100) faces of COD (Fig. 3.4.43). Therefore, agar may be decreasing the interfacial energy of (100) faces of COD. As a result, the COD nuclei are not dissolved and agar retards the growth of COM by adsorbing on the active growth sites.

According to classical crystallization, in the range of spontaneous nucleation, many small crystals are formed, but few big ones may also be found in the metastable range. When the aggregates grow, the formed crystals/ aggregates serve as nuclei for further crystallization. So, it seems that these crystallization events are most likely located in the "Ostwald-Miers" space (Fig. 3.4.58). Ostwald-Miers space is the space between spontaneous nucleation curve and saturation curve in a saturation-temperature diagram. In this range nucleation does not take place but seed crystals can grow because of supersaturation. Nevertheless, the supersaturation remains unaffected so that any particle acting as crystallization base may increase in size. The breadth of the Ostwald-Miers range depends on nucleation energy. This may be varied by the presence of additives.

A similar study on the influence of magnesium ions on the solubility of calcium oxalates by Wunderlich *et al.* [193] showed that metastable COD crystals were formed when Mg^{2+} concentration, reaction temperature and precipitation velocity were combined in the proper way. It was opined that Mg^{2+} ions may be broadening the Ostwald-Miers space, thus favouring the formation of larger crystals.

Presence of agar may be increasing the breadth of Ostwald-Miers space. As a result the supersaturation threshold value to nucleate calcium oxalate crystals may be increased. Also the spontaneous nucleation of COM is inhibited. Smaller nuclei may be formed in the upper Ostwald-Miers space. Such nuclei may act as seeds for the growth of big crystals. A continuous crystal growth on such a seed crystal will occur if the

supersaturation of the solution is located within the Ostwald-Miers range. However, under such conditions, the growth rate on the seed crystal is usually low. In order to increase the growth rate, a higher supersaturation above the upper limit of Ostwald-Miers region is necessary.

The present work is mainly focused on the phase occurrence and morphologies of COM, COD and COT in the presence of organic additives. For the measurement of the breadth of the Ostwald-Miers space of such a complicated system, many investigations of the kinetics of crystallization under these conditions are necessary. Therefore, objectives of future research involve investigating if agar at elevated pH values: 1) increases the supersaturation by enhancing the diffusion of ions, 2) decreases the interfacial energy of COD and stabilizes COD nuclei, 3) increases the threshold supersaturation for the formation of COM, 4) broadens the Ostwald-Miers space.

It has also been found that the crystallization temperature influences the aggregation of crystals. For instance, crystallization studies at 25 °C showed that the COD aggregates formed is just symmetric dendrites of the normal tetragonal crystals (Appendix Fig. 6.23). An increase in temperature (37 °C) resulted in the increase in the amount of COM aggregates. COT has not been found during our experiments, and it is also only rarely found in urine and kidney stones. As urinary stone formation (including nucleation, growth and agglomeration of crystals) takes place in human kidney in a fixed, gel-like state from a flow of supersaturated urine, this model is relevant for simulating the growth and morphology of urinary stones. Moreover our results validate the recent finding that calcium phosphate substrates are not required for the renal deposition and other factors such as local supersaturations are involved [57,180].

It is widely accepted that the morphologies and hydration states of calcium oxalate are extremely sensitive to alterations in growth conditions. Spherulitic crystallization is common among inorganic salts crystallizing in gels of high viscosity and relative by crystallization [191]. Without further investigations, it is intricate to attempt to discuss the prominence of spherulites in this system. Keith and Padden [184] proposed a phenomenological theory including the presence of impurity-rich layers around the crystallization front limiting the diffusion of material to the crystallization front and causing fibrillation of crystallites resulting in spherulites. An alternative point of view is that high viscosity inducing diffusion-limited conditions is the driving force behind spherulitic crystallization [192], and kinetic effects are dominating.

3.4.2 Growth of calcium oxalates in other organic gels

3.4.2.1 Agarose

The formation of COD aggregates in agar gel at higher pH values is assumed to be due to the presence of agarose component in agar. In order to get more insight into the development of COD, the growth of calcium oxalates was also conducted in pure agarose gels.

Synthesis: Crystallization of calcium oxalate by the double diffusion technique was performed in 2 wt.-% agarose (SeaKem LE Agarose, Biozym Scientific GmbH) with the pH of the gel pre-adjusted to 11.5. The stock solutions, 0.05 M of both $\text{CaCl}_2 \cdot 2\text{H}_2\text{O}$ and $\text{Na}_2\text{C}_2\text{O}_4$ were also adjusted to the pH 12.0 to increase the initial supersaturation. The required amount of agarose was slowly added to water at 90 °C and stirred until it formed a clear solution. A clear gel was formed upon cooling to 4 °C. The entire set-up was kept in a water bath at 20 °C. After a period of 2 days, the aggregates formed were separated and treated with water and the products were washed five times in hot distilled water, centrifuged and finally dried at 40 °C.

Results and discussions: Over a period of two days, calcium oxalate aggregates were formed inside the gel in two bands. The XRD pattern indicated that the aggregates in the C band consisted of COD and the aggregates in the M band were COM (Appendix Fig. 6.26). The morphology of the aggregates is shown in figure 3.4.57. COM spheres formed with sizes ranging from 80 to 100 μm showed rough surfaces (Fig. 3.4.57 c). COD aggregates formed were poor in yield. However, the cross-section of COD spheres shows radially arranged fibre crystallites (Fig. 3.4.57 e,f).

Agarose gels were stable only at temperatures less than 25 °C. Also, the gels obtained after the double diffusion reactions were not firm at all and therefore the products could not be isolated well. Therefore, a definite phase analysis was difficult. Such an instability and poor handling properties of agarose gel made it difficult to study the reactions under various conditions. The results were not reproducible as well. As the morphological features produced in agar gels were not reproducible by using pure agarose gels, it can be inferred that the agarpectin component of agar is also necessary for the specific morphologies of COM and COD.

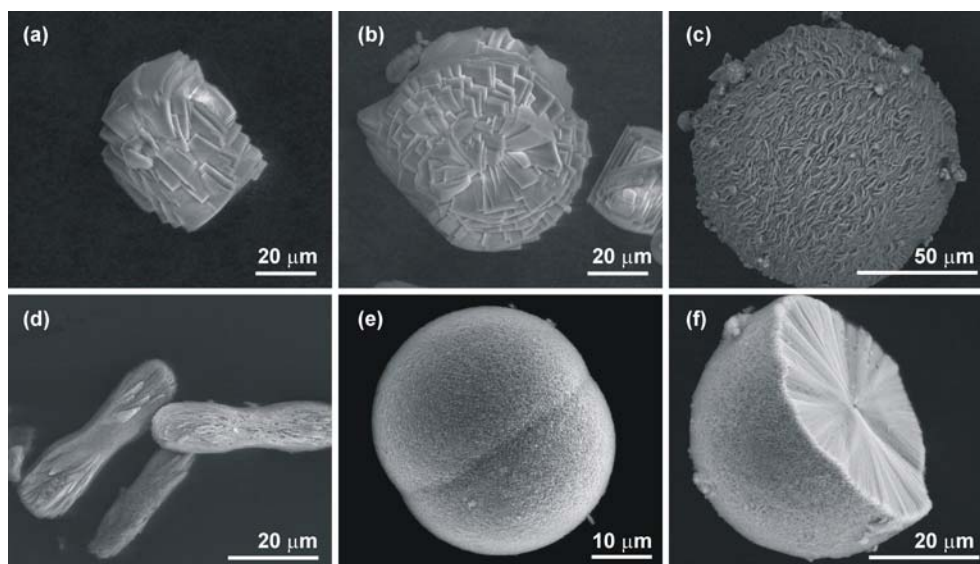


Fig. 3.4.57. SEM images of calcium oxalate aggregates formed in 2 wt.-% agarose gel of pH 11.5. (a-c) COM aggregates formed in the M band, (d-f) COD aggregates formed in the C band.

3.4.2.2 Carrageenan

Synthesis: Crystallization of calcium oxalates by the double diffusion technique was performed in 3 wt.-% carrageenan gel with 0.05 M stock solutions ($\text{CaCl}_2 \cdot 2\text{H}_2\text{O}$ and $\text{K}_2\text{C}_2\text{O}_4$). Potassium oxalate instead of sodium oxalate was used as the oxalate source. This was because the gel retrieved after the diffusion of sodium oxalate was unstable. The resultant gel after the diffusion of potassium oxalate and calcium chloride solutions stayed firm and the aggregates could be easily separated [99,100].

A 3 wt.-% carrageenan gel is unstable at pH values less than 5 and greater than 9. Therefore, the experiments were performed with 3 wt.-% carrageenan gel at pH 8.5. The required amount of carrageenan (CP Kelco Aps, Denmark) (Type III, from *Eucheuma cottoni*) was slowly added to water at 90 °C and the pH was adjusted to 8.5 with 2 N NaOH. A transparent gel was formed upon cooling to room temperature. The pH of the stock solutions was adjusted to 7.5 using tris (hydroxymethyl) methylamine/ HCl. The entire set-up was kept in a water bath at 37 °C. Over a period of 10 days, a single band was formed closer to the Ca source. The isolated products were treated with hot distilled water and dried at 40 °C.

Results and discussions: The reaction over a period of 10 days in 3 wt.-% carrageenan gel of pH 8.5 resulted in the formation of COM aggregates as shown in figure 3.4.58.

Along with COM, a minor fraction of COD dendrites were also observed (Appendix Fig. 6.27).

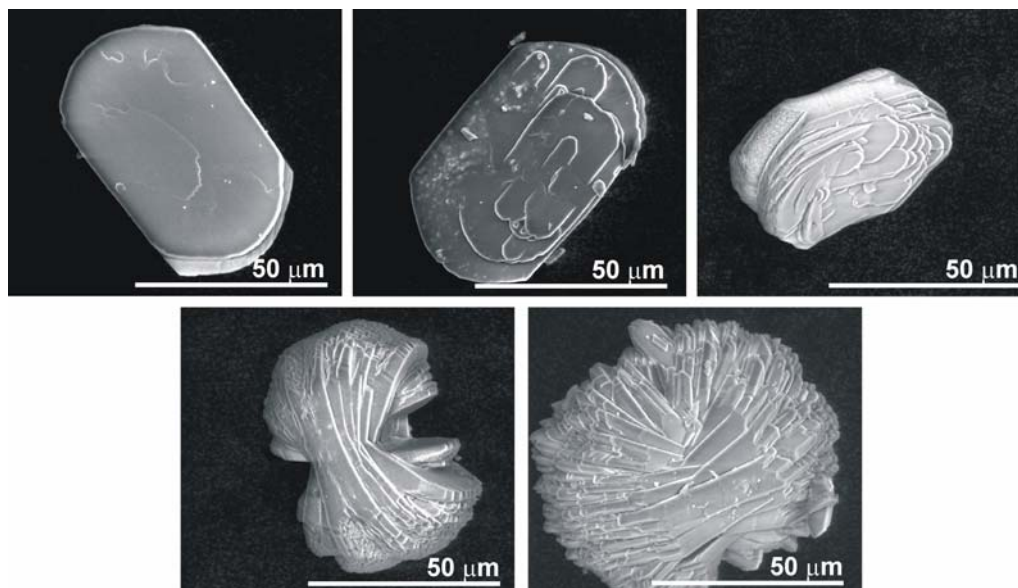


Fig. 3.4.58. SEM images of COM aggregates formed in 3 wt.-% carrageenan gel of pH 8.5.

As in the case of pure agarose gels, the results obtained were not reproducible and instability of the gel made further investigations difficult to carry out. The aggregates were distributed throughout the gel and the gel obtained after the reactions were brittle. Even after repeated washing at elevated temperatures, the calcium oxalate aggregates could not be retrieved.

3.4.2.3 Gelatine

Synthesis: Double diffusion experiments were also performed in 10 wt.-% gelatine gel. The stock solutions, 0.05 M of both $\text{CaCl}_2 \cdot 2\text{H}_2\text{O}$ and $\text{Na}_2\text{C}_2\text{O}_4$ were adjusted to the physiological pH of 7.4 with tris(hydroxymethyl)methylamine/HCl. A bacteriostatic agent consisting of 1g/L of benzoic acid, n-propyl-4-hydroxy benzoate and sorbic acid was also added to the stock solutions to preserve the gel. The experiments were performed with different pH values of the gel and the reactions were allowed to proceed at a constant temperature (25 °C) for 14 days. The bands formed at the middle of the gel matrix was separated by cutting and washed with hot distilled water to get rid of gelatine. Finally the sample was dried at 40 °C for 6 hours and stored at room temperature.

Results and discussions: After 14 days the calcium oxalates formed in 10 wt.-% gelatine gel of pH 3 and 5 were identified as COM grown as agglomerates of twinned crystallites

as shown in figure 3.4.59. The aggregates formed are identified as COM as confirmed by XRD and TG (Appendix Fig. 6.28). The chemical analysis of the COM aggregates grown from 10% gelatine gel of pH 5 indicated 26.66(\pm 0.20) wt.-% Ca, 16.71(\pm 0.03) wt.-% C, 1.66(\pm 0.01) wt.-% H and 35.56(\pm 0.38) wt.-% O in comparison to the calculated values of 27.43 wt.-%, 16.44 wt.-%, 1.38 wt.-% and 54.75 wt.-% respectively. These aggregates also contains less than 0.18 wt.-% of nitrogen which implies that the gelatine content in these samples are less than 1.07 wt.-%.

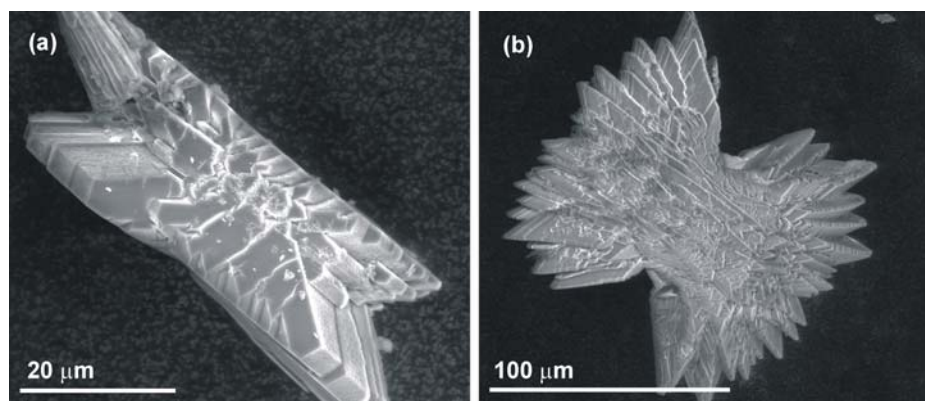


Fig. 3.4.59. SEM images of COM grown in 10 wt.-% gelatine gel of (a) pH 3, (b) pH 5.

The degree of aggregation was found to increase with increasing pH value of the gel. COM aggregates grown in 10 wt.-% gelatine gel of pH 8 to 9 appeared to be formed by less controlled aggregation processes (Fig. 3.4.60).

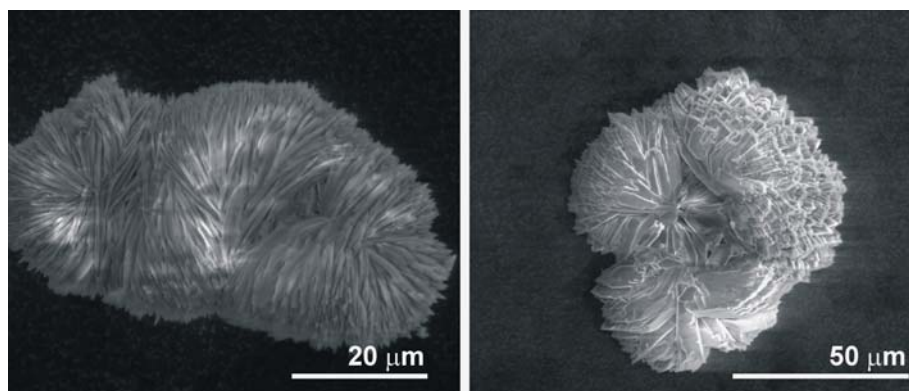


Fig. 3.4.60. SEM images of COM aggregates grown in 10 wt.-% gelatine gel of pH 8.5.

The aggregates formed in gelatine gel at all pH values were identified as COM. The presence of COD or COT was not observed in pure gelatine gels. Moreover, the gel was not stable at higher pH values ($\text{pH} > 9$) which implies the limited applicability of gelatine gels to study calcium oxalate stone genesis.

4 Conclusion and outlook

With respect to the principles of biomineralization, it is of interest to study the crystallization of calcium oxalates under various experimental conditions. Calcium oxalates (COM: calcium oxalate monohydrate; COD: - dihydrate; COT: - trihydrate) play decisive roles as biominerals in plants and as pathological “stones” in vertebrates. As a first step to unravel the complex pathology of uro/nephro lithiasis, we started to investigate the structure and morphology of calcium oxalates crystallized in the presence of organic additives. The present work is mainly devoted to the morphological control of calcium oxalate hydrates in the presence of the sodium salt of polyacrylic acid (PAA) as well as in agar gel.

Apart from the investigations on the hydrated forms of calcium oxalate, the crystal structure of anhydrous calcium oxalate was determined by a combination of atomistic simulations and rietveld refinements [104]. For this, the dehydration of COM was mimicked *in silico* to receive an initial model of the crystal structure of anhydrous calcium oxalate. This general approach may also be accessible for other decomposition processes ending up with crystalline powders of unknown crystal structure.

Biomimetic growth and morphological control of calcium oxalates were achieved in the presence of polyacrylate (PAA) and in agar gel. The products were characterized mainly with powder X-ray diffraction, optical and electron microscopic techniques.

Initially, the crystallization of calcium oxalates from aqueous solution was investigated in the absence and in the presence of PAA by varying the pH value and the initial supersaturation. In both cases, these two parameters turned out to be critical in determining the hydration state of calcium oxalates. The results are summarized in form of morphology maps in figures 3.1.2 and 3.3.3.

The growth pattern of crystals and aggregates is clearly dependent on the concentration of PAA. Apart from these experiments, the interaction of PAA with (100) and (101) crystal faces of COD was explored with the aid of atomistic simulations which confirmed that during crystal growth, specific adsorption processes of PAA on (100) faces seems to control the shape development. Our investigations show that the inner architecture of all the morphological varieties of COD was found to be dominated by an inner core consisting of thin elongated crystallites together with incorporated PAA and an outer shell formed as part of secondary nucleation processes. From our investigations

we propose that for all types of COD aggregates, relative proportion of calcium oxalate and PAA dictates the shape and formation of nanometer sized crystallites which then aggregate and align to form the less crystalline core. Such cores enriched with PAA may act as the sites for secondary nucleation events of calcium oxalate crystallites which then cover the core like a shell.

Although our results offer better insights on the COD-PAA system in matter of pH dependence, superstarurations and concentrations, the damage of the samples by electron beam irradiation made further analysis intricate. The hypothesis on morphogenesis can be validated only by tracking the time-resolved particle growth *in situ*. Due to the problems associated with irradiation damage, different stages of particle formation from nanoscale to microscale could not be followed.

In addition, our results show that the double diffusion technique in agar gel is a convenient route to grow calcium oxalate aggregates showing close resemblance to biogenic calculi and to study their ontogeny. The results are summarized in the map presented in figure 3.4.56. Agar gel at pH 8.5 was found to form COM dumbbells and spherulites and at pH 11.5 forms COD aggregates. Finally it was noted that pure gelatine gel gives COM at all pH values where as agar gives COM and COD with variation in pH. This reflects the fact that the condition of thermodynamic instability is brought forth by the presence of polysaccharides and therefore agar gel is more similar to the conditions prevailing *in vivo*. Also, these results emphasize the dual role of agar as mineralization promoters of and inhibitors of COM.

The present work constitutes first evidence of the promotory effect of polysaccharides based on the agar gel model and on the aggregation of calcium oxalates which is an obligatory step in urolithiasis. To date, the models used to simulate the morphology of urinary calculi are either animal models based on intoxicating and sacrificing rats, or the gel model by the overgrowth of calcium oxalate on calcium phosphate [57,194]. Our method provides a convenient route to study the ontogeny of urinary calculi. Atomistic simulations may be useful to explore the interaction of agar at different pH values with specific faces of COM and COD. Such an approach can provide further insight into the morphological control gained in this system. If the phenomena and processes that can only be observed under *in vivo* conditions can be deduced, the true role of polysaccharides in “calculogenesis” can be discovered which may be helpful in the design of synthetic therapeutics against kidney stone formation.

5 References

1. S. Mann.
Biom mineralization - Principles and Concepts in Bioinorganic Materials Chemistry.
Oxford University Press, Oxford, **2001**.
2. H.A. Lowenstam, S. Weiner.
On Biom mineralization.
Oxford University Press, Oxford, **1989**.
3. S. Mann.
The Chemistry of Form.
Angew. Chem. Int. Ed., **2000**, 39(19), 3392-3406.
Angew. Chem., **2000**, 112(19), 3532-3548.
4. S.W. Weiner, L. Addadi.
Design Strategies in Mineralized Biological Materials.
J. Mater. Chem., **1997**, 7(5), 689-702.
5. T. Kato, A. Sugawara, N. Hosoda,
Calcium carbonate – Organic Hybrid Materials.
Adv. Mater., **2002**, 14(12), 869-877.
6. R. Kniep, P. Simon.
Fluorapatite-gelatine-nanocomposites: Self-organized Morphogenesis, Real Structure and Relations to Natural Hard Materials.
Top. Curr. Chem., **2007**, 270, 73-125.
7. R. Kniep, S. Busch.
Biomimetic Growth and Self-Assembly of Fluorapatite Aggregates by Diffusion into Denatured Collagen Matrices.
Angew. Chem. Int. Ed Engl., **1996**, 35(22), 2623-2626.
Angew. Chem., **1996**, 108(22), 2788-2791.
8. S. Busch, U. Schwarz, R. Kniep.
Morphogenesis and Structure of Human Teeth in Relation to Biomimetically Grown Fluorapatite-gelatine Composites.
Chem. Mater., **2001**, 13(10), 3260-3271.
9. H. Cölfen, L. Qi.
A Systematic Examination of the Morphogenesis of Calcium Carbonate in the Presence of a Double-Hydrophilic Block Copolymer.
Chem. Eur. J., **2001**, 7(1) 106-116.
10. S.H. Yu, H. Cölfen, A.W. Xu, W.F. Dong.
Complex Spherical BaCO₃ Superstructures Self-Assembled by a Facile Mineralization Process under Control of Simple Polyelectrolytes.
Cryst. Growth Des., **2004**, 4(1), 33-37.

11. L.M. Qi, H. Cölfen, M. Antonietti, M. Li, J.D. Hopwood, A.J. Ashley, S. Mann. Formation of BaSO₄ Fibres with Morphological Complexity in Aqueous Polymer Solutions. *Chem. Eur. J.*, **2001**, 7(16), 3526-3532.
12. A. Bigi, E. Boanini, D. Walsh, S. Mann. Morphosynthesis of Octacalcium Phosphate Hollow Microspheres by Polyelectrolyte-Mediated Crystallization. *Angew. Chem. Int. Ed.*, **2002**, 41(12), 2163-2166. *Angew. Chem.*, **2002**, 114(12), 2255-2257.
13. J. Yu, H. Tang, B. Cheng, X. Zhao. Morphological Control of Calcium Oxalate Particles in the Presence of Poly(styrene-alt-maleic acid). *J. Solid State Chem.*, **2004**, 177, 3368-3374.
14. F. Grases, A. Costa-Bauza, L. Garcia-Ferragut. Biopathological; Crystallization: A General View About the Mechanisms of Renal Stone Formation. *Adv. Colloid. Interface Sci.*, **1998**, 74, 169-194.
15. E.J. Westbury. Some Observations on the Quantitative Analysis of Over 1000 Urinary Calculi. *Br. J. Urol.*, **1974**, 46, 215-227.
16. L.H. Smith. The Many Roles of Oxalate in Nature. *Trans. Am. Clin. Climatol. Assoc.*, **2002**, 113, 1-20.
17. V.R. Franceschi, H.T. Horner, Jr. Calcium Oxalate Crystals in Plants. *Botanical Review*, **1980**, 46(4), 361-427.
18. M.A. Webb. Cell-mediated Crystallization of Calcium Oxalate in Plants. *Plant Cell*, **1999**, 11, 751-761.
19. P.V. Monje, E.J. Baran. Characterization of Calcium Oxalates Generated as Biominerals in Cacti. *Plant Physiol.*, **2002**, 128, 707-713.
20. V. Tazzoli, C. Domeneghetti. The Crystal Structure of Whewellite and Weddellite: Re-examination and Comparison. *Am. Mineral.*, **1980**, 65 (3-4), 327-334.
21. T. Echigo, M. Kimata, A. Kyono, M. Shimizu, T. Hatta. Re-investigation of the Crystal Structure of Whewellite [Ca(C₂O₄)·H₂O] and the Dehydration Mechanism of Caoxite [Ca(C₂O₄)·3H₂O]. *Mineral. Magazine*, **2005**, 69(1), 77-88.

22. G. Schubert, B. Ziemer.
A New Calcium Oxalate Monohydrate produced by Thermal Dehydration of Weddellite.
Cryst. Res. Technol., **1981**, 16(9), 1025-1031.
23. S. Deganello, O.E. Piro.
The Crystal Structure of Calcium Oxalate Monohydrate (Whewellite).
N. Jb. Miner. Mh., **1981**, 2, 81-88.
24. S. Deganello.
The Basic and Derivative Structures of Calcium Oxalate Monohydrate.
Z. Kristallogr., **1980a**, 152, 247-252.
25. S. Deganello.
The Structure of Whewellite, $\text{CaC}_2\text{O}_4 \cdot \text{H}_2\text{O}$, at 328K.
Acta. Cryst., **1981**, 37B, 826-829.
26. D. Aquilano, M. F-Angela.
Twin Laws of Whewellite, $\text{CaC}_2\text{O}_4 \cdot \text{H}_2\text{O}$. A Structural and Growth Approach.
Phys. Chem. Minerals, **1981**, 7, 124-129.
27. A. Millan.
Crystal Growth Shape of Whewellite Polymorphs: Influence of Structure Distortions on Crystal Shape.
Cryst. Growth Des., **2001**, 1(3), 245-254.
28. A.M. Cody, R.D. Cody.
Contact and Penetration Twinning of Calcium Oxalate Monohydrate ($\text{CaC}_2\text{O}_4 \cdot \text{H}_2\text{O}$).
J. Cryst. Growth, **1987**, 83, 485-498.
29. L. Brecevic, D. Skrtic, J. Garside.
Transformation of Calcium Oxalate Hydrates.
J. Cryst. Growth, **1986**, 74, 399-408.
30. F. Grases, A. Millan, A. Conte.
Production of Calcium Oxalate Monohydrate, Dihydrate or Trihydrate. A Comparative Study.
Urol. Res., **1990**, 18, 17-20.
31. H. Yu, R. Sheikholeslami, W.O.S. Doherty.
Calcium Oxalate Crystallization in Silica and Sugar Solutions- Characterization of Crystal Phases and Habit.
Powder Technol., **2005**, 160, 2-6.
32. C. Sterling.
Crystal Structure Analysis of Weddellite, $\text{CaC}_2\text{O}_4 \cdot (2+x)\text{H}_2\text{O}$.
Acta Cryst., **1965**, 18, 917-921.
33. J.A. Mandarino, V.W. Noble.

- Weddellite from Biggs, Oregon, U.S.A.
Can. Mineral., **1983**, 21, 503-508.
34. S. Deganello, A.R. Kampf, P.B. Moore.
The Crystals Structure of Calcium Oxalate Trihydrate : $\text{Ca}(\text{H}_2\text{O})_3\text{C}_2\text{O}_4$.
Am. Mineral., **1981**, 66(7-8), 859-865.
35. N.S. Blom, J.A. Kantere, W.M. Heijnen.
Calcium Oxalate Trihydrate, $\text{CaC}_2\text{O}_4 \cdot 3\text{H}_2\text{O}$.
Cryst. Struct. Comm., **1981**, 10, 1283-1288.
36. W.M.M. Heijnen.
The Growth Morphology of Calcium Oxalate Trihydrate: A Contribution to
Urinary Stone Research.
J. Cryst. Growth, **1982**, 57, 216-232.
37. R.L. Frost, M.L. Weier.
Thermal Treatment of Whewellite- a Thermal Analysis and Raman
Spectroscopic Study.
Thermochim. Acta, **2004**, 409(1), 79-85.
38. R.L. Frost, M.L. Weier
Thermal Treatment of Weddellite- a Raman and Infrared Emission Spectroscopic
Study.
Thermochim. Acta, **2003**, 406(1-2), 221-232.
39. L. Walter-Levy, J. Laniece
Sur la thermolyse des hydrates de l'Oxalate de calcium.
C.R. Acad. Sc. Paris **1964**, 259, 4685-4688.
40. R. Hocart, G. Watelle-Marion, G. Thrierr-Sorel, A. Gerard.
Nature topotactique de la deshydratation.
N.C.R. Acad. Sc. Paris **1965**, 260, 2509-2511.
41. N. Gerard.
Diagramme pression- temperature de $\text{CaC}_2\text{O}_4 \cdot \text{H}_2\text{O}$ et des deux varieties
polymorphiques de CaC_2O_4 .
C.R. Acad. Sc. Paris **1965**, 261, 2363-2366.
42. T.A. Shippey.
Vibrational Studies of Calcium Oxalate Monohydrate (Whewellite) and an
Anhydrous Phase of Calcium Oxalate.
J. Mol. Struct., **1980**, 63, 157-166.
43. R. Hocart, N. Gerard, G. Watelle-Marion.
Sur la pyrolyse des Oxalates de calcium hydrates.
C.R. Acad. Sc. Paris **1964**, 258, 3709-3712.
44. D. Duval, R.A. Condrate.
A Raman Spectral Study of the Dehydration of Calcium Oxalate Monohydrate.

- Appl. Spectrosc., **1988**, 42(4), 701-703.
45. E. Sokol, E. Nigmatulina, N. Maksimova, A. Chiglintsev.
CaC₂O₄·H₂O Spherulites in Human Kidney Stones: Morphology, Chemical Composition and Growth Regime.
Eur. J. Mineral., **2005**, 17, 285-295.
46. F.J. Opalko, S.R. Khan.
Heterogeneous Nucleation of Calcium Oxalate Trihydrate in Artificial Urine by Constant Composition.
J. Cryst. Growth, **1997**, 181, 410-417.
47. D. Ward, M. Spiegel, D. Saltz.
Gazelle Herbivory and Interpopulation Differences in Calcium Oxalate Content of Leaves of a Desert Lily.
J. Chem. Ecol., **1997**, 23(2), 333-346.
48. H. Katayama, Y. Fujibayashi, S. Nagaoka, Y. Sugimura.
Cell wall Sheath Surrounding Calcium Oxalate Crystals in Mulberry Idioblasts.
Protoplasma, **2007**, 231, 245-248.
49. J.A. Wesson, M.D. Ward.
Pathological Biomineralization of Kidney stones.
Elements, **2007**, 3(6), 415-421.
50. S.R. Khan, D.J. Kok.
Modulators of Urinary Stone Formation.
Front. Biosci., **2004**, 9, 1450-1482.
51. W.H. Boyce.
Organic Matrix of Urinary Concretions.
Am. J Med., **1968**, 45, 672-683.
52. I. Thorne, M.I. Resnick.
Urinary Macromolecules and Renal Lithiasis.
World J. Urol., **1983**, 1, 138-145.
53. S. Sandersius, P. Rez.
Morphology of Crystals in Calcium Oxalate Monohydrate Kidney Stones.
Urol. Res., **2007**, 35(6), 287-293.
54. A. Millan.
Crystal Morphology and Texture in Calcium Oxalate Monohydrate Renal Calculi.
J. Mat. Sci., Materials in medicine, **1997**, 8(5), 247-250.
55. J.A. Carr.
The Pathology of Urinary Calculi: Radial Striation.
Br. J. Urol., **1953**, 25(1), 26-23.

56. K.M. Kim, F.B. Johnson.
Calcium Oxalate Crystal Growth in Human Urinary Stones.
Scanning Elect. Microsc. III, **1981**, 146, 147-154.
57. S.R. Khan, P.A. Glenton.
Calcium Oxalate Crystal Deposition in Kidneys of Hypercalciuric Mice with Disrupted type IIa Sodium-phosphate Cotransporter.
Am. J. Physiol. Renal Physiol., **2008**, 294(5), F1109-F1115.
58. F. Grases, L. Masarova, O. sohnel, A. C-Bauza.
Agglomeration of Calcium Oxalate Monohydrate in Synthetic Urine.
Br. J. Urol., **1992**, 70(3), 240-246.
59. T. Jung, X. Sheng, C.K. Choi, W. -S. Kim, J.A. Wesson, M.D. Ward.
Probing Crystallization of Calcium Oxalate Monohydrate and the Role of Macromolecule Additives with in Situ Atomic Force Microscopy.
Langmuir, **2004**, 20 (20), 8587-8596.
60. H. Shiraga, W. Min, W.J. VanDusen, M.D. Clayman, D. Miner, C.H. Terrell, J.R. Sherbotie, J.W. Foreman, C. Przysiecki, E.G. Neilson, J.R. Hoyer.
Inhibition of Calcium Oxalate Crystal Growth in vitro by Uropontin: Another member of the Aspartic acid-rich Protein Superfamily.
Proc. Natl. Acad. Sci., **1992**, 89(1), 426-430.
61. I. Sunagawa.
Crystals Growth, Morphology and Perfection.
Cambridge University Press, Cambridge, **2005**.
62. H. Imai, Y. Oaki, A. Kotachi.
A Biomimetic Approach for Hierarchically Structured Inorganic Crystals Through Self-organization.
Bull. Chem. Soc. Jpn., **2006**, 79(12), 1834-1851.
63. J. Hulliger.
Chemistry and Crystal Growth.
Angew. Chem., Int. Ed. Engl., **1994**, 33(2), 143-162.
Angew. Chem., **1994**, 106(2), 151-171.
64. P.L. Blackwelder, N. Watanabe.
Research Reports Biomineralisation.
Vol. 9, Ed.: H. K. Erben, F. K. Schattauer Verlag, Stuttgart-New York, **1977**.
65. L. Granasy, T. Pusztai, G. Tegze, J.A. Warren, J.F. Douglas.
Growth and Form of Spherulites.
Phys. Rev. E., **2005**, 72, 011605, 1-15.
66. L. Fernandez-Diaz, A. Putnis, M. Prieto, C.V. Putnis.
The Role of Magnesium in the Crystallization of Calcite and Aragonite in a Porous Medium.
J. Sed. Res., **1996**, 66(3), 482-491.

67. D.P. Grigorev.
Ontogeny of Minerals.
English translation, Israel Program for Scientific Translations, Jerusalem **1965**.
Daniel Davey and Co., Inc., NY.
68. C.A. Self.
The Internal Organization of Speleothems.
Acta Carsologica, **2004**, 33(1), 245-255.
69. M.N. Maleev.
Diagnostic Features of Spherulites formed by Splitting of a Single-crystal Nucleus. Growth mechanism of chalcedony.
Tschermaks Min. Petr. Mitt., **1972**, 18, 1-16.
70. P. Simon, D. Zahn, H. Lichte, R. Kniep.
Intrinsic Electric Dipole Fields and the Induction of Hierarchical Form Developments in Fluorapatite-Gelatine Nanocomposites: A General Principle for Morphogenesis of Biominerals?
Angew. Chem., Int. Ed., **2006**, 45(12), 1911–1915.
Angew. Chem., **2006**, 118(12), 1945-1949.
71. P. Simon, W. Carrillo-Cabrera, P. Formanek, C. Göbel, D. Geiger, R. Ramlau, H. Tlatlik, J. Buder, R. Kniep.
On the Real-structure of Biomimetically Grown Hexagonal Prismatic Seeds of Fluorapatite-gelatine-composites: TEM investigations along [001].
J. Mater. Chem., **2004**, 14(14), 2218-2224.
72. R. Kniep, P. Simon.
“Hidden” Hierarchy of Microfibrils within 3D- periodic Fluorapatite-Gelatine nanocomposites: Development of Complexity and Form in a Biomimetic System.
Angew. Chem., Int. Ed., **2008**, 47(8), 1405–1409.
Angew. Chem., **2008**, 120(8), 1427-1431.
73. R.L. Penn, J.F. Banfield.
Imperfect Oriented Attachment: Dislocation Generation in Defect-Free Nanocrystals.
Science, **1998**, 281, 969- 971.
74. A. Chemseddine, T. Moritz.
Nanostructuring Titania: Control over Nanocrystal Structure, Size, Shape, and Organization.
Eur. J. Inorg. Chem., **1999**, 2, 235-245.
75. O. Pujol, P. Bowen, P.A. Stadelmann, H. Hofmann.
Growth and Self-assembly of Nanostructured $\text{CoC}_2\text{O}_4 \cdot 2\text{H}_2\text{O}$ Particles.
J. Phys.Chem. B, **2004**, 108(35), 13128-13136.
76. L.C. Soare, P.L. Bowen, J. Lemaitre, H. Hofmann.
Precipitation of Nanostructured Copper Oxalate: Substructure and Growth Mechanism.

- J. Phys. Chem. B, **2006**, 110(36), 17763-17771.
77. H. Cölfen, M. Antonietti.
Mesocrystals: Inorganic Superstructures Made by Highly Parallel Crystallization and Controlled Alignment.
Angew. Chem. Int. Ed., **2005**, 44(35), 5576-5591.
Angew. Chem., **2005**, 117(35), 5714-5730.
78. H. Cölfen, M. Antonietti.
Mesocrystals and Nonclassical Crystallization: New Self-assembled Structures.
John Wiley & sons, Chichester, **2008**.
79. L.-P. Zhu, H.-M. Xiao, S.-Y. Fu.
Template-Free Synthesis of Monodispersed and Single-Crystalline Cantaloupe-like Fe₂O₃ Superstructures.
Cryst. Growth. Des., **2007**, 7(2), 177-182.
80. L.J.M.J. Blomen, E.J. Will, O.L.M. Bijvoet, H. Vanderlinden.
Growth Kinetics of Calcium Oxalate Monohydrate II. The Variation of Seed Concentration.
J. Cryst. Growth, **1983**, 64, 306-315.
81. B.B. Tomazic, G.H. Nancollas.
The Kinetics of Dissolution of Calcium Oxalate Hydrates, II. The Dihydrate.
Invest. Urol., **1980**, 18(2), 97-101.
82. B.B. Tomazic, G.H. Nancollas.
A Study of the Phase Transformation of Calcium Oxalate Trihydrate–Monohydrate.
Invest. Urol., **1979**, 16(5), 329-335.
83. J.E. Crawford, E.P. Crematy, A.E. Alexander.
The Effect of Natural and Synthetic Polyelectrolytes on the Crystallization of Calcium Oxalate.
Aust. J. Chem., **1968**, 21(4), 1067–1072.
84. T. Jung, W-S. Kim, C.K. Choi.
Crystal Structure and Morphology Control of Calcium Oxalate using Biopolymeric Additives in Crystallization.
J. Cryst. Growth, **2005**, 279, 154-162.
85. D.B. Zhang, L.M. Qi, J.M. Ma, H.M. Cheng.
Morphological Control of Calcium Oxalate Dihydrate by a Double-Hydrophilic Block Copolymer.
Chem. Mater., **2002**, 14(6), 2450-2457.
86. K-Th. Wilke, J. Bohm,
Kristallzuechtung.
Verlag Harri Deutsch, Thun, Frankfurt/Main, **1988**.

87. H.K. Henisch.
Crystal Growth in Gels.
Dover Publications Inc., New York, **1996**.
88. J. Johnston.
The Utilization of Diffusion Processes in the Preparation of Pure Substances.
J. Am. Chem. Soc., **1914**, 36(1), 16-19.
89. S. Bisailon, R. Tawashi.
Growth of Calcium Oxalate in Gel systems.
J. Pharm. Sci., **1975**, 64(3), 458-459.
90. A. Frey-Wyssling.
Crystallography of the two Hydrates of Crystalline Calcium Oxalate in Plants.
Am. J. Bot., **1981**, 68, 130-141.
91. A. Hodgkinson, B.E.C. Nordin.
Physical Chemistry of Calcium Stone Formation.
J. Biochem., **1971**, 122(1), 5P-6P.
92. R.Z. LeGeros, P. Morales.
Renal stone. Crystals grown in Gel system: A Preliminary Report.
Invest. Urol., **1973**, 11(1), 12-20.
93. A.M. Cody, H.T. Horner, R.D. Cody.
SEM Study of the Fine Surface Features of Synthetic Calcium Oxalate Monohydrate Crystals.
Scanning Elect. Microsc. I, **1982**, 185-197.
94. E.V. Petrova, N.V. Gvozdev, L.N. Rashkovich.
Growth and Dissolution of Calcium Oxalate Monohydrate (COM) Crystals.
J. Optoelectron. Adv. Mater., **2004**, 6 (1), 261-268.
95. S. Arnott, A. Fulmer, W.E. Scott.
The Agarose Double Helix and its Function in Agarose Gel Structure.
J. Molec. Biol., **1974**, 90(2), 269-284.
96. M. Djabourov, A.H. Clark, D.W. Rowlands, S.B. Ross-Murphy.
Small Angle X-ray Scattering Characterization of Agarose Sols and Gels.
Macromolecules, **1989**, 22(1), 180-188.
97. M. Watase, K. Nishinari, A.H. Clark, S.B. Ross-Murphy.
Differential Scanning Calorimetry, Rheology, X-ray, and NMR of Very Concentrated Agarose Gels.
Macromolecules, **1989**, 22(3), 1196-1201.
98. D.A. Rees.
Structure, Conformation, Mechanism in the Formation of Polysaccharide Gels and Networks.
Advances Carbohyd. Chem. Biochem., **1969**, 24, 267-332.

99. M.R. Mangione, D. Giacomazza, D. Bulone, V. Martorana, P.L. San Biagio. Thermoreversible Gelation of κ -Carrageenan: Relation between Conformational Transition and Aggregation. *Biophys. Chem.*, **2003**, 104(1), 95-105.
100. C. Rochas, M. Rinaudo. Mechanism of Gel Formation in κ -Carrageenan. *Biopolymers*, **1984**, 23(4), 735-745.
101. A. Bigi, S. Panzavolta, K. Rubini. Relationship Between Triple-helix Content and Mechanical properties of Gelatine Films. *Biomater.*, **2004**, 25(25), 5675-5680.
102. K. Okuyama, X. Xu, M. Iguchi, K. Noguchi. Revision of Collagen Molecular Structure. *Biopolymers*, **2006**, 84(2), 181-191.
103. C. Göbel. Einfluss von Fluorid auf die Morphogenese und mikroskopische Struktur von Calciumphosphat-Gelatine-Kompositen. Ph.D. Thesis, Technical University, Dresden, **2006**.
104. O. Hochrein, A. Thomas, R. Kniep. Revealing the Crystal Structure of Anhydrous Calcium Oxalate, $\text{Ca} [\text{C}_2\text{O}_4]$, by a Combination of Atomistic Simulation and Rietveld Refinement. *Z. Anorg. Allg. Chem.*, **2008**, 634, 1826-1829.
105. J.S. Manne, N. Biala, A.D. Smith, C.C. Gryte. The Effect of Anionic Polyelectrolytes on the Crystallization of Calcium Oxalate Hydrates. *J. Cryst. Growth*, **1990**, 100, 627-634.
106. E. Akyol, M. Öner. Inhibition of Calcium Oxalate Monohydrate Crystal growth using Polyelectrolytes. *J. Cryst. Growth*, **2007**, 307, 137-144.
107. B. Akin, M. Öner, Y. Bayram, K.D. Demadis. Effects of Carboxylate-Modified, "Green" Inulin Biopolymers on the Crystal Growth of Calcium Oxalate. *Cryst. Growth. Des.*, **2008**, 8(6), 1997-2005.
108. A.C. Lanzalaco, R.P. Singh, S.A. Smeko, G.H. Nancollas, G. Sufrin, M. Binette, J.P. Binette. The Influence of Urinary Macromolecules on Calcium Oxalate Monohydrate Crystal Growth. *J. Urol.*, **1988**, 139, 190-195.
109. J.A. Wesson, E.M. Worcester, J.G. Kleinman.

- Role of Anionic Proteins in Kidney Stone Formation: Interaction Between Model Anionic Polypeptides and Calcium oxalate Crystals.
J. Urol., **2000**, 163, 1343-1348.
110. S.R. Khan, P.N. Shevock, R.L. Hackett.
Invitro Precipitation of Calcium Oxalate in the Presence of Whole Matrix or Lipid Components of the Urinary Stones.
J. Urol., **1988**, 139, 418-422.
111. Y. Shirane, Y. Kurokawa, Y. Sumiyoshi, S. Kagawa.
Morphological Effects of Glycosaminoglycans on Calcium Oxalate Monohydrate Crystals.
Scanning Microsc., **1995**, 9, 1081 -1088.
112. F. Grases, A. Millan, A. Garcia-Raso.
Polyhydroxycarboxylic Acids as Inhibitors of Calcium Oxalate Crystal Growth; Relation Between Inhibitory Capacity and Chemical Structure.
J. Cryst. Growth, **1988**, 89, 496-500.
113. P. Brown, D. Ackermann, B. Finlayson.
Calcium Oxalate Dihydrate (Weddellite) Precipitation.
J. Cryst. Growth, **1989**, 98, 285-292.
114. J.L Meyer, H.L. Smith.
Growth of Calcium Oxalate crystals: I. A Model for Urinary Stone Growth.
Invest. Urol., **1975**, 13(1), 36-39.
115. L.G. Akselrud, P.Y. Zavalii, Yu.N. Grin, V.K. Pecharsky, B. Baumgartner, E. Wölfel.
Use of the CSD Program Package for Structure Determination from Powder Data.
Mater. Sci. Forum, **1993**, 335, 133–136.
116. D. Strtic, M. Markovic, H. Furedi-Milhofer.
Precipitation of Calcium Oxalate from High Ionic Strength Solutions.
J. Cryst. Growth, **1986**, 79, 791-796.
117. F. Grases, J.G. March, F. Bibiloni, E. Amat.
The Crystallization of Calcium Oxalate in the Presence of Aminoacids.
J. Cryst. Growth, **1988**, 87, 299-304.
118. R.J. Ferguson.
Predicting Calcium Oxalate Scale.
Corrosion, **2002**, 399, 1-9.
119. T. Jung, W-S. Kim, C.K. Choi.
Biom mineralization of Calcium Oxalate for Controlling Crystal Structure and Morphology.
Mater. Sci. Eng., **2004**, C.24, 31-33.

120. D. Duval, R.A. Condrate.
Temperature Dependence of the Raman Spectra of Calcium Oxalate Monohydrate.
Phys. Status Solidi B, **1985**, 132, 83-92.
121. R.L. White, J. Ai.
Variable-Temperature Diffuse Reflectance Infrared Studies of Calcium Oxalate Monohydrate.
Appl. Spectrosc., **1992**, 46(1), 93-99.
122. M. Trpkovska, B. Soptrajanov, Lj. Pejov.
Reinvestigation of the Infrared spectra of Calcium Oxalate Monohydrate and its Partially Deuterated Analogues- An Experimental and Theoretical Study.
Bullet. Chem. Technol. Macedonia, **2002**, 21(2), 111-116.
123. I. Petrov, B.Soptrajanov.
Infrared Spectrum of Whewellite.
Spectrochim. Acta, **1975**, 31A, 309-316.
124. K.J. Kociba, P.K. Gallagher.
A Study of Calcium Oxalate Monohydrate using Dynamic Differential Scanning Calorimetry and other Thermoanalytical Techniques.
Thermochim. Acta, **1996**, 282/283, 277-296.
125. A. Le Bail.
Monte Carlo Indexing with Mc Maille.
Powder Diffraction, **2004**, 19(3), 249-254.
126. A. Le Bail.
Whole Powder Pattern Decomposition Methods and Applications: A Retrospection.
Powder Diffraction, **2005**, 20 (4), 316-326.
127. P. Ordejon , E. Artacho, J.M. Soler.
Self Consistent Order-N Density-Functional Calculations for Very Large Systems.
Phys. Rev. B, **1996**, 53(16), 10441-10444.
128. J.M. Soler, E. Artacho, J.D. Gale, A. Garcia, J. Junquera, P. Ordejon, D. Sanchez-Portal
The SIESTA Method for *ab initio* Order-N Materials Simulation.
J. Phys.: Condens. Matter, **2002**, 14, 2745-2779.
129. J.P. Perdew, K. Burke, M. Ernzerhof.
Generalized Gradient Approximation Made Simple.
Phys. Rev. Lett., **1996**, 77(18), 3865-3868.
130. N. Troullier, J.L. Martins.
Efficient Pseudopotentials for Plane Wave Calculations.
Phys. Rev. B, **1991**, 43(3), 1993-2006.

131. N. Troullier, J.L. Martins.
Efficient Pseudopotentials for Plane Wave Calculations. 2 Operations for Fast Iterative Diagonalization.
Phys. Rev. B, **1991**, 43(11), 8861-8869.
132. Y.-X. Huang, O. Hochrein, D. Zahn, Y. Prots, H. Borrmann, R. Kniep.
Control of Channel Shapes in a Microporous Manganese (II)-Borophosphate Framework by Variation of Size and Shape of Organic Template Cations.
Chem. Eur. J., **2007**, 13, 1737-1745.
133. D. Zahn, O. Hochrein.
The Role of Substitutional Defects in Order/Disorder Phenomena of OH⁻ Ions in Hydroxyapatite.
Z. Anorg. Allg. Chem., **2006**, 632, 79-83.
134. A. L. Spek.
Single-crystal Structure Validation with the Program *PLATON*.
J. Appl. Cryst., **2003**, 36, 7-13.
135. A.C. Larson, R.B. Von Dreele.
General Structure Analysis System (GSAS).
Los Alamos National Laboratory Report LAUR, **2000**, 86-748.
136. O. Hochrein.
Force Field for Calcium oxalates.
Unpublished results.
137. A. Kawska, J. Brickmann, R. Kniep, O. Hochrein, D. Zahn.
An atomistic Simulation Scheme for Modeling Crystal Formation from Solution.
J. Chem. Phys., **2006**, 124, 24513-24520.
138. H. Tlatlik, P. Simon, A. Kawska, D. Zahn, R. Kniep.
Biomimetic Fluorapatite-Gelatine-Nanocomposites: Pre-Structuring of Gelatine Matrices by Ion Impregnation and its Effect on Form-Development.
Angew. Chem. Int. Ed., **2006**, 45(12), 1905-1910.
Angew. Chem., **2006**, 118(12), 1939-1944.
139. N. Jongen, P. Bowen, J. Lemaitre, J. -Christophe Vamalette, H. Hofmann.
Precipitation of Self-Organized Copper Oxalate Polycrystalline Particles in the Presence of Hydroxypropylmethylcellulose (HPMC): Control of Morphology.
J. Colloid Interface Sci., **2000**, 226(2), 189-198.
140. W.D. Emmerich, E. Kaisersberger.
Simultaneous TG-DTA Mass-Spectrometry to 1550 °C.
J. Thermal. Anal., **1979**, 17, 197 – 212.
141. J. Kaloustian, T.F. El-Moselhy, H. Portugal.
Determination of Calcium Oxalate (Mono- and Dihydrate) in Mixtures with Magnesium Ammonium Phosphate or Uric Acid: The Use of Simultaneous Thermal Analysis in Urinary Calculi.

- Clinica Chimica Acta, **2003**, 334, 117-129.
142. M.A. Moharram, M.G. Khafagi.
Thermal Behavior of Poly(acrylic acid)–Poly(vinyl pyrrolidone) and Poly(acrylic acid)–Metal–Poly(vinyl pyrrolidone) Complexes.
J. Appl. Polym. Sci., **2006**, 102, 4049–4057.
143. I.C. Mc Neill, A. Alston.
Thermal Degradation Behaviour of Acrylic salt Polymers and Ionomers.
Die Angew. Makromol. Chem., **1998**, 261/262, 157–172.
144. M.A. Moharram, M.A. Allam.
Study of the Interaction of Poly(acrylic acid) and Poly(acrylic acid-Poly acrylamide) Complex with Bone Powders and Hydroxyapatite by Using TGA and DSC.
J. Appl. Polym. Sci., **2007**, 105, 3220–3227.
145. J. Yu, H. Tang, B. Cheng.
Influence of PSSS Additive and Temperature on Morphology and Phase Structures of Calcium Oxalate.
J. Colloid Interface Sci., **2005**, 288(2), 407-411.
146. A. Taller, B. Grohe, K. Rogers, H.A. Goldberg, G.K. Hunter.
Specific Adsorption of Ostopontin and Synthetic Polypeptides to Calcium Oxalate Monohydrate Crystals.
Biophys. J., **2007**, 93, 1768-1777.
147. P.J. Kay, F.E. Treloar.
The Intrinsic Viscosity of Poly (acrylic acid) at Different Ionic Strengths: Random Coil and Rigid Rod Behaviour.
Makromol. Chem., **1974**, 175, 3207-3223.
148. J.D. Pinkston, T.E. Delaney, D.J. Bowling.
Characterization of Low Molecular Weight Poly (acrylic acid) Samples by Capillary Supercritical Fluid Chromatography and Capillary Supercritical Fluid Chromatography-Mass Spectrometry.
J. Microcol. Sep., **1990**, 2(4), 181-187.
149. F. Fantinel, J. Rieger, F. Molnar, P. Hubler.
Complexation of Polyacrylates by Ca²⁺ ions. Time-Resolved Studies Using Attenuated Total Reflectance Fourier Transform Infrared Dialysis Spectroscopy.
Langmuir, **2004**, 20(7), 2539-2542.
150. T. Kitano, A. Taguchi, I. Noda, M. Nagasawa.
Conformation of Polyelectrolytes in Aqueous Solution.
Macromolecules, **1980**, 13, 63-65.
151. T.J. Taylor, S.S. Stivala.
Small-angle X-ray Scattering Study of a Weak Polyelectrolyte in Water.
J. Polym. Sci.: Part B: Polym. Phys., **2003**, 41(12), 1263–1272.

152. I. Sabbagh, M. Delsanti, P. Lesieur.
Ionic Distribution and Polymer Conformation, Near Phase Separation, in Sodium Polyacrylate/Divalent Cations Mixtures: Small Angle X-ray and Neutron Scattering.
Eur. Phys. J. B, **1999**, 12, 253-260.
153. V.R. Franceschi, P.A. Nakata.
Calcium Oxalate in Plants: Formation and Function.
Annual Rev. Plant. Biol., **2005**, 56, 41-71.
154. R. Armisen, F. Galatas.
Production and Utilization of Products from Commercial Seaweeds.
Chapter 1: Production, Properties and Uses of Agar.
Fish. Tech. Pap., (FAO), 288, Italy, **1987**.
155. J.A. Thom, J.E. Morris, A. Bishop, N.J. Blacklock.
The Influence of Refined Carbohydrate on Urinary Calcium Excretion.
Br. J. Urol., **1978**, 50, 459-464.
156. A. Hodgkinson, F.W. Heaton.
The Effect of Food Ingestion on the Urinary Excretion of Calcium and Magnesium.
Clinica Chimi. Acta, **1965**, 11, 354-362.
157. B.T. Murphy, L.N. Pyrah.
The Composition, Structure and Mechanisms of the Formation of Urinary Calculi.
Br. J. Urol., **1962**, 34, 129-159.
158. J.-M. Ouyang, H. Zheng, S.-P. Deng.
Simultaneous Formation of Calcium Oxalate (mono-, di-, and trihydrate) Induced by Potassium Tartrate in Gelatinous system.
J. Cryst. Growth, **2006**, 293, 118-123.
159. A.A. Chernov.
Modern Crystallography. Vol III. Crystal Growth.
Springer Verlag, Berlin, **1984**.
160. S.R. Qiu, A. Wierzbicki, C.A. Orme, A.M. Cody, J.R. Hoyer, G.H. Nancollas, S. Zapeda, J.J. De Yoreo.
Molecular Modulation of Calcium Oxalate Crystallization by Osteopontin and Citrate.
Proc. Nat. Acad. Sci. USA, **2004**, 101(7), 1811-1815.
161. S. Deganello.
Interaction Between Nephrocalcin and Calcium Oxalate Monohydrate: A Structural Study.
Calcif. Tissue Int., **1991**, 48, 421-428.
162. A. Wierzbicki, C.S. Sikes, J.D. Sallis, J.D. Madura, E.D. Stevens, K.L. Martin.
Scanning Electron Microscopy and Molecular Modeling of Inhibition of Calcium

- Oxalate Monohydrate Crystal Growth by Citrate and Phosphocitrate.
Calcif. Tissue Int., **1995**, 56, 297-304.
163. R.L. Ryall, R.M. Harnett, V.R. Marshall.
The Effect of Urine, Pyrophosphate, Citrate, Magnesium and Glycosaminoglycans on the Growth and Aggregation of Calcium Oxalate Crystals in vitro.
Clin. Chim. Acta., **1981**, 112, 349-356.
164. X.M. Wu, J. -Ming. Ouyang, S.-P. Deng, Y.Z. Cen.
Inhibition of the Crystal Growth and Aggregation of Calcium Oxalate by Algae Sulfated Polysaccharide in vitro.
Chin. Chem. Lett., **2006**, 17(1), 97-100.
165. H.H. Dorian, P. Rez, G.W. Drach.
Evidence for Aggregation in Oxalate Stone Formation: Atomic Force and Low Voltage Scanning Electron Microscopy.
J. Urol., **1996**, 156, 1833-1837.
166. J.A. Wesson, M.D. Ward.
Role of Crystal Surface Adhesion in Kidney Stone Disease.
Curr. Opin. Nephrol. Hypertens., **2006**, 15, 386-393.
167. H. Iwata, S. Nishio, A. Wakatsuki, K. Ochi, M. Takeuchi.
Architecture of Calcium Oxalate Monohydrate Urinary Calculi.
J. Urol., **1985**, 133, 334-338.
168. P.G. Werness, J.H. Bergert, L.H. Smith.
Crystalluria.
J. Cryst. Growth, **1981**, 53, 166-181.
169. R. Backov, C.M. Lee, S.R. Khan, C. Mingotaud, G.E. Fanucci, D.R. Talham.
Calcium Oxalate Monohydrate Precipitation at Phosphatidylglycerol Langmuir Monolayers.
Langmuir, **2000**, 16 (14), 6013-6019.
170. A. Millan, F. Grases, O. Sohnle, I. Krivankova.
Semi-batch Precipitation of Calcium Oxalate Monohydrate.
Cryst. Res. Technol., **1992**, 27(1), 31-39.
171. J. Morfin, A. Chin.
Images in Clinical Medicine. Urinary Calcium Oxalate Crystals in Ethylene Glycol Intoxication.
N. Engl. J. Med., **2005**, 353(24), e21.
172. S.R. Khan, R.L. Hackett.
Crystal – Matrix Relationships in Experimentally Induced Urinary Calcium Oxalate Monohydrate Crystals, an Ultra Structural Study.
Calcif. Tissue Int., **1987**, 41, 157-163.
173. S.R. Khan, R.L. Hackett.

- Developmental morphology of Calcium Oxalate Foreign Body Urinary Stones in Rats.
Calcif. Tissue Int., **1985**, 37(2), 165-173.
174. Bo-L. Johansson, M. Andersson, J. Lausmaa, P. Sjovall.
Chemical Characterization of Different Separation Media Based on Agarose by Static Time-Of-Flight Secondary Ion Mass Spectrometry.
J. Chromat. A, **2004**, 1023, 49-56.
175. F. Grases, A. Costa-Bauza, A. Conte.
Studies on Structure of Calcium Oxalate Monohydrate Renal Papillary Calculi. Mechanism of Formation.
Scanning Microsc., **1993**, 7, 1067–1073.
176. F. Grases, O. Sohnel, A. Millan, A. Costa-Bauza.
Calcium Oxalate Crystallization and Renal Calculi Formation.
Cur. Top. Cryst. Growth Res., **1994**, 1, 367–389.
177. R. Dyer, B.E. Nordin.
Urinary Crystals and their Relation to Stone Formation.
Nature, **1967**, 215(12), 751-752.
178. M.G. Canti.
An Investigation of Microscopic Calcareous Spherulites from Herbivore Dungs.
J. Arch. Sci., **1997**, 24, 219-231.
179. F. Grases, A. Costa-Bauza.
Study of Factors Affecting Calcium Oxalate Crystalline Aggregation.
Br. J. Urol., **1990**, 66, 240-244.
180. J.P. Kavanagh.
Supersaturation and Renal Precipitation: the Key to Stone Formation?
Urol. Res., **2006**, 34, 81-85.
181. M. Akbarieh, R. Tawashi.
Calcium Oxalate Crystal Growth in the Presence of Mucin.
Scanning Microsc., **1991**, 5, 1019-1027.
182. H. Iwata, S. Iio, S. Nishio, M. Takeuchi.
Architecture of Mixed Calcium Oxalate Dihydrate and Monohydrate Stones.
Scanning Microsc. **1992**, 6(1), 231-238.
183. K. Lonsdale.
Epitaxy as a Growth Factor in Urinary Calculi and Gall Stones.
Nature, **1968**, 217, 56-58.
184. H.D. Keith, F.J. Padden.
A Phenomenological Theory of Spherulitic Crystallization.
J. Appl. Phys., **1963**, 34(8), 2409-2421.

185. P. Harting.
Recherches de morphologie synthétique sur la production artificielle de quelques formations calcaires organiques.
van der Post, Amsterdam, **1872**.
186. A. Putnis, M. Prieto, L. F-Diaz.
Fluid Supersaturation and Crystallization in Porous Media.
Geol. Mag., **1995**, 132(1), 1-13.
187. J. Tang, A.P. Alivisatos.
Crystal Splitting in the Growth of Bi_2S_3 .
Nano. Lett., **2006**, 6(12), 2701-2706.
188. D. Nenow, L. Vitkov.
Effect of the Opposite Directions on the Crystal Face Upon the Growth Kinetics of Weddellite.
J. Cryst. Growth, **1997**, 182, 461-464.
189. R.L. Ryall, D.E. Fleming, I.R. Doyle, N.A. Evans, C.J. Dean, V.R. Marshall.
Intracrystalline Proteins and the Hidden Ultrastructure of Calcium Oxalate Urinary Crystals: Implications for Kidney Stone Formation.
J. Struct. Biol., **2001**, 134, 5-14.
190. F. Grases, O. Sohnel, A. Costa-Bauza, M. Ramis, Z. Wang.
Study on Concretions Developed around Urinary Catheters and Mechanisms of Renal Calculi Development.
Nephron, **2001**, 88, 320-328.
191. N. Goldenfeld.
Theory of Spherulitic Crystallization.
J. Cryst. Growth, **1987**, 84, 601-608.
192. J.H. Magil.
Spherulites: A Personal Perspective.
J. Mater. Sci., **2001**, 36, 3143- 3164.
193. W. Wunderlich.
Aspects of the Influence of Magnesium Ions on the Formation of Calcium Oxalate.
Urol. Res., **1981**, 9, 157-161.
194. W. Achilles, R. Freitag, B. Kiss, H. Riedmiller.
Quantification of Crystal Growth of Calcium Oxalate in Gel and its Modification by Urinary Constituents in a New Flow Model of Crystallization.
J. Urol., **1995**, 154, 1552-1556.

6 Appendix

Table 6.1. Macromolecules so-far detected and identified in urinary stones [50].

Proteins	Albumin, α -1-microglobulin, α -1-acidglycoprotein, α and γ globulins, α -1-antitrypsin, Apolipoprotein A1, β -2-microglobulin, Calprotectin, Haemoglobin, Inter- α -Inhibitor, Nephrocalcin, Neutrophil elastase, Osteopontin (Uropontin), Porin, Renal lithostatin, Retinol binding protein, Superoxide dismutase, Tamm-Horsfall Protein, Transferin
Glycosaminoglycans	Heparan sulfate, Hyaluronic acid
Lipids	Phospholipids, Cholesterol, Glycolipids
Small molecules	Pyrophosphate

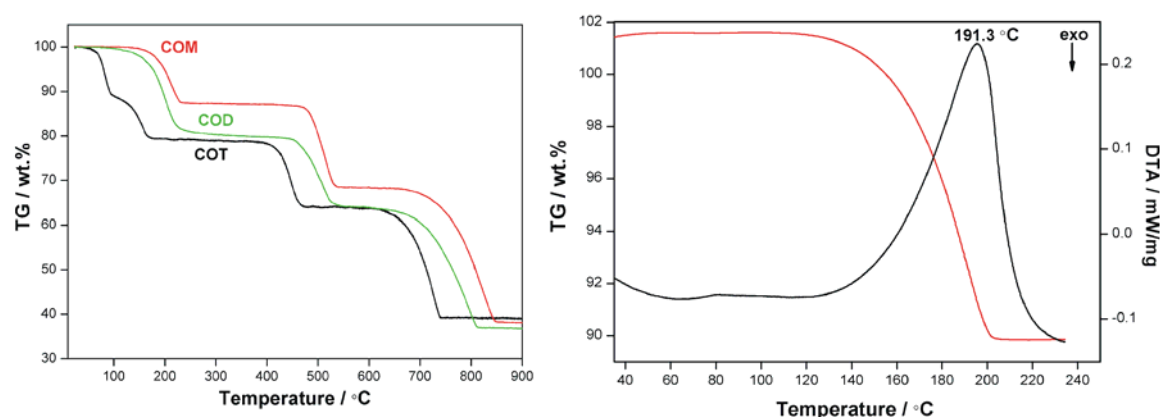


Fig. 6.1. (Left) Overlapped thermogram of COM, COD and COT. The dehydration of COT takes place *via* COM instead of COD and hence shows four weight losses (refer to section 1.2.2). (Right) TG/DTA of COM up to 370 °C resulting in COA.

Table 6.2. Thermal decomposition processes of COM, COD and COT and their assignments with the calculated values in parentheses. (Refer to section 3.1.2).

	DTA peak (°C)	Process	Mass loss (wt.%)
COM	219.5	-H ₂ O	12.89 (12.33)
	518.6	-CO	18.84 (19.7)
	809.2	-CO ₂	30.20 (31.2)
COD	207.5	-2H ₂ O	20.14 (21.6)
	514.9	-CO	15.78 (17.4)
	781.2	-CO ₂	27.36 (26.8)
COT	83.7	-2H ₂ O	11.10 (19.78)
	158.4	-H ₂ O	9.31 (9.89)
	447.4	-CO	15.54 (15.38)
	710	-CO ₂	24.70 (24.16)

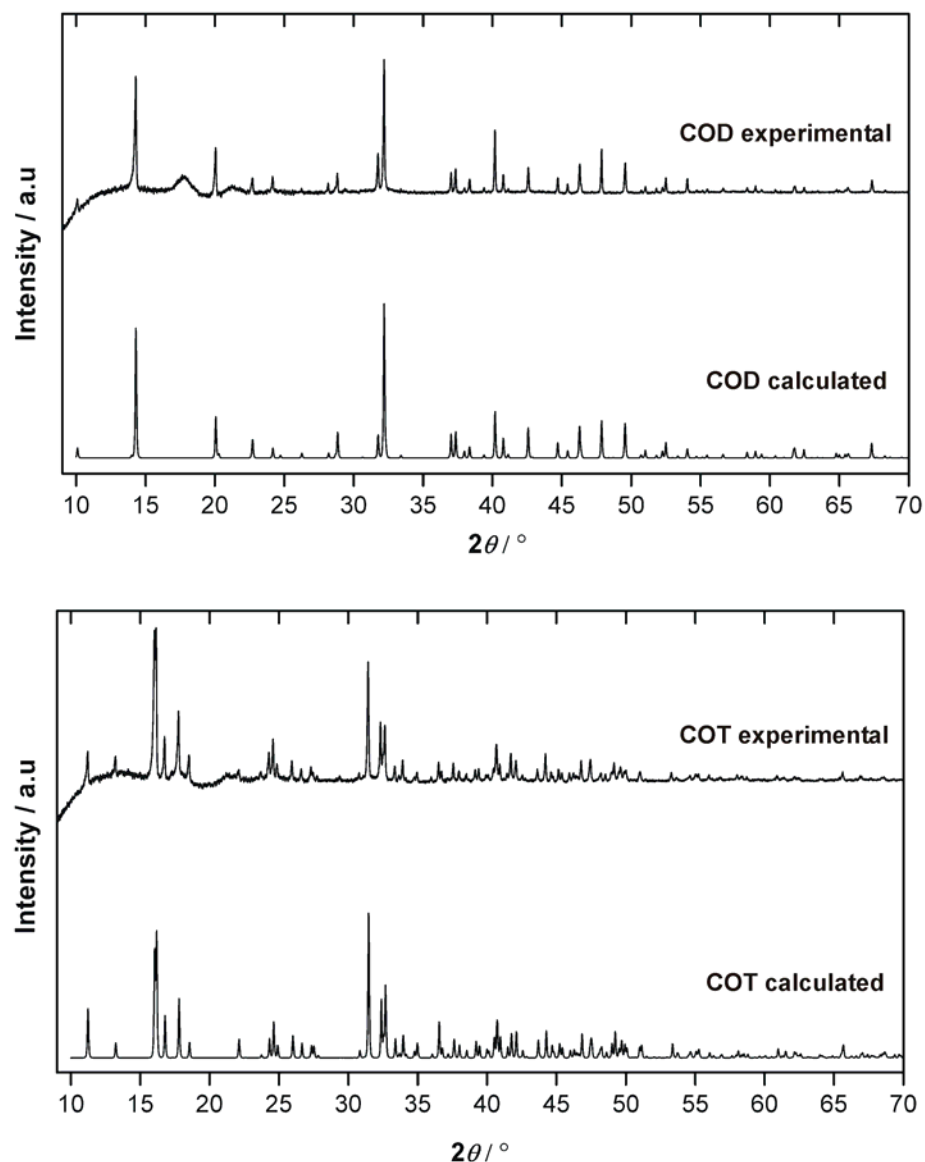


Fig. 6.2. The XRD patterns of COD (top) and COT (bottom) crystallized from aqueous solutions. The experimental data are measured using Cu $K\alpha_1$ - radiation. COD is grown from 0.8 mM CaOx at pH 9 and COD from 0.9 mM CaOx without controlling the pH values. For more details refer to section 3.1.1.

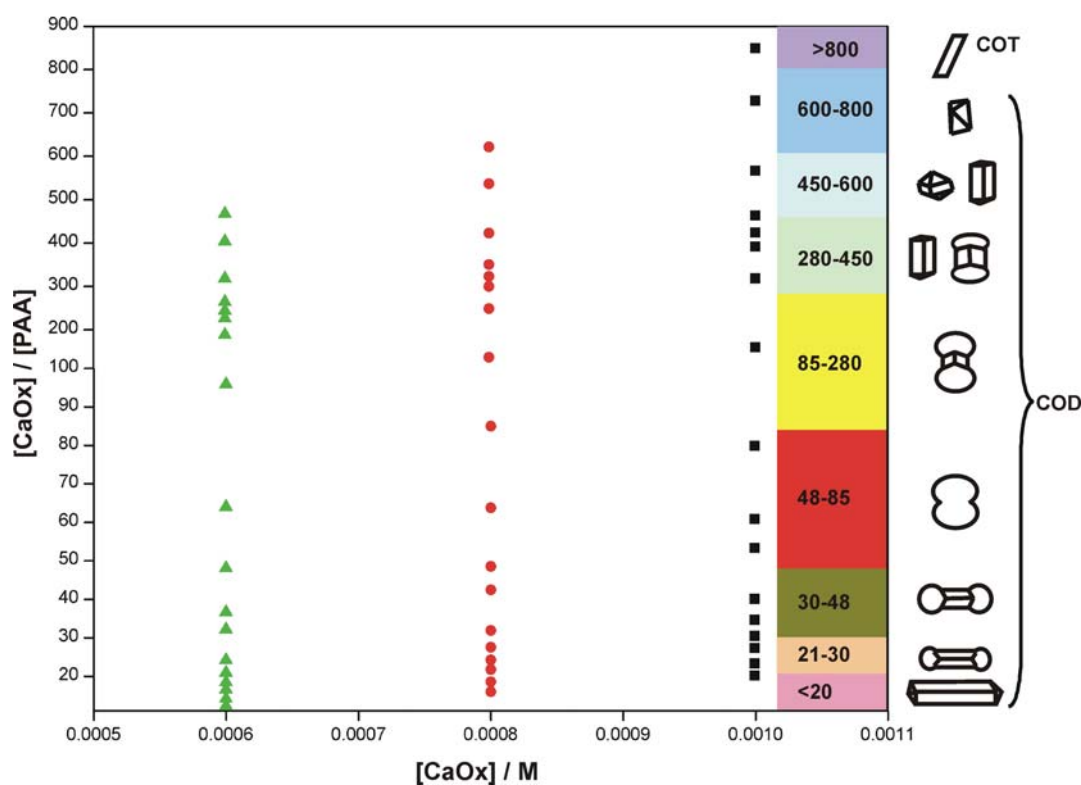


Fig. 6.3. Morphology map of calcium oxalates in the presence of PAA for different initial CaOx and PAA concentrations. The relative proportion of the concentrations of CaOx and PAA determines the morphology. (More details in section 3.3).

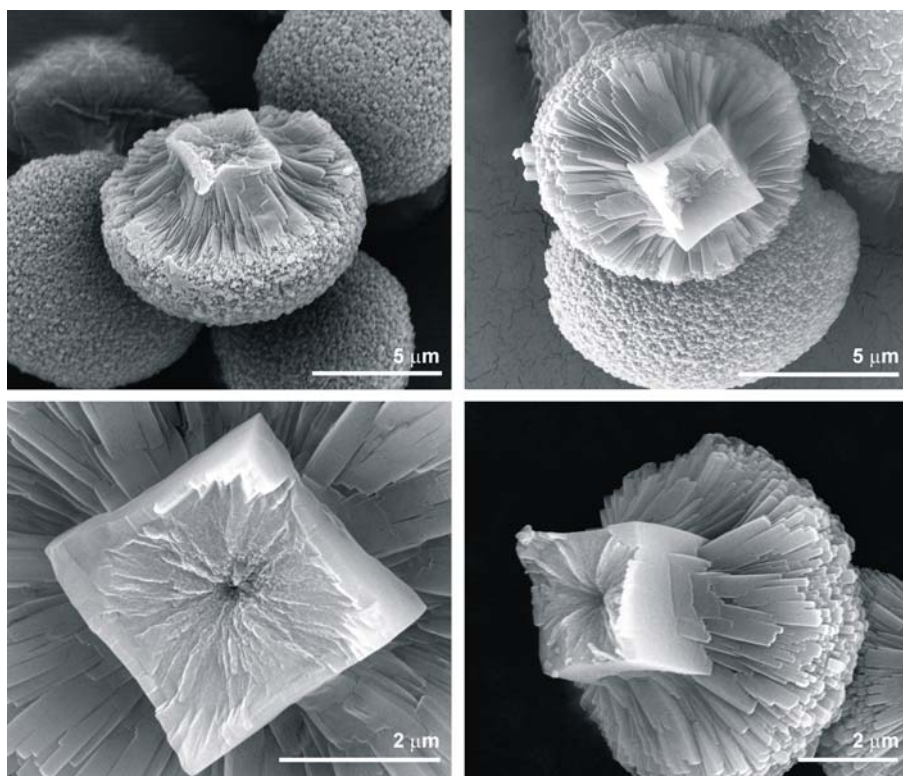


Fig. 6.4. SEM images of the cross-section of COD dumbbells grown from 0.8 mM CaOx and 96 $\mu\text{g}/\text{mL}$ PAA. The tetragonal cross-section indicates that the dumbbells are grown from tetragonal seed crystal. More details in section 3.3.1.

Table 6.3. Lattice parameters of COD crystals grown in the presence of 0.8 mM CaOx and different concentrations of PAA. The powder X-ray diffraction pattern is measured using Cu $K\alpha_1$ - radiation. The lattice parameters are calculated by least square refinements using LaB₆ (cubic, $a = 4.15692 \text{ \AA}$) as internal standard and the program package WinCSD [115]. For more details refer to section 3.3.1 and figure 3.3.9.

PAA ($\mu\text{g/mL}$)	a (\AA)	c (\AA)	a/c	e.s.d. for a/c
3	12.371(1)	7.3583(8)	1.681231	2.28E-04
6	12.3723(8)	7.359(1)	1.681247	2.53E-04
14	12.3767(7)	7.3593(9)	1.681777	2.27E-04
24	12.3739(6)	7.3567(9)	1.681991	2.21E-04
48	12.3621(9)	7.3621(9)	1.679154	2.39E-04
64	12.3668(8)	7.3659(7)	1.678926	1.93E-04
84	12.3732(7)	7.3579(9)	1.681621	2.27 E-04
96	12.3749(8)	7.3581(6)	1.681806	1.75E-04
128	12.371(5)	7.357(1)	1.681528	7.17E-04
148	12.3621(9)	7.3571(9)	1.680295	2.39E-04
168	12.3635(5)	7.358(1)	1.68028	2.38E-04
188	12.365(1)	7.3569(9)	1.680735	2.46E-04
200	12.3718(7)	7.358(1)	1.681408	2.48E-04
225	12.376(3)	7.356(3)	1.682436	7.98E-04
230	12.373(2)	7.3566(6)	1.681891	3.05E-04
235	12.3707(8)	7.361(1)	1.680573	2.53E-04
256	12.376(3)	7.359(2)	1.68175	6.12E-04

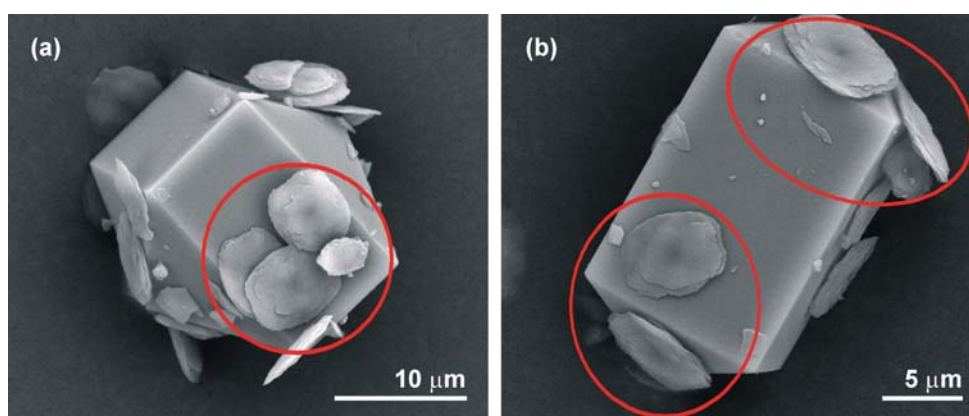


Fig. 6.5. SEM images of the COD crystals grown in the presence of 0.8 mM CaOx at pH 3 in presence of (a) 148 $\mu\text{g/mL}$ (b) 168 $\mu\text{g/mL}$ PAA. The aggregates shown inside red circles are COM. More details in section 3.3.1.

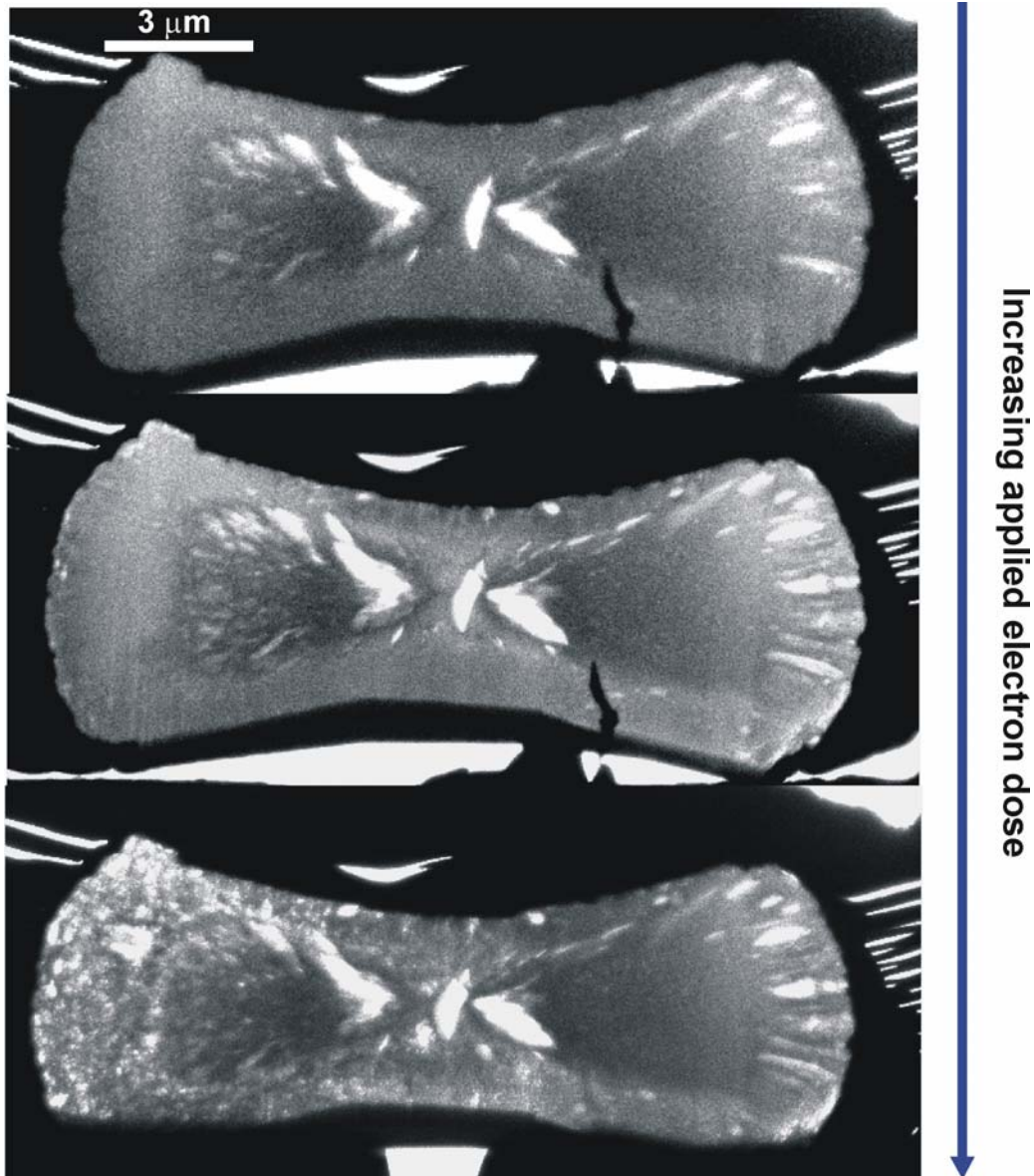


Fig. 6.6. TEM images of [100] cross-section of a COD dumbbell with sample damage by electron irradiation evident. With increasing electron dose, cracks appear in the sample. As a result any of these samples could not be studied under higher magnifications. This is the major draw back of this system.

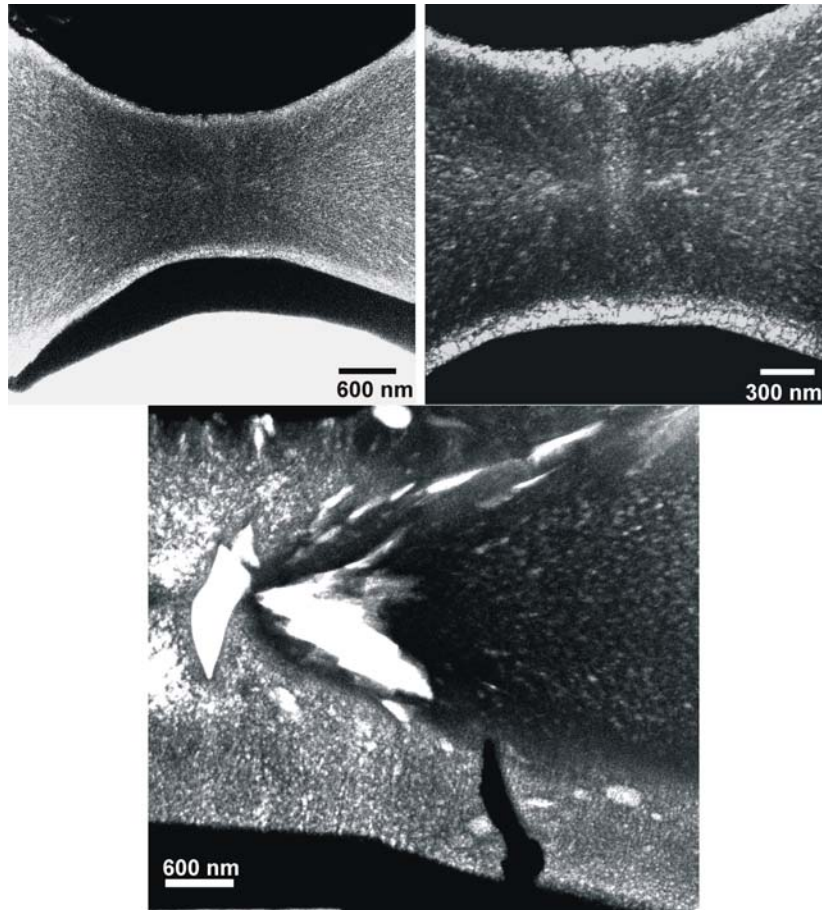


Fig. 6.7. TEM images of the stem region of the [100] cross-section of a COD dumbbell grown from 0.8 mM CaOx and 96 $\mu\text{g}/\text{mL}$ PAA. Note that the crystallites constituting the core and the shell appear different. In the morphogenesis proposed by us the crystallites constituting the core are coloured with blue and those constituting the shell with black (Fig. 3.3.44). More details in section 3.3.2.

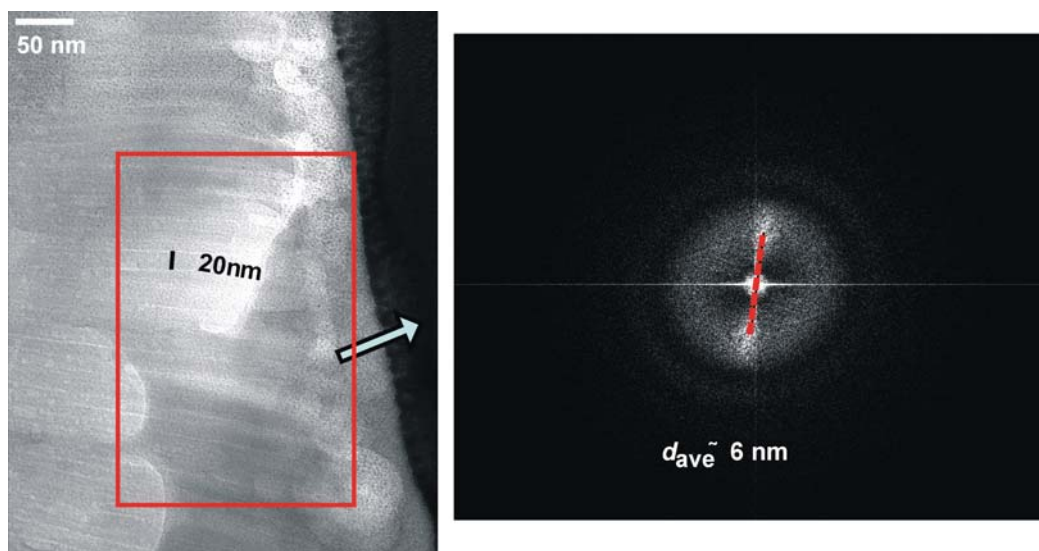


Fig. 6.8. (Left) TEM image of part of a COD dumbbell with the well-spaced domains. The thicknesses of the domains are *ca.* 20 nm. The sample was severely damaged by ethanol used for sample mounting onto FIB holder. (Right) ED pattern recorded from the red framed area. The patterning is due to overlapping of needle-like domains. Also see figure 3.3.37.

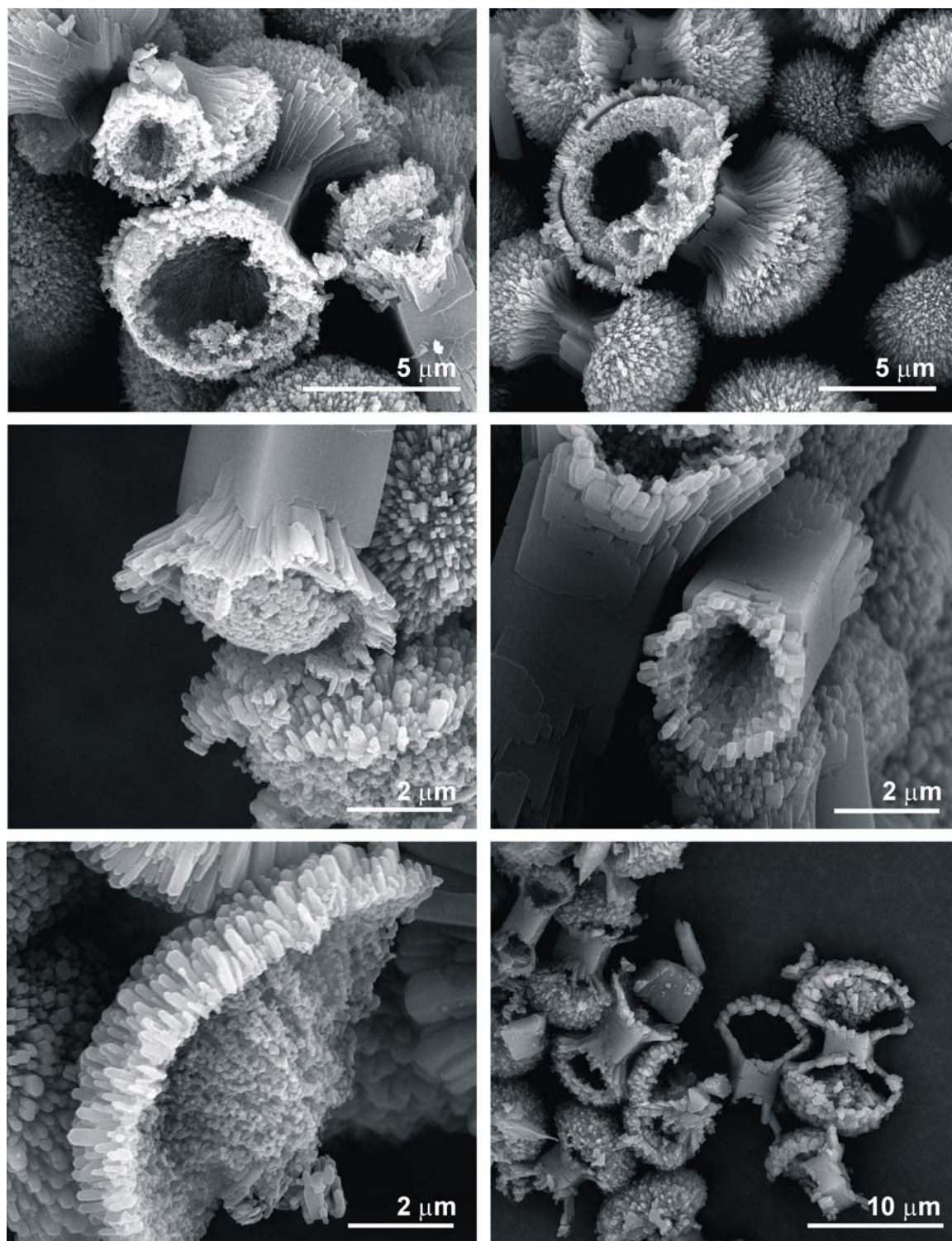


Fig. 6.9. SEM images of COD dumbbells (grown from 0.8 mM CaOx and 96 μg/mL PAA) after immersing in 0.25 N EDTA for 10 minutes. Note that in all the cases crystallites constituting the core are decalcified faster than the crystallites in the shell and the tetragonal rod connecting the two hemispheres appear intact. (Refer to section 3.3.2).

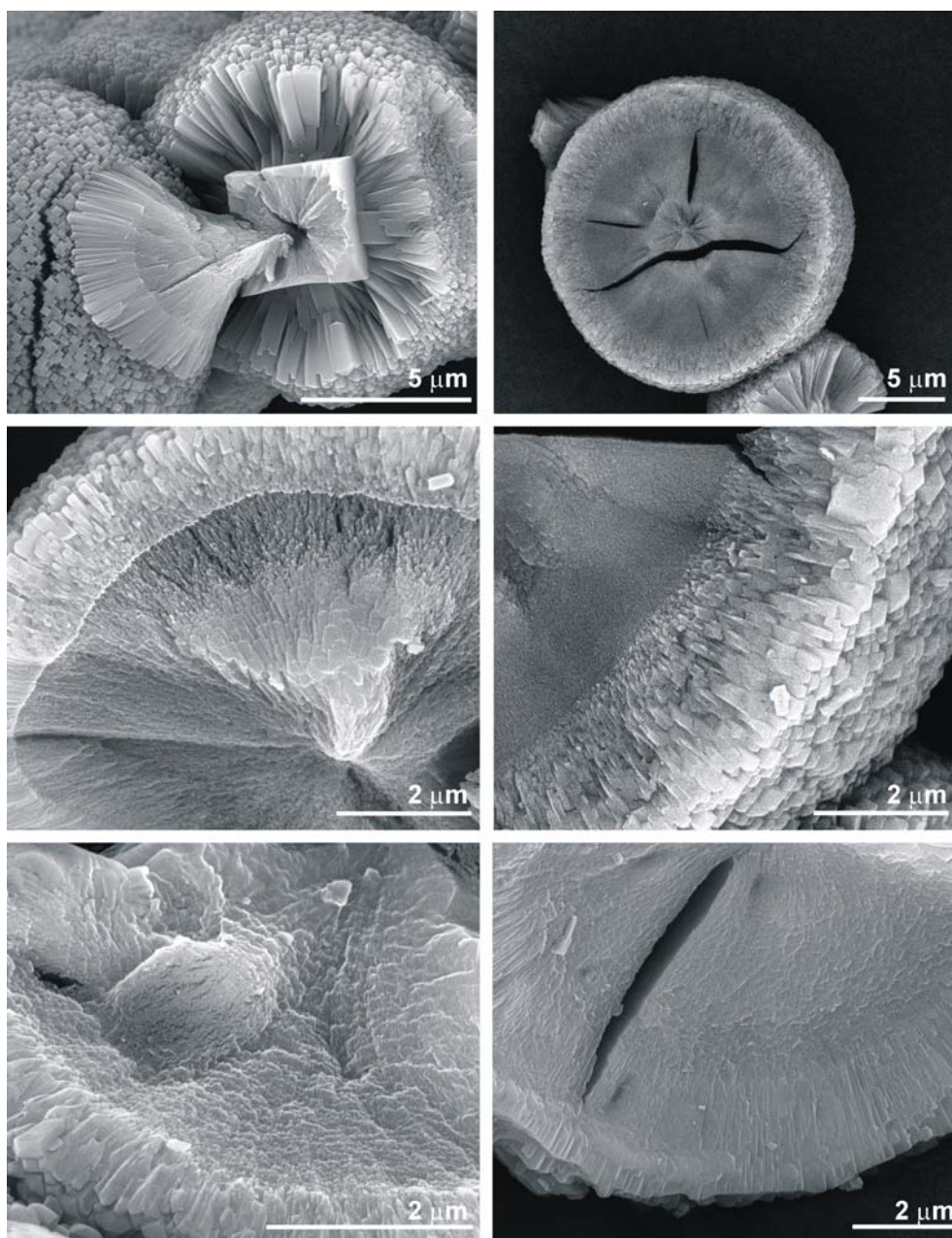


Fig. 6.10. SEM images of broken COD dumbbells (grown from 0.8 mM CaOx and 96 $\mu\text{g/mL}$ PAA). These images clearly support the core-shell structure of the dumbbells. Note that the crystallites constituting the core are smaller and are arranged layer by layer. (Refer to section 3.3.2).

Table 6.4. Experimental parameters of the double diffusion experiments in 0.5 to 4 wt.-% agar gel at pH 5.

Agar (wt.-%)	pH of gel		pH of 0.05M Ca		pH of 0.05M Ox		Yield (mg)
	before	after	before	after	before	after	
0.5	5.73	5.93	7.73	7.59	7.86	7.67	21.67
1	5.45	5.68	7.73	7.6	7.86	7.66	18.26
2	5.23	5.51	7.73	7.52	7.86	7.65	17.23
3	5.2	5.5	7.73	7.53	7.86	7.65	10.29
4	5.11	5.42	7.73	7.55	7.86	7.66	9.66

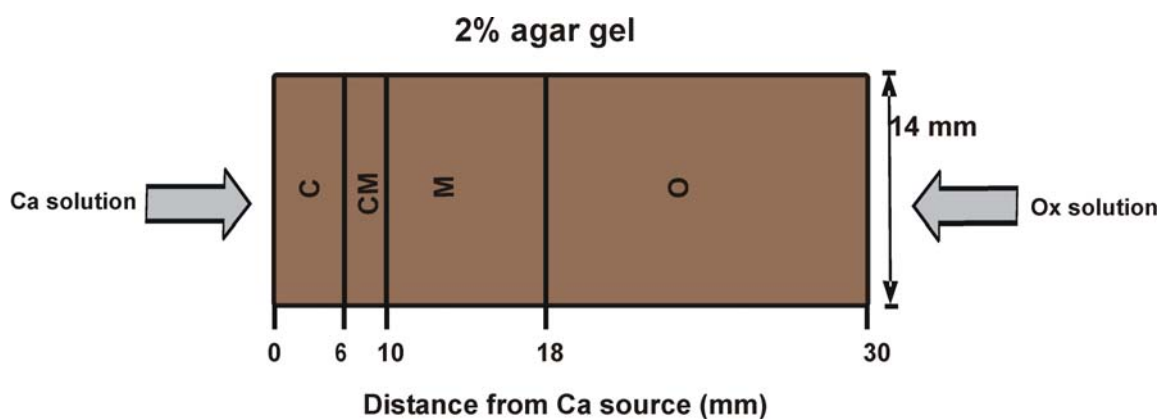


Fig. 6.11. The Liesegang band assignments in 2 wt.-% agar gel of 30 mm length.

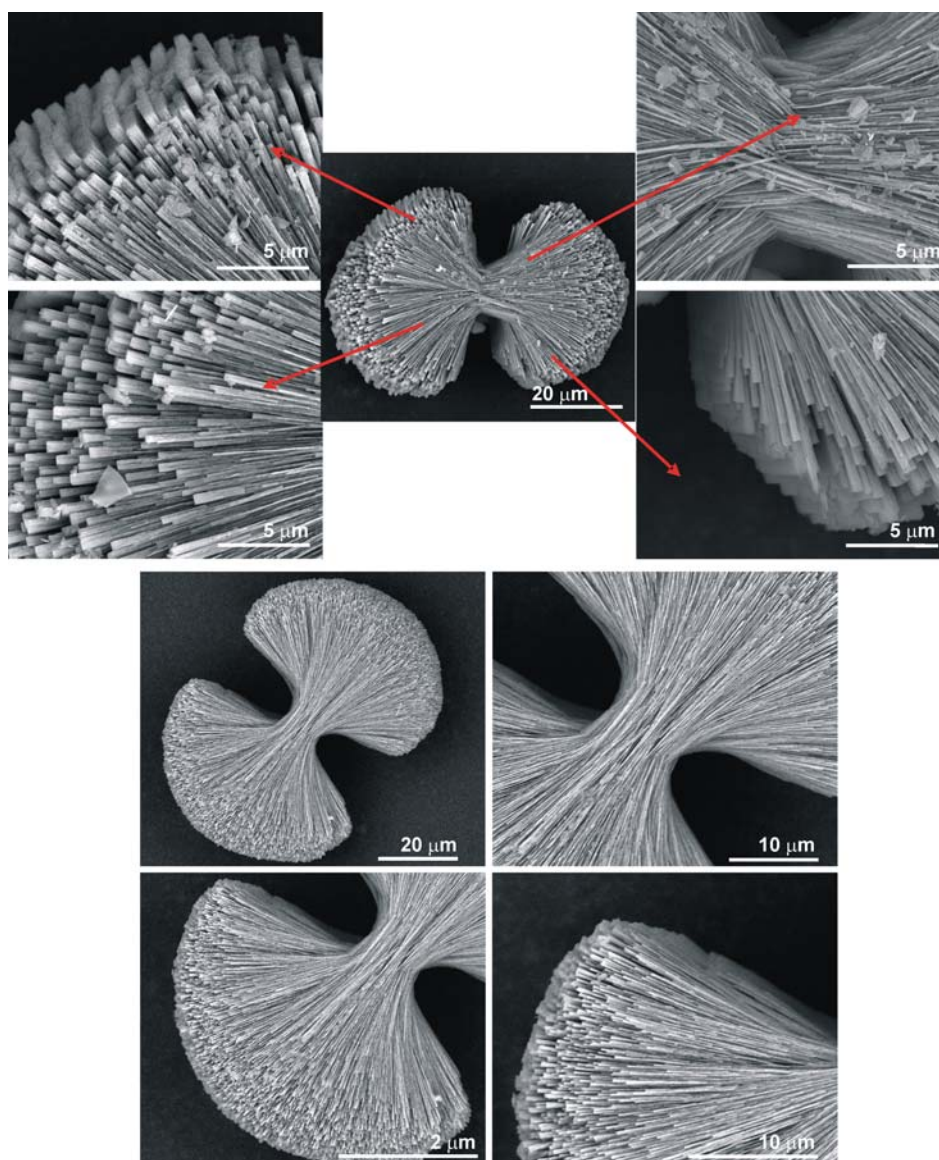


Fig. 6.12. SEM images of COM dumbbells grown in the CM band of 2% agar gel of pH 8.5 at 37 °C. The dumbbell shape is caused by the stacking of rectangular platy crystallites one above the other. Specific areas marked with red arrow from the figure on top are enlarged. For more details refer to section 3.4.1.2.

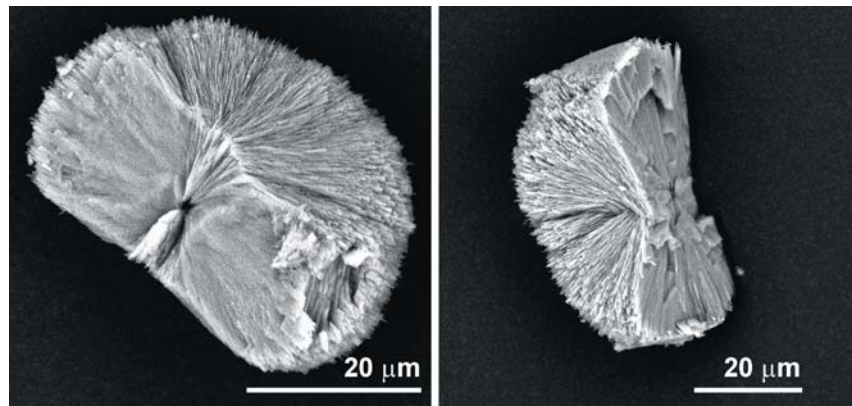


Fig. 6.13. SEM images of the cross-section of a 2D spherulite of COM formed in 2 wt.-% agar gel of pH 8.5 at 37 °C. See also figure 3.4.18.

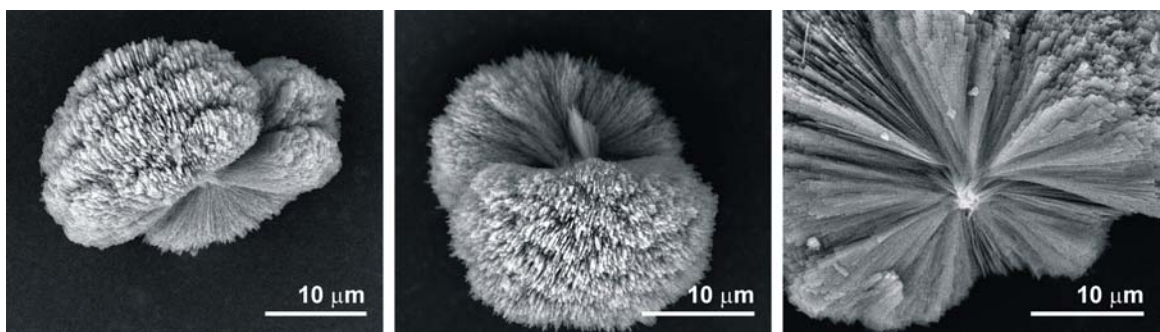


Fig. 6.14. SEM images of COM aggregates formed in 2 wt.-% agar gel of pH 8.5 at 37 °C. Note the layer by layer stacking of the crystallites. For more details refer to section 3.4.1.2.

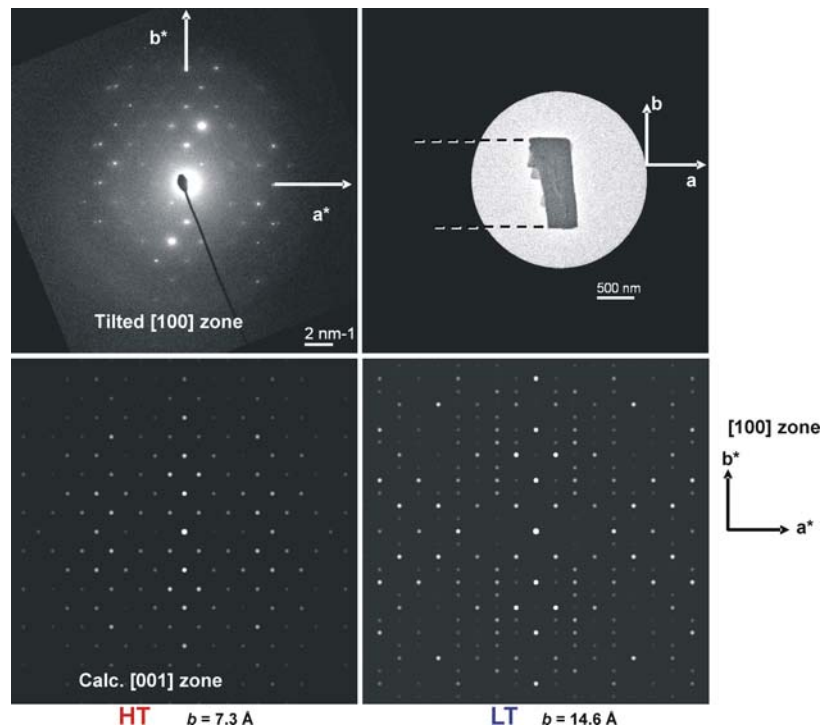


Fig. 6.15. ED pattern from [100] zone axis of a broken needle-like rectangular crystallite detached from the COM dumbbell obtained from the M band of 2 wt.-% agar gel of pH 8.5. This indicates the occurrence LT phase of COM (Simulated patterns of HT and LT phases of COM is shown at the bottom).

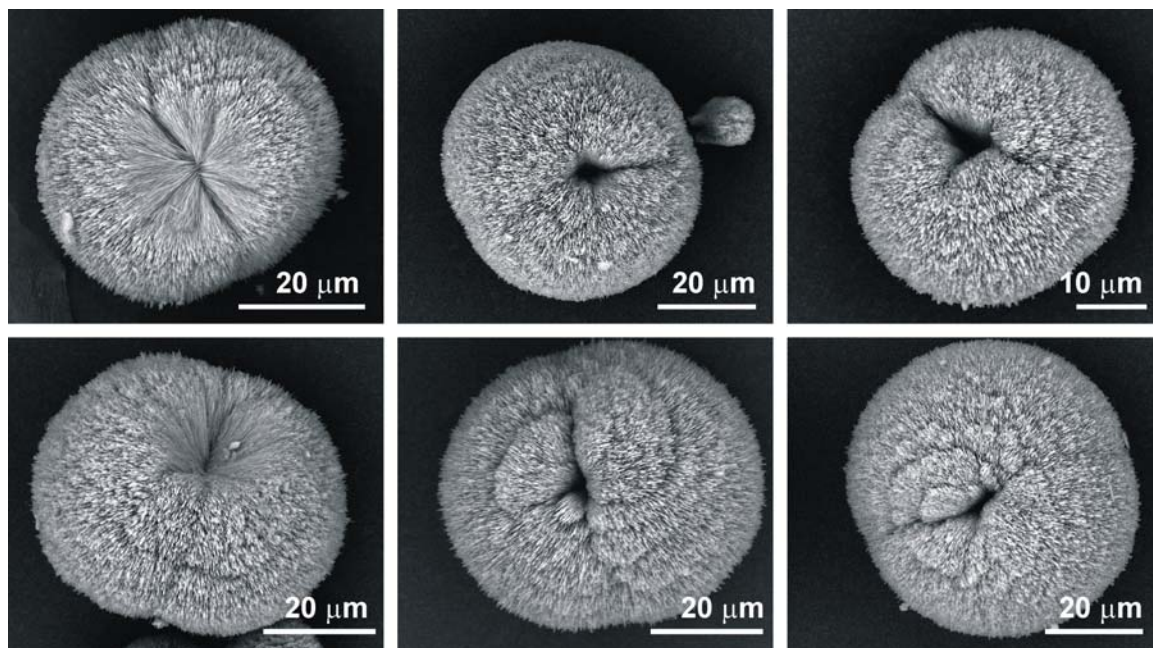


Fig. 6.16. SEM images of COM aggregates formed in 2 wt.-% agar gel of pH 8.5 at 37 °C. Layer by layer sacking of the crystallites occur to form a final 3D spherulite with an equatorial notch. For more details refer to section 3.4.1.2.

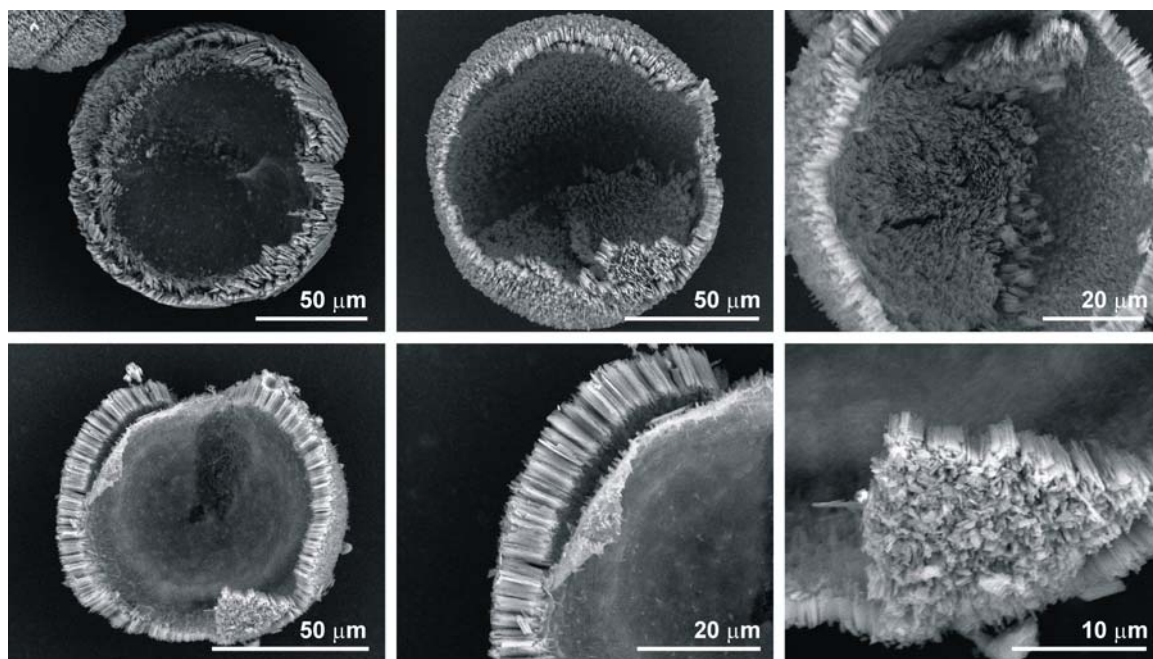


Fig. 6.17. SEM images of partially decalcified COM spherulites formed in 2 wt.-% agar gel of pH 8.5 at 37 °C. These images indicate that the inner region is decalcified faster than the outer layer. The outer layer consists of needle-like crystallites in random orientations. For more details refer to section 3.4.1.2.

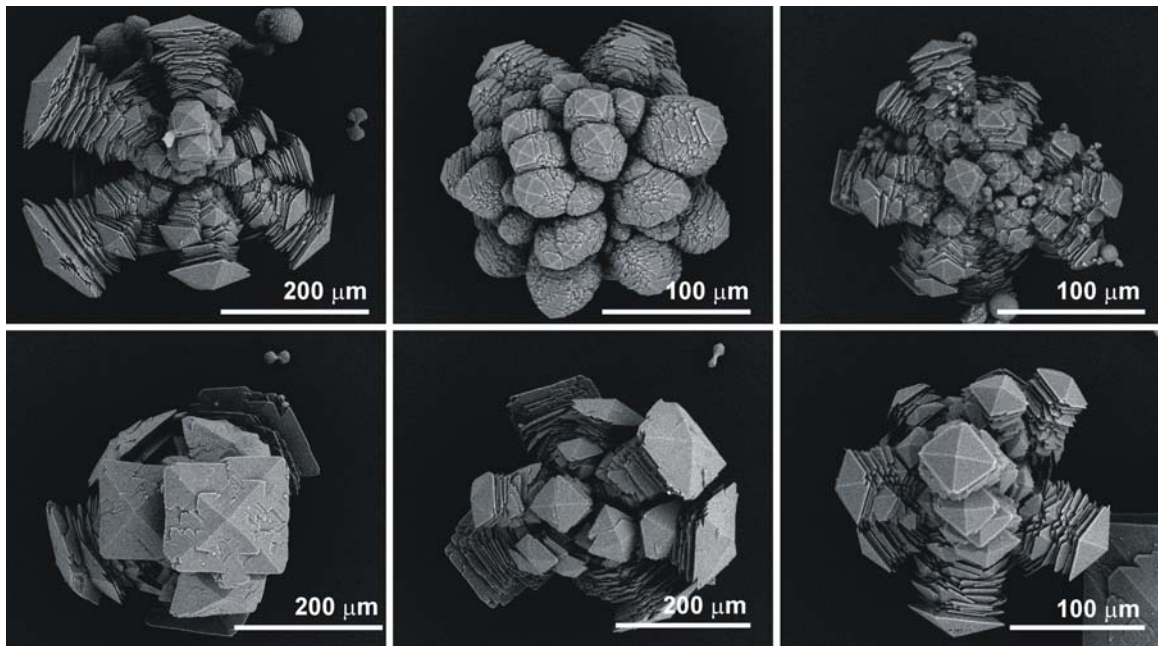


Fig. 6.18. SEM images of COD dendrites in the M band along with the COM aggregates obtained from 2 wt.-% agar gel of pH 8.5 (37 °C). For more details refer to section 3.4.1.2.

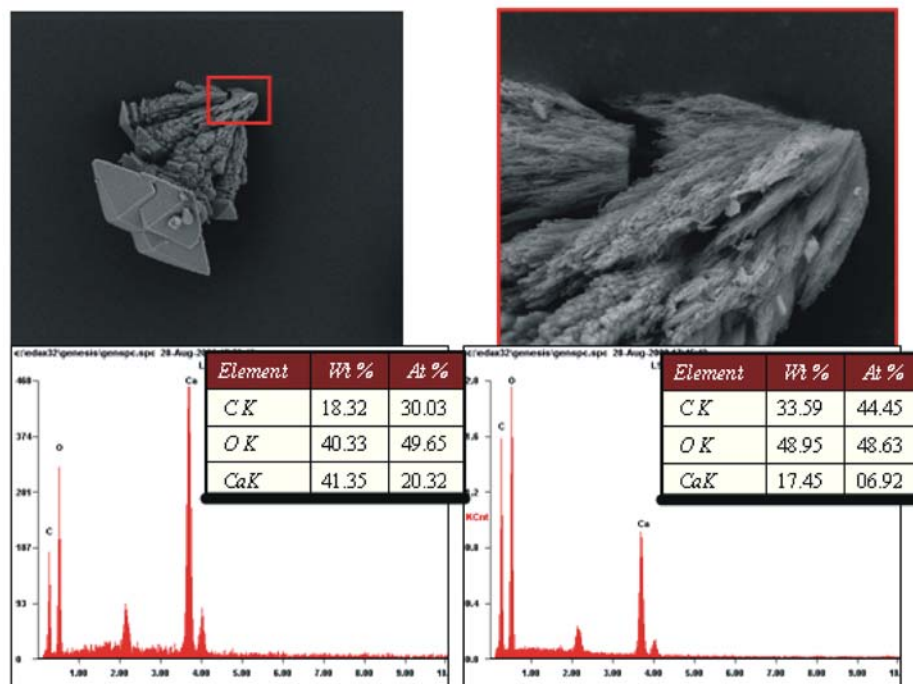


Fig. 6.19. SEM image with EDX analysis of a COD dendrite formed in the M band of 2 wt.-% agar gel of pH 8.5 (37 °C). The EDX is analyzed from the top most part and the base (red border) of the dendrite. (Wt.-% Ca:C for top = 2.257%, for bottom = 0.52%). It gives a notion that the base constitutes more organic material than the upper crystalline area. For more details refer to section 3.4.1.2.

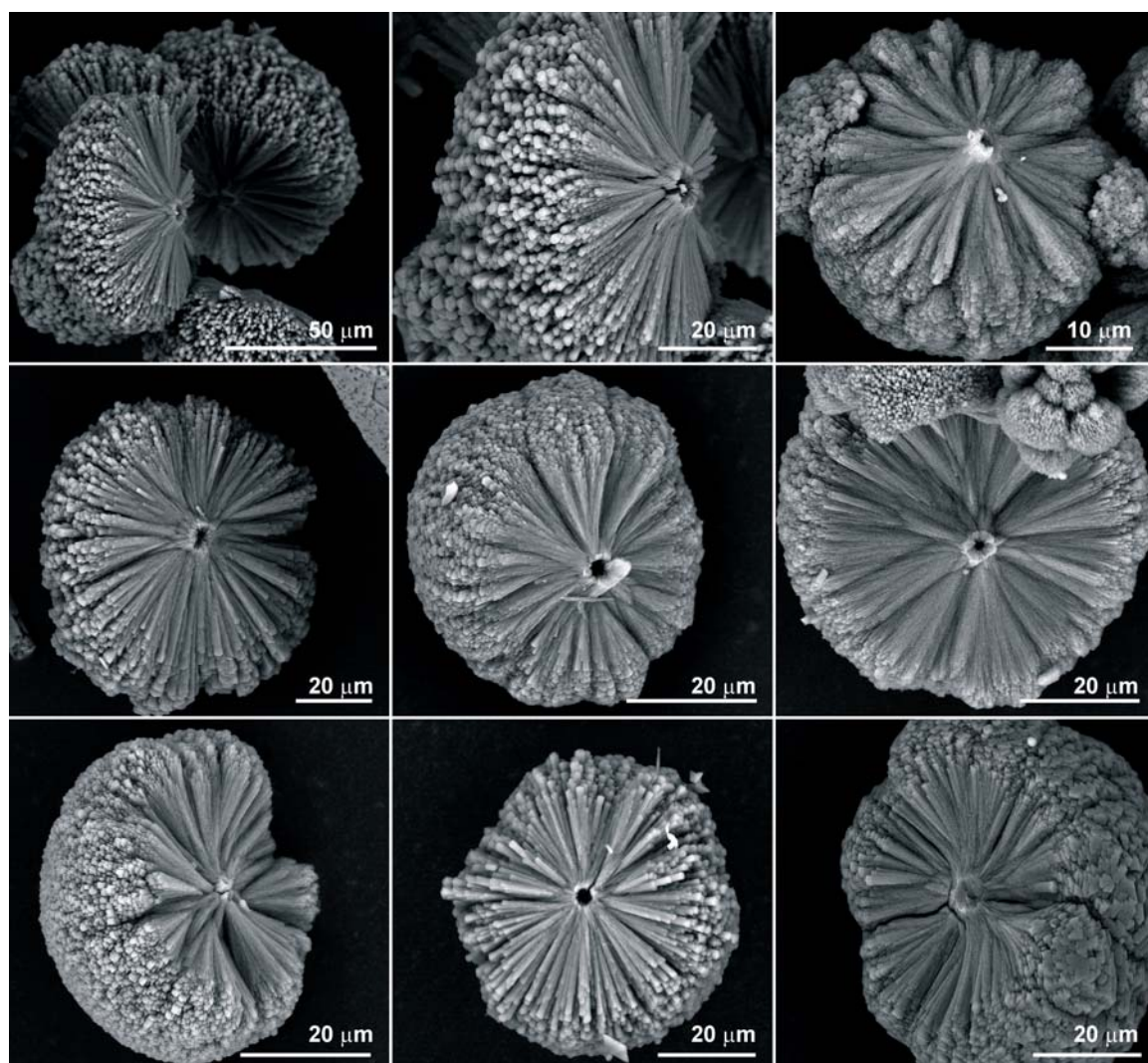


Fig. 6.20. SEM images of the cross-section of COD dumbbells grown in 2 wt.-% agar gel of pH 11.5 (Ca:Ox = 1:3). See also figure 3.4.40 under section 3.4.1.3. These consist of small tetragonal prismatic crystals.

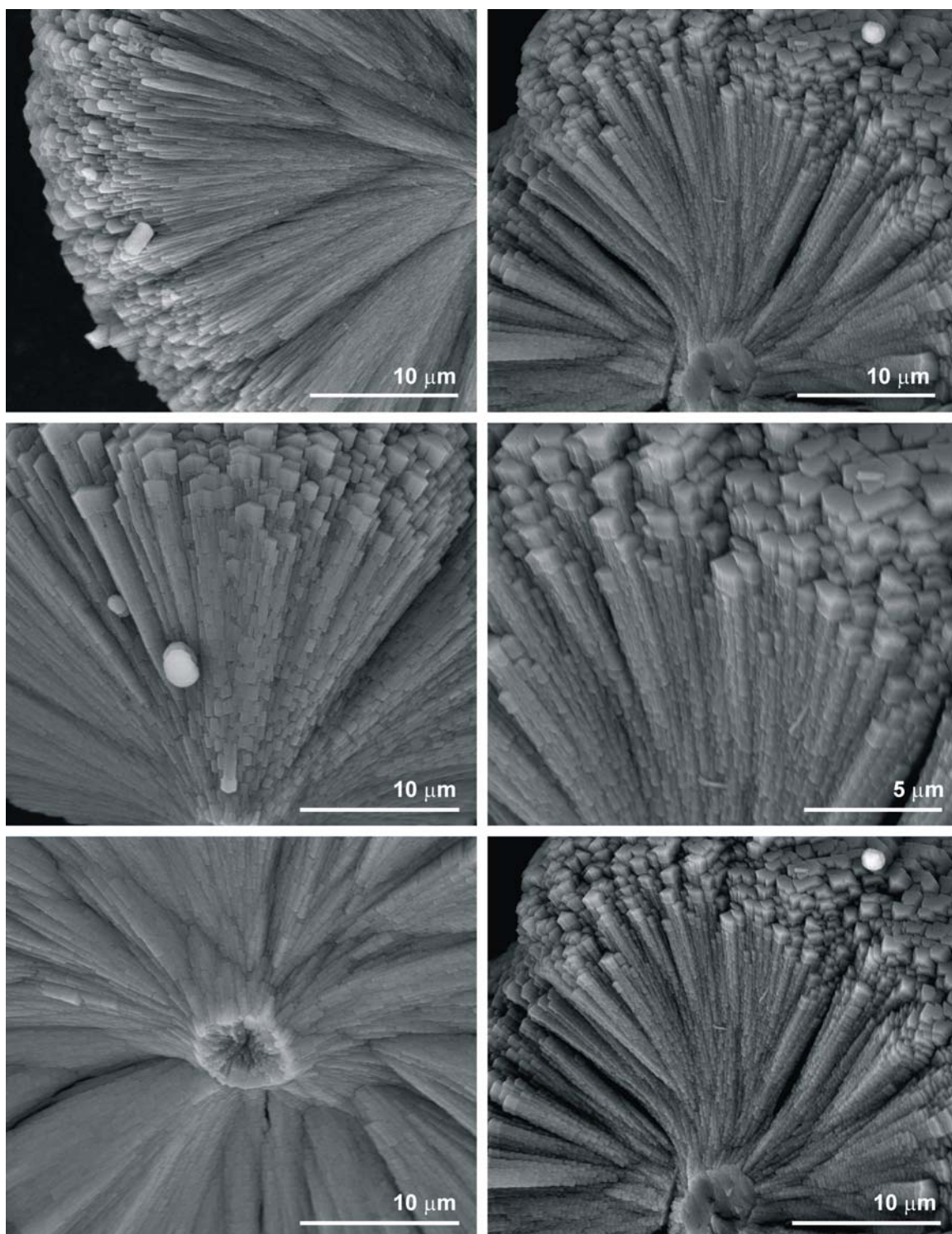


Fig. 6.21. SEM images of enlarged view of the cross-section of COD dumbbells formed in 2 wt.-% agar gel of pH 11.5 (Ca:Ox = 1:3). For more details refer to section 3.4.1.3. Compare these images with those in figure 6.4. Note that the tetragonal cross-section is not evident in the COD dumbbells grown in 2 wt.-% agar gel of pH 11.5.

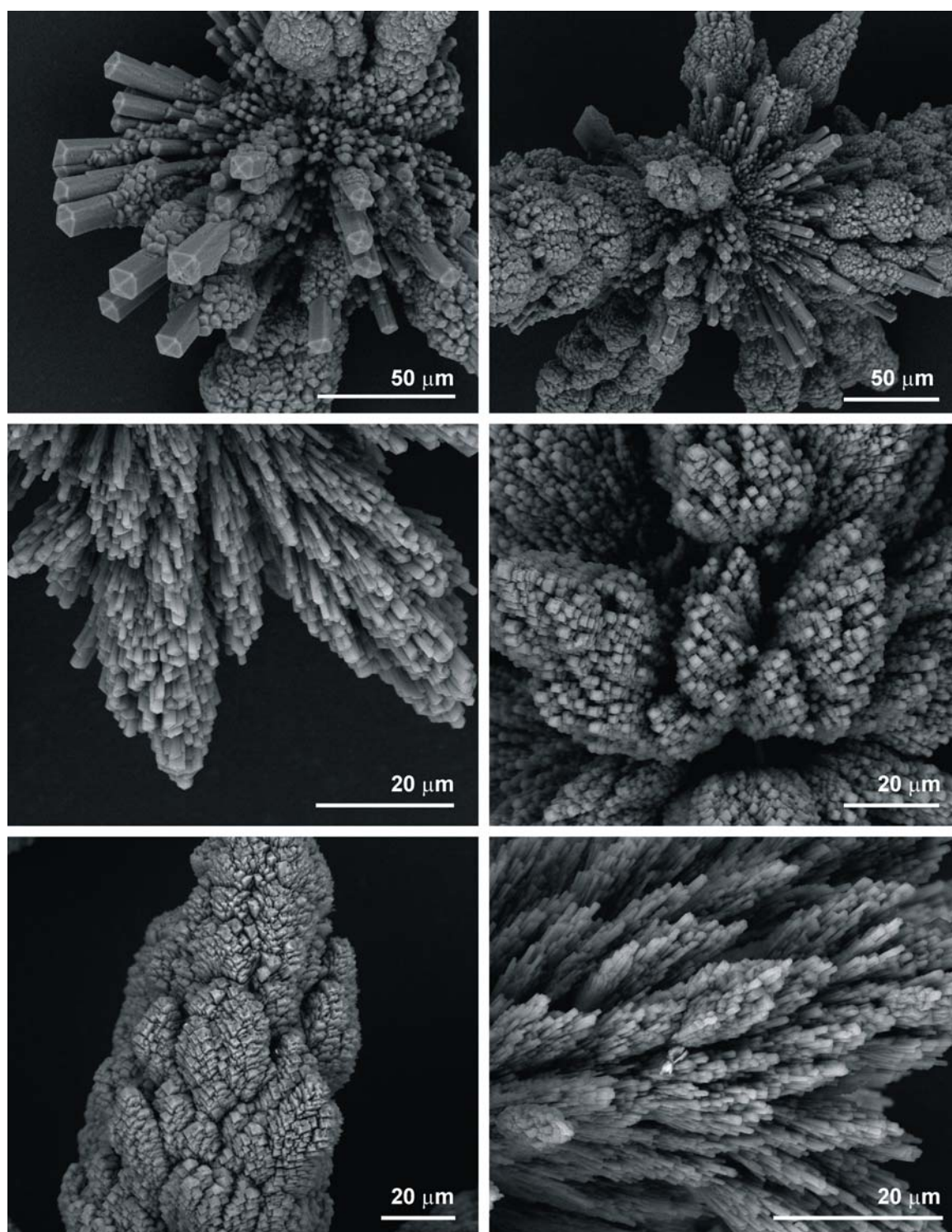


Fig. 6.22. SEM images of COD dendrites formed in 2 wt.-% agar gel of pH 11.5 (Ca:Ox = 1:1) at 37 °C. These dendrites consist of smaller tetragonal prismatic COD crystallites. Compare these dendrites with those formed at lower temperature as shown in figure 6.24. For more details refer to section 3.4.1.3.

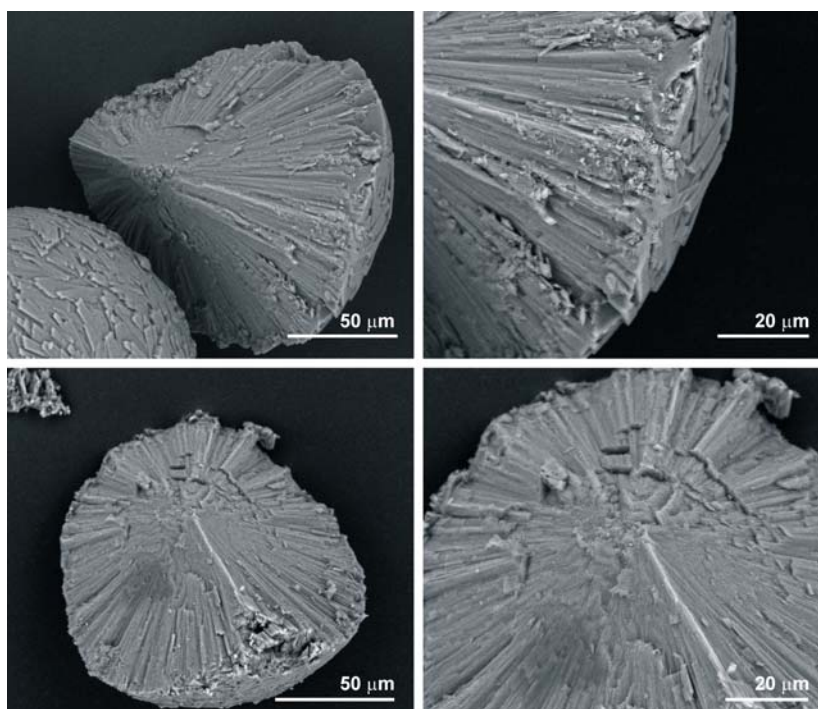


Fig.6.23. SEM images of the cross-section of COM spheres formed in 2 wt.-% agar gel of pH 11.5 (Ca:Ox = 1:1). Note that the arrangement of the core is different from the shell consisting of bigger columnar crystals. Complete spheres are shown in figure 3.4.49.

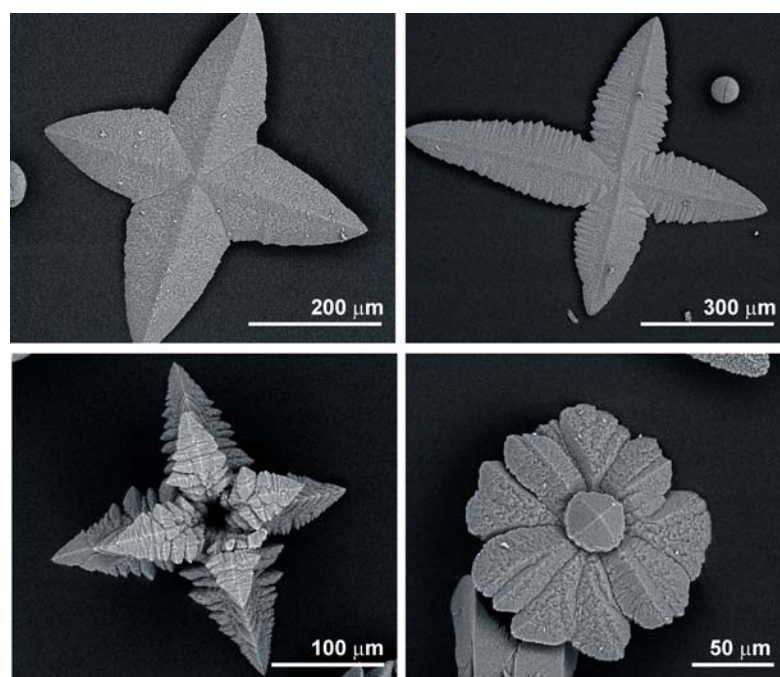


Fig. 6.24. SEM images of COD dendrites formed in 2 wt.-% agar gel of pH 11.5 (Ca:Ox = 1:1) at 25 °C. Note that these dendrites more simple than the dendrites formed in figure 6.22 which are grown under the same conditions except for a higher temperature.

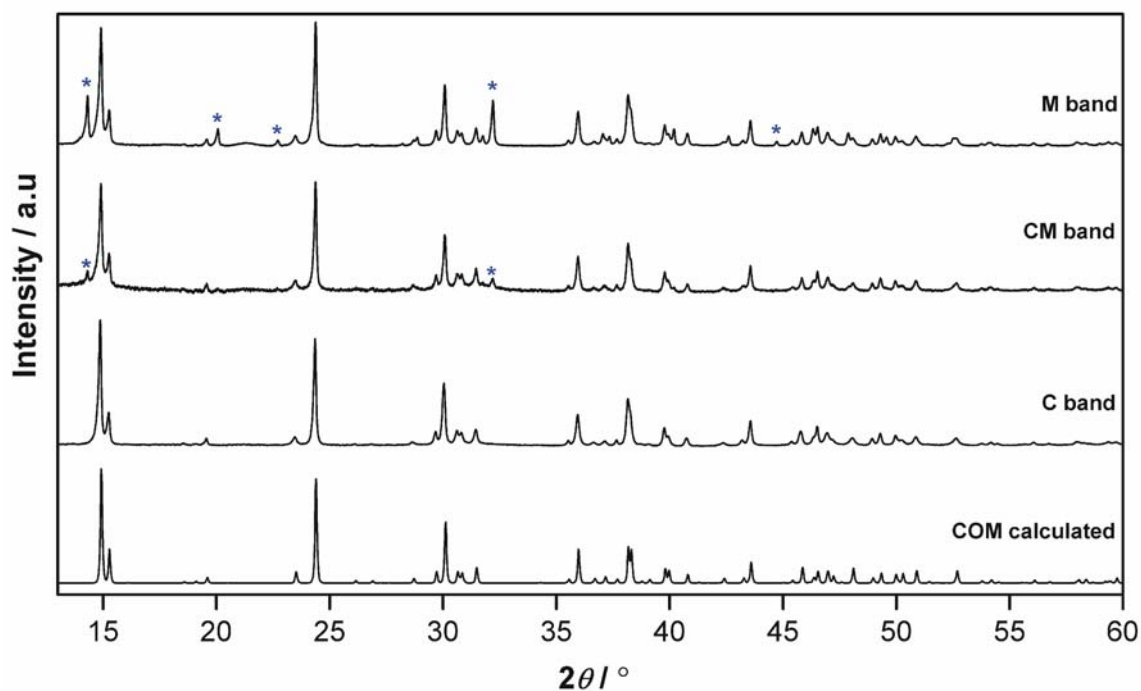


Fig. 6.25. XRD patterns of the aggregates formed in specific bands of 2 wt.-% agar gel of pH 8.5 (Ca:Ox = 1:3) at 37 °C in comparison with the calculated pattern for COM. The experimental data is measured using Cu $K\alpha_1$ - radiation. Note that the fraction of COD formed (reflection from COD are marked with *) increases on moving from C to M band. The estimated fraction of COD in the CM and M bands are approximately 29.25% and 36.57% respectively. This means, the M band which is formed earlier than CM and C bands have more fraction of COD aggregates. For more details, refer to section 3.4.1.4.

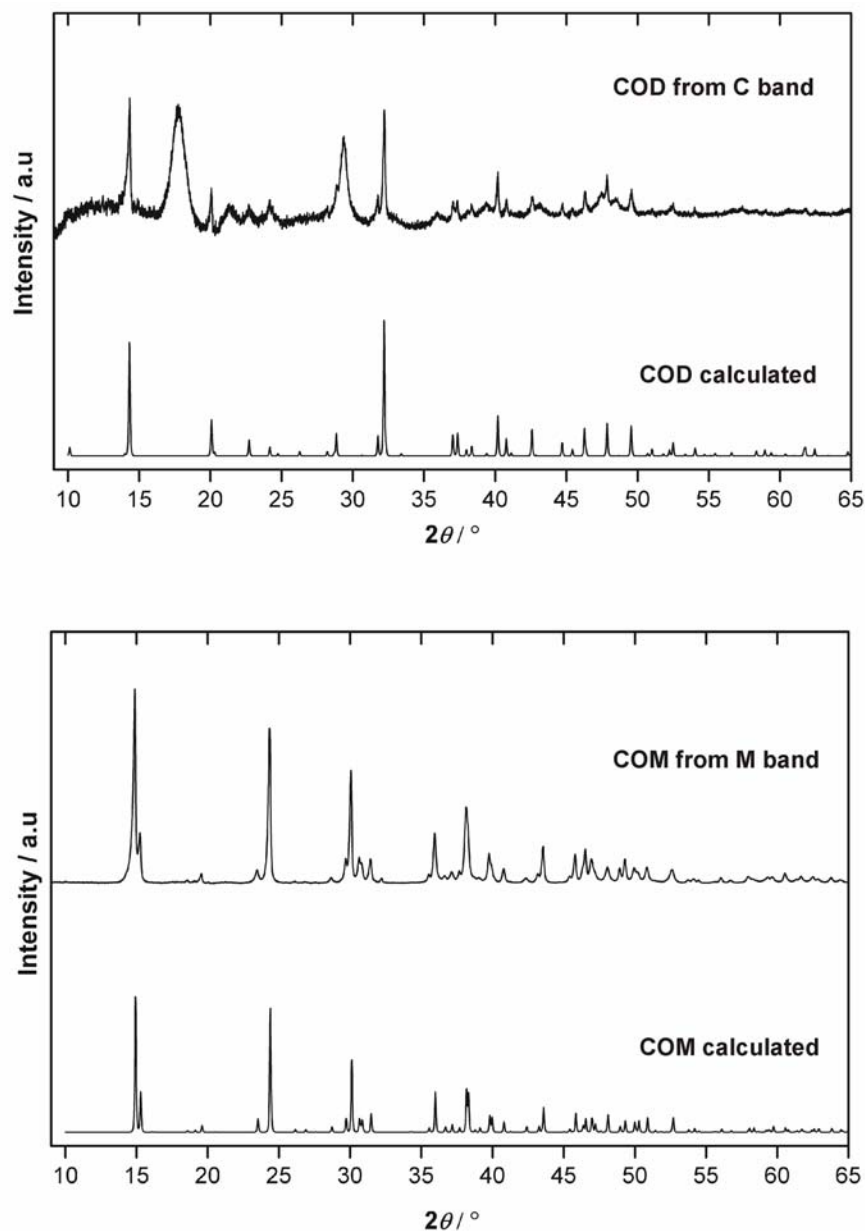


Fig. 6.26. XRD patterns of the aggregates formed in 2 wt.-% agarose gel of pH 11.5 (Ca:Ox = 1:1) at 20 °C. (Top) XRD pattern of COD obtained from the C band of the gel. (Bottom) XRD pattern of COM obtained from the M band of the gel. (Measured using Cu $K\alpha_1$ - radiation). The calculated XRD patterns of COD and COM are according to crystal structures proposed by Tazzoli [20]. For more details, refer to section 3.4.2.1.

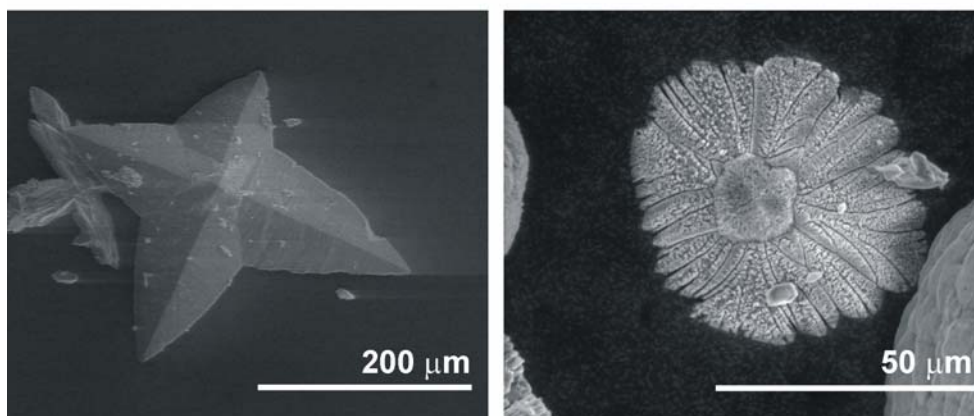
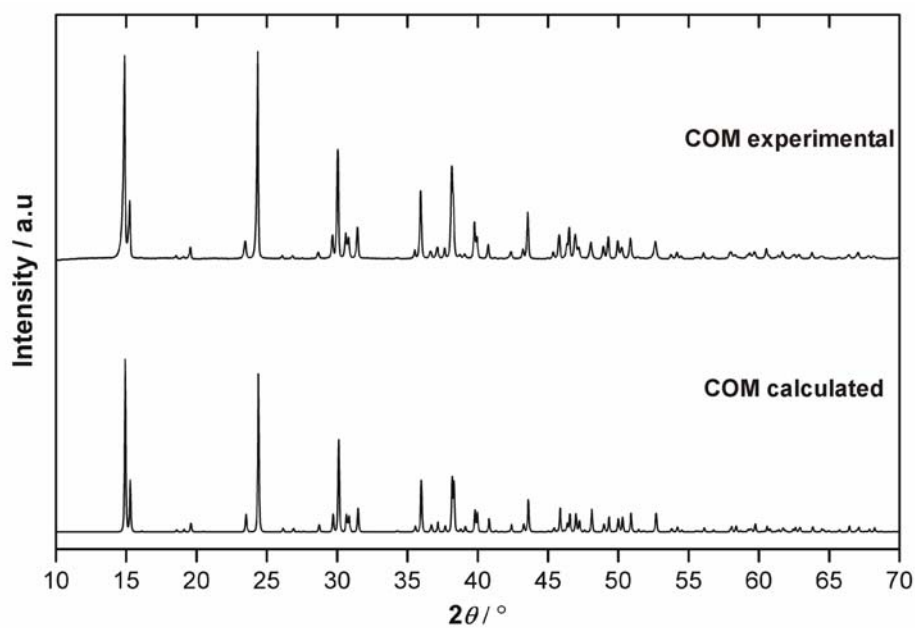


Fig. 6.27. (Top) XRD patterns of COM aggregates formed in 3 wt.-% carrageenan gel of pH 8.5 (Ca:Ox = 1:1) at 37 °C. (Measured using Cu $K\alpha_1$ - radiation). It is compared with the XRD pattern calculated according to crystal structure proposed by Tazzoli [20]. (Bottom) SEM images of the COD dendrites formed along with the COM aggregates in 3 wt.-% carrageenan gel of pH 8.5. For more details, refer to section 3.4.2.2.

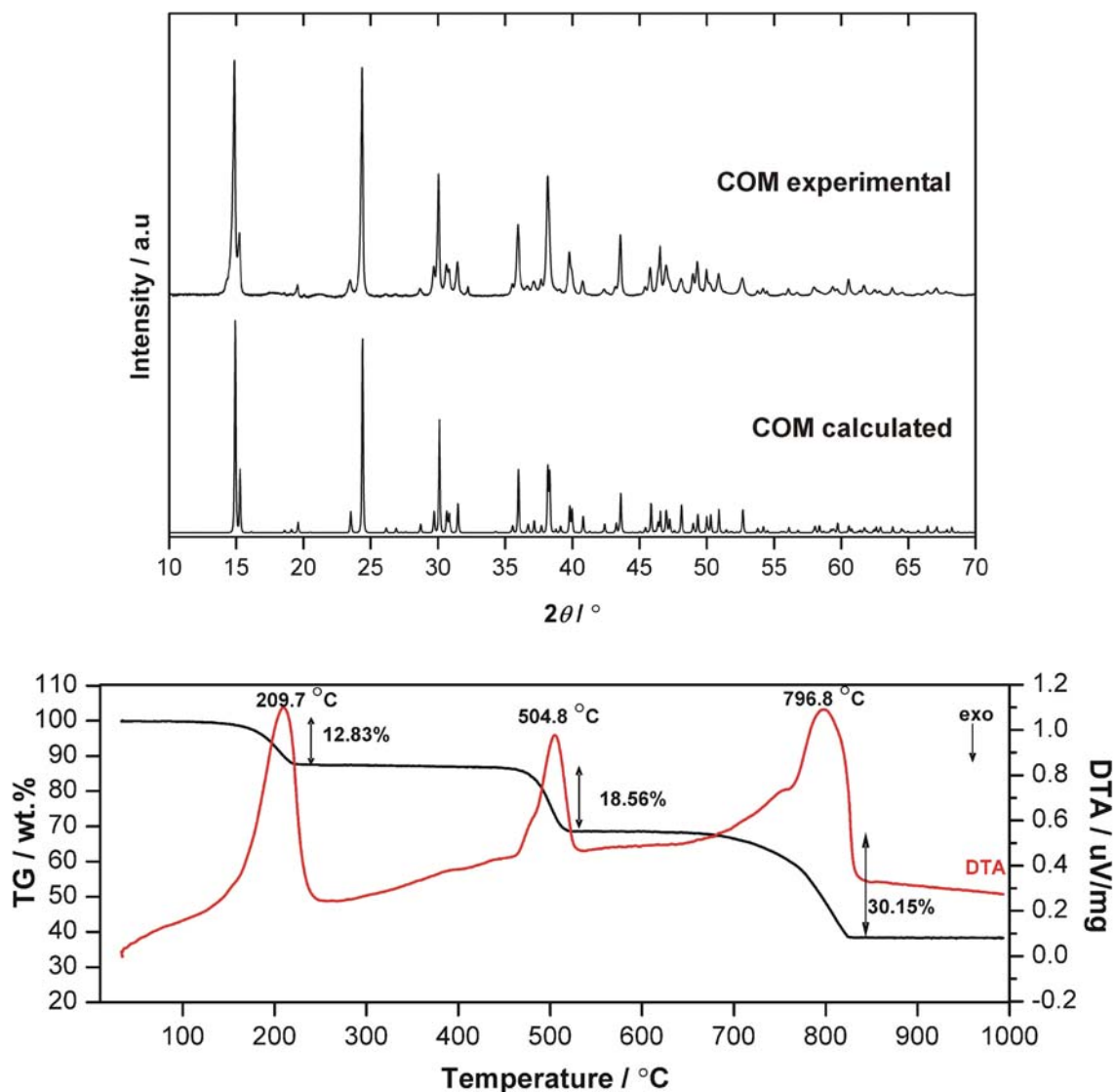


Fig. 6.28. (Top) XRD patterns of COM aggregates formed in 10 wt.-% gelatine gel of pH 5 (Ca:Ox = 1:1) at 25 °C. (Measured using Cu $K\alpha_1$ - radiation). It is compared with the XRD pattern calculated according to crystal structure proposed by Tazzoli [20]. (Bottom) TG/DTA of the COM aggregates formed in 10 wt.-% gelatine gel of pH 5. The thermogravimetric measurements were performed under nitrogen atmosphere with a heating rate of 10 K/minute. The three endothermic peaks correspond to loss of H₂O, CO and CO₂. For more details, refer to section 3.4.2.3.

CURRICULUM VITAE

PERSONAL DATA

Name : **Annu Thomas**
Date of Birth : 06 December 1979
Place of Birth : Calicut, Kerala, India
Nationality : Indian
Marital Status : Married

ACADEMIC QUALIFICATIONS

Duration	Course	Institute
Oct. 2005 – current	Ph.D Topic: Biomimetic Growth and Morphology Control of Calcium Oxalates	Max Planck Institute for Chemical Physics of Solids, Dresden (Germany)
Sep. 2001 – Apr. 2004	M.Sc. Chemistry (Physical Chemistry)	Mahatma Gandhi University, Kottayam (India)

RESEARCH PROFILE

Oct. 2005 – current Research Scholar under Prof. Dr. Rüdiger Kniep, MPI-CPfS, Dresden,
Germany
Topic: Biomineralization of Calcium Oxalates

Mar. 2005 - Aug. 2005 Research and Development Assistant under Dr. M. Eswaramoorthy,
Faculty Fellow, CPMU, JNCASR (Jawaharlal Nehru Centre for Advanced
Scientific Research), Bangalore, India
Topic: Template Assisted Synthesis of Mesoporous Materials

Sep. 2003 – Jan. 2004 Project Student under Dr. K. Vijayamohanam, Scientist, Physical
Chemistry Division, NCL (National Chemical Laboratory), Pune, India.
Topic: Polyimide Encapsulated CaCO₃ Nanoparticles- Synthesis,
Characterization and Applications

AWARDS AND SCHOLARSHIPS

2001 I Rank, Mahatma Gandhi University, B.Sc. Chemistry
2004 I Rank, Mahatma Gandhi University, M.Sc. Chemistry
2004 Junior Research Fellowship (JRF) of Council of Scientific and Industrial
Research (CSIR)
2008 Best Oral-Poster Presentation, Junior Euromat – The Federation of European
Material Societies at Lausanne, Switzerland

PUBLICATIONS & PRESENTATIONS

Oliver Hochrein, Annu Thomas, Rüdiger Kniep.

Revealing the Crystal Structure of Anhydrous Calcium Oxalate, Ca[C₂O₄], by a Combination of Atomistic Simulation and Rietveld Refinement.

Z. Anorg. Allg. Chem. **2008**, 634, 1826-1829.

Annu Thomas, Oliver Hochrein, Paul Simon, Wilder Carrillo-Cabrera, Rüdiger Kniep.
Biomimetic Growth and Morphology Control of Calcium Oxalates.

Junior Euromat – Oral Poster-Lausanne, Switzerland - July **2008**.

Annu Thomas, Oliver Hochrein, Rüdiger Kniep.

Control of the Crystal Growth of Calcium Oxalates.

ECSSC XI, 2007, Abstracts, W 20. (Poster Abstract- European Conference on Solid State Chemistry-Caen, France - Sept. 2007).

Annu Thomas, Oliver Hochrein, Rüdiger Kniep.

Control of the Crystal Growth of Calcium Oxalates.

Z. Anorg. Allg. Chem. **2006**, 2109. (Poster Abstract -13.Vortragstagung-Modellierung in der Festkoerper und Materialchemie-Aachen, Germany - Sept. 2006).

Annu Thomas, Oliver Hochrein, Rüdiger Kniep.

Dynamic Processes during composite formation – Simulation and Experiment.

Baltic Boat Conference – (Oral Presentation) Sweden - May, **2006**.

Annu Thomas, Balakrishnapillai Premlal, Muthusamy Eswaramoorthy.

Synthesis of mesoporous Zn–Al spinel oxide nanorods with membrane like morphology.

Mat. Res. Bullet., **2006**, 41, 1008–1014.

SCHOOLS ATTENDED

2nd Bilateral Workshop on Solid State and Materials chemistry-Dresden, MPI-CPfS – July 17-19, **2006**.

The Spring 2006 Seminar of the International Max Planck Research School, Institute for Low Temperature and Structure Research, Wroclaw, Poland, May 22-25, **2006**.

Versicherung

Hiermit versichere ich, dass ich die vorliegende Arbeit ohne unzulässige Hilfe Dritter und ohne Benutzung anderer als der angegebenen Hilfsmittel angefertigt habe; die aus fremden Quellen direkt oder indirekt übernommenen Gedanken sind als solche kenntlich gemacht. Die Arbeit wurde bisher weder im Inland noch im Ausland in gleicher oder ähnlicher Form einer anderen Prüfungsbehörde vorgelegt.

Die vorliegende Dissertation wurde unter Betreuung von Herrn Prof. Dr. Rüdiger Kniep in der Arbeitsgruppe Anorganische Chemie im Max-Planck-Institut für Chemische Physik fester Stoffe im Rahmen der International Max Planck Research School in Dresden angefertigt.

Dresden, den 30.07.2009

(Annu Thomas)